NASA Contractor Report 3709

Design, Implementation and Flight Testing of PIF Autopilots for General Aviation Aircraft

John R. Broussard

25

25th Anniversary
1958-1983

NASA

NASA Contractor Report 3709

Design, Implementation and Flight Testing of PIF Autopilots for General Aviation Aircraft

John R. Broussard
Information & Control Systems, Incorporated
Hampton, Virginia

NASA

National Aeronautics
and Space Administration

**Scientific and Technical
Information Branch**

1983

TABLE OF CONTENTS

LIST OF TABLES

LIST OF FIGURES

page

I. INTRODUCTION

Commercially available General Aviation (GA) autopilots are currently in transition from an analog circuit system to a state-of-the-art computer implemented digital flight control system (Ref. 1). Advantages of the digital autopilot are well known. These advantages include enhanced modes, self-test capacity, fault detection and greater computational capacity. A digital autopilot's computational capacity can be used to full advantage by increasing the sophistication of the digital autopilot's chief function, stability and control. Direct digital design techniques along with proven computerized design and evaluation tools should be used to efficiently develop low-iteration rate advanced digital autopilots.

The General Aviation Terminal Area Operation Research (GATOR) program of the National Aeronautics and Space Administration is developing and evaluating advanced flight control and display concepts that make use of the recent advances in digital flight control theory, digital control hardware and electronic displays. The GATOR program uses the Princeton Avionics Research Aircraft to flight tests digital controllers programmed in the ROLM 1666 digital flight computer. Figure 1 shows the flight tests operation facilities. Recent work in the GATOR program evaluating electronic displays has been reported in Ref. 2.

The purpose of this report is to present the development, design and flight test results of a proportional-integral-filter (PIF) digital auto-pilot design flown on the research aircraft. The PIF control law is a direct digital design operating at a low iteration rate (10 cycles per sec) that employs modern multivariable control theory to compute control gains. A basic block diagram of the control law is shown in Fig. 2. The PIF control law is specially structured to be designed using linear models but implemented to control and stabilize non-linear aircraft dynamics. The PIF control law does not require trim information in flight. The PIF control law has features to accommodate computation delay, suppress high frequency noise and track commands using integral control. An earlier version of PIF has been investigated and successfully flight tested in the VALT autoland program (Refs. 3 and 4). The new feature is the command model shown in Fig. 2 which is different for each autopilot mode.

A. AUTOPILOT SUMMARY

The General Aviation 3-axis PIF autopilot incorporates recent theoretical developments in multivariable command generator tracking to easily design roll select, pitch select, heading select, altitude select and glideslope/localizer capture and hold autopilot modes. The roll and

pitch select autopilots hold the aircraft attitude that exists at engage and can track pilot input from a pitch wheel and roll turn knob. In the heading select mode, the pilot enters in the desired heading, the autopilot command model commands the PIF control law to bank the aircraft, fly a coordinated turn in the shortest direction to the new heading, and roll the aircraft out of the turn to smoothly capture the new heading. In the altitude select mode, (which currently exists in abbreviated form in only the most sophisticated and expansive commercial GA autopilots), the pilot enters in the desired altitude and the autopilot command model commands the PIF control law to gradually ascend (or descend) the aircraft, establish a constant rate of climb (or descent) then smoothly capture and hold the new altitude. The glideslope/localizer autopilot modes use command models to construct horizontal and vertical paths the aircraft flys to capture and track precision Instrument Landing System (ILS) beams. These approach modes have a built-in potential to operate under and take advantage of the microwave landing system (MLS).

The PIF autopilot uses a standard set of General Aviation instrument sensors; rate gyros, accelerometers, attitude gyros, barometeric altimeter, ILS beam receiver and airspeed sensor. Analog prefilters and digital complementary filters are used to smooth sensor output for improved ride quality.

B. PIFCGT COMPUTER PROGRAM

A second purpose of this investigation is the development and documentation of an easy-to-use computer aided design program for PIF. A PIF autopilot design computer program (PIFCGT) which can accommodate most GA aircraft dynamics is described in Ref. 5.

All the designs described in this report are obtained with the PIFCGT program. The PIFCGT program uses the NASA Langley developed ORACLS subroutine package, Ref. 6, to solve matrix equations encountered in modern control design. The PIFCGT program internally constructs linear aircraft models from user supplied nondimensional stability derivatives. The user design parameters are the quadratic weights in the Linear Quadratic Regulator Cost function. Evaluations are performed using closed-loop equivalent s-plane eigenvalues and simulations using linear aerodynamics.

C. DISCUSSION OF RESULTS

All autopilot modes were successfully programmed and successfully flight-tested using a sampling interval of 0.1 seconds. Flight tests at different airspeeds were performed in heavy, medium and light turbulence. The PIFCGT program was used to successfully adjust and completely redesign some autopilot modes during flight testing. In some instances flight testing, redesign, flight code reconfiguration and flight testing of the modifications occurred daily. Optimal control quadratic weight selections based on in-flight pilot comments of preference among different gain sets were performed using this procedure. An analog prefilter study was performed

2

using different filter time constants to suppress aliasing effects. An analog prefilter time constant of 0.1 sec gave a good compromise between noise suppression and closed-loop stability.

D. ORGANIZATION OF THE REPORT

There are a number of equations in the report and an attempt is made to clarify the importance of each equation. An equation with "( )" around the equation number is a standard result. An equation with "[ ]" around the equation number is an important equation useful in understanding and implementing the PIF control law. An equation that is in a bordered region (such as the PIF equations - Eqs. 56 - 58) is an equation that was actually programmed in the onboard computer.

Chapter II presents an overview of the aircraft, PIF control law and flight computer. A summary of advanced commercially available autopilot functions is also given. Chapter III is a detailed mathematical discussion of the theory behind the PIF control law. A complete derivation of the control law is presented. The chapter ends with a block diagram of the PIF software organization programmed in the ROLM computer. The command model parameters, control gains, filter gains and design quadratic weights are detailed in Chapter IV. Time histories from linear simulations show the command model and aircraft response for different autopilot modes. Chapter V discusses the flight tests results. Chapter VI summarizes the report and suggest areas where further developments not within the scope of this work could improve the PIF autopilot. Research results which advance the state-of-the-art of the linear quadratic regulator (Refs. 7, 8 and 9, for example) advanced the state-of-the-art of the PIF control law. Linear and nonlinear aircraft equations of motion are presented in Appendix A. The NAVION aircraft aerodynamic model and stability derivatives used in this report are listed in Appendix B. The linear and nonlinear command generator models and command control systems are described in Appendix C. The relationship between feedforward control and trim is reviewed in Appendix D. Appendix E discusses discrete structures useful in understanding how the PIF discrete plant representation is constructed.

II. CONTROL SYSTEM OVERVIEW

A. VEHICLE, SENSOR, AND CONTROL CHARACTERISTICS

The PIF autopilots are designed for the Princeton Avionics Research Aircraft (ARA). The Princeton ARA is a NAVION airplane and is typical of a complex single engine general aviation aircraft. Independent control of the aircraft is provided by commands to the elevator, ailerons, rudder, throttle, and direct-lift flaps. The autopilot designs are restricted to use elevator, ailerons and rudder. These fast acting control surfaces are driven by hydraulic servos orginally fitted to the B-58 aircraft.

Characteristics of the control actuators are summarized in Table 1 (taken from Ref. 10). The actuator dynamics are not included in the PIF design model. The time constants in Table 1 presume the actuators can be modeled by a first order lag. The autopilot designs are allowed full control authority displacement. The maximum specific moments are given at 53.8 m/s airspeed. The aerodynamic model for the NAVION is given in Appendix B. The estimated stability derivatives in the model are only available at one flight condition (44.0 m/s airspeed, straight and level flight) in the aircraft's normal operating speed range (33.3 m/s (65 kt) to 69 m/s (135 kt)). All the autopilot control laws are designed using the aerodynamic model at the one available flight condition. This restriction is typical of the type of aircraft model information available to commercial general aviation autopilot designers. Step response comparisons in Figs. 3 and 4 between the linear model and the aircraft response also shows the linear model only "approximately" matches the aerodynamic response, another typical autopilot design uncertainty.

Neglecting disturbance inputs, the nonlinear equations which govern vehicle motion are presented in Appendix A, Eqs. 73 to 76. The total aircraft states and controls can be divided into nominal and perturbation components

$$\underline{x} = \underline{x}_o + \Delta\underline{x} \tag{1}$$

$$\underline{u} = \underline{u}_o + \Delta\underline{u} \tag{2}$$

The linear time-invariant model of the perturbation states of the aircraft is derived from the nonlinear equations at the design flight condition as shown in Appendix A and has the following form

4

$$\Delta \dot{\underline{x}} = A \ \Delta \underline{x} + B \ \Delta \underline{u} \tag{3}$$

$\Delta \underline{x}$ is the rigid-body state vector of the aircraft

$$\Delta \underline{x}^T = [\Delta u \ \Delta w \ \Delta q \ \Delta \theta \ \Delta x \ \Delta z \ \Delta v \ \Delta r \ \Delta p \ \Delta \phi \ \Delta \psi \ \Delta y] \tag{4}$$

and $\Delta \underline{u}$ is the control vector of the aircraft previously discussed,

$$\Delta \underline{u}^T = [\Delta \delta_e \ \Delta \delta_a \ \Delta \delta_r] \tag{5}$$

The NAVION research aircraft is fully instrumented and all sensor outputs can be recorded at the digital control law sampling interval. The PIF autopilot designs are restricted to only use sensors commercially available in typical avionics packages. These sensors include angular rate gyros for all three axis, lateral and vertical body-axis accelerometers, attitude and heading gyros, indicated airspeed, barometric altimeter, localizer/glideslope angular deviation measurements and an indication of when the aircraft crosses the outer marker (see Chapter V, Section D). Measurement noise standard deviations and bias standard deviations estimated from in-flight recordings are shown in Table 2 for these sensors. Sensors available, but not explicitly used in the design, include angle-of-attack and sideslip vanes, radar altimeter, and range, azimuth and elevation from a two-way ground-to-air digital data link to radar. The autopilot configuration, command model designs and feedback gains would change if these sensors were made available.

The general arrangement of the ARA system is shown in Fig. 5. The aircraft is flown by a two-man crew during all research; a safety pilot and an evaluation pilot. The safety pilot can disengage the control system at any time. Disengage software is also included in the control software for some flights. The control/display panel is illustrated in Fig. 6. The interface between the evaluation pilot and the autopilot is made through the keyboard/display shown at the bottome center of Fig. 6.

B. ROLM COMPUTER CHARACTERISTICS

The ROLM 1666 computer is used to implement the PIF control law. The ROLM 1666 is a state-of-the-art digital flight computer designed to MIL-E-5400. The control law is implemented in a high level language (FORTRAN), operates in floating point arithmetic, and can be modified easily using text editors. The existence of these features permitted efficient and rapid implementation (1 week for ALT SEL, HDG SEL, ROLL SEL, and PITCH SEL, 1 week for APR GS and APR LOC) and evaluation of the autopilot modes. Table 3 presents the main features of the ROLM 1666 (taken from Ref. 10).

C. SAMPLE SURVEY OF COMMERICALLY AVAILABLE AUTOPILOTS

A sample survey of advanced 3-axis commercially available autopilots is shown in Table 4. The results in the survey are taken from autopilot manuals, Refs. 11 - 16 and a NASA Langley Sponsored GA Survey report, Ref. 17. Also shown in the last row in Table 4 are the PIF controller modes whose designs are discussed in this report. Most of the autopilots shown in Table 4 have become available within the last three years. Some show trends in the direction of full digital implementation.

An autopilot is an add-on feature to GA aircraft. The units in an autopilot typically include actuator servos, sensors, mode controller, displays and an autopilot computer. The mode controller is the interface between the desires of the pilot and the available features of the autopilot shown at the top of Table 4. Autopilots are usually not command augmentation systems. In most operations the pilot pushes a button to activate the desired mode, then the autopilot holds the current flight conditions of the aircraft (θ, ϕ, ψ, z etc.). The capability to maneuver the aircraft is available in advanced autopilots through a select feature. The pilot enters a new desired condition (altitude, heading, pitch) using alphanumerics, heading bug or wheel and the autopilot commands the aircraft surfaces to cause the aircraft to satisfy the new flight condition.

How most commercial autopilots are designed and implemented in hardware and software is not public information. One available source for autopilot design techniques is Ref. 18. Results in Ref. 18 indicate that commercial autopilots tend to be nested regulator designs. A pitch hold mode, when activated, forms a regulation error between the pitch angle at the time of engage and the pitch angle measured thereafter by the attitude gyro. The error is fed back through a gain to the elevator. The gain is easily designed by trial and error. Other longitudinal states are rarely fed back for improved stability unless the aircraft is aerodynamically deficient in some respect (poor short period damping, etc.). The economics dictate using few sensors. An altitude hold mode is nested into the pitch hold mode by forming an altitude command error and using the error to adjust the pitch command. A similiar operation is performed with IAS hold. Nested designs usually retain control feedback gain values for each loop even after engaging the next control feedback loop in the hierachy. References 11-16 indicate that altitude select in advanced autopilots is performed through a series of automatic mode switches: vertical speed hold to altitude capture to altitude hold.

The lateral directional modes have a similiar nested design. Roll angle error is fed back to aileron. A yaw damper is used to feedback washed-out (high pass filtered) yaw rate to rudder to improve Dutch roll damping. A nested heading hold is performed by feeding back heading error to the roll command. An additional outer loop is made during landing approaches by feeding back localizer deviation error to the heading command.

D. PIF CONTROL LAW

The PIF control law uses a different design approach from commercially

6

available autopilots. A summary of control law features are as follows:

- The multivariable PIF control law is designed using modern control theory and is a direct digital design.

- The control law is composed of five basic units: a command generator, state feedback for stability, command error integration for command tracking, complementary filtering for sensor noise suppression and a control filter for computation delay accommodation as shown in Fig. 2.

- The control law is structually formed to stabilize and command augment any nonlinear systems. PIF works particularly well for aircraft nonlinear dynamics as has been demonstrated by flight tests and non-linear simulations for differing aerodynamic vehicles (PIF-Tandem Rotor Helicopter, Ref. 3, PI-High Performance Fighter, Ref. 19).

- The control law is designed using perturbation variables but does not use nominals, u_0 and x_0, in the implemented control logic. Computing nominals in flight as suggested in Ref. 20 is impractical for GA auto-pilots and not necessary because the control law uses the incremental form, Ref. 21.

- PIF is a command augmentation system design. To perform the "select" feature a command model representing simplified aircraft dynamics uses a nonlinear control law to transfer internal command states from one desired condition (ex: altitude) to a different desired condition. The PIF control law tracks the command model states. The command tracking is performed by combining the derivation of the PIF control law with the theory of feedforward control, Refs. 22 and 23. The derivation is detailed in Chapter III, Section B. The command models are discussed in Appendix C for each mode shown in Table 4.

- A computer program is available to design any of the autopilots in this report for any aircraft with known stability derivatives. The program automatically linearizes the nonlinear aircraft dynamics to construct A and B in Eq. 3, computes feedback and feedforward gains, determines closed-loop eigenvalues and simulates the completed PIF design.

- PIF is not a nested control design in implementation. When a new command mode is engaged, the PIF gains are updated to optimally match the new command mode. Alternate software sections of code are executed for each command mode. Approximately 75% of the PIF control software, however, is always executed independent of the command mode. Nested control law implementation is to be distinguished from a nested construction of the command error. The increase in complexity of the command error from Eq. 142 from the ROLL SEL mode, then Eq. 145 for the HDG SEL mode to Eq. 191 for the APR LOCR mode is a result of nested construction.

III. DIGITAL FLIGHT CONTROL SYSTEM

This chapter derives the PIF control law. A derivation of the PIF control law optimally transferring a linear plant from tracking one constant command input to another is given in Ref. 3. This chapter generalizes the derivation to include feedforward control and model output tracking and is unique to this report. The derivation is accomplished by formulating a continuous-time optimal regulator problem, converting the problem to a sampled-data regulator, incorporating the "star trajectory" (defined later), solving the discrete-time regulator problem, then constructing the final <u>implementable</u> solution.

The PIF drivation uses assumptions about the command model control input and incorporates knowledge of digital structures during the construction of the aircraft design model. These assumptions and structures are reviewed in the next section and Appendices D and E.

A. COMMAND MODEL AND FEEDFORWARD CONTROL

The main objective of the PIF control law derivation is to cause the output of a linear aircraft model given by

$$\Delta \underline{y} = H \, \Delta \underline{x} + D \, \Delta \underline{u} \qquad [6]$$

to optimally track the output of a linearized command model,

$$\Delta \dot{\underline{x}}_m = A_m \, \Delta \underline{x}_m + B_m \, \Delta \underline{u}_m \qquad [7]$$

$$\Delta \underline{y}_m = H_m \, \Delta \underline{x}_m + D_m \, \Delta \underline{u}_m \qquad [8]$$

The PIF derivation causes $\Delta \underline{y}$ to track $\Delta \underline{y}_m$ assuming the command model control input, $\Delta \underline{u}_m$, is constant for $t \geq 0$. The model control input is not constant in implementation. The rest of this section explains the reason behind the $\Delta \underline{u}_m$ assumption and its impact on control system performance.

There are at least three methods, or approaches, to solving the command model tracking problem so that $\Delta \underline{y}$ tracks $\Delta \underline{y}_m$.

1) Ignore the command model dynamics, assume $\Delta \underline{y}_m$ is constant and feedback the command error $\Delta \underline{y} - \Delta \underline{y}_m$ with a high gain feedback loop.

2) Include a judicious part of the command model, assume $\Delta \underline{u}_m$ is constant and feedback the command error $\Delta \underline{y} - \Delta \underline{y}_m$ with moderate feedback so that $\Delta \underline{y}$ tracks $\Delta \underline{y}_m$ when $\Delta \underline{u}_m$ is constant.

3) The exact command model is used, $\Delta\underline{u}_m$ is assumed to be arbitrary, after a brief initial condition mismatch transient, $\Delta\underline{y}$ tracks $\Delta\underline{y}_m$ perfectly no matter how $\Delta\underline{u}_m$ changes.

The first approach has been used successfully in many practical designs. The PIF control law used in the VALT program, Ref. 3, is designed using the first approach. Velocity commands are tracked by the PIF control law and are assumed to be constant during the design. In implementation the velocity commands have low frequency variations caused by feeding back position error as the helicopter is required to track a complex 4-dimensional trajectory.

A state-space solution to the third approach is given in Ref. 23 and is similiar in formulation to exact model matching (Refs. 24 and 25). Reference 26 shows that certain adaptive controllers are adapting their internal gains to achieve exact model matching in steady state. Experience with Approach 3 has shown that for autopilot designs, the approach is impractical. Exact pole/zero cancellation is required, the control law is sensitive to noise, the required effector response is not achievable by motor driven rate limited actuators and the discrete-time solution requires future values of $\Delta\underline{u}_m$.

A practical method and the one pursued in this report is method 2. When $\Delta\underline{u}_m$ is changing, $\Delta\underline{y}$ and $\Delta\underline{y}_m$ became mismatched and their error is governed by the control law in a manner similiar to approach 1. When $\Delta\underline{u}_m$ is constant, $\Delta\underline{y}$ eventually tracks $\Delta\underline{y}_m$ as in approach 3 but suffers none of approach 3's disadvantages that stem from the arbitrary $\Delta\underline{u}_m$ assumption. The PIF control law using approach 2 is designed to optimally govern the discrete time transient response of $\Delta\underline{y}$ when $\Delta\underline{u}_m$ changes once and remains constant thereafter. In practice the control law performs well if $\Delta\underline{u}_m$ changes intermittently or slowly varies.

The *feedforward control solution* where $\Delta\underline{y}$ tracks $\Delta\underline{y}_m$ with $\Delta\underline{u}_m$ constant is presented in Appendix D. The feedforward control solution is independent of the control law used and is as follows:

$$\begin{bmatrix} \Delta\underline{x}_k^* \\ \Delta\underline{u}_k^* \end{bmatrix} = \begin{bmatrix} A_{11} & A_{12} \\ A_{21} & A_{22} \end{bmatrix} \begin{bmatrix} \Delta\underline{x}_{m,k} \\ \Delta\underline{u}_m \end{bmatrix} \qquad\qquad [9]$$

The output $\Delta\underline{y}$ tracks $\Delta\underline{y}_m$ when $\Delta\underline{x}$ follows $\Delta\underline{x}^*$ and the feedback control is $\Delta\underline{u}^*$, i.e., the state and control star trajectory. The solution is unique if the number of plant outputs equals the number of plant controls. The *feedforward matrices* A_{ij} satisfy Eq. 227; a solvable matrix algebraic equation (Ref. 5).

The star trajectory is a convenient notational abstract and is not physically generated when the control law is implemented. All the linear simulations of the PIF control law (see Chapter IV, Section D) however, show the star trajectory for clarity. The relationship between the linear star trajectory and trim in Eqs. 228 and 229 is assumed to remain valid and is

exploited when the PIF control law is derived in the next section.

B. PIF DERIVATION

The continuous-time design model and cost function for PIF are as follows:

$$\begin{bmatrix} \Delta \dot{\underline{x}} \\ \Delta \dot{\underline{u}} \\ \Delta \dot{\underline{\xi}} \end{bmatrix} = \begin{bmatrix} A & B & 0 \\ 0 & 0 & 0 \\ H & D & 0 \end{bmatrix} \begin{bmatrix} \Delta \underline{x} \\ \Delta \underline{u} \\ \Delta \underline{\xi} \end{bmatrix} + \begin{bmatrix} 0 \\ I \\ 0 \end{bmatrix} \Delta \underline{v} \tag{10}$$

$$J = \int_0^\infty \{ [\Delta \underline{x}^T \; \Delta \underline{u}^T \; \Delta \underline{\xi}^T] \begin{bmatrix} Q & 0 & 0 \\ 0 & R & 0 \\ 0 & 0 & QZ \end{bmatrix} \begin{bmatrix} \Delta \underline{x} \\ \Delta \underline{u} \\ \Delta \underline{\xi} \end{bmatrix} + \Delta \underline{v}^T \; RD \; \Delta \underline{v} \} dt \tag{11}$$

The linear model of the aircraft shown in Eq. 3 is augmented with an equation for control rate and an equation for the integration of the command output, $\Delta \underline{y}$. The augmented plant model and quadratic cost function are in standard infinite-time linear quadratic regulator form.

Four problems a digital flight control system should address are (1) the type of control data-hold employed, (2) the effect of the computation delay, (3) high frequency noise suppression and (4) trim accommodation. These problems are discussed in Appendix E. The PIF control law addresses the first three problems by including $\Delta \underline{\dot{u}}$ dynamics in the model and weighting $\Delta \underline{v}$ in the cost function. The trim problem is partially addressed by using the integrator, $\Delta \underline{\xi}$, in the augmented model.

Precisely converting Eqs. 10 and 11 using the sampled-data regulator, Ref. 27, where $\Delta \underline{v}_k$ is assumed constant between equally spaced sampling points, yields a preliminary version of the discrete-time PIF design model

$$\begin{bmatrix} \Delta \underline{x} \\ \Delta \underline{u} \\ \Delta \underline{\xi} \end{bmatrix}_{k+1} = \begin{bmatrix} \Phi & \Gamma & 0 \\ 0 & I & 0 \\ \Phi_1 & \Phi_2 & I \end{bmatrix} \begin{bmatrix} \Delta \underline{x} \\ \Delta \underline{u} \\ \Delta \underline{\xi} \end{bmatrix}_k + \begin{bmatrix} \Gamma_1 \\ \Delta t I \\ \Gamma_3 \end{bmatrix} \Delta \underline{v}_k \tag{12}$$

The matrices Φ, Γ, and Γ_1 are defined in Eqs. 218, 219, 239. The discrete-time model in Eq. 12, if used to design a PIF control law, requires that the control law be implemented with a triangular data-hold (compare Eqs. 12 and 238). Similarly, the discrete dynamic model for the integrator in Eq. 12 is a discrete representation of the implementation

10

$$\Delta \underline{\xi}(t) = \Delta \underline{\xi}_k + \int_{t_k}^{t} \Delta \underline{y}(t) \, dt \qquad t_{k+1} > t \geq t_k \qquad (13)$$

The required analog integration of $\Delta \underline{y}(t)$ between samples as shown in Eq. 13 is not desired in implementation.

The problems with using Eq. 12 as the discrete model representation are eliminated using approximations. The discrete cost function obtained using the sampled-data regulator and shown later in Eq. 22 is not changed when the approximations are introduced. Hence, the optimization problem PIF solves is not precisely a sampled-data regulator but the effect is small, (Ref. 28), because the terms eliminated are of the order Δt^2.

The first approximation is performed by setting Γ_1 to zero in Eq. 12. When Γ_1 is zero, the required implementation for $\Delta \underline{u}_k$ changes from a triangular data hold to a zero-order hold. The resulting control law is also required to be implemented with a modeled one sample period computation delay (compare Eq. 12 with Γ_1 zero and Eq. 243).

The simplification of the integrator in Eq. 13 can be performed by using any number of discrete integration formulas, such as

$$\Delta \underline{\xi}_{k+1} = \Delta \underline{\xi}_k + \Delta t \, \Delta \underline{y}_k \qquad \text{Euler} \qquad (14)$$

$$\Delta \underline{\xi}_{k+1} = \Delta \underline{\xi}_k + \frac{\Delta t}{2}(\Delta \underline{y}_{k+1} + \Delta \underline{y}_k) \qquad \text{Trapezoidal} \qquad (15)$$

$$\Delta \underline{\xi}_{k+1} = \Delta \underline{\xi}_k + \Delta t \, \Delta \underline{y}_{k+1} \qquad \text{Rectangular} \qquad (16)$$

Euler integration is used for simplicity. Euler integration implies that the integration error is delayed two sampling intervals in implementation (see Eq. 51). Using rectangular integration instead of Euler integration would cause the integration error to be delayed only one sampling interval but would produce difficult but not insurmountable implementation problems.

The star trajectory in Eq. 9 is introduced into the PIF model by defining the variables

$$\Delta \underline{\tilde{x}}_k = \Delta \underline{x}_k - \Delta \underline{x}_k^* \qquad (17)$$

$$\Delta \underline{\tilde{u}}_k = \Delta \underline{u}_k - \Delta \underline{u}_k^* \qquad (18)$$

$$\Delta \underline{\tilde{v}}_k = \Delta \underline{v}_k - \Delta \underline{v}_k^* \doteq \Delta \underline{v}_k - A_{21} \, (\Delta \underline{x}_{m,k+1} - \Delta \underline{x}_{m,k})/\Delta t \qquad (19)$$

11

$$\Delta \tilde{\underline{\xi}}_k = \Delta \underline{\xi}_k - \Delta \underline{\xi}^*$$

(20)

The star trajectory for $\Delta \underline{\xi}$ is defined later (see Eq. 37). Combining the simplifications with Eqs. 17 to 20 results in the discrete PIF model,

$$\begin{bmatrix} \Delta \tilde{\underline{x}} \\ \Delta \tilde{\underline{u}} \\ \Delta \tilde{\underline{\xi}} \end{bmatrix}_{k+1} = \begin{bmatrix} \Phi & \Gamma & 0 \\ 0 & I & 0 \\ \Delta t H & \Delta t D & I \end{bmatrix} \begin{bmatrix} \Delta \tilde{\underline{x}} \\ \Delta \tilde{\underline{u}} \\ \Delta \tilde{\underline{\xi}} \end{bmatrix}_k + \begin{bmatrix} 0 \\ \Delta t I \\ 0 \end{bmatrix} \Delta \tilde{\underline{v}}_k$$

[21]

The integrator model in Eq. 21 is obtained using the following steps: (1) $\Delta \underline{y}_k$ in Eq. 14 is replaced with $\Delta \underline{y}_k - \Delta \underline{y}_{m,k}$, (2) $\underline{y}_k$ is replaced with $H \Delta \underline{x}_k + D \Delta \underline{u}_k$ using Eq. 6, (3) $\Delta \underline{y}_{m,k}$ is replaced with $\Delta \underline{y}_k^*$ using results from Appendix D, (4) $\Delta \underline{y}_k^*$ is replaced with $H \Delta \underline{x}_k^* + D \Delta \underline{u}_k^*$, (5) $\Delta \underline{\xi}^*$ is subtracted from both sides of the integrator equation to obtain the model for $\Delta \tilde{\underline{\xi}}_k$, (6) the model for $\Delta \tilde{\underline{\xi}}_k$ replaces the model for $\Delta \underline{\xi}_k$ in Eq. 12 to obtain the model following integrator dynamics.

The cost function is the sampled-data cost function obtained using Eqs. 10 and 11 but starting at k = -1 instead of k = 0.

$$J = \sum_{k=-1}^{\infty} \left[\Delta \tilde{\underline{x}}_k^T \Delta \tilde{\underline{u}}_k^T \Delta \tilde{\underline{\xi}}_k^T \Delta \tilde{\underline{v}}_k^T \right] \begin{bmatrix} \hat{Q}_{xx} & \hat{Q}_{xu} & \hat{Q}_{x\xi} & \hat{M}_{xv} \\ \hat{Q}_{xu}^T & \hat{Q}_{uu} & \hat{Q}_{u\xi} & \hat{M}_{uv} \\ \hat{Q}_{x\xi}^T & \hat{Q}_{u\xi}^T & \hat{Q}_{\xi\xi} & \hat{M}_{\xi v} \\ \hat{M}_{xv}^T & \hat{M}_{uv}^T & \hat{M}_{\xi v}^T & \hat{R} \end{bmatrix} \begin{bmatrix} \Delta \tilde{\underline{x}}_k \\ \Delta \tilde{\underline{u}}_k \\ \Delta \tilde{\underline{\xi}}_k \\ \Delta \tilde{\underline{v}}_k \end{bmatrix}$$

[22]

The cost function starts at k = -1 since $\Delta \underline{u}_0$ and $\Delta \underline{v}_{-1}$ are unspecified. The cost function is minimized by assuming $\Delta \underline{u}_{m,k}$ changes at k = 0 and remains constant thereafter. The plant is assumed to be tracking the star trajectory for $\Delta \underline{u}_{m,-1} = \Delta \underline{u}_{m,-2} = \ldots$ previous to the time instant k = 0.

The changing model input at k = 0 introduces a contradiction in the value of $\Delta \underline{x}_0^*$. The ideal plant dynamics indicate

$$\Delta \underline{x}_0^* = \Phi \Delta \underline{x}_{-1}^* + \Gamma \Delta \underline{u}_{-1}^*$$

(23)

where

$$\begin{bmatrix} \Delta \underline{x}_{-1}^* \\ \Delta \underline{u}_{-1}^* \end{bmatrix} = \begin{bmatrix} A_{11} & A_{12} \\ A_{21} & A_{22} \end{bmatrix} \begin{bmatrix} \Delta \underline{x}_{m,-1} \\ \Delta \underline{u}_{m,-1} \end{bmatrix}$$

(24)

12

At k = 0, a different values for $\Delta \underline{x}_0^*$ is obtained using Eq. 9 which uses $\Delta \underline{u}_{m,0}$,

$$\begin{bmatrix} \Delta \underline{x}_0^* \\ \Delta \underline{u}_0^* \end{bmatrix} = \begin{bmatrix} A_{11} & A_{12} \\ A_{21} & A_{22} \end{bmatrix} \begin{bmatrix} \Delta \underline{x}_{m,0} \\ \Delta \underline{u}_{m,0} \end{bmatrix} \qquad (25)$$

Substituting Eq. 24 into Eq. 23 and simplifying does not result in Eq. 25.

The contradiction can be resolved in the model and feedforward equations, by advancing the time index on $\Delta \underline{u}_m$ one step as follows

$$\Delta \underline{x}_{m,k} = \phi_m \, \Delta \underline{x}_{m,k-1} + \Gamma_m \, \Delta \underline{u}_{m,k} \qquad k = -1, 0, 1, \ldots \qquad (26)$$

$$\begin{bmatrix} \Delta \underline{x}_k^* \\ \Delta \underline{u}_k^* \end{bmatrix} = \begin{bmatrix} A_{11} & A_{12} \\ A_{21} & A_{22} \end{bmatrix} \begin{bmatrix} \Delta \underline{x}_{m,k} \\ \Delta \underline{u}_{m,k+1} \end{bmatrix} \qquad (27)$$

Substituting Eq. 27 at k = -1 into Eq. 23 and simplifying produces

$$\Delta \underline{x}_0^* = \phi \Delta \underline{x}_{-1}^* + \Gamma \Delta \underline{u}_{-1}^* = \phi[A_{11} \Delta \underline{x}_{m,-1} + A_{12} \Delta \underline{u}_{m,0}] + \Gamma[A_{21} \Delta \underline{x}_{m,-1} + A_{22} \Delta \underline{u}_{m,0}]$$

$$= A_{11} \Delta \underline{x}_{m,0} + A_{12} \Delta \underline{u}_{m,0} \qquad (28)$$

the required result. The derivation of Eq. 28 uses Eq. 227 to perform the required substitutions. The redefined model does not alter the derivation in Appendix D for k $\geq$ 0, but does beneficially change the PIF implementation and command response.

Equations 21 and 22 are in the proper regulator format and yield the solution,

$$\frac{1}{\Delta t} (\Delta \tilde{\underline{u}}_k - \Delta \tilde{\underline{u}}_{k-1}) = \Delta \tilde{\underline{v}}_{k-1} = C_1 \, \Delta \tilde{\underline{x}}_{k-1} + C_2 \, \Delta \tilde{\underline{u}}_{k-1} + C_3 \, \Delta \tilde{\underline{\xi}}_{k-1} \qquad (29)$$

where the gains C_1, C_2, and C_3 are determined from the algebraic Riccati equation solution associated with the optimal regulator (Ref. 5). The integrator star trajectory is still unknown in Eq. 29.

It is well known that the minimum cost for the optimal regulator is

$$\min J = \Delta \underline{x}_0^T P \Delta \underline{x}_0$$

where P is the steady-state solution to the discrete algebraic Riccati equation. It follows that the minimum value of the performance index, shown in Eq. 22, is (for fixed $\Delta \underline{\xi}^*$)

$$\min J = \begin{bmatrix} \Delta \underline{\tilde{x}}_{-1}^T & \Delta \underline{\tilde{u}}_{-1}^T & \Delta \underline{\tilde{\xi}}_{-1}^T \end{bmatrix} \begin{bmatrix} P_{xx} & P_{xu} & P_{x\xi} \\ P_{xu}^T & P_{uu} & P_{u\xi} \\ P_{x\xi}^T & P_{u\xi}^T & P_{\xi\xi} \end{bmatrix} \begin{bmatrix} \Delta \underline{\tilde{x}}_{-1} \\ \Delta \underline{\tilde{u}}_{-1} \\ \Delta \underline{\tilde{\xi}}_{-1} \end{bmatrix} \tag{31}$$

Further minimizing J by setting $\partial J / \partial \Delta \underline{\tilde{\xi}}_{-1} = 0$, because $\Delta \underline{\xi}^*$ is unspecified produces

$$\Delta \underline{\tilde{\xi}}_{-1} = \Delta \underline{\xi}_{-1} - \underline{\xi}_{-1}^* = -P_{\xi\xi}^{-1} \left[P_{u\xi}^T (\Delta \underline{u}_{-1} - \Delta \underline{u}_{-1}^*) + P_{x\xi}^T (\Delta \underline{x}_{-1} - \Delta \underline{x}_{-1}^*) \right] \tag{32}$$

Recalling that $\Delta \underline{u}_{-1}$ and $\Delta \underline{x}_{-1}$ are assumed to be tracking the star trajectory for $\Delta \underline{u}_{m,-1}$ produces

$$\Delta \underline{x}_{-1} - \Delta \underline{x}_{-1}^* = (A_{11} \Delta \underline{x}_{m,-1} + A_{12} \Delta \underline{u}_{m,-1}) - (A_{11} \Delta \underline{x}_{m,-1} + A_{12} \Delta \underline{u}_{m,0}) \tag{33}$$

$$= A_{12} (\Delta \underline{u}_{m,-1} - \Delta \underline{u}_{m,0})$$

and

$$\Delta \underline{u}_{-1} - \Delta \underline{u}_{-1}^* = A_{22} (\Delta \underline{u}_{m,-1} - \Delta \underline{u}_{m,0}) \tag{34}$$

Substituting Eqs. 33 and 34 into Eq. 32 and simplifying produces

$$\Delta \underline{\xi}_{-1} = \Delta \underline{\xi}_{-1}^* + A (\Delta \underline{u}_{m,-1} - \Delta \underline{u}_{m,0}) \tag{35}$$

$$A = -P_{\xi\xi}^{-1} \left[P_{x\xi}^T A_{12} + P_{u\xi}^T A_{22} \right] \tag{36}$$

$\Delta \underline{\xi}_k$ is assumed to be tracking a star trajectory for $\Delta \underline{u}_{m,-1}$ previous to $k = 0$, hence, Eq. 35 implies that the optimal star trajectory for the integrator state is

$$\Delta \underline{\xi}_k^* = [0 \quad A] \begin{bmatrix} \Delta \underline{x}_{m,k} \\ \Delta \underline{u}_{m,k+1} \end{bmatrix} \quad k = -1, 0, 1, \ldots \tag{37}$$

The control law in Eq. 29 can be written as follows

$$\Delta \tilde{\underline{u}}_k = \Delta \tilde{\underline{u}}_{k-1} + \Delta t \, \Delta \tilde{\underline{v}}_{k-1} \tag{38}$$

$$\Delta \tilde{\underline{v}}_{k-1} = C_1 \Delta \tilde{\underline{x}}_{k-1} + C_2 \Delta \tilde{\underline{u}}_{k-1} + C_3 \Delta \tilde{\underline{\xi}}_{k-1} \tag{39}$$

$$\Delta \tilde{\underline{\xi}}_k = \Delta \tilde{\underline{\xi}}_{k-1} + \Delta t \, \Delta \tilde{\underline{y}}_{k-1} \tag{40}$$

Subtracting $\Delta \tilde{\underline{v}}_{k-2}$ from $\Delta \tilde{\underline{v}}_{k-1}$ in Eq. 39 changes Eq. 39 to

$$\Delta \tilde{\underline{v}}_{k-1} = (I + \Delta t \, C_2) \Delta \tilde{\underline{v}}_{k-2} + C_1 (\Delta \tilde{\underline{x}}_{k-1} - \Delta \tilde{\underline{x}}_{k-2})$$

$$+ C_3 (\Delta \tilde{\underline{\xi}}_{k-1} - \Delta \tilde{\underline{\xi}}_{k-2}) \tag{41}$$

The perturbation variables are eliminated from Eqs. 38 and 41 using a large number of substitutions and cancellations. An example of the substitutions and cancellations is demonstrated for the incremental state feedback term $C_1 (\Delta \tilde{\underline{x}}_{k-1} - \Delta \tilde{\underline{x}}_{k-2})$ in Eq. 41

The state feedback increment is simplified as follows

$$\Delta \tilde{\underline{x}}_{k-1} - \Delta \tilde{\underline{x}}_{k-2} = (\Delta \underline{x}_{k-1} - \Delta \underline{x}_{k-2}) - (\Delta \underline{x}_{k-1}^* - \Delta \underline{x}_{k-2}^*) \tag{42}$$

$$\Delta \underline{x}_{k-1} - \Delta \underline{x}_{k-2} = (\underline{x}_{k-1} - \underline{x}_{k-2}) - (\underline{x}_{0,k-1} - \underline{x}_{0,k-2}) \tag{43}$$

$$\Delta \underline{x}_{k-1}^* - \Delta \underline{x}_{k-1}^* = A_{11}(\Delta \underline{x}_{m,k-1} - \Delta \underline{x}_{m,k-2}) + A_{12}(\Delta \underline{u}_{m,k} - \Delta \underline{u}_{m,k-1}) \tag{44}$$

$$\Delta \underline{x}_{m,k-1} - \Delta \underline{x}_{m,k-2} = (\underline{x}_{m,k-1} - \underline{x}_{m,k-2}) - (\underline{x}_{m,0,k-1} - \underline{x}_{m,0,k-2}) \tag{45}$$

$$\Delta \underline{u}_{m,k} - \Delta \underline{u}_{m,k-1} = (\underline{u}_{m,k} - \underline{u}_{m,k-1}) - (\underline{u}_{m,0} - \underline{u}_{m,0}) \tag{46}$$

15

but

$$x_{0,k-1} - x_{0,k-2} \simeq A_{11}(\underline{x}_{m,0,k-1} - \underline{x}_{m,0,k-2}) + A_{12}(\underline{u}_{m,0} - \underline{u}_{m,0}) \qquad (47)$$

hence

$$\Delta\underline{\tilde{x}}_{k-1} - \Delta\underline{\tilde{x}}_{k-2} = (\underline{x}_{k-1} - \underline{x}_{k-2}) - A_{11}(\underline{x}_{m,k-1} - \underline{x}_{m,k-2})$$

$$- A_{12}(\underline{u}_{m,k} - \underline{u}_{m,k-1}) \qquad (48)$$

Using logic similiar to Eqs. 42 through 48, the PIF control equations reduce to the following

$$\underline{u}_k = \underline{u}_{k-1} + \Delta t\, \underline{v}_{k-1} + A_{21}(\underline{x}_{m,k} - \underline{x}_{m,k-1}) \qquad (49)$$

$$\underline{e}_{k-1} = \underline{x}_{k-1} - A_{11}\,\underline{x}_{m,k-1} \qquad (50)$$

$$\underline{v}_{k-1} = (I + \Delta t\, C_2)\,\underline{v}_{k-2} + C_1(\underline{e}_{k-1} \cdot \underline{e}_{k-2}) + \Delta t\, C_3(\underline{y}_{k-2} - \underline{y}_{m,k-2})$$

$$+ (-C_3 A - C_1 A_{12} - C_2 A_{22})(\underline{u}_{m,k} - \underline{u}_{m,k-1}) \qquad (51)$$

In all of the autopilot models discussed in this report, A_{21} is a zero matrix. When A_{21} is eliminated from Eqs. 49 and 51, the only changes to the PIF control law over Ref. 3 are the propagation of the command model to generate $\underline{x}_{m,k}$, new matrices are used to compute the feedforward matrix for $(\underline{u}_{m,k} - \underline{u}_{m,k-1})$ in Eq. 51 and $(\underline{e}_{k-1} - \underline{e}_{k-2})$ is used for state feedback instead of $(\underline{x}_{k-1} - \underline{x}_{k-2})$.

The last modification needed for the PIF control law is due to the sensors. The mathematical model of the aircraft in Eq. 10 uses the body axis perturbation states Δu, Δw, Δq, $\Delta\theta$, Δz, Δv, Δr, Δp, $\Delta\phi$, $\Delta\psi$, Δy, which are related to the perturbation sensors output $\Delta\underline{z}_k^T = [\Delta V,\ \Delta a_z,\ \Delta q,\ \Delta\theta,\ \Delta z,\ \Delta a_y,\ \Delta r,\ \Delta p,\ \Delta\phi,\ \Delta\psi,\ \Delta y]$ through the relationship.

$$\begin{bmatrix} C_x & C_u \\ 0 & I \end{bmatrix} \begin{bmatrix} \Delta\underline{x}_k \\ \Delta\underline{u}_k \end{bmatrix} = \begin{bmatrix} \Delta\underline{z}_k \\ \Delta\underline{u}_k \end{bmatrix} \qquad [52]$$

The matrices C_x and C_u are obtained using Eq. 135 for Δa_z and Δa_y, and Eq. 137 for ΔV. The rest of the elements in C_x are ones in the appropriate place along the diagonal for the body axis states that are directly measured. Equation 52

16

is used to incorporate sensor feedback in Eq. 39 by using the following substitution

$$[C_1 \quad C_2]\begin{bmatrix} \Delta \tilde{x}_k \\ \Delta \tilde{u}_k \end{bmatrix} = [C_1 \quad C_2]\begin{bmatrix} C_x & C_u \\ 0 & I \end{bmatrix}^{-1}\begin{bmatrix} \Delta \tilde{z}_k \\ \Delta \tilde{u}_k \end{bmatrix} = [C_5 \quad C_4]\begin{bmatrix} \Delta \tilde{z}_k \\ \Delta \tilde{u}_k \end{bmatrix} \qquad (53)$$

The feedforward matrices are similarily altered

$$\begin{bmatrix} C_x & C_u \\ 0 & I \end{bmatrix}\begin{bmatrix} \Delta x_k^* \\ \Delta u_k^* \end{bmatrix} = \begin{bmatrix} C_x & C_u \\ 0 & I \end{bmatrix}\begin{bmatrix} A_{11} & A_{12} \\ A_{21} & A_{22} \end{bmatrix}\begin{bmatrix} \Delta x_{m,k} \\ \Delta u_{m,k+1} \end{bmatrix} \qquad (54)$$

or

$$\begin{bmatrix} \Delta z_k^* \\ \Delta u_k^* \end{bmatrix} = \begin{bmatrix} S_{11} & S_{12} \\ A_{21} & A_{22} \end{bmatrix}\begin{bmatrix} \Delta x_{m,k} \\ \Delta u_{m,k+1} \end{bmatrix} \qquad (55)$$

Eliminating A_{21} and using sensor feedback, the final implementable form for the PIF controller advanced one time step is

$$u_{k+1} = u_k + \Delta t \; v_k \qquad [56]$$

$$e_k = z_k - S_{11} x_{m,k} \qquad [57]$$

$$v_k = C_6 v_{k-1} + C_5(e_k - e_{k-1}) + C_7(y_{k-1} - y_{m,k-1})$$

$$\qquad\qquad + E(u_{m,k+1} - u_{m,k}) \qquad [58]$$

where

$$C_6 = I + \Delta t \; C_4 \qquad [59]$$

$$E = -C_3 A - C_1 A_{12} - C_2 A_{22} \qquad [60]$$

$$C_7 = \Delta t \, C_3 \qquad\qquad [61]$$

The PIF simulation program in Ref. 5 and the flight computer software discussed in the next section use Eqs. 56, 57 and 58 for implementation. Figure 7 shows a detailed block diagram of the PIF equations which includes the command model equations.

C. FLIGHT COMPUTER SOFTWARE

The filter and PIF control logic implemented on board the ROLM 1666 flight computer is presented in this section. The flight computer software uses a main executive routine which calls subroutines for each part of the control computations. The flight software is written strictly to test the autopilot modes. Safety features, sensor failure detection, actuator failure detection, bad data editing (except for radar and yaw gyro), graceful degradation features and built-in-test are not included in the software.

The sequence for a single control computation frame is illustrated in the functional flow diagrams of Figs 8 to 11. The operations performed by the blocks in the functional flow diagram are described next:

MAIN EXECUTIVE

ONE TIME TASKS - Communication channels are open, and logical variables are initialized.

TERMFLEX - Software for a push button panel is executed. The alpha-numeric display prompts the pilot concerning the desired command mode and command inputs. The pilot inputs are stored and logical variables are initialized.

READ A/D SENSORS - Sensor output from the analog to digital converters (which is synchronous with the 10 per second computation loop) are scaled and stored in common blocks.

FILTER INITIALIZATION - The filter variables are reset to the sensor measurements or zero until the pilot engages the filters (depressing INITIAL).

EXECUTE FILTERS - The barometric complementary filter and yaw complementary filter computations are executed.

CONTROL INITIALIZATION - Control increments and command errors are set to zero and control commands are updated to actuator positions until the pilot engages the control law (depressing ENGAGE).

CONTROL - The PIF control law is engaged. The command values are the flight conditions that exist at the time of engagement. New commands obtained in the TERMFLEX subroutine are activated by the pilot in flight (depressing COMMAND).

18

UPDATE SERVOS – The control actuator commands are prepared to be released at the beginning of the next cycle.

WAIT REST OF INTERVAL – Execution pauses until the beginning of the next cycle.

CONTROL

COMPUTE – The control law computations are performed unless this is the first pass or the pilot has pressed the COMMAND button.

NEW COMMAND – When the pilot presses the COMMAND button the desired command change is computed and command model following begins execution.

FIRST PASS – A two-dimensional array contains the PIF control gains stored columnwise for each autopilot mode. In the first pass the desired gain set from the two-dimensional array is loaded into a vector for later use in FPIF1.

APRFILT – Estimates of lateral position, perpendicular distance to the glideslope and range are computed in this subroutine.

APR GS, ALT SEL, PITCH SEL, APR LOC, HDG SEL, AND ROLL SEL – These are the subroutines which accept command inputs, compute command model controls and propagate command model states to generate desired trajectories. The equations used in these subroutines are given in Appendix C.

FPIF2 – The feedback and feedforward error quantities for the PIF control law are computed in this subroutine which is detailed in Fig. 10.

FPIF1 – The control gains are multiplied by the feedback and feedforward errors and the new control actuator commands are determined in this subroutine which is detailed in Fig. 11.

LOC/GS – Logic is used to test when to switch from the ALT SEL and HDG SEL modes to APR GS and APR LOC modes.

IV. DIGITAL FLIGHT CONTROL SYSTEM DESIGN

The PIF autopilot design procedure is a sequence where the designer interatively improves system performance at each step. The sequence in the design procedure and the parameters adjusted are shown in Fig. 12. The PIFCGT computer program aids the designer to perform the functions enclosed in the dotted block in Fig. 12. This chapter discusses each part of the design process and presents the design parameters for the PIF autopilot control laws.

A. COMPLEMENTARY FILTERS AND PREFILTERS

This section presents the designs of the complementary filter and pre-filters used to smooth sensor output. Originally the PIF control law for the NAVION was designed and flight tested with no filtering of the digital sensor data. Flight tests indicated filters were needed for the barometric altimeter, yaw gyro and lateral accelerometer.

The barometric altimeter signal is very noisy due to quantization, atmospheric effects, and sensor performance. An example of the noisy signal is shown at the top of Fig. 13. A complementary filter discussed and designed in Ref. 3 is used to smooth the vertical height measurement. The complementary filter uses steady-state Kalman filter theory to determine the filter gains based on sensor noise statistics reported in Table 2. The 3rd order complementary filter consists of the update equation

$$
\begin{bmatrix} \hat{z}(+) \\ \hat{\dot{z}}(+) \\ \hat{b}(+) \end{bmatrix}_k = \begin{bmatrix} \hat{z}(-) \\ \hat{\dot{z}}(-) \\ \hat{b}(-) \end{bmatrix}_k + \begin{bmatrix} 0.08 \\ 0.0248 \\ -0.00095 \end{bmatrix} [h_B - \hat{z}(-)]_k \qquad [62]
$$

and the propagate equation

$$
\begin{bmatrix} \hat{z}(-) \\ \hat{\dot{z}}(-) \\ \hat{b}(-) \end{bmatrix}_{k+1} = \begin{bmatrix} 1 & \Delta t & 0 \\ 0 & 1 & 0 \\ 0 & 0 & 1 \end{bmatrix} \begin{bmatrix} \hat{z}(+) \\ \hat{\dot{z}}(+) \\ \hat{b}(+) \end{bmatrix}_k
$$

$$
+ \begin{bmatrix} \Delta t/2 \\ \Delta t \\ 0 \end{bmatrix} (\hat{a}_{z,k} - \hat{b}_k(+)) * \cos \theta_k * \cos \phi_k \qquad [63]
$$

20

The states in the filter are vertical height (positive up), $\hat{z}$, vertical velocity, $\hat{\dot{z}}$, and accelerometer bias in body axis $\hat{b}$. The accelerometer output, a_z, in flight is biased to read zero (positive up) in straight and level flight and must be corrected using gravity, g,

$$a_{z,k} = a_{z,k} + g * (1.0 - \cos \theta_k \cos \phi_k) \tag{64}$$

h_b is the sampled output of the barometric altimeter. In flight performance of the filter presented in Fig. 13 shows that the height estimate is favorably comparable to height estimated using radar.

The yaw gyro output is from 0 to $+\pi$ and 0 to $-\pi$. A complementary filter is used to smooth the sampled yaw gyro measurement when the signal crosses between $+\pi$ and $-\pi$. The complementary filter design is a modification of a design presented in Ref. 3. First, the filter residual error is computed and checked for the $\pm\pi$ rad crossing.

$$
\begin{aligned}
&\text{SWITCH = FALSE} \\[2mm]
&\psi_e = \psi_{m,k} - \hat{\psi}_k(-) \\[2mm]
&\text{IF } |\psi_e| > 0.1745 \qquad\qquad \text{THEN SWITCH = TRUE} \\[2mm]
&\text{IF } \psi_e > \pi \qquad\qquad\qquad \text{THEN } \psi_e = \psi_e - 2\pi \\[2mm]
&\text{IF } \psi_e < -\pi \qquad\qquad\quad\;\; \text{THEN } \psi_e = \psi_e + 2\pi
\end{aligned} \tag{65}
$$

The update equation is

$$\begin{bmatrix} \hat{\psi}(+) \\ \hat{b}(+) \end{bmatrix}_k = \begin{bmatrix} \hat{\psi}(-) \\ \hat{b}(-) \end{bmatrix}_k + \begin{bmatrix} K_{\psi,k} \\ K_{\psi,k}/10.0 \end{bmatrix} \psi_e \tag{66}$$

The propagate equation is

$$\begin{bmatrix} \hat{\psi}(-) \\ \hat{b}(-) \end{bmatrix}_{k+1} = \begin{bmatrix} 1 & 0 \\ 0 & 1 \end{bmatrix} \begin{bmatrix} \hat{\psi}(+) \\ \hat{b}(+) \end{bmatrix}_k + \begin{bmatrix} \Delta t \\ 0 \end{bmatrix} \left[q_k * \frac{\sin \phi_k}{\cos \theta_k} + r_k * \frac{\cos \phi_k}{\cos \theta_k} - \hat{b}_k(+) \right] \tag{67}$$

The filter gain K_ψ is adjusted to decrease near $\pm\pi$ rad as follows

$$K_{\psi,k} = -16.5024 * |\hat{\psi}_k(-)| + 51.776 \qquad\qquad [68]$$

IF $K_{\psi,k} > 0.8$ THEN $K_{\psi,k} = 0.8$

IF $K_{\psi,k} < 0.08$ THEN $K_{\psi,k} = 0.08$

IF SWITCH   THEN $K_{\psi,k} = 0.0$ for two time steps

An estimate of $\dot{\psi}_k$ using body - reference rates q and r is used in Eq. 67. The performance of the filter is shown in Fig. 14 where the aircraft heading crosses 180 deg and the flight is performed without difficulty.

All sensors began flight testing using one pole low-pass (RC) analog pre-filters with 0.01 sec time constants to reduce aliasing of very high frequency electronic noise. Initial flights with lateral accelerometer feedback yielded the high oscillatory response shown in Fig. 15. An experimental test replacing a_y with sideslip feedback eliminated the oscillation. The conclusion is that the lateral accelerometer is sensing a moderate frequency noise, probably from engine vibration, which is being aliased and caused the low-frequency oscillation in Fig. 15. The capacitor in the RC prefilter network was changed to produce prefilters with time constants of 0.10 sec and 0.22 sec. The flight test results are shown in Figs. 16 and 17. The safety pilot introduced disturbances during the flight tests by pulsing the rudder pedal through the cable system. As the prefilter time constant increased, Dutch roll damping decreased, as is evident in the a_y output. The 0.1 sec time constant prefilter is chosen as an excellent compromise between stability and noise suppression. The 0.1 time constant prefilter was used on the a_y and a_z accelerometer outputs for all other flight tests in this report.

B.   AUTOPILOT COMMAND MODELS

Each autopilot mode is determined by the desired output vector, $\underline{y}_m$, that the aircraft is required to track and the model dynamics needed to change $\underline{y}_m$ depending on the desires of the pilot. A complete discussion of the autopilot models is given in Appendix C. The model dynamics are sometimes non-linear and a linearized representation is needed to determine the feedforward matrices. Table 5 shows the model states and aircraft states along with the controls used in the PIF autopilot mode designs.

The parameter, a_k, in the lateral autopilot is the roll-to-rudder gain used to produce a coordinated turn. The parameter varies in flight according to

$$\hat{V}_k = 0.7\ \hat{V}_{k-1} + 0.3\ V_k \qquad (m/s) \qquad\qquad\qquad [69]$$

$$a_k = -0.001093\ \hat{V}_k + 0.08268 \qquad\qquad\qquad [70]$$

where a_k is limited when

$\hat{V}_k < 39.63$ THEN $a_k = 0.03937$

and $\hat{V}_k > 60.93$ THEN $a_k = 0.01605$

The paramater a_k is determined using BETA HOLD system as discussed in Appendix C.

The linear command models in Table 5 are simpler than the nonlinear command models. Experience with the models has determined that including all model states and controls in the linear models can degrade tracking performance. The basic question as discussed in Chapter III, Section A, is the amount of u_m derivative information needed by the design. More derivative information causes a faster response. If u_m is constantly and quickly changing, as $\dot{\phi}_m$ does in the HDG SEL autopilot, the PIF design overcompensates causing overshoots, and poor ride quality transients, but quickly drives $y - y_m$ to zero. Using ϕ_m as u_m instead of $\dot{\phi}_m$ in the feedforward control design causes the aircraft roll angle to lag behind the roll command. The resulting design has good ride quality transient response, however, as the flight tests demonstrate

The command models use a control system to steer command model states using the command model controls. Each control system is presented in Appendix C. Each control system is designed to produce desirable paths for the PIF control law to track. The command model control system design parameters are shown in Table 6. Pilot comments are used to fine tune model control system parameters. The command model control system designs are independent of the aircraft model, hence, a PIF autopilot for a different aircraft can use the same parameters in Table 6.

C. PIF DESIGN AND EVALUATION

The PIF design involved choosing quadratic weights, evaluating the resulting design using gain values, closed-loop s-domain eigenvalues and command response, then adjusting the quadratic weights as necessary. The PIF design process benefitted from the fact that during a flight test, the pilot was able to switch between gain sets then indicate the preferred design. The HDG SEL and ALT SEL autopilots were the first two designs accomplished with the pilot opinion approach. Once these two designs were completed, the other autopilot quadratic weights were easily obtained using HDG SEL and ALT SEL as a baseline design. The quadratic weights chosen for all the designs are given in Table 7.

The ROLL SEL autopilot was the first designed, did not use pilot opinions to obtain the weights, and was one of the last autopilots to be flight tested.

The ROLL SEL autopilot performs a simple function and the initial design did not have to be adjusted after flight testing.

The other designs all have equal, continuous-time, cost function weighting on control rate and control position. Reference 7 shows that equal weighting along the control weighting matrix diagonal produces LQR designs with good robustness properties.

The HDG SEL autopilot quadratic weights were adjusted, using criteria discussed later, until reasonable time histories and closed-loop eigenvalues were obtained. Different values for the quadratic weights were chosen to yield a baseline design and alternative designs. The pilots were satisfied with the stability and performance of the baseline design for the HDG SEL autopilot. The flight-tested control law performance and linear simulation performance were in good agreement.

The longitudinal ALT SEL autopilot flight tests and the linear simulation had only fair agreement. The PIF control design program (PIFCGT) performs a full state feedback design without knowledge of any state filtering. The implemented PIF control law uses a complementary filter to estimate vertical height from a noisy accelerometer and barometric altimeter.

The problem with designing the ALT SEL autopilot is shown in Fig. 18. Throughout the flight, atmospheric disturbances cause the autopilot to continually interplay height and pitch attitude in an oscillatory (phugoid mode frequency) manner which we classify as altitude hunting. Increasing the quadratic cost function weight on Δz and $\Delta \xi_z$ increases the frequency and causes the pilot to notice the changing pitch attitude. Decreasing the weight on Δz and $\Delta \xi_z$ eventually causes the pilot to notice the changes in height. A compromise is reached by increasing the weight on $\Delta \xi_z$ until the pilot does not notice the changes in height, then increasing the weight on $\Delta \theta$ to decrease the pitch attitude excursions. Most ALT HOLD autopilots have a "tight" pitch inner loop to increase phugoid damping (Refs. 18 and 29). The effect of increasing the weight on $\Delta \theta$ is shown in Fig. 19. When the gain set is switched from the low $\Delta \theta$ weight to the design weight gain set, the pilots perceive that the altitude hunting is eliminated and the plane is flying straight and level. A difference between the two gain sets is not evident from the figures.

The s-domain closed-loop eigenvalues for the autopilot designs are shown in Table 8. The s-domain eigenvalues are obtained by computing the eigenvalues of the natural log of the discrete closed-loop system matrix as described in Ref. 3 for the PIF control law.

The open-loop short period mode and roll mode are well damped and stable. No quadratic weights are needed on Δq, Δw and Δp. As noted in Ref. 29, another major problem with altitude hold is speed control. The speed mode in Table 8 is stable, but has a large time constant determined primarily by the aerodynamics, (a zero in the $\Delta z / \Delta \delta_e$ transfer function). Increasing the weight on Δu greatly increases control gains and degrades altitude hold performance since the control law begins to use elevator to stabilize speed by diving and climbing.

24

Changing altitude with the ALT SEL autopilot requires that the pilot adjust throttle, particularly in a climb, to maintain airspeed. The PITCH SEL autopilot speed mode is more stable, as shown in Table 8, than the ALT SEL autopilot and uses lower gains. Closing the longitudinal PIF control design loop with the Δz complementary filter in the loop porbably alters the closed-loop eigenvalues shown in Table 8 to produce the lower damped oscillatory mode which is evident in flight tests.

The APR GS autopilot aircraft model with Δd dynamics is identical to the model with Δz dynamics for straight and level flight. The difference between the two designs is that APR GS uses an even higher weight on $\Delta\theta$ than the ALT SEL design gain set.

Table 8 shows that the Dutch Roll damping for the lateral-directional autopilots is low but acceptable. A large number of quadratic weight iterations have been made in an attempt to reduce the a_y to v_{δ_r} gain which contributes to lowering the Dutch Roll damping. No weight is placed on Δv and large weights are placed on the angular positions. The large weighting on Δr in Table 7 is used to offset the zero weighting on Δv.

The reason for keeping the a_y to v_{δ_r} gain low is because of the sensitivity of the PIF Gain C_6 in Eq. 59 to Y_{δ_r}. The linear model for the lateral accelerometer discussed in Appendix A simplifies to

$$\Delta a_y = Y_v \, \Delta v + Y_{\delta_r} \, \Delta\delta_r \qquad (71)$$

in straight and level flight. A nonzero values for Y_v causes the matrix in Eq. 52 to be invertible. The Y_{δ_r} parameter is absorbed into the C_6 gain in Eq. 59. The low-pass filtering effect in PIF changes as Y_{δ_r} varies with flight condition. PIF designs computed for a large number of different flight conditions in Ref. 3 indicate that C_6 (without using accelerometer feedback) is essentially constant and relatively insensitive to changing flight conditions.

A 400% mismatch between Y_{δ_r} in Ref. 30 and Y_{δ_r} identified from flight data using the a_y, β, δ_r measurements and Eq. 71 was the cause for early flight tests of PIF to be unstable. After Y_{δ_r} was reasonably identified, no further difficulties were encountered in flight tests due to accelerometer feedback.

The closed-loop properties of the three APR LOC auotpilot modes are shown in Table 8. The closed-loop properties of the three APR LOC autopilot modes are shown in Table 8. The closed-loop eigenvalues of the three modes are similiar, indicating the difference between the three modes is primarily due to different command following properties. The quadratic weights in Table 7 are chosen so that the three modes have similar closed-loop eigenvalues.

The PIF autopilot feedback and feedforward gains are shown in Tables 9 and 12. The gains are constant in flight and are designed at 44.0 m/s (85 kts) straight and level flight. The diagonal elements in the PIF gain C_6 in Eq. 59,

based on previous studies (Refs. 3 and 19), appears to yield a good design for values between 0.6 and 0.7. The control rate weights in Table 7 are adjusted until the diagonal elements in C_6 approach this desired range. The $v_{\delta_r} - v_{\delta_r}$ rudder gains in Tables 10 and 12 include the effect of Y_{δ_r} and are actually in the range of 0.66 to 0.69.

The ALT SEL and HDG SEL autopilot gains, which were obtained by pilot opinion between different gain sets, serve as a baseline for the APR LOC modes. The weightings on Δy and $\Delta \xi_y$ in Table 7 were obtained by iterative adjustment until the $y - v_{\delta_a}$ and $y - v_{\delta_r}$ gains were near the $z - v_{\delta_e}$ gain and gave adequate tracking performance. Gain adjustment through quadratic weight selection for the APR LOC modes were not performed during flight testing.

The S_{11} matrix elements needed to implement Eq. 57 are shown in Table 13. The order of the aircraft states, $\underline{x}$, and model states, $\underline{x}_m$, are shown in Table 5. The APR LOCR is the only design that requires an S_{11} element that is not a 0.0 and 1.0. The 0.31 element is caused by the way $(\underline{y} - \underline{y}_m)$ is constructed in the APR LOCR autopilot and has little effect on $(\underline{y} - \underline{y}_m)$ since ψ is in radians and $\underline{y}$ is in meters. The 0.31 gain depends on the values of k_ψ and k_y in Eq. 191 and the aerodynamics.

D. PIF LINEAR SIMULATION

The linear simulation time histories used to evaluate the PIF autopilot designs are shown in this section. The simulations use the linear time invariant model shown in Eq. 3 to generate the time histories for $\Delta \underline{x}$. The actual nonlinear command models are used in the linear simulation to generate the time histories for $\underline{y}_m$. The ALT SEL, HDG SEL, and ROLL SEL simulations start with all initial conditions and commands zero. One second into the simulation a step command (altitude, heading or roll angle) is issued to the command model system initiating control action. The APR GS, APR LOCI, APR LOCR and APR LOCP autopilot linear simulations begin with nonzero initial condition offsets in d or y position. The contorl law drives these offsets to zero.

Each simulation plot contains two curves. The solid line curve is the output of the linear aircraft system model. The dotted line curve is the star trajectory generated by Eq. 9. The difference between the solid curve and dotted curve is the regulation error that is weighted in the quadratic cost function and forced to zero.

The ALT SEL simulation is shown in Fig. 20 for a 30.48m (100 ft) descent in height. The command model deceleration is initally limited resulting in gradual transition to a steady descent. As the command model approaches the desired height, the vehicle vertical velocity is vigorously returned to zero resulting in a smooth capture with virtually no overshoot. The pilot prefers the higher acceleration at the end of the altitude change since this serves as an anticipatory cue that the autopilot is completing the maneuver. The height regulation error, which is the primary error of interest, is small; while the other regulation errors in Fig. 20 are large. The large regulation errors are caused by the slow response of the speed mode when throttle is not activated. Attempting to reduce the regulation errors in states other than Δz degrades the Δz response.

26

The HDG SEL mode response for a 45 degree change in heading is shown in Fig. 21. When the heading change is entered, the autopilot banks the aircraft using a constant roll rate up to a specified roll angle limit in the command model. The bank angle direction flys the shortest turn to the new heading. The command system begins rolling the aircraft out of the turn before reaching the new heading producing no heading angle overshoot. The ROLL SEL autopilot simulation in Fig. 22 executes a step command in roll angle with modest overshoot and rapid settling.

The APR LOC linear simulations shown in Figs. 23 and 30 are, as expected, very similiar. The APR LOCI has the best capture performance. The APR LOCR simulation has larger yaw angle and lateral acceleration deviations while the APR LOCP autopilot uses larger the necessary roll angles. The simulations in Figs. 23 and 25 use an initial intercept angle of 0.0 degree. The flight tests use steeper intercept angles in the range of 30 to 60 degrees.

The APR GS linear simulation initially positions the aircraft below the glideslip as shown in Fig. 26. The d position below the glideslope approaches 0.0 as the aircraft flys towards the runway. Before the d position reaches 0.0, the autopilot pitches down and executes a smooth capture with no overshoot. The distance, d, is the perpendicular distance between the aircraft cg and the glideslope and is discussed further in Appendix B.

The approach autopilots exhibit highly nonlinear behavior because of the complexity of the command model and perform differently depending on the intercept initial conditions. Continued discussion of the approach autopilots design and flight test performance is given in Chapter V, Section D.

V. DIGITAL FLIGHT CONTROL SYSTEM FLIGHT TESTS

Flight test results for the PIF autopilot designs described in the previous chapter are presented in this chapter. The flight tests are made with the aircraft and equipment described in Chapter 2. The data are from a series of tests that occurred over a five month period. Turbulence and wind conditions encountered varied from heavy to light and their effect is evident in the data. The plotted data includes measurements available onboard but not used by the autopilot (namely, radar positions, sideslip, range). When the autopilot is engaged, all the recorded sensor outputs show a small amount of bias shift as evidenced by small early transients in plots that include the system engage.

The orientation of the axis system for the flight tests and for the linear simulation is different as discussed in Appendix B. In the flight tests, the vertical axis is positive up. In the linear simulation, the vertical axis is positive down.

A. ALT SEL FLIGHT TESTS

The ALT SEL flight tests presented use the following options to investigate performance

- Design gain set

- Low-pitch-weight gain set

- 30.5 m (100 ft) descent-constant throttle

- 152.4 m (500 ft) ascent - manual throttle

- 152.4 m (500 ft) descent - manual throttle

- 152.4 m (500 ft) ascent - constant throttle

- 152.4 m (500 ft) descent - constant throttle

- Heavy turbulence

- Moderate turbulence

- Light turbulence

- HDG SEL operational

Standard operating procedure with the ALT SEL autopilot requires the pilot to manually adjust throttle to maintain airspeed. Flight tests with constant

throttle are used to test the autopilot at varying flight conditions.

The pilot opinions for different ALT SEL gain sets are made by performing a series of 30.5 m (100 ft) descents. Figures 13, 18, 19, 27 and 28 show the effect of the gain sets and turbulence conditions. Figures 27 and 28 are conducted with the same low pitch weight gain set but have heavy and medium turbulence conditions, respectively. Turbulence increases altitude hunting amplitudes as expected. The pilots judged the ride quality in Fig. 27 typical for heavy turbulence conditions. The variable, ZF, shown in the figures is the best indication of actual vehicle altitude estimated from a complementary filter using radar position and onboard accelerometers. HEIGHT ESTIMATE in Fig. 13 is the output of the barometric altimeter complementary filter (z(+)) used by the control law and HBARM is the barometric altimeter sensor output.

Figures 20 and 31 show ± 152.4 m (500 ft) altitude changes for the design gain set. In Fig. 30, the autopilot is attempting to execute a 152.4 m ascent without increasing throttle. Airspeed steadily decreases and pitch angle and angle of attack increase until the pilot disengages the autopilot near stall at the onset of buffeting. The HDG SEL autopilot is operational during the flight. The autopilot did not cause the aircraft to depart from flight at a high angle of attack. The autopilot properly ascends when the pilot adjusts throttle as shown in Fig. 29. The autopilot properly descends with or without throttle activity. The ALT SEL autopilot has a favorable comparison to Fig. 32 which shows a manual 152.4 m altitude descent with constant throttle.

The data in Figs. 28 and 29 exhibit only a slight difference in performance between gain sets while the pilot has a stron preference to the performance in Fig. 29. Evaluating performance strictly from data (or nonlinear simulations as is typically done) is helpful but usually does not replace actual pilot opinions.

B. HDG SEL FLIGHT TESTS

The HDG SEL flight tests presented use the following options to investigate performance:

- No a_y prefilter

- 0.1 sec time constant a_y prefilter

- 0.22 sec time constant a_y prefilter

- Large airspeed variations

- Heavy Turbulence

- Moderate Turbulence

- Light Turbulence

- Pilot entered disturbances through rudder cable

- Multiple turns

- ALT SEL is operational

The investigation of different prefilters is discussed in Chapter IV, Section A. The flight tests results are shown in Figs. 15 to 17. The performance of the HDG SEL autopilot under moderate turbulence conditions with the 0.1 sec time constant a_y prefilter, (the nominal design), compares favorably to the linear simulation in Fig. 21. The autopilot banks the aircraft, flys a co-ordinated turn with little sldeslip in the shortest direction to the new heading, then rolls out of the turn just before reaching the new heading for a smooth capture. The HDG SEL autopilot uses the value of rudder at control activation as the nominal value. The value should change with airspeed since the nonzero rudder position is used to offset propeller effects. A flight test to gauge the effect of not changing the commanded rudder position is shown in Fig. 33.

In Fig. 33, the HDG SEL autopilot is activated at 53 m/s in heavy turbulence. The airspeed is decreased to 35 m/s by adjusting throttle and a 45 degree turn is executed. The HDG SEL autopilot performed the maneuver with no unusual difficulty due to either turbulence or rudder position and the pilot gave a favorable opinion of the maneuver.

Commands to the ALT SEL and HDG SEL autopilots can be made simultaneously. Figure 14 shows the aircraft performing a spiral descent. Multiple spirals in Fig. 14 show the autopilot transferring between straight and level flight and turning, descending flight during the same engagement period. The pass through a 180 deg course in Fig. 14 demonstrates that the yaw complementary filter adequately suppresses the heading gyro discontinuity at 180 degrees. Flight tests on a 180 deg course (not presented) could not be distinguished from any other course heading.

C. PITCH SEL AND ROLL SEL FLIGHT TESTS

The PITCH SEL and ROLL SEL autopilots are simplier versions of the ALT SEL and HDG SEL autopilots. The feedback gains are similiar, but not identical, and the command model is a simple rate limit of the amount the angle commands can change in 0.1 seconds. A pitch angle command of +5 degrees above the trim pitch angle, with constant throttle, at 18 seconds into the test is shown in Fig. 34. The altitude hunting in Fig. 34 compares favorably to the ALT SEL response during the early pitch hold phase of the flight tests.

A roll angle command of +5 degrees is shown in Fig. 35. Prior to engaging the autopilot, the aircraft was trimmed with a 4.0 degree roll angle for straight and level flight. The ROLL SEL autopilot uses an internal roll command of 0.0 degrees at engage time. At ROLL SEL autopilot engage in Fig. 35, the 0.0 roll command causes the aircraft to initiate a turn. The 5 deg command is initiated 28 seconds into the flight test. The roll command to rudder position crossfeed gain is used and the aircraft performs a coordinated turn. The sideslip offset shown in Fig. 35 and evident in other figures is believed to be sensor bias. The steady state sideslip value remains the same

30

before and after engaging the autopilots.

D. APPROACH MODE FLIGHT TESTS

The approach modes, APR GS, APR LOCI, APR LOCR, and APR LOCP are the most complicated of the autopilots designed in this report. An effort was made to take advantage of the command model formulation and design approach modes which work best with a Microwave Landing System (MLS) but are operational with an Instrument Landing System (ILS). The flight test results presented in this section use the Wallops Island Radar to emulate ILS signals only. In the future, airports will be converting to the microwave landing system. The MLS has a large volumetric coverage and supplies azimuth, elevation and range information to approaching aircraft. Knowing the geometry of the MLS transmitters, the aircraft can compute its position in cartesian coordinates with high accuracy, allowing the aircraft to make steep approaches along curved flight paths in the terminal area. In the interim period, aircraft autopilots will utilize either MLS or ILS.

The ILS, which is in use today, has limited coverage with information supplied to the aircraft in the airspace surrounding a particular glideslope. Accurate deviations from the beam center line (localizer) extend 2.5 degrees (typically) to either side and accurate deviations from the glideslope extend 0.7 degrees (typically) up and down. The only range information occurs when the aircraft receives a signal from the outer marker (about 9700 m) and from the middle marker (about 800 m) enroute to touchdown as the aircraft passes over either marker. Pilot handbooks supply information about runway heading, glideslope angle (2.5 - 3.0 deg.), transmitter location and actual outer marker and middle marker distances.

Typical operation of a commercial autopilot requires the pilot to set up an intercept angle (between 45 and 90 degrees), then arm the approach modes. The autopilot captures the glideslope and localizer and feeds back the localizer/glideslope errors. The feedback gains for the errors are sometimes reduced as the aircraft approaches the runway to counteract increased angular deviation sensitivity.

The approach modes for PIF are an attempt at designing autopilots which accommodate either ILS or MLS transmitted information. The approach modes command model use a range estimate, localizer deviation signals and glideslope deviation signals to generate vertical and horizontal paths, (d and y), the aircraft should follow to touchdown. The path and path errors are trivial to construct using MLS but are more difficult to compute using ILS. The primary issue is whether the range estimate shown in Eqs. 178 and 180 is sufficiently accurate to allow path construction. Feeding back path error rather than angular deviation error allows the PIF control gains to be constant throughout the approach mode flight.

The operating procedure for the approach autopilots requires the pilot to maneuver the aircraft to the desired altitude and intercept angle for ILS capture. The autopilot is engaged and automatically activates the HDG SEL and ALT SEL modes. After the aircraft enters the localizer signal coverage,

the software switches automatically from HDG SEL to APR LOC. The APR LOC mode initializes a y-position and generates a path on line for y to approach 0.0 using bank angle and yaw angle maneuvers and simple kinematics (Appendix C). The errors between the commmand model path and y estimated from Eq. 200 are fed back and integrated along with roll and yaw. If the intercept angle is large enough (greater than 30 deg), the aircraft initially rolls away from the beam centerline to intercept with a tangential trajectory.

The APR LOC mode tested is designed to capture two seconds after receiving a valid localizer signal. If the aircraft remains banked for shallow intercept angles the capture sequence willl undershoot the beam centerline. The command model contról system does not allow the undershoot to occur by stopping the turn sequence when a 30 degree intercept is reached and holding the 30 degree intercept until the capture can be continued for a smooth intercept. Pilot comments indicated that the autopilot should delay capture until this sequence can be performed with a single banked turn. This approach is discussed further in Chapter VI.

The APR GS mode command model is activated when the glideslope signal coverage is entered. If the aircraft is below the glideslope and the APR GS model control is commanding a positive flight path angle, (pitch up), the aircraft remains in the ALT SEL mode. When the APR GS model commands a negative flight path angle, the current perpendicular position between the aircraft and glideslope (d position) is initialized in the model and the model generates a path on line for d to approach 0.0 The d position is reduced to zero gradually so that the aircraft approaches the glideslope tangentially (no overshoot).

The flight test shown in Fig. 36 has the pilot nulling the localizer signal and the autopilot flying only the APR GS/ALT SEL modes. The range estimate is constant until the aircraft approaches the outer marker then propagated open loop using Eq. 178 only. This method for estimating range is not accurate enough after capture and the aircraft began "porpoising" at a range near 1600 m (1 mile) before touchdown. The pilot does not lower flaps during the capture and approach sequence. The aircraft smoothly captured the glideslope without overshoot. Altitude hunting is evident throughout the data in the sequence but is not noted by the pilot.

The flight test shown in Fig. 37 uses the range estimate consisting of Eqs. 180 and 178. The aircraft began to smoothly capture the glideslope at 190 seconds. As shown in the figure, the pilot lowered the flaps in two steps, one near 120 seconds and the other near 200 seconds. The increased lift due to flaps caused the aircraft to ascend. The autopilot counteracts the flap movement and pitched the aircraft down further at each flap change. The autopilot accurately followed the glideslope after the second flap change until the pilot took over at 60 m (200 ft.) altitude.

The flight test in Fig. 38 is performed with the pilot flying an approach mode where the pilot purposely intercepted the beam centerline after the outer marker. The outer marker signal was not received and the range estimate was held at a constant value until the glideslope signal

was within range and both Eqs. 178 and 180 were activated. The adaptive comple-
mentary gain in the update equation for range is used to keep large initial
range errors from disturbing the control system. The APR GS (and APR LOCR) auto-
pilot performed as designed even though the initial range estimate was poor.
The pilot lowered flaps in one step coincidently with the autopilot capturing
the glideslope as shown in Fig. 38.

The flight tests for the APR LOCI, APR LOCR, and APR LOCP autopilots are
shown in Figs. 39 to 41 for a 45 degree (approximagely) intercept. While the
pilot favored the APR LOCI mode capture, a wings level flight along the beam
centerline indicated APR LOCI could not accommodate the 4.0 m/s (8 kt) cross-
wind present during flight tests. Comparing sideslip (BETA) in Figs. 39 and
41, the APR LOCI mode sideslip gradually departs from coordinated flight as the
aircraft tracks the beam centerline and is the source of pilot discomfort. The
sideslip during capture indicated the APR LOCR has the worst capture performance
while APR LOCI and APR LOCP are comparable. The APR LOCR and APR LOCP auto-
pilots automatically accommodate the crosswind while remaining on the runway
centerline which keeps the sideslip angle small. This is achieved without
estimating wind magnitude or using it in the control system. The pilot could
not distinguish between APR LOCR and APR LOCP performance and choose APR LOCR
as the approach mode for continued flight testing. APR LOCR is similar in
integrator command error construction to a method suggested in Ref. 18. The
flight test data suggest that APR LOCP is the better design.

The APR GS flight test shown in Fig. 28 had the safety pilot track the
localizer deviation signal. The time history of the pilot's localizer tracking
performance is shown in Fig. 42. The autopilot's significantly greater accu-
racy in localizer tracking with less roll angle activity is evident when Fig.
42 is compared to Figs. 40 to 41.

Flight test results for a 60 deg. intercept angle using the APR LOCR auto-
pilot is shown in Fig. 43. The aircraft remains banked until intercepting the
beam centerline then tracked with little overshoot. The pilot favored the 60
deg. intercept capture sequence, becasue only one roll command is executed in
this sequence.

The localizer capture and hold sequence where the aircraft purposely
misses the outer marker, is shown in Fig. 44. The results shown in Fig. 44
occur concurrently with the APR GS flight test results shown in Fig. 38. The
initial y position error is estimated to be much larger than it actually is,
resulting in a large commanded bank angle. The bank angle oscillates as the
changes in heading decrease the y position more quickly than expected. The
range estimate becomes accurate 90 seconds into the flight and the aircraft
accurately tracks the localizer error thereafter.

The APR GS and APR LOC autopilots performed exactly as designed. Perfor-
mance of the APR GS is excellent while the APR LOC command model requires ad-
ditional sophistication to achieve a desirable rating from the pilot at any
intercept angle. Favorable comparisons can be made with the autopilot ap-
proaches and piloted approaches presented in Ref. 2 for the same NAVION air-
craft flying the same approach procedure during display evaluation.

VI. CONCLUDING REMARKS

This report provides a complete and rare practical demonstration of the advantages of a particular modern optimal digital flight control system design for use in future General Aviation autopilots. A digital control law for performing general aviation autopilot functions is designed using Linear Quadratic Regulator theory and Feedforward Control theory. A discrete nonlinear command model that accepts pilot inputs is constructed for each autopilot function and outputs desired aircraft state trajectories for the command states. The output of the command model is fed forward to a proportional-integral-filter (PIF) control law. The digital PIF control law forms command errors for feedback stabilization and output command error integration for command following. The PIF control law uses standard general aviation sensors for feedback and complementary filters to smooth the output of the barometric altimeter and yaw gyro. A computer program is available to rapidly and completely design the PIF control law by the general user.

All the autopilots have been successfully programmed in FORTRAN in the on-board ROLM flight computer. All the autopilots have been successfully flight tested and performed as designed. The constant feedback gain autopilots stabilized the aircraft throughout the normal flight regime of the aircraft. The full state feedback PIF LQR design tends to be relatively insensitive to modeling errors.

A. RECOMMENDATIONS

Areas of possible improvement in the PIF design approach are discussed in this section and are recommended for further investigation.

- Output Feedback - General aviation autopilots do not use full state feedback for stability as PIF does. General avaition autopilots use output feedback, which eliminates costly sensors, improves reliability since there are fewer sensors to fail, does not require accurate aircraft models to estimate unmeasured states and is easier to design (from a classical point of view) since there are fewer gains to manually adjust. Recently, in Refs. 9 and 31, numerically solutions for determining output feedback digital control laws have been developed. The results in Ref. 9 are derived for the discrete LQG optimization problem that includes the PIF approach. The PIF control law, as designed, theoretically requires a full order Kalman filter for optimum stochastic performance. The output feedback optimal control problem solved in Ref. 9 formulates the LQG PIF design problem exactly as it implemented, without the Kalman filter. The resulting optimization solution would reduce PIF gains for noisy sensors (a_y, a_z, and h_B) and increase PIF gains optimally for accurate sensors (θ, ϕ and r). Complementary filters, actuator dynamics and sensor dynamics can be included in the PIF control design model. The PIF control law using an output feedback approach would be designed and evaluated using the implementation structure that exists in flight. The output feedback approach would replace x_k in Fig. 7 with y_k, the available sensor measurements. The feedback gain C_5 and

the feedforward gain S_{11} in Fig. 7 would change dimension to account for the fewer measurements. The rest of the structure in Fig. 7 would remain the same.

- Quadratic Weight Section – A new procedure for choosing the quadratic weights in the optimal control problem has been developed in Ref. 8. Designing PIF control laws using this approach should be investigated.

- Fuel Optimal Trajectories – The command models can be made more complex to increase features. For example, the ALT SEL autopilot changes altitude based solely on achieving good ride quality. Properly including energy and fuel dynamics (similiar to approaches in Refs. 32 and 33) in the command model enables the command model control system to be designed to change altitude with reduced fuel cost for the aircraft.

- APR LOC Improvements – The APR LOC command model control system should be improved to increase pilot acceptance. One method of improvement (Ref. 12) is to determine the maximum intercept angle versus speed for a no overshoot approach capture as a function of localizer transmitter distance and incorporate this into the APR LOC engage logic.

- Flight Tests – The approach modes should be tested with a microwave landing system. The approach modes should be tested at a commerical airport using ILS.

- Increase Robustness – New synthesis methods for increasing linear optimal regulator robustness have been developed at ICS and can be included in the PIF design procedure.

- Stall Avoidance – Stall detection and avoidance logic should be coupled with the ALT SEL and PITCH SEL autopilots. Stall may occur when the pilot ascends without properly adjusting throttle.

- Graceful Degradation – The ROLL SEL and PITCH SEL autopilots can serve as revert modes to be used automatically when sensors (heading gyro, barometric altimeter) fail or actuators (aileron, rudder) fail. The ALT SEL autopilot could switch to PITCH SEL as one method of avoiding stall. The ROLL SEL and PITCH SEL autopilots could be designed using output feedback to give deteriorated, but stable, performance using a minimum of sensors.

APPENDIX A

AIRCRAFT EQUATIONS OF MOTION

A. OVERVIEW

This appendix reviews the nonlinear and linear perturbation equations of motion for a general aviation aircraft. These derivations make extensive use of vector-matrix differential equation ("state-space") notation, and the resulting equations are written in a form suitable for analysis using concepts of modern control theory. The notation is fairly standard but a review of the List of Symbols may be desirable.

B. NONLINEAR DYNAMIC EQUATIONS

The nonlinear rigid-body equations are reviewed in this section. The equations are developed using "flat-earth" assumptions, i.e., the effects of earth curvature and rotation are assumed negligible. This means that earth-fixed and inertial reference frames are equivalent.

The origin of the inertial reference frame used here is located on the surface of the earth at the runway touchdown point. The x-axis points along the runway center line towards the approaching aircraft. The z-axis points down and the y-axis points to the right completing a right-hand coordinate system.

Detailed vehicle state equations can best be expressed in body-fixed axes. These are the axes in which the pilot, the sensors, and the control surface locations are defined. Body axes are the only axes in which the moment-of-inertia matrix is constant. Dynamic data collected from flight tests usually are expressed in body axes.

The body-fixed axis system used in this report has its origin located at the body center of mass, and is fixed in orientation with respect to the vehicle. The body x-axis extends forward out the vehicle's nose, the y-axis extends out the right wing, and the z-axis extends out the bottom of the vehicle. The x-z plane is usually a plane of geometric symmetry, if the vehicle has one. For any nominal flight condition, another commonly used body-fixed axes system can be chosen so that the x-axis is aligned with the velocity vector, and the z-axis is in the body-axis plane. This set of body-fixed axes is referred to as the stability-axis system and is not employed in this report.

A transformation from inertial to body axes is composed of a right-handed yaw through an angle ψ; then a right-handed pitch through an angle θ, and then a right-handed roll through an angle ϕ. The inertial-to-body axis transformation proceeds as follows:

36

$$H_E(\phi,\theta,\psi) = H_2^B(\phi) \; H_1^2(\theta) \; H_E^1(\psi)$$

$$= \begin{bmatrix} 1 & 0 & 0 \\ 0 & \cos\phi & \sin\phi \\ 0 & -\sin\phi & \cos\phi \end{bmatrix} \begin{bmatrix} \cos\theta & 0 & -\sin\theta \\ 0 & 1 & 0 \\ \sin\theta & 0 & \cos\theta \end{bmatrix} \begin{bmatrix} \cos\psi & \sin\psi & 0 \\ -\sin\psi & \cos\psi & 0 \\ 0 & 0 & 1 \end{bmatrix} \qquad (72)$$

Two aerodynamic angles used in this report are the angle of attack, α, and angle of sideslip, β. Angle of attack represents the aircraft body pitch angle above the velocity vector, and sideslip is the angle that the aircraft nose is yawed left of the velocity vector.

The nonlinear equations of motion of the aircraft are determined by constructing kinematic relationships between aircraft translational and angular position states and by applying Newton's Second Law to the dynamics of the vehicle. The kinematic relationships are

$$\dot{\underline{x}}_E = H_B^E \; \underline{v}_B \qquad (73)$$

$$\dot{\underline{\nu}}_B = L_B^{-1} \; \underline{\omega}_B \qquad (74)$$

and the results from applying Newton's Second Law to translational and rotational motions produces (Ref. 34)

$$\dot{\underline{v}}_B = (F_B + T_B)/m + H_E^B \; \underline{g}_E - \tilde{\omega}_B \underline{v}_B \qquad (75)$$

$$\dot{\underline{\omega}}_B = I_B^{-1} (M_B + G_B) - I_B^{-1} \tilde{\underline{\omega}}_B \; I_B \; \underline{\omega}_B \qquad (76)$$

The vector $\underline{x}_E$, is the position of the vehicle relative to the earth fixed coordinate system $\underline{x}_E^T = [x_E, y_E, z_E]$. The inertial-body Euler angle vector is $\underline{\nu}_B$, $\underline{\nu}_B^T = [\phi, \theta, \psi]$. The Euler angle derivatives occur in three different references frames and are related to the body-axis vehicle rates as shown in Eq. 74 where

$$L_B = \begin{bmatrix} 1 & 0 & -\sin\theta \\ 0 & \cos\phi & \sin\phi\cos\theta \\ 0 & -\sin\phi & \cos\phi\cos\theta \end{bmatrix} \qquad (77)$$

The applied specific forces consist of gravitional forces and contact forces as shown in Eq. 75. The specific contact force is broken into two components,

37

one of which is due to aerodynamic forces, $\underline{F}_B$, and one of which is due to thrust, $\underline{T}_B$. The gravity force is $\underline{g}_E^T = [0 \quad 0 \quad g]$. $\tilde{\omega}_B$ in Eq. 75 is the cross product equivalent matrix for $\underline{\omega}_B$ and is given by

$$\tilde{\omega}_B = \begin{bmatrix} 0 & -r & q \\ r & 0 & -p \\ -q & p & 0 \end{bmatrix} \tag{78}$$

The inertia matrix, I_B, in Eq. 76 contains all products and moments of inertia;

$$I_B = \begin{bmatrix} I_x & -I_{xy} & -I_{xz} \\ -I_{xy} & I_y & -I_{yz} \\ -I_{xz} & -I_{yz} & I_z \end{bmatrix} \tag{79}$$

while the contact moments consist of aerodynamic components, $\underline{M}_B$, and thrust components, $\underline{G}_B$. Equations 73 to 76 when combined fall into the general state equation form

$$\underline{\dot{x}} = \underline{f}(\underline{x}, \underline{u}) \tag{80}$$

by defining the state vector

$$\underline{x}^T = \begin{bmatrix} \underline{v}_B^T & \underline{\omega}_B^T & \underline{v}_B^T & \underline{x}_E^T \end{bmatrix} \tag{81}$$

and noting that the aerodynamic forces and moments are functions of states, controls, and to some extent, the state history.

C. LINEAR DYNAMIC EQUATIONS

The linearization procedure is performed by construction of a Taylor series expansion representing the nonlinear equations about some nominal trajectory:

$$\underline{\dot{x}} = \underline{\dot{x}}_0 + \Delta\underline{\dot{x}} + \text{Higher Order Terms}$$

$$= \underline{f}(\underline{x}_0, \underline{u}_0) + \left.\frac{\partial \underline{f}}{\partial \underline{x}}\right|_{\substack{\underline{x}=\underline{x}_0 \\ \underline{u}=\underline{u}_0}} \Delta\underline{x} + \left.\frac{\partial \underline{f}}{\partial \underline{u}}\right|_{\substack{\underline{x}=\underline{x}_0 \\ \underline{u}=\underline{u}_0}} \Delta\underline{u} + \text{Higher Order Terms} \tag{82}$$

Here, the subscript "0" indicates the nominal value and the prefix "Δ" denotes a small perturbation. All except first-order terms are then neglected by arguing that the higher-order terms are small compared to linear terms. The results of this procedure are separated into a nonlinear equation describing the nominal trajectory (Eq. 83) and a linear equation defining the dynamics of the perturbations about the nominal trajectory (Eq. 84):

38

$$\dot{\underline{x}}_O = \underline{f}(\underline{x}_O, \underline{u}_O) \tag{83}$$

$$\Delta\dot{\underline{x}} = A\Delta\underline{x} + B\Delta\underline{u} \tag{84}$$

The formal linearization of the aerodynamic forces and moments and non-linear dyanmic kinematic equations is a lengthy but straight forward process which can be found in a number of references (Refs. 18, and 34). The linear-ization of each nonlinear dynamic equation in Eq. 78 results in the following:

$$\Delta\dot{\underline{x}}_E = H^E_B \Delta\underline{v}_B - (\overbrace{\dot{x}_{E_O}}) H^E_{B_O} L_{B_O} \Delta\underline{v}_B \tag{85}$$

$$\Delta\dot{\underline{v}}_B = L^{-1}_{B_O} \Delta\underline{\omega}_B - L^{-1}_{B_O} L^{'}_{B_O} \Delta\underline{v}_B \tag{86}$$

$$\Delta\dot{\underline{v}}_B = (\Delta F_B + \Delta T_B)/m + (H^B_{E_O} \underline{g}_E)L_{B_O}\Delta\underline{v}_B + \tilde{v}_{B_O}\Delta\underline{\omega}_B - \tilde{\omega}_{B_O}\Delta\underline{v}_B \tag{87}$$

$$\Delta\dot{\underline{\omega}}_B = I^{-1}_B (\Delta M_B + \Delta G_B) - I^{-1}_B \left[\tilde{\omega}_{B_O}I_B - (\overbrace{I_B\underline{\omega}_{B_O}})\right]\Delta\underline{\omega}_B \tag{88}$$

The perturbation equations contain as yet only general terms for the perturbation aerodynamic effects. The only remaining undefined term is in Eq. 86,

$$L^{'}_{B_O} = \left.\frac{\partial(L_B\underline{v}_B)}{\partial\underline{v}_B}\right|_{\underline{v}_B = \underline{v}_{B_O}} \tag{89}$$

$$-L^{-1}_{B_O} L^{'}_{B_O} = \begin{bmatrix} \dot{\theta}_O \tan\theta_O & \dot{\psi}_O \sec\theta_O & 0 \\ -\dot{\psi}_O \cos\theta_O & 0 & 0 \\ \dot{\theta}_O \sec\theta_O & \dot{\psi}_O \tan\theta_O & 0 \end{bmatrix} \tag{90}$$

The perturbation aerodynamic effects are assumed to be linear functions of the perturbation states, of the time derivatives of the perturbation states and of the perturbation values of the vehicle control variables. This viewpoint leads to the conventional name of aerodynamic stability derivatives for the coefficients that relate the pertrubation states, state rates and controls to the perturbation forces and moments. Assuming insignificant altitude and orient-ation effects on contact forces and moments, and assuming insignificant state derivative and angular rate effects on thrust forces and moments, the pertur-bation aerodynamic forces and moments are as follows:

$$\Delta \underline{F}_B = \left[\frac{\partial \underline{F}_B}{\partial \underline{v}_B}\right] \Delta \underline{v}_B + \left[\frac{\partial \underline{F}_B}{\partial \underline{\omega}^I}\right] \Delta \underline{\omega}_B^I + \left[\frac{\partial \underline{F}_B}{\partial \underline{u}}\right] \Delta \underline{u} + \left[\frac{\partial \underline{F}_B}{\partial \dot{\underline{v}}_B}\right] \Delta \dot{\underline{v}}_B \qquad (91)$$

$$\Delta \underline{M}_B = \left[\frac{\partial \underline{M}_B}{\partial \underline{v}_B}\right] \Delta \underline{v}_B + \left[\frac{\partial \underline{M}_B}{\partial \underline{\omega}}\right] \Delta \underline{\omega}_B^I + \left[\frac{\partial \underline{M}_B}{\partial \underline{u}}\right] \Delta \underline{u} + \left[\frac{\partial \underline{M}_B}{\partial \dot{\underline{v}}_B}\right] \Delta \dot{\underline{v}}_B \qquad (92)$$

$$\Delta \underline{T}_B = \left[\frac{\partial \underline{T}_B}{\partial \underline{v}_B}\right] \Delta \underline{v}_B + \left[\frac{\partial \underline{T}_B}{\partial \underline{u}}\right] \Delta \underline{u} \qquad (93)$$

$$\Delta \underline{G}_B = \left[\frac{\partial \underline{G}_B}{\partial \underline{v}_B}\right] \Delta \underline{v}_B + \left[\frac{\partial \underline{G}_B}{\partial \underline{u}}\right] \Delta \underline{u} \qquad (94)$$

By using the definition of non-dimensional stability derivatives given in Ref. 24, it is possible to define the dimensional stability derivative matrices in Eqs. 91 to 94 in terms of the usual body axis non-dimensional stability derivatives. This is done in Eqs. 95 to 102.

$$\left[\frac{\partial \underline{F}_B}{\partial \underline{v}_B}\right] = \rho_0 A \begin{bmatrix} u_0 C_{X_0} + \tfrac{1}{2} V_0 C_{X_u} & v_0 C_{X_0} + \tfrac{1}{2} V_0 C_{X_v} & w_0 C_{X_0} + \tfrac{1}{2} V_0 C_{X_w} \\ u_0 C_{Y_0} + \tfrac{1}{2} V_0 C_{Y_u} & v_0 C_{Y_0} + \tfrac{1}{2} V_0 C_{Y_v} & w_0 C_{Y_0} + \tfrac{1}{2} V_0 C_{Y_w} \\ u_0 C_{Z_0} + \tfrac{1}{2} V_0 C_{Z_u} & v_0 C_{Z_0} + \tfrac{1}{2} V_0 C_{Z_v} & w_0 C_{Z_0} + \tfrac{1}{2} V_0 C_{Z_w} \end{bmatrix} \qquad (95)$$

$$\left[\frac{\partial \underline{F}_B}{\partial \underline{\omega}_B^I}\right] = \frac{\rho_0}{4} V_0 A \begin{bmatrix} b C_{X_p} & \bar{c} C_{X_q} & b C_{X_r} \\ b C_{Y_p} & \bar{c} C_{Y_q} & b C_{Y_r} \\ b C_{Z_p} & \bar{c} C_{Z_q} & b C_{Z_r} \end{bmatrix} \qquad (96)$$

$$\left[\frac{\partial \underline{F}_B}{\partial \underline{u}}\right] = \tfrac{1}{2}\rho_0 V_0^2 A \begin{bmatrix} C_{X_{\delta_T}} & C_{X_{\delta_e}} & C_{X_{\delta_a}} & C_{X_{\delta_r}} \\ C_{Y_{\delta_T}} & C_{Y_{\delta_e}} & C_{Y_{\delta_a}} & C_{Y_{\delta_r}} \\ C_{Z_{\delta_T}} & C_{Z_{\delta_e}} & C_{Z_{\delta_a}} & C_{Z_{\delta_r}} \end{bmatrix} \qquad (97)$$

$$\left[\frac{\partial F_B}{\partial \dot{\underline{v}}_B}\right] = \frac{\rho_0}{4} A \begin{bmatrix} \bar{c}C_{X_{\dot{u}}} & bC_{X_{\dot{v}}} & \bar{c}C_{X_{\dot{w}}} \\ \bar{c}C_{Y_{\dot{u}}} & bC_{Y_{\dot{v}}} & \bar{c}C_{Y_{\dot{w}}} \\ \bar{c}C_{Z_{\dot{u}}} & bC_{Z_{\dot{v}}} & \bar{c}C_{Z_{\dot{w}}} \end{bmatrix} \tag{98}$$

$$\left[\frac{\partial \underline{M}_B}{\partial \underline{v}_B}\right] = \rho_0 A \begin{bmatrix} u_0 bC_{\ell_0} + \frac{1}{2} V_0 bC_{\ell_u} & v_0 bC_{\ell_0} + \frac{1}{2} V_0 bC_{\ell_v} & w_0 bC_{\ell_0} + \frac{1}{2} V_0 bC_{\ell_w} \\ u_0 \bar{c}C_{m_0} + \frac{1}{2} V_0 \bar{c}C_{m_u} & v_0 \bar{c}C_{m_0} + \frac{1}{2} V_0 \bar{c}C_{m_v} & w_0 \bar{c}C_{m_0} + \frac{1}{2} V_0 \bar{c}C_{m_w} \\ u_0 bC_{n_0} + \frac{1}{2} V_0 bC_{n_u} & v_0 bC_{n_0} + \frac{1}{2} V_0 bC_{n_v} & w_0 bC_{n_0} + \frac{1}{2} V_0 bC_{n_w} \end{bmatrix} \tag{99}$$

$$\left[\frac{\partial \underline{M}_B}{\partial \underline{\omega}_B^I}\right] = \frac{\rho_0}{4} V_0 A \begin{bmatrix} b^2 C_{\ell_p} & b\bar{c}C_{\ell_q} & b^2 C_{\ell_r} \\ b\bar{c}C_{m_p} & \bar{c}^2 C_{m_q} & b\bar{c}C_{m_r} \\ b^2 C_{n_p} & b\bar{c}C_{n_q} & b^2 C_{n_r} \end{bmatrix} \tag{100}$$

$$\left[\frac{\partial \underline{M}_B}{\partial \underline{u}}\right] = \frac{1}{2}\rho_0 V_0^2 A \begin{bmatrix} bC_{\ell_{\delta T}} & bC_{\ell_{\delta_e}} & bC_{\ell_{\delta_a}} & bC_{\ell_{\delta_r}} \\ \bar{c}C_{m_{\delta T}} & \bar{c}C_{m_{\delta_e}} & \bar{c}C_{m_{\delta_a}} & \bar{c}C_{m_{\delta_r}} \\ bC_{n_{\delta T}} & bC_{n_{\delta_e}} & bC_{n_{\delta_a}} & bC_{n_{\delta_r}} \end{bmatrix} \tag{101}$$

$$\left[\frac{\partial \underline{M}_B}{\partial \dot{\underline{v}}_B^I}\right] = \frac{\rho_0}{4} A \begin{bmatrix} b\bar{c}C_{\ell_{\dot{u}}} & b^2 C_{\ell_{\dot{v}}} & b\bar{c}C_{\ell_{\dot{w}}} \\ \bar{c}^2 C_{m_{\dot{u}}} & b\bar{c}C_{m_{\dot{v}}} & \bar{c}^2 C_{m_{\dot{w}}} \\ b\bar{c}C_{n_{\dot{u}}} & b^2 C_{n_{\dot{v}}} & b\bar{c}C_{n_{\dot{w}}} \end{bmatrix} \tag{102}$$

The $\Delta \dot{v}_B$ term in Eqs. 98 and 102 is included because of the affect of $\dot{\alpha}$ on ΔM_B.

The subroutine FGAERO in the program PIFGCT, Ref. 5, accepts the non-dimensional stability derivatives and trim conditions shown in Eqs. 95 to 102 and uses the information and the derivation in this section to construct A and B in Eq. 84. Further details of the linear model construction are given in documentation of FGAERO.

Many elements in the stability matrices are known to be zero or can be neglected in all cases of interest. Considerable simplification of the equations of motion for a specific vehicle can be performed and this is done for the NAVION aircraft in Appendix B.

APPENDIX B

AIRCRAFT AERODYNAMIC MODEL

The aerodynamic and mass data and simplified equations of motion used in the NAVION model are discussed in this appendix. Comparisons of the model response to the actual aircraft response for a pilot induced pulse in the aircraft control surface is also shown.

A. AERODYNAMIC AND MASS DATA

The aerodynamic data for the NAVION aircraft is taken from Ref. 30. Reference 30 uses flight data rather than wind tunnel data to identify the aerodynamic coefficients and therefore captures rate effects due to q, r, p, and $\dot{\alpha}$. A comparison of flight test results with linear model simulations caused some of the aerodynamic coefficients from Ref. 30 to be adjusted to better represent the aircraft dynamics. The original mismatch between the model and the aircraft was sufficient to cause the lateral-axis PIF control law to be unstable. The aircraft wheels in current flight tests are in the takeoff and landing configuration (increased drag) while the wheels in Ref. 30 are believed to be retracted. The NAVION airplane parameters are shown in Table 14. The gross mass value represents the best estimate of the current fully instrumented NAVION. The mass value (WT) is 204.8 kg (452 lbs) heavier due to instruments than the value given in Ref. 30. The instruments are near the c.g. The values for I_X, I_Y, and I_Z remain unchanged from those given in Ref. 30.

The matrix differential equations for the nonlinear aircraft model in Appendix A can be simplified to the following series of scalar nonlinear equations for the NAVION aircraft.

$$\dot{u} = rv - qw - \sin(\theta)g + \tfrac{1}{2} \rho V^2 A \frac{q}{WT} C_X \tag{103}$$

$$\dot{v} = pw - ru - \cos(\theta)\sin(\phi)g + \tfrac{1}{2} \rho V^2 A \frac{q}{WT} C_Y \tag{104}$$

$$\dot{w} = qu - pv + \cos(\theta)\cos(\phi)g + \tfrac{1}{2} \rho V^2 A \frac{q}{WT} C_Z \tag{105}$$

$$\dot{p} = \frac{1}{I_x} ((I_y - I_z)qr + \tfrac{1}{2} \rho V^2 A\, b\, C_L) \tag{106}$$

$$\dot{q} = \frac{1}{I_y} ((I_z - I_x)rp + \tfrac{1}{2} \rho V^2 A\, \bar{c}\, C_M) \tag{107}$$

$$\dot{r} = \frac{1}{I_z} ((I_x - I_y)pq + \tfrac{1}{2} \rho V^2 A\, b\, C_N) \tag{108}$$

43

$$\dot{\theta} = \cos(\phi)q - \sin(\phi)r \tag{109}$$

$$\dot{\phi} = p + (q \sin(\phi) + r \cos(\phi)) \tan(\theta) \tag{110}$$

$$\dot{\psi} = (\sin(\phi)q + \cos(\phi)r)/\cos(\theta) \tag{111}$$

$$C_X = C_{Xo} + C_{X_\alpha}(\alpha - \alpha_o) + C_{X_{\delta_T}}(\delta_T - \delta_{To}) \tag{112}$$

$$C_Y = C_{Yo} + C_{Y_\beta}(\beta - \beta_o) + C_{Y_r} \frac{b}{2V}(r - r_o) + C_{Y_p} \frac{b}{2V}(p - p_o)$$
$$+ C_{Y_{\delta_r}}(\delta_r - \delta_{ro}) \tag{113}$$

$$C_Z = C_{Zo} + C_{Z_\alpha}(\alpha - \alpha_o) + C_{Z_{\delta_e}}(\delta_e - \delta_{eo}) + C_{Z_q} \frac{\bar{c}}{2V}(q - q_o) \tag{114}$$

$$C_L = C_{Lo} + C_{L_\beta}(\beta - \beta_o) + C_{L_{\delta_a}}(\delta_a - \delta_{ao}) + C_{L_{\delta_r}}(\delta_r - \delta_{ro})$$
$$+ C_{L_p}(p - p_o) + C_{L_r}(r - r_o) \tag{115}$$

$$C_M = C_{Mo} + C_{M_\alpha}(\alpha - \alpha_o) + C_{M_{\delta_e}}(\delta_e - \delta_{eo}) + C_{M_q} \frac{\bar{c}}{2V}(q - q_o)$$
$$+ C_{M_{\dot{\alpha}}} \frac{\bar{c}}{2V}(\dot{\alpha} - \dot{\alpha}_o) \tag{116}$$

$$C_N = C_{No} + C_{N_\beta}(\beta - \beta_o) + C_{N_r} \frac{b}{2V}(r - r_o) + C_{N_p} \frac{b}{2V}(p - p_o)$$
$$+ C_{N_{\delta_a}}(\delta_a - \delta_{ao}) + C_{N_{\delta_r}}(\delta_r - \delta_{ro}) \tag{117}$$

Two flight conditions are used in Ref. 30 to extract aerodynamic parameters. They are shown in Table 15. The wheels down fully weighted NAVION used in flight tests cannot fly as fast as condition I. Corrections based on flight tests data have only been performed for condition II. The longitudinal aerodynamic parameters at the two flight conditions are shown in Table 16. The lateral aerodynamic parameters at the two flight conditions are shown in Table 17. The two parameters which have been adjusted after flight tests are $C_{Y_{\delta_r}}$ (from -0.68 to -0.143) and $C_{L_{\delta_r}}$ (from -0.007 to -0.023).

Reference 35 was obtained after the completion of the PIF design and flight testing. The analog match from Ref. 35, and shown in Tables 16 and 17,

is for the second NAVION, a variable stability aircraft equipped with side force pannels on the wings. $C_{Y\delta_r}$ and $C_{L\delta_r}$ from Ref. 35 are in general agreement with the modifications used in the PIF design. The analog match in Ref. 35 did not use C_{Z_q} and $C_{M\dot{\alpha}}$ as identifiable parameters and for this reason, the other longitudinal parameters in Table 16 do not agree well with Ref. 30.

B. SIGN CONVENTION

In implementing a control law it is crucial that the sign conventions used during the control law design be explicitly detailed. For the following presentation of sign conventions, the aircraft is assumed to be near the glidepath approaching the runway. Left and right is referenced to the pilot perspective while setting in the cockpit. Vertical height and normal acceleration plotting from flight test are opposite in sign to the convention used in this section. The barometric altimeter complimentary filter also has the opposite sign convention.

The earth fixed (inertial) coordinate system and body axis coordinate system sign conventions are discussed in Appendix A. The following are sign conventions for positive step changes in control variables. The sign convention is chosen to match the sign convention onboard the NAVION aircraft

        Positive Rudder   - Positive Yaw

        Positive Yaw   - Aircraft Nose Rotates Right

        Positive Rudder   - Rudder Trailing Edge Rotates Towards Right Wing

        Positive Aileron   - Positive Roll

        Positive Roll   - Right Wing Down

        Positive Aileron   - Left Aileron Trailing Edge Rotates Down, Right Aileron Trailing Edge Rotates Up

        Positive Elevator   - Positive Pitch

        Positive Pitch   - Nose Up

        Positive Elevator   - Elevator Trailing Edge Rotates Up

As the aircraft progresses down the glideslope the flight path angle, γ is given by

$$\gamma = \sin^{-1}(-\dot{z}/V) \qquad\qquad (118)$$

V is the aircraft total earth relative velocity and $\dot{z}$ is the aircraft's earth relative vertical velocity. If the aircraft is descending the flight path angle is negative. When the aircraft has no lateral error, the distance in the vertical plane from the aircraft c.g. in a perpendicular line to the glidepath is d, and satisfies the equation

$$\dot{d} = V \sin(\lambda_{GS} + \lambda) \tag{119}$$

Figure 45 shows the aircraft below the glideslope. The variable λ_{GS} is the glideslope angle and is defined to be positive for typical glideslopes. Hence for a desired glideslope angle of 3 deg, the aircraft's flight path angle must be -3 deg for the aircraft to be tracking the glideslope, i.e., $\dot{d} = 0$. If the aircraft is above the glidepath, d is positive. The angular error, Γ, relative to the glidepath is

$$\Gamma = \sin^{-1}(d/R) \tag{120}$$

where R is the range to the aircraft. If the aircraft is above the glidepath, Γ is positive. In an MLS environment, d can be computed from x and z position using the equation

$$d = x \sin(\lambda_{GS}) - z \cos(\lambda_{GS}) \tag{121}$$

The localizer beam centerline intercept and hold geometry is shown in Fig. 46. Projecting the velocity vector onto y produces

$$\dot{y} = V \cos\gamma \, \sin(\xi - \xi_{ref}) \tag{122}$$

where ξ is the velocity heading angle measured relative to a reference value ξ_{ref}. The lateral distance y satisfies the equation

$$y = R_h \sin(\Xi) \tag{123}$$

The localizer deviation angle, Ξ, and the distance y shown in Fig. 46 are negative. The distance R_h is the projection of R onto the horizontal plane.

If the assumptions are made that the flight path angle and sideslip angle are small, (and the aircraft is in the approach mode) then the above equations can be simplified to

$$\dot{y} \simeq V \sin(\psi - \psi_{ref}) \tag{124}$$

46

$$y \simeq R \sin(\Xi) \qquad\qquad [125]$$

The lateral position, y, and rate, $\dot{y}$, can be estimated using Eqs. 124 and 125 and sensor information available onboard the aircraft. Projecting the velocity vector onto R and using the same simplifying assumptions produces

$$R \simeq V \cos(\psi-\psi_{ref} - \Xi) \qquad\qquad [126]$$

C. SIMULATION AND FLIGHT TEST COMPARISON

During early flight tests, the safety pilot purposely made separate small pulse inputs to each aircraft surface. The resulting NAVION aircraft response from the sensors was recorded for comparison with the linear open-loop model simulation response for similiar pulse inputs. The results of the comparison for an elevator input and a rudder input are shown in Figs. 4 and 3, respectively.

The normal accelerometer sampled output (10 samples per sec) and pitch rate gyro sampled output for an elevator input agree well with the linear simulation as shown in Fig. 4. The normal accelerometer output sign convention is positive up and biased by -1.0 g to give zero output in level flight.

The aircraft response to a rudder pulse originally had poor agreement with the model response. After adjusting two aerodynamic coefficients as discussed in Section B, the new comparison in Fig. 3 is considered to be adequate. The initial response for the first few seconds match well then begin to diverge as the simulation continues. The cross-axis aircraft response of roll rate for a rudder change has less agreement with the simulation than sideslip and the lateral accelerometer output. The aircraft's Dutch Roll mode appears to be better damped than the model response. The small rudder movements made by the pilot during the pulse command may have contributed towards the simulation and aircraft disagreements. The linear model simulation disagreements did not adversely affect the PIF control law performance in flight. On the other hand, better identification of all aerodynamic coefficients should further improve PIF control law performance.

D. SENSOR MEASUREMENT PERTURBATION EXPRESSIONS

The PIF control law employs, as much as possible, sampled sensor outputs for direct feedback. The output of some sensors, particularly the accelerometers, the pitot tube, the sideslip vane, and the angle-of-attack vane, are nonlinear functions of the aircraft body-axis states used in PIF feedback. The PIF design procedure at a trim flight condition requires an expression for the perturbation sensor output in the form

$$\Delta\underline{z} = H \ \Delta\underline{x} + D \ \Delta\underline{u} \qquad\qquad (127)$$

where H and D are constant aircraft state control observation matrices. The

purpose of this section is to derive perturbation expressions in the form of Eq. 127 for the previously mentioned sensors. Sensor inaccuracies and noise effects are neglected.

The output of an orthogonal traid of body-mounted accelerometers aligned with body coordinates is expressed as (Ref. 3).

$$\underline{a}_b = \underline{\dot{v}}_B + \tilde{\omega}_B \underline{v}_B + \left[\tilde{\omega}_B \tilde{\omega}_B + \dot{\tilde{\omega}}_B\right] \Delta\underline{x}_B - H_E^B \underline{g}_E \tag{128}$$

A flat, non-rotating earth surface is assumed. The gravity vector, $\underline{g}_E$, the Euler angle transformation matrix H_E^B, the cross product notation $\tilde{\omega}_B$, and the body-axis velocity vector, $\underline{v}_B$ are defined in Appendix A. $\Delta\underline{x}_B$ is the position of the accelerometers with respect to the center of gravity in body axis.

$$\Delta\underline{x}_B = \begin{bmatrix} \Delta x_s \\ \Delta y_s \\ \Delta z_s \end{bmatrix} \tag{129}$$

Perturbation expressions from individual componets in Eq. 127 are derived in Ref. 3 except for the third term which follows,

$$\Delta\left(\left[\tilde{\omega}_B^E \tilde{\omega}_B^E + \dot{\tilde{\omega}}_B^E\right]\Delta\underline{x}_B\right) = \Delta\left(-\tilde{\omega}_B^E \Delta\tilde{x}_B \underline{\omega}_B^E\right) + \Delta\left(-\Delta\tilde{x}_B \dot{\underline{\omega}}_B^E\right)$$

$$= \left[\left(\Delta\tilde{x}_B \underline{\omega}_{B_o}^E\right) - \tilde{\omega}_{B_o}^E \Delta\tilde{x}_B\right]\Delta\underline{\omega}_B^E - \Delta x_B \Delta\dot{\underline{\omega}}_B^E \tag{130}$$

The perturbation expression for the accelerometers becomes

$$\Delta\underline{a}_B = \Delta\underline{\dot{v}}_B + \tilde{\omega}_{B_o}^E \Delta\underline{v}_B + \left[\left(\Delta\tilde{x}_B \underline{\omega}_{B_o}^E\right) - \tilde{\omega}_{B_o}^E \Delta\tilde{x}_B - \tilde{v}_{B_o}\right]\Delta\underline{\omega}_B^E$$

$$- \Delta x_B \Delta\dot{\underline{\omega}}_B^E - \left(H_{E_o}^B \underline{g}_E\right) L_{B_o} \Delta\underline{v}_B \tag{131}$$

where L_B is defined in Eq. 77. The variables $\Delta\underline{v}_B$ and $\Delta\underline{\omega}_B^E$ are part of the perturbation aircraft dynamics,

$$\Delta\underline{\dot{x}} = A \Delta\underline{x} + B \Delta\underline{u} \tag{132}$$

discussed in Appendix A.

Partitioning $\Delta\underline{x}$, A and B, it follows that

48

$$\Delta \dot{\underline{v}}_B = A_{vv} \Delta \underline{v}_B + A_{v\omega} \Delta \underline{\omega}_B^E + A_{v\nu} \Delta \underline{\nu}_B + B_{vu} \Delta \underline{u} \tag{133}$$

$$\Delta \dot{\underline{\omega}}_B^E = A_{\omega v} \Delta \underline{v}_B + A_{\omega\omega} \Delta \underline{\omega}_B^E + A_{\omega\nu} \Delta \underline{\nu}_B + B_{\omega u} \Delta \underline{u} \tag{134}$$

Substituting Eqs. 133 and 134 into Eq. 131 and combining terms results in the perturbation measurement equation for the body mounted accelerometers

$$\Delta \underline{a}_B = \left[A_{vv} + \tilde{\omega}_{B_o}^E - \Delta \tilde{x}_B A_{\omega v} \right] \Delta \underline{v}_B + \left[\Delta \tilde{x} \omega_{B_o}^E - \tilde{\omega}_B^E \Delta \tilde{x}_B - \tilde{\underline{v}}_{B_o} + A_{v\omega} - \Delta \tilde{x}_B A_{\omega\omega} \right] \Delta \underline{\omega}_B^E$$

$$+ \left[A_{v\nu} - \Delta \tilde{x}_B A_{\omega\nu} - \left(H_{E_o}^B \underline{g}_E \right) L_{B_o} \right] \Delta \underline{\nu}_B + \left[B_{vu} - \Delta \tilde{x}_B B_{\omega u} \right] \Delta \underline{u} \tag{135}$$

If Eq. 135 is used as the measurement equation in constructing the PIF gain matrices then a sampled accelerometer output can be used directly as a feedback state in the control law without adding in gravity or correcting for off center of gravity locations. There are certain advantages which can be obtained using off c.g. located accelerometers as discussed in Ref. 29. Although it was not feasible, the Y_{δ_r} problem discussed in Chapter IV, Section C could have been alleviated by moving the lateral accelerometer forward along the body x-axis. Corrections for gravity and off c.g. locations must be performed when the accelerometer outputs are used in complementary filtering as discussed in Chapter IV, Section A.

The pitot tube measurement of velocity magnitude, V, the sideslip vane measurement, β, and the angle of attach vane measurement, α, are related to the body-axis velocities by

$$\begin{bmatrix} V \\ \beta \\ \alpha \end{bmatrix} = \begin{bmatrix} \sqrt{u^2 + v^2 + w^2} \\ \tan^{-1}(v/\sqrt{u^2 + w^2}) \\ \tan^{-1}(w/u) \end{bmatrix} \tag{136}$$

Perturbations of the above equation results in

$$\begin{bmatrix} \Delta V \\ \Delta \beta \\ \Delta \alpha \end{bmatrix} = J_w^{-1} \left(V_o, \beta_o \right) H_B^W (\alpha_o, \beta_o) \begin{bmatrix} \Delta u \\ \Delta v \\ \Delta w \end{bmatrix} \tag{137}$$

J_w is a diagonal matrix which has elements 1.0, V_o, and $V_o \cos \beta_o$. H_B^W is the body to wind axis transformation and is the transpose of

49

$$H_w^B (\alpha_o, \beta_o) = \begin{bmatrix} \cos\alpha_o & 0 & -\sin\alpha_o \\ 0 & 1 & 0 \\ \sin\alpha_o & 0 & \cos\alpha_o \end{bmatrix} \begin{bmatrix} \cos\beta_o & \sin\beta_o & 0 \\ -\sin\beta_o & \cos\beta_o & 0 \\ 0 & 0 & 1 \end{bmatrix} \qquad (138)$$

Equation 137 can be used to form H and D in Eq. 127 when the air data sensor information is needed for feedback.

APPENDIX C

AUTOPILOT MODE MODELS AND CONTROL SYSTEMS

Each autopilot mode is composed of a dynamic model and a dynamic model control system which are described in this appendix. When an autopilot mode is engaged, the internal states in the command model are initialized to the aircraft states. After initialization, the command model is propagated to generate state trajectories the PIF control law follows. Some variables in the command models (airspeed, range, pitch angle) are continually updated to match aircraft conditions. Other variables (yaw, roll, height, lateral position) are internal to the command model.

When the ALT SEL, HDG SEL, APR GS and APR LOC command models receive a pilot command, a nonlinear feedback control system maneuvers the command model to the new conditions. The feedback control system allows the autopilot command models to operate over a wide range of initial (boundary) conditions in real time. The nonlinear feedback control systems are designed solely to provide good ride quality. The simple autopilots BETA HOLD, ROLL SEL and PITCH SEL operate open loop. The PIF design process requires that linear representations of the command model be used, hence, both linear and nonlinear models, where applicable, are given in each of the following sections. The basic linear command model representation is shown in Eqs. 6 and 7.

A. β_m, ϕ_m COMMAND SYSTEM - BETA HOLD

The sideslip, β_m, roll angle, ϕ_m, command system is used to compute the roll command to rudder command crossfeed gain used in ROLL SEL. The crossfeed gain, a_k, is computed as an element in the feedforward matrix A_{22} in Eq. 9. The linear and nonlinear command models are identical for this command system,

$$\underline{x}_{m,k+1} = 0 \; \underline{x}_{m,k} + 0 \begin{bmatrix} \beta_m \\ \phi_m \end{bmatrix}_k \tag{139}$$

$$\underline{y}_{m,k} = 0 \; \underline{x}_{m,k} + I \begin{bmatrix} \beta_m \\ \phi_m \end{bmatrix}_k \tag{140}$$

BETA HOLD is not intended to be an inflight command system.

B. ϕ_m, δ_{rm} COMMAND SYSTEM - ROLL SEL

The roll angle, ϕ_m, rudder position, δ_{rm}, command system performs the

standard wing leveler plus yaw damper autopilot feature. The linear and non-linear command models are identical for this command system,

$$\underline{x}_{m,k+1} = 0 \; \underline{x}_{m,k} + I \begin{bmatrix} \phi_m \\ \delta_{rm} \end{bmatrix}_k \qquad (141)$$

$$\underline{y}_k - \underline{y}_{m,k} = \begin{bmatrix} \phi \\ \delta_r \end{bmatrix}_k - \left(0 \; \underline{x}_{m,k} + \begin{bmatrix} 1.0 & 0.0 \\ a_k & 1.0 \end{bmatrix} \begin{bmatrix} \phi_m \\ \delta_{rm} \end{bmatrix}_k \right) \qquad [142]$$

The crossfeed gain, a_k, is scheduled as a function of airspeed as shown in Eq. 70. The PIF autopilot with the ROLL SEL command model is designed to accept a roll command, ϕ_m, (usually 0.0) and a rudder command, δ_{rm}, (usually rudder pedal trim position) and hold these values. The autopilot will also capture and hold a nonzero roll command input from the pilot.

C. $\phi_m + \psi_m$, δ_{rm} COMMAND SYSTEM - HDG SEL

The Heading Select and Hold command system performs the bank-to-turn autopilot feature. When the autopilot is turned on, it holds the current aircraft heading of the aircraft until a different heading is requested. When a new heading is requested, the autopilot banks the aircraft into a steady coordinated turn, then establishes and holds the new heading.

The bank to steady turn feature of the autopilot is accomplished using the basic nonlinear kinematics

$$\psi_{m,k+1} = \psi_{m,k} + \Delta t \frac{g}{\hat{V}_k} \tan \phi_{m,k} \qquad [143]$$

$$\phi_{m,k+1} = \phi_{m,k} + \Delta t \; \dot{\phi}_{m,k} \qquad [144]$$

The nonlinear relationship between ψ_m and ϕ_m is derived in Ref. 34 and attempts to produce a coordinated turn where the areodynamic force lies in the body-axis xz plane. The difference between actual and command heading is used to form a roll angle command

$$\underline{y}_k - \underline{y}_{m_k} = \begin{bmatrix} \phi \\ \delta_r \end{bmatrix}_k - \begin{bmatrix} 1.0 & 0.0 \\ a_k & 1.0 \end{bmatrix} \begin{bmatrix} k_\psi (\psi_k - \psi_{m,k}) \\ \delta_{rm,k} \end{bmatrix} \qquad [145]$$

The command error resembles a typical feature of a nested autopilot design where the heading error is used to compute a roll command in the ROLL SEL mode to provide a heading select capability (Ref. 18).

The linear perturbation command used in the PIF design model is obtained by linearizing Eq. 143 and regrouping Eq. 145. The roll dynamics in Eq. 144, as discussed in Chapter 3, Section A, are not represented in the linear model because poor transient behavior occurs if ϕ_m is used as the linear models control input, u_m. The linear model is

$$\Delta\psi_{m,k+1} = \Delta\psi_{m,k} + \left[\begin{array}{cc} \dfrac{(g + V_o\,\dot\psi_o\,\tan\phi_o)}{V_o} & 0 \end{array}\right]\left[\begin{array}{c} \Delta\phi_{m,k} \\ \Delta\delta_{rm,k} \end{array}\right] \tag{146}$$

$$\Delta\underline{y}_{m,k} = \left[\begin{array}{c} -k_\psi \\ -a_o k_\psi \end{array}\right]\Delta\psi_{m,k} + \left[\begin{array}{cc} 0.0 & 0.0 \\ 0.0 & 1.0 \end{array}\right]\left[\begin{array}{c} \Delta\phi_{m,k} \\ \Delta\delta_{rm,k} \end{array}\right] \tag{147}$$

$$\Delta\underline{y}_k = \left[\begin{array}{c} \Delta\phi_k - k_\psi\,\Delta\psi_k \\ -a_o k_\psi\,\Delta\psi_k + \Delta\delta_{r,k} \end{array}\right] \tag{148}$$

The HDG SEL $\underline{\text{nonlinear}}$ command model uses $\dot\phi_{m,k}$ as a model control variable to cause $\psi_{m,k}$ to smoothly transfer from one pilot requesting heading command, ψ_c, to another. The nonlinear command model control system used to follow the pilot command inputs is as follows:

IF FIRST PASS THEN $\psi_{m,o} = \psi_k,\ \phi_{m,o} = \psi_k,\ \delta_{rm,o} = \delta_{r,k}$

$\psi_E = \psi_{c,k} - \psi_{m,k}$;compute command model yaw error (149)

$UC = HSK_1*\psi_E - HSK_2*\psi_{m,k}$;compute command model feedback (150) control command

$\dot\phi_{m,k} = UC$;initialize roll rate command (151)

IF $|\phi_{m,k}| \geq \phi_{max}$ THEN $\dot\phi_{m,k} = 0.0$;set roll rate to zero if in steady turn

IF $|\psi_E| \leq \psi_{close}$ THEN $\dot\phi_{m,k} = UC$;reset roll rate command if approaching desired heading

$\dot\phi_{max2} = 0.0$ (152)

IF $\dot{\psi}_E$ AND $\dot{\phi}_{m,k}$ ARE OPPOSITE SIGN   THEN $\dot{\phi}_{max2} = \dot{\phi}_{m,k}$

$\dot{\phi}_{max}$ = MAXIMUM$(\dot{\phi}_{max2}, \dot{\phi}_{max1})$;apply full rate command if   (153)
                                                    opposite sign occurs otherwise
                                                    hold roll rate command below
                                                    $\dot{\phi}_{max1}$

IF $|\dot{\phi}_{m,k}| > \dot{\phi}_{max}$ THEN $\dot{\phi}_{m,k}$=SIGN$(\dot{\phi}_{m,k})*\dot{\phi}_{max}$

$\phi_{max1} = \tan^{-1}(\hat{V}_k^2/R_T*g)$;check to see if low velocity   (154)
                                                    is decreasing turn radius

ϕ_{max} = MINIMUM$(\phi_{max1}, \phi_{max2})$;keep roll angle below ϕ_{max2} (155)
                                                    unless ϕ_{max1} indicates it
                                                    should be lower

The control system feeds back the model yaw error and model roll angle using the gains HSK_1 and HSK_2. If the model roll angle exceeds a specified value, the control, $\phi_{m,k}$, is reset to zero. During this phase the model dynamics are in a steady turn. If the roll rate control command causes the yaw angle to accelerate in the direction of the yaw angle command, ψ_C, the roll rate control command is limited to the value ϕ_{max1}. If the yaw angle error is below a threshold, ψ_{CLOSE}, full yaw angle deceleration through the roll rate control command is used. The last feature causes the model and the aircraft to anticipate the roll back to zero just before completing the turn so that the yaw angle overshoot is small. A minimum radius of turn, R_T, is used to reduce the maximum allowed back angle, ϕ_{max1}, if the filtered airspeed, $\hat{V}$, drops to low values. The computed value of $\phi_{m,k}$, after Eq. 153, is used in Eq. 144 to generate the ϕ_m trajectory. The resulting ϕ_m trajectory is used in Eq. 143 to generate the ψ_m trajectory in flight.

D. z_m COMMAND SYSTEM - ALT SEL

The Altitude Select and Hold command system allows the pilot to hold the current altitude or select a new altitude the aircraft should establish. When the pilot selects a new altitude, the autopilot slowly accelerates (or decelerates) the aircraft into a steady climb (or steady descent) until the new altitude is reached then captures and holds the aircraft at the new selected altitude.

The altitude select feature of the autopilot is accomplished using the basic command model

$$\begin{bmatrix} z_{m,k+1} \\ \dot{z}_{m,k+1} \end{bmatrix} = \begin{bmatrix} 1.0 & \Delta t \\ 0.0 & 0.1 \end{bmatrix} \begin{bmatrix} z_{m,k} \\ \dot{z}_{m,k} \end{bmatrix} + \begin{bmatrix} 0.0 \\ \Delta t \end{bmatrix} \ddot{z}_{m,k} \qquad [156]$$

$$\underline{Y}_k - \underline{Y}_{m,k} = z_k - z_{m,k} \qquad [157]$$

54

The altitude acceleration, $\ddot{z}_{m,k}$, is used as a control variable to transfer z_m from one desired altitude value to another. The linear command model used in the PIF design does not use $\ddot{z}_m$, and has the following simple form

$$\Delta z_{m,k+1} = \Delta z_{m,k} + \Delta t\, \dot{z}_{m,k} \tag{158}$$

$$\Delta \underline{y}_k = \Delta z_k \tag{159}$$

$$\Delta \underline{y}_{m,k} = \Delta z_{m,k} \tag{160}$$

The altitude select command model control system is as follows where z_c is the requested altitude made by the pilot.

IF FIRST PASS   THEN $z_{m,o} = \hat{z}_k$, $\dot{z}_{m,o} = 0.0$

$z_E = z_{c,k} - z_{m,k}$;compute command model height   (161)
    error

$UC = ASK_1 * z_E - ASK_2 * \dot{z}_{m,k}$;compute command model feedback   (162)
    control command

$\ddot{z}_{m,k} = UC$;initialize acceleration command   (163)

IF $|\dot{z}_{m,k}| \geq \dot{z}_{max}$ THEN $\ddot{z}_{m,k} = 0.0$;set acceleration to zero if in
    steady descent (or ascent)

IF $|z_E| \leq z_{CLOSE}$ THEN $\ddot{z}_{m,k} = UC$;reset acceleration command if
    approaching desired height

$\ddot{z}_{max2} = 0.0$ (164)

IF z_E AND $\ddot{z}_{m,k}$ ARE OPPOSITE SIGN   THEN $\ddot{z}_{max2} = |\ddot{z}_{m,k}|$

$\ddot{z}_{max} = MAXIMUM\ (\ddot{z}_{max2}, \ddot{z}_{max1})$;apply full acceleration if   (165)
    opposite sign occurs otherwise
    hold acceleration command below
    $\ddot{z}_{max1}$

The control system feeds back the model height error and model vertical velocity using the gains ASK_1 and ASK_2. If the model vertical velocity exceeds a specific value, the control, $\ddot{z}_{m,k}$, is reset to zero. During this phase the model dyanmics are in a steady descent (or ascent). If the vertical acceleration command causes the model height to accelerate in the direction of the vertical height command, the vertical acceleration control command is limited to the

55

value $\ddot{z}_{maxl}$. If the height error is below a threshold, z_{CLOSE}, full deceleration through the vertical acceleration control command is used. The computed value of $\ddot{z}_{m,k}$ after Eq. 165 is used in Eq. 156 to generate the $z_{m,k}$ trajectory in flight. The altitude select and heading select model control systems are coincidently structurally identical.

E. θ_m COMMAND SYSTEM - PITCH SEL

The pitch angle command systems holds the current pitch angle or commands a new one using the simple model.

$$\underline{x}_{m,k+1} = 0.0 \; \underline{x}_{m,k} + 0.0 \; \theta_{m,k} \tag{166}$$

$$\underline{y}_{m,k} = 0.0 \; \underline{x}_{m,k} + 1.0 \; \theta_{m,k} \tag{167}$$

F. GLIDESLOPE CAPTURE AND HOLD - APR GS

The Approach Glideslope autopilot mode captures and tracks the glideslope. The switch from ALT SEL to the APR GS mode occurs automatically when the aircraft is approaching the runway. The ALT SEL mode must be engaged and the aircraft must be holding a desired altitude prior to capturing the glideslope. Glideslope capture can be performed either above or below the glideslope. The localizer capture and track should occur prior to glideslope capture. These requirements are standard in most autopilots.

Glideslope capture and track is accomplished using the nonlinear model

$$d_{m,k+1} = d_{m,k} + \Delta t \; V_k * \sin(\lambda_{GS} + \lambda_{m,k}) \tag{168}$$

$$y_k - y_{m,k} = R_k \sin \Gamma_k - d_{m,k} = \hat{d}_k - d_{m,k} \tag{169}$$

The distance, $d_{m,k}$ is the perpendicular distance from the aircraft to the glideslope, λ_{GS} is the glideslope angle, $\lambda_{m,k}$ is the commanded aircraft flight path angle and V is the ground speed. In the PIF control law, Eq. 168, is used to define a path that the measured value d tracks to zero. The values used for V, λ_G, and λ_m do not have to be accurate in flight since inaccuracies only imply a perturbation of the trajectory d_m traces to zero. In flight, V is obtained using measured airspeed, λ_{GS} is initialized by the pilot and λ_m is a control feedforward variable. A measured aircraft flight path angle is not required for feedback. The linear perturbation command model used in the PIF design is obtained by linearizing Eq. 168,

$$\Delta d_{m,k+1} = \Delta d_{m,k} + \Delta t \; V_k \; \Delta\lambda_{m,k} \tag{170}$$

$$\Delta y_{m,k} = \Delta d_{m,k} \tag{171}$$

$$\Delta y_k = \Delta d_k \tag{172}$$

The APR GS nonlinear command model uses $\lambda_{m,k}$ as a control variable to cause $d_{m,k}$ to smoothly transfer to zero from the measured value of d that occurs when the glideslope engage logic activates the APR GS command model controller. The command model control system used to construct the path, which includes the range estimation equations, is as follows

```
      DATA GSENGAE/FALSE/           ;initialize APR GS flag

      DATA UC/0.1/                  ;initialize US to 0.1

      DATA OMKRCK/FALSE/            ;initial outer marker flag

      IF OMKRSOLID     THEN OMKRCK=TRUE
                                    ;change flag when aircraft passes
                                     over outer marker
      IF NOT OMKRCK AND NOT GSENGAE

                        THEN R̂ₖ=OUTMARK  ;initialize distance estimate   (173)
                                          to outer marker distance
      ELSE
BEGIN

      RK = 0.0                      ;initialize range estimate          (174)
                                     filter gain to zero

      IF LOCENGE       THEN
```

$$\hat{R}_k = \hat{R}_{k-1} - \Delta t \cdot v_k \cdot \cos(\hat{\psi}_k - \Xi_k) \qquad \text{;propagate distance extimate} \quad (175)$$
                                                              if Ξ is a valid signal

$$\text{RMEAS} = \hat{z}_k(t)/\lambda_{GS} \qquad \text{;estimate R using height} \quad (176)$$
                                                           estimate and glideslope angle

```
      IF GSENGAE       THEN
```

$$\text{RK} = r_1 \cdot \hat{z}_k + r_2 \qquad \text{;increase RK as aircraft} \quad (177)$$
                                                           descends on glideslope

```
      IF RK < 0.0      THEN RK=0.0

      IF RK > RKMAX    THEN RK=RKMAX
```

$$\hat{R}_k = \hat{R}_k + \text{RK} \cdot (\text{RMEAS} - \hat{R}_k) \qquad \text{;update distance estimate} \quad (178)$$

```
END
```

```
IF  R̂_k < R̂_min        THEN R̂_k=R_min        ;keep distance estimate above
                                                 R_min

IF  |Γ_k| < Γ_max       THEN

BEGIN

     d̂_k = R̂_k sin(Γ_k)                        ;calculate d estimate when      (179)
                                                 glideslope is in range

     IF UC > 0.0         THEN d_m,k=d̂_k         ;reset d_m to d until the APR GS
                                                 model command control system
                                                 causes a pitch down command

     IF UC < 0.0         THEN GSENGAE=TRUE

     d_E = (0.0 - d_m,k) * 3.281                ;convert to feet                (180)

     GSK = g_1 |d_m,k| + g_2                    ;compute APR GS command model   (181)
                                                 control system gain

     IF GSK > g_3        THEN GSK=g_3

     IF GSK < g_4        THEN GSK=g_4

     UC = GSK * d_E * 0.01745                   ;convert to radians             (182)

     UC = -λ_GS + UC                                                           (183)

     IF UC ≥ λ_max       THEN UC=λ_max          ;λ_max should be 0.0

     IF UC ≤ λ_min       THEN UC=λ_min          ;keep flight path angle command
                                                 above λ_min

     λ̇_m = (UC - λ_m,k-1)                                                      (184)

     IF |λ̇_m| > λ̇        THEN

     λ̇_m = SIGN(λ̇_m) * λ̇_max                    ;keep flight path angle rate of (185)
                                                 change below λ̇_max

     λ_m,k = λ_m,k-1 + λ̇_m                      ;propagate command model        (186)

     d_m,k = d_m,k + Δt V̂_k sin(λ_GS + λ_m,k)                                  (187)

END
```

At the beginning of the control law computation, the glideslope angle is initial-
ized by the pilot. The distance, R, is initialized to a typical outer marker
distance. If the aircraft has intercepted or passed the outer marker and the
localizer deviation angle is in range, the distance R is propagated. When the

aircraft is descending on the glideslope an alternative estimate of R is made using the barometric altimeter $\hat{z}$ estimate and the geometry involved. The propagated R and estimated R are combined in a complementary filter fashion. The filter gain, RK, is increased as the aircraft descends. When the estimated R falls below a prespecified value, R is fixed to the value. Equation 180 forms the command model control error. When $-GSK * d_{m,k}$ is less than λ_{GS}, the flight path angle command, λ, begins to command the aircraft to pitch down even when the aircraft is below the glideslope. The aircraft follows a d trajectory which intercepts the glideslope with no overshoot. The gain GSK is programmed to increase as the aircraft closes in to the glideslope. The computations after Eq. 183 check to determine if the commanded flight path angle is within specified limits. Setting λ_{max} to zero ensures the command only executes pitch down glideslope captures. The rate of change of the flight path angle is also checked to keep the vertical accelerations small during capture.

G.   LOCALIZER CAPTURE AND TRACK - APR LOCI, APR LOCR, APR LOCP

The localizer capture and track autopilot mode is the most complicated command model design in the PIF control entourage. A number of options are available to specify a command model which captures and tracks the localizer beam centerline. Each option has advantages and disadvantages which are described in the flight test discussion, Chapter V. Three APR LOC command modes are presented (APR LOCI, APR LOCR, APR LOCP). PIF control law designs for all three modes are discussed in Chapters IV and V.

The APR LOC autopilot captures and tracks the inbound localizer beam centerline. All three approach localizer autopilot designs use the same basic command model. The autopilots differ in the construction of the command error signal which the PIF control law must regulate to zero.

The APR LOC mode requires that the aircraft be in HDG SEL mode prior to engage. The engage logic for transferring from HDG SEL to APR LOC is performed when the localizer signal is in range. The internal intercept angle in the command model control system during capture is fixed. The APR LOC command system has considerable room for improvement as discussed in the recommendations section of Chapter 6.

Localizer capture and track is accomplished using the nonlinear dynamics shown in Eqs. 124 and 143 where, for simplicity, the reference value is assumed to be 0.0,

$$y_{m,k+1} = y_{m,k} + \Delta t \, V_k * \sin \psi_{m,k} \qquad [188]$$

$$\psi_{m,k+1} = \psi_{m,k} + \Delta t \, \frac{g}{V_k} \, \tan \phi_{m,k} \qquad [189]$$

The three APR LOC modes have the following command errors

APR LOCI

$$\underline{y}_k - \underline{y}_{m,k} = \begin{bmatrix} \phi_k \\ \underline{y}_k \end{bmatrix} - \begin{bmatrix} \phi_{m,k} \\ y_{m,k} \end{bmatrix} \tag{190}$$

APR LOCR

$$\underline{y}_k - \underline{y}_{m,k} = \begin{bmatrix} \phi_k \\ \delta_{r,k} \end{bmatrix} - \begin{bmatrix} 1.0 & 0.0 \\ a_k & 1.0 \end{bmatrix} \begin{bmatrix} k_\psi(\psi_k - (\psi_{m,k} - k_y(y_k - y_{m,k}))) \\ \delta_{mr,k} \end{bmatrix} \tag{191}$$

APR LOCP

$$\underline{y}_k - \underline{y}_{m,k} = \begin{bmatrix} \phi_k \\ \delta_{r,k} \end{bmatrix} - \begin{bmatrix} 1.0 & 0.0 \\ a_k & 1.0 \end{bmatrix} \begin{bmatrix} k_y(y_k - y_{m,k}) \\ \delta_{mr,k} \end{bmatrix} \tag{192}$$

The roll angle command, ϕ_m, is the control variable for the nonlinear command model control system.

The APR LOCI mode forms the command errors shown in Eq. 190 using roll angle and y position. The aircraft's y position is estimated from Ξ measurements using Eq. 123.

The APR LOCR mode shown in Eq. 191 is simply the HDG SEL mode with an additional modification. The $\psi_{m,k}$ command in Eq. 145 is replaced with $\psi_{m,k} - k_y(y_k - \underline{y}_m,k)$. An error in y position causes a ψ angle error which in turn causes a coordinated roll command to bank the aircraft in the direction to null the y position error. The APR LOCR mode is similiar in principle to a localizer autopilot mode discussed in Ref. 18.

The APR LOCP mode is similiar to the APR LOCR mode except that the ψ error is removed and only y position error commands the bank angle. The ψ_m state remains in the model dynamics and is used in the PIF control law to form the $\underline{x}-\underline{x}^*$ error (see Eq. 57) for ψ. The APR LOCP mode is able to perform a coordinated turn, intercept the localizer beam centerline and track the beam centerline crabbed, if necessary.

The linear perturbation command models used in the PIF designs are obtained by linearizing Eqs. 188 to 192,

$$\begin{bmatrix} \Delta y_m \\ \Delta \psi_m \end{bmatrix}_{k+1} = \begin{bmatrix} 1.0 & \Delta t\ V_o\ \cos\ \psi_o\ *\ (1.0/57.3) \\ 1.0 & 1.0 \end{bmatrix} \begin{bmatrix} \Delta y_m \\ \Delta \psi_m \end{bmatrix}_k$$

$$+ \begin{bmatrix} 0.0 & 0.0 \\ \dfrac{\Delta t(g + V_o\ \psi_o\ \tan\ \phi_o)}{V_o} & 0.0 \end{bmatrix} \begin{bmatrix} \Delta \phi_{m,k} \\ \Delta \delta_{rm,k} \end{bmatrix} \tag{193}$$

APR LOCI

$$\Delta \underline{y}_{m,k} = \begin{bmatrix} 0.0 & 0.0 \\ 1.0 & 0.0 \end{bmatrix} \begin{bmatrix} \Delta y_m \\ \Delta \psi_m \end{bmatrix}_k + \begin{bmatrix} 1.0 & 0.0 \\ 0.0 & 0.0 \end{bmatrix} \begin{bmatrix} \Delta \phi_{m,k} \\ \Delta \delta_{rm,k} \end{bmatrix} \tag{194}$$

$$\Delta \underline{y}_k = \begin{bmatrix} \Delta \phi \\ \Delta y \end{bmatrix}_k \tag{195}$$

APR LOCR

$$\Delta \underline{y}_{m,k} = \begin{bmatrix} -k_\psi k_y & -k_\psi \\ -a_k k_\psi k_y & 0.0 \end{bmatrix} \begin{bmatrix} \Delta y_m \\ \Delta \psi_m \end{bmatrix}_k + \begin{bmatrix} 0.0 & 0.0 \\ 0.0 & 1.0 \end{bmatrix} \begin{bmatrix} \Delta \phi_{m,k} \\ \Delta \delta_{rm,k} \end{bmatrix} \tag{196}$$

$$\Delta \underline{y}_k = \begin{bmatrix} \Delta \phi_k - k_\psi\ \Delta \psi_k + k_\psi\ k_y\ \Delta y_k \\ \Delta \delta_{r,k} - a_k\ k_\psi\ \Delta \psi_k + a_k\ k_\psi\ k_y\ \Delta y_k \end{bmatrix} \tag{197}$$

APR LOCP

$$\Delta \underline{y}_{m,k} = \begin{bmatrix} -k_y & 0.0 \\ -a_k k_y & 0.0 \end{bmatrix} \begin{bmatrix} \Delta y_m \\ \Delta \phi_m \end{bmatrix}_k + \begin{bmatrix} 0.0 & 0.0 \\ 0.0 & 1.0 \end{bmatrix} \begin{bmatrix} \phi_m \\ \delta_{rm} \end{bmatrix}_k \tag{198}$$

$$\Delta \underline{y}_k = \begin{bmatrix} \Delta \phi_k - k_y\ \Delta y_k \\ \Delta \delta_{r,k} - a_k\ k_y\ \Delta y_k \end{bmatrix} \tag{199}$$

The APR LOC autopilots use ϕ_m as a control variable to cause y_m to smoothly transfer to zero from the measured value of y that occurs when the localizer engage logic activates the APR LOC command model controller. The command model control system used to construct the path is as follows:

```
    DATA LOCENGE/FALSE/              ;initiaze APR LOC flag
```

$$\hat{y}_k = (\hat{R}_k + RLOC)\ \sin\ (\Xi_k) \qquad \text{;estimate the y position using} \quad (200)$$
the range estimate

```
    IF |Ξ_k|<Ξ_max      THEN LOCENGE=TRUE
```

$$\text{IF NOT LOCENGE} \quad \text{THEN}\ y_{m,k}=\hat{y}_k \qquad \text{;reset the internal command model states}$$
until Ξ is in range

$$\phi_{m,k}=\phi_k$$
$$\psi_{m,k}=\hat{\psi}_k$$
$$\delta_{rm,k}=\delta_{rk}$$

```
    IF LOCENGE          THEN

BEGIN
```

$$LOC_1 = \ell_1 * |y_{m,k} * 3.2808| + \ell_2 \qquad \text{;compute APR LOC command model} \quad (201)$$
control system gain

```
    IF LOC_1>ℓ_3        THEN LOC_1=ℓ_3
    IF LOC_1<ℓ_4        THEN LOC_1=ℓ_4
```

$$LK1 = LOC_1 (\hat{V}_k * 3.28) \qquad \text{;try to keep closed-loop system} \quad (202)$$
invariant by varying control
gains with velocity

$$LK2 = LOC_2 / (g/\hat{V}_k) \qquad\qquad\qquad\qquad\qquad (203)$$

$$\psi_c = LK_1 * (0.0 - y_{m,k}) \qquad \text{;compute}\ \psi_m\ \text{command} \qquad (204)$$

```
    IF |ψ_c|>ψ_cmax      THEN
```

$$\psi_c = sign(\psi_c) * \psi_{cmax} \qquad \text{;}\psi_c\ \text{should be less than the}$$
ψ_{cmax} intercept angle

$$UC = LK_2 * (\psi_c - \psi_{m,k}) \qquad \text{;compute}\ \phi_m\ \text{command} \qquad (205)$$

IF $|UC|>\phi_{max}$ THEN $UC=\text{sign}(UC)*\phi_{max}$

$\dot{\phi}_m=UC-\phi_{m,k-1}$;keep roll and roll rate below   (206)
                                                        maximum values

IF $|\dot{\phi}_m|>\dot{\phi}_{max}$ THEN $\dot{\phi}_m=\text{sign}(\dot{\phi}_m)*\dot{\phi}_{max}$

$\phi_{m,k}=\phi_{m,k-1}+\dot{\phi}_m$;the computed roll command used   (207)
                                                        in Eqs. 188 and 189

END

The localizer model control system will begin to intercept the localizer beam centerline if the pilot has activated the approach mode (APR = TRUE) and a valid localizer signal is available. The pilot must set up an intercept angle. The APR LOC mode performs best if the pilot orients the aircraft at a ~60 deg intercept just before the outer marker. The command model values for y_m, ψ_m, and ϕ_m are continually updated to the corresponding measured aircraft's values as long as the APR LOC control system has not been activated. Equation 204 forms the command models heading command whose upper value is limited to the intercept angle set in the control system. As the aircraft nears the beam centerline the heading command gradually changes to the reference 0.0 deg runway heading. The measured heading is referenced to the runway heading. After the heading command is computed, the rest of the control system resembles the HDG SEL command model system discussed in Section C.

APPENDIX D

TRIM, STEADY STATE AND THE STAR TRAJECTORY

This appendix discusses trim for nonlinear systems, steady state for linear systems and the relationship between the two. Steady state for linear systems is generalized to include the theory of feedforward control and model following. Feedforward control theory is used in the PIF derivation in Chapter IV.

For a constant command,

$$\underline{y}_o = h(\underline{x}_o, \underline{u}_o) \tag{208}$$

$$\dot{\underline{y}}_o = 0.0 \tag{209}$$

an aircraft is in static trim if there is a $\underline{u}_o$ such that Eqs. 208 and 209 are true and the nonlinear aircraft dynamics, shown in Eq. 80, satisfy

$$0 = \underline{f}(\underline{x}_o, \underline{u}_o) \tag{210}$$

The outer-loop states x, y, z, ψ are not included in Eq. 210. For the perturbation linear system, static trim or steady state is similiarily defined

$$0 = A\,\Delta\underline{x}^* + B\,\Delta\underline{u}^* \tag{211}$$

$$\Delta\underline{y}^* = H\,\Delta\underline{x}^* + D\,\Delta\underline{u}^* = \Delta\underline{y}_m \tag{212}$$

$$\Delta\dot{\underline{y}}^* = 0.0 \tag{213}$$

Grouping the linear equations, static trim for linear systems can be easily computed by solving the linear matrix equation

$$\begin{bmatrix} A & B \\ H & D \end{bmatrix} \begin{bmatrix} \Delta \underline{x}^* \\ \Delta \underline{u}^* \end{bmatrix} = \begin{bmatrix} 0 \\ I \end{bmatrix} \Delta \underline{y}_m \tag{214}$$

for $\Delta \underline{x}^*$ and $\Delta \underline{u}^*$. $\Delta \underline{x}^*$ and $\Delta \underline{u}^*$ are defined to be the "star trajectories" of the plant for constant $\Delta \underline{y}_m$. A solution to Eq. 214 exists if the plant has no transmission zeroes at zero, i.e., the quad partition matrix in Eq. 214 has full rank. Using the definition of perturbation systems, and the Taylor series expansion, different nonlinear trim points caused by perturbation changes in $\underline{y}_o$, represented as $\Delta \underline{y}_m$, are related through the following equations,

$$\underline{y}_o + \Delta \underline{y}_m = \underline{y}_o + \Delta \underline{y}^* = \underline{y}_{o,new} \tag{215}$$

$$\underline{x}_o + \Delta \underline{x}^* \cong \underline{x}_{o,new} \tag{216}$$

$$\underline{u}_o + \Delta \underline{u}^* \cong \underline{u}_{o,new} \tag{217}$$

Steady-state for discrete systems is similiarly derived. The state transition equation for a linear system is, Ref. 36,

$$\Delta \underline{x}(t) = e^{A(t-t_o)} \Delta \underline{x}(t_o) + \int_{t_o}^{t} e^{A(t-\tau)} B \Delta \underline{u}(\tau) \, d\tau \tag{218}$$

Starting from time t_o, Eq. 218 describes how $\Delta x(t)$ evolves if $\Delta \underline{u}(\tau)$ is known. If $\Delta \underline{u}(\tau)$ is held constant over the constant interval Δt (a zero-order hold implementation) then Eq. 218 can be represented at each time instant t_k, where $t_{k+1} = t_k + \Delta t$, by

$$\Delta \underline{x}_{k+1} = \phi \Delta \underline{x}_k + \Gamma \Delta \underline{u}_k \tag{219}$$

which is an exact representation.

The discrete PIF control law uses Eq. 219 as the discrete plant model. In steady state, Eq. 219 can be combined with Eq. 212 to produce a result similiar to Eq. 214,

$$\begin{bmatrix} (\phi - I) & \Gamma \\ H & D \end{bmatrix} \begin{bmatrix} \Delta \underline{x}^* \\ \Delta \underline{u}^* \end{bmatrix} = \begin{bmatrix} 0 \\ I \end{bmatrix} \Delta \underline{y}_m \tag{220}$$

If the discrete plant has no transmission zeroes at 1.0 then $\Delta \underline{x}^*$ and $\Delta \underline{u}^*$ can be computed by

$$\begin{bmatrix} \Delta \underline{x}^* \\ \Delta \underline{u}^* \end{bmatrix} = \begin{bmatrix} \Omega_{11} & \Omega_{12} \\ \Omega_{21} & \Omega_{22} \end{bmatrix} \begin{bmatrix} 0 \\ \Delta \underline{y}_m \end{bmatrix} \tag{221}$$

where

$$\begin{bmatrix} (\phi - I) & \Gamma \\ H & D \end{bmatrix} \begin{bmatrix} \Omega_{11} & \Omega_{12} \\ \Omega_{21} & \Omega_{22} \end{bmatrix} = \begin{bmatrix} I & 0 \\ 0 & I \end{bmatrix} \tag{222}$$

The steady-state star trajectory computed for the discrete-time plant model is identical to the values computed using Eq. 214.

Tracking a constant command can be generalized to command model output tracking. The discrete-time plant representation for the command model shown in Eq. 7 and 8 is determined using Eq. 218, where $\Delta \underline{u}_{m,k}$ is constant between sampling intervals, and has the following form

$$\Delta \underline{x}_{m,k+1} = \phi_m \Delta \underline{x}_{m,k} + \Gamma_m \Delta \underline{u}_{m,k} \tag{223}$$

The solution for the control, $\Delta \underline{u}_k$, which causes $\Delta \underline{y}_k$ to track $\Delta \underline{y}_{m,k}$ for the discrete-time command model is accomplished by generalizing Eq. 220. The generalization primarily occurs by interpreting $\Delta \underline{x}_k^*$ and $\Delta \underline{u}_k^*$ as ideal trajectories (the star trajectories) that occur when $\Delta \underline{y}^* = \Delta \underline{y}_m$.

To derive the equation for the star trajectories, the star trajectories are assumed to be related to the discrete model through constant matrices

$$\begin{bmatrix} \Delta \underline{x}^* \\ \Delta \underline{u}^* \end{bmatrix}_k = \begin{bmatrix} A_{11} & A_{12} \\ A_{21} & A_{22} \end{bmatrix} \begin{bmatrix} \Delta \underline{x}_{m,k} \\ \Delta \underline{u}_{m,k} \end{bmatrix} \tag{224}$$

The matrices A_{ij} in Eq. 224 are the feedforward matrices and remain to be determined.

The derivation for a solvable expression for the feedforward matrices proceeds by forming two different expressions for $\begin{bmatrix} \Delta \underline{x}_{k+1}^* - \Delta \underline{x}_k^* \\ \Delta \underline{y}_k^* \end{bmatrix}$ then

66

equating them. One expression is obtained using the plant dynamics,

$$\begin{bmatrix} \Delta \underline{x}^*_{k+1} - \Delta \underline{x}^*_k \\ \Delta \underline{y}^*_k \end{bmatrix} = \begin{bmatrix} (\phi-I) & \Gamma \\ H & D \end{bmatrix} \begin{bmatrix} A_{11} & A_{12} \\ A_{21} & A_{22} \end{bmatrix} \begin{bmatrix} \Delta \underline{x}_{m,k} \\ \Delta \underline{u}_{m,k} \end{bmatrix} \tag{225}$$

The other expression is obtained using Eq. 224,

$$\begin{bmatrix} \Delta \underline{x}^*_{k+1} - \Delta \underline{x}^*_k \\ \Delta \underline{y}^*_k \end{bmatrix} = \begin{bmatrix} A_{11}(\phi_m-I) & A_{11}\Gamma_m & A_{12} \\ H_m & D_m & 0 \end{bmatrix} \begin{bmatrix} \Delta \underline{x}_{m,k} \\ \Delta \underline{u}_{m,k} \\ \Delta \underline{u}_{m,k+1} - \Delta \underline{u}_{m,k} \end{bmatrix} \tag{226}$$

To proceed with the derivation, $\Delta \underline{u}_{m,k+1} - \Delta \underline{u}_{m,k}$ in Eq. 226 is required to be zero, i.e., $\Delta \underline{u}_{m,k}$ is assumed to be constant. Equating Eq. 225 and Eq. 226 results in the solvable feedforward matrix equation

$$\begin{bmatrix} (\phi-I) & \Gamma \\ H & D \end{bmatrix} \begin{bmatrix} A_{11} & A_{12} \\ A_{21} & A_{22} \end{bmatrix} = \begin{bmatrix} A_{11}(\phi_m-I) & A_{11}\Gamma_m \\ H_m & D_m \end{bmatrix} \tag{227}$$

A solution for the feedforward matrices in Eq. 227 exists if the plant has no transmission zeroes at 1.0 and no transmission zero equal to an eigenvalue of ϕ_m. A numerical solution to Eq. 227 is given in Ref. 5 (the subroutine CGTPIF). The solution is unique if the number of plant controls and plant outputs are equal.

Assuming a solution with unknown coefficients then determining the values of the unknown coefficients by substituting the solution back into the equations, as is done for the feedforward control solution, is a technique also used in differential equations to determine the homogeneous and particular solutions. If the forcing function to a differential equation can be represented as a model, Eq. 223, with no control input, than the feedforward control solution in Eq. 229 can be shown to be the particular solution for that forcing function. Assuming the proper form for the solution has been simple for only the single-rate discrete-time case. The feedforward control solution for the multi-rate case has yet to be determined.

The feedforward control matrices can be used to relate incremental changes in nonlinear trim to incremental changes in the command model similiar to results in Eqs. 215 to 217. For a constant command model input, the relationship

is

$$\underline{x}_{o,k} - \underline{x}_{o,k-1} \simeq A_{11}(\underline{x}_{mo,k} - \underline{x}_{mo,k-1}) + A_{12}(\underline{u}_{mo,k} - \underline{u}_{mo,k-1}) \tag{228}$$

$$\underline{u}_{o,k} - \underline{u}_{o,k-1} \simeq A_{21}(\underline{x}_{mo,k} - \underline{x}_{mo,k-1}) + A_{22}(\underline{u}_{mo,k} - \underline{u}_{mo,k-1}) \tag{229}$$

Small changes in $\underline{u}_m$ serves the same purpose as small changes in $\underline{y}_m$ did in Eq. 215 and the PIF derivation in Ref. 3,

$$\underline{u}_{mo,k_{NEW}} = \underline{u}_{mo,k} + \Delta\underline{u}_{m,k} \tag{230}$$

$$\underline{x}_{mo,k_{NEW}} = \underline{x}_{mo,k} + \Delta\underline{x}_{m,k} \tag{231}$$

The PIF control law is designed in this report to accommodate small changes in $\Delta\underline{u}_m$.

APPENDIX E

CONTROL DATA HOLDS, COMPUTATION DELAY

AND TRIM ACCOMMODATION

This appendix shows how different control data holds and modeled control law computation delay affect discrete-time plant model representations. Trim accommodation procedures are reviewed. The concepts in this appendix aid in understanding the PIF derivation in Chapter IV and command model construction in Appendix C.

A. CONTROL DATA HOLD

A control data hold is a procedure for constructing in continuous-time the control that commands the actuator surface. A zero-order hold, for example has the following continuous-time representation

$$\Delta \underline{u}(t) = \Delta \underline{u}_k \qquad \text{for } t_{k+1} > t > t_k \tag{232}$$

A triangular data hold has the following representation

$$\Delta \underline{u}(t) = \Delta \underline{u}_k + (t-t_k)(\Delta \underline{u}_{k+1} - \Delta \underline{u}_k)/\Delta t \qquad \text{for } t_{k+1} > t \geq t_k \tag{233}$$

Similiar expressions can be determined for the first-order hold, slewer data hold and others. If the intermediate variable

$$\Delta \underline{v}_k = \frac{1}{\Delta t}(\Delta \underline{u}_{k+1} - \Delta \underline{u}_k) \tag{234}$$

is defined, then the triangular data hold becomes

$$\Delta \underline{u}(t) = \Delta \underline{u}_k + (t-t_k)\Delta \underline{v}_k \tag{235}$$

$$\Delta \underline{u}_{k+1} = \Delta \underline{u}_k + \Delta t \, \Delta \underline{v}_k \tag{236}$$

The discrete plant representation at the sample points for the triangular data hold is obtained by substituting Eq. 235 into Eq. 218,

$$\Delta \underline{x}(t_{k+1}) = e^{F\Delta t} \, \Delta \underline{x}(t_k) + \int_0^{\Delta t} e^{F\tau} \, d\tau G \Delta \underline{u}_k + e^{F\Delta t} \int_0^{\Delta t} \tau e^{-F\tau} \, d\tau G \Delta \underline{v}_k \qquad (237)$$

The equation can be rewritten as

$$\begin{bmatrix} \Delta \underline{x}_{k+1} \\ \Delta \underline{u}_{k+1} \end{bmatrix} = \begin{bmatrix} \phi & \Gamma \\ 0 & I \end{bmatrix} \begin{bmatrix} \Delta \underline{x}_k \\ \Delta \underline{u}_k \end{bmatrix} + \begin{bmatrix} \Gamma_1 \\ \Delta t I \end{bmatrix} \Delta \underline{v}_k \qquad [238]$$

where

$$\Gamma_1 = \int_0^{\Delta t - \sigma} e^{Fs} \, ds \, G \qquad \Gamma_2 = \int_0^{\sigma} e^{Fs} \, ds \, G \qquad (239)$$

Equation 238 occurs exactly as shown as a partition when the sampled data regulator PIF discrete plant model is formed. The result is altered to obtain the desired autopilot zero-order hold mechanization.

B. COMPUTATION DELAY

Digital control laws do not necessarily output the control command to the actuators at the sample points. There is a delay caused by computation and other factors that cause the control command to be released to actuator channels between sample points. The control command with computation delay can be represented in continuous-time as

$$\Delta \underline{u}(t) = \begin{cases} \Delta \underline{u}_k & t_{k+1} > t \geq t_k + \sigma \\ \Delta \underline{u}_{k-1} & t_k + \sigma > t \geq t_k \end{cases} \qquad (240)$$

where σ is the computational delay. Substituting Eq. 240 into 218 and simplifying produces

$$\Delta \underline{x}_{k+1} = \phi \Delta \underline{x}_k + \Gamma_1 \, \Delta \underline{u}_k + \Gamma_2 \, \Delta \underline{u}_{k-1} \qquad (241)$$

where

$$\Gamma_1 = \phi \int_0^{\Delta t} \tau e^{-F\tau} \, d\tau \, G = \int_0^{\Delta t} \int_0^{\tau} e^{Fs} \, ds d\tau \, G \qquad (242)$$

70

A discrete contro law can accommodate the computation delay, (that is the design evaluation and simulation exactly corresponds to the implementation response), by using Eq. 241 as the discrete model representation of the plant. Rather than guess at σ to perform a design, the PIF autopilot construction simply assumes the control is released to the actuators delayed one full cycle. Equation 241 with a full cycle delay can be represented as follows

$$\begin{bmatrix} \Delta \underline{x}_{k+1} \\ \Delta \underline{u}_k \end{bmatrix} = \begin{bmatrix} \phi & \Gamma \\ 0 & I \end{bmatrix} \begin{bmatrix} \Delta \underline{x}_k \\ \Delta \underline{u}_{k-1} \end{bmatrix} + \begin{bmatrix} 0 \\ \Delta t I \end{bmatrix} \Delta \underline{v}_{k-1} \qquad [243]$$

where $\Delta \underline{u}_k$ is the control applied at time t_{k+1}. Equation 243 (with the u_k index moved up one sample, the implementation is identical) occurs when the discrete PIF plant model is simplified.

C. TRIM ACCOMMODATION

In typical autopilot operation, the autopilot feeds back an error signal to the actuators to drive the error signal to zero. The error signal is formed by subtracting the sensed signal from a command or trim value. Four popular ways to generate trim information in flight are 1) prestore. trim values with flight condition, 2) load the measured aircraft states at control initiation as the trim values, 3) estimate the trim value of a signal by low-pass filtering the signal (the error signal is constructed using a "wash-out" filter) and 4) estimate trim using integral control. The PIF control law uses the second, third and fourth mechanizations. The second mechanization is part of the control and command model initialization procedure. The third mechanization is part of the integral control implementation where the rudder command error is integrated and fed back. The following simple example demonstrates the effect of control error integral feedback.

Consider a scalar plant

$$\dot{x} = ax + bu \qquad (244)$$

A control law using integral control is formed which feeds back the integral of control error from some command value

$$u = u_c + k_1 x + k_2 \int (u - u_c) . \qquad (245)$$

An implementable form for Eq. 245 is obtained by taking the derivative and simplifying. If the variable

71

$$z = u - u_c \qquad (246)$$

is substituted into Eq. 245, the Laplace transform of the control law becomes

$$u = z + u_c \qquad (247)$$

$$z = \left(\frac{k_1 s}{s-k_2}\right) x \qquad (248)$$

Equation 248 is recognized as a wash-out filter. Digitally integrating the rudder control command error in a manner similiar to Eq. 245 is used in most of the lateral-directional PIF autopilots. The effect is similiar to a yaw damper except that all the lateral states fed back are washed out simultaneously. The value of u_c in Eq. 247 for the PIF autopilots is the control position at engage.

REFERENCES

1. Larson, G. C.; "The Future of 'Autopilots'", Business and Commerical Aviation, March 1981.

2. Downing, D. R., Bryant, W. H. and Yenni, K. R.; "Flight Test Evaluation of Advanced Symbology for General Aviation Approach to Landing Displays", Proceedings of the AIAA Aircraft Systems and Technology Meeting, Dayton, Ohio, August 1981.

3. Broussard, J. R., Berry, P. W. and Stengel, R. R.; "Modern Digital Flight Control System Design for VTOL Aircraft", NASA CR-159019, March 1979.

4. Downing, D. R., Bryant, W. H. and Ostroff, A. J.; "Flight Test of a VTOL Digital Autoland System Along Complex Trajectories", Proceedings of the 1979 AIAA Guidance and Control Conference, Boulder, Colorado, August 1979.

5. Broussard, J. R.; "PIFCGT – a PIF Autopilot Design Program for General Aviation Aircraft", NASA CR-166123, 1983.

6. Armstrong, E. S.; <u>ORACLS – A Design System for Linear Multivariable Control</u>, Marcel Dekker, Inc., New York, c.1980.

7. Lehtomaki, N. A., Sandell, N. R. and Athans, M.; "Robustness Results in Linear-Quadratic Gaussian Based Multivariable Control Designs", <u>IEEE Trans. Auto. Control</u>, Vol. AC-26, February 1981, pp. 75-93.

8. Broussard, J. R.; "A Quadratic Weight Selection Algorithm", Proceedings of the Joint Automatic Control Conference (JACC), Charlottesville, Virginia, June 1981.

9. Halyo, N. and Broussard, J. R.; "A Convergent Algorithm for the Stochastic Infinite-Time Discrete Optimal Output Feedback Problem", Proceedings of the Joint Automatic Control Conference (JACC), Charlottesville, Virginia, June 1981.

10. Downing, D. R., Bryant, W. H. and Stengel, R. F.; "NASA/Princeton Digital Avionics Flight Test Facility", Proceedings of the 3rd Digital Avionics Systems Conference, Fort Worth, Texas, November 1979.

11. Jet Electronics and Technology; FC-200 Automatic Flight Control System Pilot's Manual, Grand Rapids, Michigan, January 1975.

12. King Radio Corporation; KFC 300 Flight Control System, Olathe, Kansas, August 1979.

13. Sperry Flight Systems, Avionics Division; SPZ-500 Pilot's Manual, Phoenix, Arizona, April 1980.

14. Bendix Avionics Division; M-4D Automatic Flight Control System Pilot's Manual, Fort Lauderdale, Florida.

15. Edo-Aire Mitchell; Century 41 Autopilot Operator's Manual, Mineral Wells, Texas, January 1979.

16. Brittian Industries; Operating Manual for NAV-FLITE II B-5 B-7 Autopilot Systems, Tulsa, Oklahoma, January 1970.

17. Roskam, J. and See, M. J.; "The State of the Art of General Aviation Autopilots - Now and in the Future", Society of Automotive Engineers, Business Aircraft Meeting and Exposition, Wichita, Kansas, April 1981.

18. Roskam, J.; Airplane Flight Dynamics and Automatic Flight Controls, Parts I and II, Second Edition, Roskam Aviation Engineering Corp., Lawrence, Kansas, 1979.

19. Berry, P. W. and Broussard, J. R.; "Verification of Fighter Aircraft Command Augmentation Control Laws by Nonlinear Simulation", AIAA Atmospheric Flight Mechanics Conference, Palo Alto, California, August 1978.

20. Smith, G. A. and Meyer, G.; "Total Aircraft Flight Control System-Balance Open-Loop and Closed-Loop Control with Dynamic Trim Maps", Proceedings of the 3rd Digital Avionics Systems Conference, Fort Worth, Texas, November 1979.

21. Smith, C. L.; Digital Computer Process Control, International Textbook Company, Scranton, Pennsylvania.

22. Maybeck, P. S.; Stochastic Models, Estimation, and Control, Vol. 3, Academic Press, New York, 1982.

23. Broussard, J. R. and O'Brien, M. J.; "Feedforward Control to Track the Output of a Forced Model", IEEE Trans. Auto. Control, Vol. AC-25, August 1980, pp. 851-852.

24. Pernebo, L.; "An Algebraic Theory for the Design of Controllers for Linear Multivariable System - Part I: Structure Matrics and Feedforward Design", IEEE Trans. Auto. Control, Vol. AC-26, No. 1, February 1981, pp. 171-182.

25. Wang. S. H. and Davison, E. J.; "A Minimization Algorithm for the Design of Linear Systems", IEEE Trans. Auto Control, Vol. AC-18, 1973, pp. 220-225.

26. Mabius, L. E.; "Model Reference Control and its Application to the Cromby Electric Generating Plant Model", Proceedings of the Joint Automatic Control Conference (JACC), Charlottesville, Virginia, June 1981.

27. Dorato, P. and Levis, A. H.; "Optimal Linear Regulators: The Discrete-Time Case", IEEE Trans. Auto. Control, Vol. AC-16, No. 6, December 1971, pp. 613-620.

74

28. Broussard, J. R., Berry, P. W. and Gully, S. W.; "Synthesis of Digital Controllers for a Fighter Aircraft Using Continuous-Time Specifications", Proceedings of the Flight Control Systems Criteria Symposium, Monterey, California, July 1978.

29. McRuer, D. T. and Johnston, D. E.; "Flight Control Systems Properties and Problems", Vol. I, NASA CR-2500, February 1975.

30. Suit, W. T.; "Aerodynamic Parameters of the Navion Airplane Extracted From Flight Data", NASA TN D-6643, March 1972.

31. Broussard, J. R.; "Output Feedback Implicit Model Following", Proceedings of the 20th CDC, San Diego, California, December 1981.

32. Bryson, A. E., Jr., and Hedrick, J. K.; "Three-Dimensional Minimum-Fuel Turns for a Supersonic Aircraft", J. Aircraft, Vol. 9, March 1972, pp. 223-229.

33. Calise, A. J.; "Extended Energy Management for Flight Performance Optimization", AIAA Paper No. 75-30, 13th AIAA Aerospace Sciences Meeting, January 1975.

34. Etkin, B.; Dynamics of Atmospheric Flight, John Wiley & Sons, Inc., New York, 1972.

35. Fernand, J. M.; "Determination of Stability and Control Derivatives for Variable-Response Research Aircraft Using a Modified Maximum Likelihood Estimator', Master's Thesis, Princeton University, Department of Mechanical and Aerospace Engineering, September 1978 (also available as AFT-CI-79-43T).

36. Franklin, G. F. and Powell, J. D.; Digital Control of Dynamic Systems, Addison-Wesley, Reading, Massachusetts, 1980.

LIST OF SYMBOLS

In general, matrices are represented by capital letters and vectors are underscored; exceptions to these rules are only made when they are contradicted by standard aerodynamic notation.

VARIABLE	DESCRIPTION
A	Discrete time feedforward matrix Fundamental matrix (continuous-time system) Wing reference area
ASK	Gain in ALT SEL command model control system
a	Acceleration Roll to rudder crossfeed gain
a_n	Component of the earth-relative acceleration in the aircraft x-z plane normal to the velocity vector
a_y	Component of the earth-relative acceleration normal to the aircraft x-z plane
B	Control effect matrix (continuous-time system)
b	Wing span Bias estimate
C	Control law feedback gains
C_{l_2}	Partial derivative of the nondimensional coefficient of force or moment 1 with respect to the nondimensional variable 2 (scalar)
c	Mean aerodynamic chord
D	Control observation matrix Drag
d	Perpendicular position from the glideslope to the aircraft
$\underline{F}$	Aerodynamic contact force vector
$\underline{f}$	Vector-valued nonlinear function
GSK	Gain in APR GS command model control system

VARIABLE	DESCRIPTION
g	Magnitude of gravitational acceleration vector Scalar gain value
H	Command observation matrix
HSK	Gain in HDG SEL command model control system
H_1^2	Euler angle transformation form Frame 1 axes to Frame 2 axes
$\underline{h}$	Vector-valued nonlinear observation function
h_B	Barometric altimeter output
I	Identity matrix Moment of inertia
i	Index integer
J	Cost functional matrix
j	$\sqrt{-1}$
K	Gain value
k	Index integer
LK	Gain in APR LOC command model control system
LOC	Gain in APR LOC command model control system
L	Aerodynamic moment about the x-axis (scalar)
l	Scalar gain value
ℓ	Number of commands
M	Aerodynamic moment about the y-axis (scalar) Cross weighting matrix between states and controls
m	Mass of the vehicle Number of controls Meters
N	Aerodynamic moment about the z-axis (scalar) Newtons ($kg \cdot m/sec^{-2}$)
n	Number of states

VARIABLE	DESCRIPTION
P	Riccati matrix in the optimal regulator problem
p	Rotational rate about the body x-axis
Q	State weighting matrix
QZ	Integrator state weighting matrix
q	Rotational rate about the body y-axis
q	Free stream dynamic pressure $(= \frac{1}{2}\rho V_o^2)$
R	Control weighting matrix
RD	Control rate weighting matrix
RLOC	Range position from localizer transmitter to touchdown point
RMEAS	Estimate value of range using vertical position and glideslope angle
r	Rotational rate about the body z-axis
S	Feedforward matrix for sensor measurements
s	Laplace transform variable
T	Thrust
t	Time
UC	Command model control variable
u	Body x-axis velocity component
$\underline{u}$	Control vector
V	Velocity magnitude
v	Body y-axis velocity component Control difference
w	Body z-axis velocity component
X	Aerodynamic force along the x-axis (scalar)
x	Position along the x-axis

VARIABLE	DESCRIPTION
$\underline{x}$	State vector
Y	Aerodynamic force along the y-axis (scalar)
y	position along the y-axis
Z	Aerodynamic force along the z-axis (scalar)
z	Position along the z-axis

VARIABLE (GREEK)	DESCRIPTION
α	Wind-body pitch Euler Angle (angle of attack)
β	Negative of wind-body yaw Euler angle (sideslip angle)
Γ	Discrete time control effect matrix Glideslope deviation angle
γ	Inertial-velocity axis pitch Euler angle (flight-path)
δ_a	Aileron deflection
δ_e	Elevator deflection
δ_r	Rudder deflection
ζ	Damping ratio
θ	Inertial-body pitch Euler angle
λ	Eigenvalue
$\underline{\nu}$	Euler angle position vector
Ξ	Localizer deviation angle
ξ	Eigenvector Integrator state
ρ	Air density
σ	Summation
$\dot{\sigma}$	Real part of an eigenvalue in radians/sec Time delay

VARIABLE (GREEK)	DESCRIPTION
τ	Time constant
Φ	Discrete-time system matrix
ϕ	Inertial-body axis roll Euler angle
ψ	Inertial-body axis yaw Euler angle
Ω	Matrix in quad partition matrix inverse
ω	Frequency in radians/sec Imaginary part of an eigenvalue
$\underline{\omega}_B^E$	Body angular rate vector

SUBSCRIPTS	DESCRIPTION
a	Aileron
B	Body axis
b	Bias
c	Command value
E	Earth-relative axis
e	Error quantity
GS	Glideslope
H	Horizontal
i	Element index for vectors and matrices
j	Element index for vectors and matrices
k	Sampling instant index
l	Aerodynamic moment about the x-axis
m	Aerodynamic moment about the y-axis model variable
n	Aerodynamic moment about the z-axis
o	Nominal value

SUBSCRIPTS	DESCRIPTION
s	Static pressure Accelerometer offset from the cg
w	Wind
x	Horizontal perpendicular to y and z
y	Horizontal perpendicular to x and z
z	Vertical perpendicular to x and y
X	Aerodynamic force along the x-axis
Y	Aerodynamic force along the y-axis
Z	Aerodynamic force along the z-axis

SUPERSCRIPTS	DESCRIPTION
E	Earth (inertial) axis
T	Transpose of matrix
W	Wind axis
-1	Inverse of matrix
*	Steady state Trim

PUNCTUATION	DESCRIPTION
$(\dot{\ })$	Derivative of quantity with respect to time
$(\underline{\ })$	Vector quantity
$\partial(\ )/\partial(\ )$	Partial derivative of one variable with respect to another
$\Delta(\ )$	Perturbation variable
$(\ )^*$	Star trajectory
$(\hat{\ })$	Estimated quantity Discrete cost function weighting matrix
∞	Infinity

81

PUNCTUATION	DESCRIPTION
$\int$	Integral
[•]	Important Equation
(•)	Equation
(~)	Matrix equivalent to vector cross product, Specifically, if $\underline{x}$ is the three-dimensional vector

$$\underline{x} = \begin{bmatrix} x \\ y \\ z \end{bmatrix} \qquad \text{then } \tilde{x} = \begin{bmatrix} 0 & -z & y \\ z & 0 & -x \\ -y & x & 0 \end{bmatrix}$$

and the cross product of $\underline{x}$ and $\underline{f}$ is equal to the product of the matrix $\tilde{x}$ and the vector $\underline{f}$,

$$\underline{x} \times \underline{f} = \tilde{x}\underline{f}$$

ACRONYM	CORRESPONDING PHRASE
ARA	Avionics Research Aircraft
cg	Center of gravity
DME	Distance Measuring Equipment
GA	General Aviation
GATOR	General Aviation Terminal Area Operation Research
ILS	Instrument Landing System
kt	Knot
MAX	Maximum
MLS	Microwave Landing System
NASA	National Aeronautics and Space Administration
PI	Proportional-Integral
PIF	Proportional-Integral-Filter
rad	Radians
sec	Seconds

ACRONYM	CORRESPONDING PHRASE
VALT	VTOL Approach and Landing Technology
VTOL	Vertical Takeoff and Landing

TABLE 1   NAVION ACTUATOR CHARACTERISTICS

CONTROL	DISPLACEMENT LIMIT, deg	RATE LIMIT, deg/sec	TIME CONSTANT, τ, (sec)	MAXIMUM SPECIFIC MOMENT (IAS=53.8m/s (105kt))
AILERON	±20.0	70.0	0.17	9.2 rad/sec^2 roll acceleration
ELEVATOR	-30.0 +20.0	70.0	0.17	9.9 rad/sec^2 pitch acceleration
RUDDER	±20.0	70.0	0.17	4.2 rad/sec^2

TABLE 2   SENSOR NOISE AND BIAS CHARACTERISTICS
FOR THE NAVION RESEARCH AIRCRAFT

SENSOR	NOISE STANDARD DEVIATION	BIAS STANDARD DEVIATION
Lateral Accelerometer	0.3 m/s^2	0.6 m/s^2
Vertical Accelerometer	0.6 m/s^2	0.6 m/s^2
Rate Gyro	0.2 deg/sec	0.2 deg/sec
Attitude Gyro	0.1 deg	0.2 deg
Heading Gyro	0.1 deg	0.5 deg
Indicated Airspeed	0.05 m/s (0.15 fps)	0.15 m/s (0.5 fps)
Barometric Altimeter	3.0 m (10 ft)	15.0 m (50 ft)
Localizer/Glideslope Angular Deviation	0.02 deg	0.012 deg
Outer Marker Indication	---	500.0 m (1640 ft)

TABLE 3   ROLM 1666 CHARACTERISTICS

DESCRIPTION	–	General purpose 16 – bit minicomputer designed to MIL-E-5400 specifications
MEMORY	–	65,536 words of 1 μsec ferrite core
EXECUTION TIME	–	(Time in μsec, register to register operations)

INSTRUCTION	FIXED POINT (16 bit)	FLOATING POINT (32 bit)
Add	1.0	1.8 – 4.8
Multiply	5.2 – 5.4	3.6 – 4.8
Divide	9.2 – 9.6	8.0 – 8.8
Load, Store	2.0	4.8

TABLE 4   SAMPLE SUMMARY OF COMMERCIALLY AVAILABLE AUTOPILOTS

	NO. OF AXES	ROLL HOLD	PITCH HOLD	PITCH SELECT	HEADING HOLD	HEADING SELECT	ALTITUDE SELECT AND TURN	ALTITUDE HOLD	ALTITUDE SELECT	LOC CAPTURE AND HOLD	GS CAPTURE AND HOLD	AUTO TURN CORRDINATION	AUTO TRIM	YAW DAMPER	IAS HOLD	MACH HOLD	VERT. SPEED HOLD	BACK COURSE	GO AROUND	FLIGHT DIRECTOR
SPERRY SPZ 500	3	●	●	●	●	●	●	●	●	●	●	●	●	●	●	●	●	⸱		●
EDO-AIRE MITCHEL CENTURY 41	3	●	●	●	●		●		●	●		●	●					●	●	●
KING KFC 300	3	●	●	●	●	●	●	●	●	●	●	●	●	●				●	●	●
COLLINS APS-80	3	●	●	●	●	●	●		●	●	●		●	●	●			●	●	●
JET FC-200	3	●	●	●	●	●	●		●	●		●	●	●	●	●	●	●	●	●
BRITAIN B-5, B-7	3	●	●		●	●	●		●		●			●						
BENDIX M4-D	3	●	●	●	●	●	●		●	●		●	●					●	●	●
ARC 1000A	3	●	●	●	●	●	●	●	●	●	●		●	●				●	●	●
THIS REPORT PIF	3	●	●	●	●	●	●	●	●	●	●	●	●	●						

TABLE 5   STATES AND CONTROLS FOR AUTOPILOT MODE DESIGNS

BETA HOLD	MODEL
	$\underline{u}_m^T = [\beta_m \quad \phi_m]$
	$\underline{x}_m^T = [\beta_m \quad \phi_m]$
	$\underline{y}_m^T = [\beta_m \quad \phi_m]$
	$\underline{x}^T = [\beta \quad r \quad p \quad \phi]$
	$\underline{u}^T = [\delta_a \quad \delta_r]$
	$\underline{y}^T = [\beta \quad \phi]$
ROLL SEL	MODEL
	$\underline{u}_m^T = [\phi_m \quad \delta_{rm}]$
	$\underline{x}_m^T = [\phi_m \quad \delta_{rm}]$
	$\underline{y}_m^T = [\phi_m \quad (a_k \phi_m + \delta_{rm})]$
	$\underline{x}^T = [a_y \quad r \quad p \quad \phi]$
	$\underline{u}^T = [\delta_a \quad \delta_r]$
	$\underline{y}^T = [\phi \quad \delta_r]$
HDG SEL	NONLINEAR MODEL
	$\underline{u}_m^T = [\dot{\phi}_m \quad \delta_{rm}]$
	$\underline{x}_m^T = [\psi_m \quad \phi_m]$
	$\underline{y}_m^T = [(\psi-\psi_m) \quad (a_k(\psi-\psi_m) + \delta_{rm})]$
	$\underline{x}^T = [a_y \quad r \quad p \quad \phi \quad \psi]$
	$\underline{u}^T = [\delta_a \quad \delta_r]$
	$\underline{y}^T = [\phi \quad \delta_r]$

TABLE 5   (CONTINUED) STATES AND CONTROLS FOR AUTOPILOT MODE DESIGNS

HDG SEL	LINEAR MODEL
	$\Delta \underline{u}_m^T = [\Delta\phi_m \quad \Delta\delta_{rm}]$
	$\Delta \underline{x}_m^T = [\Delta\psi_m]$
	$\Delta \underline{y}_m^T = [-\Delta\psi_m \quad -a_k \Delta\psi_m + \Delta\delta_{rm}]$
	$\Delta \underline{x}^T = [\Delta a_y \quad \Delta r \quad \Delta p \quad \Delta\phi]$
	$\Delta \underline{u}^T = [\Delta\delta_a \quad \Delta\delta_r]$
	$\Delta \underline{y}^T = [\Delta\phi - \Delta\psi \quad -a_k \Delta\psi + \delta_r]$
ALT SEL	MODEL
	$\underline{u}_m = [\ddot{z}_m]$
	$\underline{x}_m^T = [z_m \quad \dot{z}_m]$
	$\underline{y}_m = [z_m]$
	$\underline{x}^T = [V \quad a_n \quad q \quad \theta \quad z]$
	$u = [\delta_e]$
	$y = [z]$
	LINEAR MODEL
	$\Delta \underline{u}_m = [\Delta z_m]$
	$\Delta \underline{x}_m = [\Delta z_m]$
	$\Delta \underline{y}_m = [\Delta z_m]$
	$\Delta \underline{x}^T = [\Delta V \quad \Delta a_n \quad \Delta q \quad \Delta\theta \quad \Delta z]$
	$\Delta u = [\Delta\delta_e]$
	$\Delta y = [\Delta z]$

TABLE 5 (CONTINUED) STATES AND CONTROLS FOR AUTOPILOT MODE DESIGNS

PITCH SEL	MODEL
	$u_m = [\theta_m]$
	$x_m = [\theta_m]$
	$y_m = [\theta_m]$
	$\underline{x}^T = [V \quad a_n \quad q \quad \theta]$
	$u = [\delta_e]$
	$y = [\theta]$
ARP GS	NONLINEAR MODEL
	$u_m = [\lambda_m]$
	$x_m = [d_m]$
	$y_m = [d_m]$
	$\underline{x}^T = [V \quad a_n \quad q \quad \theta \quad d]$
	$u = [\delta_e]$
	$y = [d]$
	LINEAR MODEL
	$\Delta u_m = [\Delta\lambda_m]$
	$\Delta x_m = [\Delta d_m]$
	$\Delta y_m = [\Delta d_m]$
	$\Delta\underline{x}^T = [\Delta V \quad \Delta a_n \quad \Delta q \quad \Delta\theta \quad \Delta d]$
	$\Delta u = [\Delta\delta_e]$
	$\Delta y = [\Delta d]$

TABLE 5 (CONTINUED) STATES AND CONTROLS FOR AUTOPILOT MODE DESIGNS

APR LOC	NONLINEAR MODEL
	$\underline{u}_m^T = [\phi_m \quad \delta_{rm}]$
	$\underline{x}_m^T = [y_m \quad \psi_m]$
	$\underline{x}^T = [a_y \quad r \quad p \quad \phi \quad \psi \quad y]$
	$\underline{u}^T = [\delta_a \quad \delta_r]$
APR LOCI	$\underline{y}_m^T = [\phi_m \quad y_m]$
	$\underline{y}^T = [\phi \quad y]$
APR LOCR	$\underline{y}_m^T = [k_\psi(\psi - k_y(y - y_m)) \quad \delta_{rm}]$
	$\underline{y}^T = [\phi \quad \delta_r]$
APR LOCP	$\underline{y}_m^T = [k_y(y - y_m) \quad \delta_{rm}]$
	$\underline{y}^T = [\phi \quad \delta_r]$
	LINEAR MODEL
APR LOC	$\Delta\underline{u}_m^T = [\Delta\phi_m \quad \Delta\delta_{rm}]$
	$\Delta\underline{x}_m^T = [\Delta y_m \quad \Delta\psi_m]$
	$\Delta\underline{x}^T = [\Delta a_y \quad \Delta r \quad \Delta p \quad \Delta\phi \quad \Delta\psi \quad \Delta y]$
	$\Delta\underline{u}^T = [\Delta\delta_a \quad \Delta\delta_r]$
APR LOCI	$\Delta\underline{y}_m^T = [\Delta\phi_m \quad \Delta y_m]$
	$\Delta\underline{y}^T = [\Delta\phi \quad \Delta y]$
APR LOCR	$\Delta\underline{y}_m^T = [k_\psi k_y \Delta y_m \quad a_k k_\psi k_y \Delta y_m + \Delta\delta_{rm}]$
	$\Delta\underline{y}^T = [\Delta\phi - k_\psi\Delta\psi + k_\psi k_y \Delta y$
	$\quad\quad -a_k k_\psi \Delta\psi + a_k k_\psi k_y \Delta y + \Delta\delta_r]$
APR LOCP	$\Delta\underline{y}_m^T = [-k_y\Delta y_m \quad -a_k k_y \Delta y_m + \Delta\delta_{rm}]$
	$\Delta\underline{y}^T = [\Delta\phi - k_y\Delta y \quad -a_k k_y\Delta y + \Delta\delta_r]$

TABLE 6   AUTOPILOT MODEL DESIGN PARAMETERS

AUTOPILOT	EQUATION	PARAMETERS	VALUE	UNITS
HDG SEL	150	HSK_1	1.0	---
	150	HSK_2	2.0	---
	155	ϕ_{max1}	0.262	radians
	---	ψ_{close}	0.157	radians
	153	ϕ_{max1}	0.0873	radians
	145	k_ψ	10.0	---
	154	R_T	914.4	m
ALT SEL	162	ASK_1	0.8	---
	162	ASK_2	2.0	---
	---	$\ddot{z}_{close}$	6.0	m/s^2
	165	$\ddot{z}_{max1}$	0.2286	m/s^2
	167	$\dot{z}_{max2}$	2.53	m/s
	166	α_{max}	0.24	radians
APR GS	177	OUTMARK	9879.0	m
	---	RMIN	100.0	m
	---	Γ_{max}	0.0436	radians
	182	g_1	-0.0004	ft^{-1}
	182	g_2	0.07	---
	---	g_3	0.07	---
	---	g_4	0.04	---
	184	λ_{GS}	0.0523	radians
	---	λ_{max}	0.0	radians
	---	λ_{min}	-0.08726	radians
	---	$\dot{\lambda}_{max}$	0.000524	radians
	---	r_1	-0.00037	m^{-1}
	---	r_2	0.112776	---
	---	RKMAX	0.08	---
APR LOC	200	RLOC	2205.0	m
	---	Ξ_{max}	0.0122	radians
	201	ℓ_1	-0.0002	ft^{-1}
	201	ℓ_2	0.2	---
	---	ℓ_3	0.2	---
	---	ℓ_4	0.11	---
	203	g	9.81	m/s^2
	203	LOC_2	1.2	---
	---	ψ_{cmax}	0.523	radians
	---	ϕ_{cmax}	0.175	radians
	---	$\dot{\phi}_{max}$	0.00873	radians
APR LOCR	191	k_ψ	3.0	---
	191	k_y	0.017	---
APR LOCP	192	k_y	0.04	---

TABLE 7   SQUARE ROOT OF Q AND R DIAGONAL WEIGHTS IN THE PIF COST FUNCTIONS

STATE* OR CONTROL	AUTOPILOT MODE			
	ALT SEL (DESIGN)	ALT SEL (LOWER θ WEIGHT)	PITCH SEL	APR GS
$\Delta\delta_e$	0.0	0.0	0.0	0.0
$\Delta\delta_a$	---	---	---	---
$\Delta\delta_r$	---	---	---	---
Δu	0.0	0.0	0.0	0.0
Δw	0.0	0.0	0.0	0.0
Δq	0.0	0.0	0.0	0.0
$\Delta\theta$	11.0	5.0	8.0	12.5
Δz	0.5	0.5	0.0	0.0
Δd	---	---	---	0.5
Δv	---	---	---	---
Δr	---	---	---	---
Δp	---	---	---	---
$\Delta\phi$	---	---	---	---
$\Delta\psi$	---	---	---	---
Δy	---	---	---	---
$\Delta\xi_{long}$	0.25	0.25	3.0	0.25
$\Delta\xi_{lat1}$	---	---	---	---
$\Delta\xi_{lat2}$				
$\Delta\dot{\delta}_e$	7.0	7.0	7.0	7.0
$\Delta\dot{\delta}_a$	---	---	---	---
$\Delta\dot{\delta}_r$	---	---	---	---
$(\Delta\dot{z}$ or $\Delta\dot{d})$	1.0	1.0	0.0	1.0

* units are degrees and meters

STATE* OR CONTROL	AUTOPILOT MODE		
	APR LOCI	APR LOCR	APR LOCP
$\Delta\delta$	---	---	---
$\Delta\delta_e$	0.1	0.1	0.1
$\Delta\delta_a$	0.1	0.1	0.1
Δu_r	---	---	---
Δw	---	---	---
Δq	---	---	---
$\Delta\theta$	---	---	---
Δz	---	---	---
Δd	---	---	---
Δv	0.0	0.0	0.0
Δr	11.0	11.0	11.0
Δp	0.0	0.0	0.0
$\Delta\phi$	10.0	10.0	10.0
$\Delta\psi$	14.0	11.0	14.0
Δy	0.0	0.0	0.0
$\int\Delta y_{long}$	---	---	---
$\int\Delta y_{lat1}$	2.5	1.0	1.0
$\int\Delta y_{lat2}$	0.15	2.2	2.2
$\Delta\dot\delta_e$	---	---	---
$\Delta\dot\delta_a$	7.0	7.0	7.0
$\Delta\dot\delta_r$	7.0	7.0	7.0

* units are degrees and meters

TABLE 7 (CONTINUED) SQUARE ROOT OF Q AND R DIAGONAL
WEIGHTS IN THE PIF COST FUNCTIONS

STATE* OR CONTROL	AUTOPILOT MODE	
	ROLL HOLD	HDG SEL
$\Delta\delta_e$	---	---
$\Delta\delta_a$	3.5	0.1
$\Delta\delta_r$	1.8	0.1
Δu	---	---
Δw	---	---
Δq	---	---
$\Delta\theta$	---	---
Δz	---	---
Δd	---	---
Δv	0.0	0.0
Δr	8.0	11.0
Δp	0.0	0.0
$\Delta\phi$	6.0	10.0
$\Delta\psi$	---	10.0
Δy	---	---
$\int\Delta y_{long}$	---	---
$\int\Delta y_{lat1}$	3.0	3.0
$\int\Delta y_{lat2}$	2.5	2.5
$\Delta\dot\delta_e$	---	---
$\Delta\dot\delta_a$	3.5	7.0
$\Delta\dot\delta_r$	4.0	7.0
$\Delta\dot z$	---	---

* units are degrees and meters

94

TABLE 8   OPEN- AND CLOSED-LOOP s-DOMAIN EIGENVALUES

DYNAMIC MODE	OPEN LOOP			ALT SEL (DESIGN)			ALT SEL (LOWER θ WEIGHT)		
	ω_n, rad/sec	ξ, –	τ, sec	ω_n, rad/sec	ξ, –	τ, sec	ω_n, rad/sec	ξ, –	τ, sec
SHORT PERIOD	3.0	0.78	---	3.07	0.69	---	3.07	0.77	---
PHUGOID	0.25	0.025	---	---	---	---	---	---	---
z	---	---	$-\infty$	---	---	---	---	---	---
δ_e–θ				1.58	0.99	---	1.12	0.81	---
$z \triangleq \int z$				0.25	0.77	---	0.36	0.80	---
v				---	---	24.2	---	---	24.3

DYNAMIC MODE	PITCH SEL			APR GS					
	ω_n, rad/sec	ξ, –	τ, sec	ω_n, rad/sec	ξ, –	τ, sec			
SHORT PERIOD	3.04	0.74	---	3.21	0.67	---			
PHUGOID	---	---	---	---	---	$\left(\begin{array}{c}0.74\\0.50\end{array}\right)$†			
δ_d–θ	1.35	0.91	---	---	---	---			
$d \triangleq \int d$	---	---	---	0.24	0.77	---			
v	---	---	8.3	---	---	24.2			
$\int \theta$	---	---	2.7	---	---	---			

DYNAMIC MODE	OPEN LOOP			ROLL HOLD			HDG SEL		
	ω_n, rad/sec	ξ, –	τ, sec	ω_n, rad/sec	ξ, –	τ, sec	ω_n, rad/sec	ξ, –	τ, sec
DUTCH ROLL	2.07	0.22	---	---	---	---	---	---	---
ROLL	---	---	0.16	---	---	0.16	---	---	0.16
SPIRAL	---	---	-31.0	---	---	---	---	---	---
HEADING	---	---	$-\infty$	---	---	---	---	---	---
DUTCH ROLL-δ_r				3.06	0.53	---	2.84	0.46	---
$\int \delta_r$–v				0.55	0.74	---	0.24	0.79	---
δ_a–ϕ				1.83	0.72	---	1.77	0.67	---
$\int \phi$–ψ or $\int \phi$				---	---	2.0	1.42	0.82	---

DYNAMIC MODE	APR LOCI			APR LOCR			APR LOCP		
	ω_n, rad/sec	ξ, –	τ, sec	ω_n, rad/sec	ξ, –	τ, sec	ω_n, rad/sec	ξ, –	τ, sec
DUTCH ROLL-δ_r	2.9	0.47	---	2.84	0.48	---	2.9	0.47	---
ROLL	---	---	0.16	---	---	0.16	---	---	0.16
$\int$y–v	0.29	0.58	---	0.36	0.56	---	0.35	0.61	---
δ_a–ϕ	1.73	0.69	---	1.72	0.69	---	1.77	0.69	---
ψ	---	---	1.05	(0.60	0.99)§		---	---	1.07
y	---	---	2.00				---	---	3.08
$\int \phi$	---	---	5.9	---	---	5.6	---	---	6.04

† The mode split into two real roots.
§ The roots combined to form a complex pair.

TABLE 9 ELEVATOR CONTROL GAINS FOR THE LONGITUDINAL AUTOPILOTS

STATE*	AUTOPILOT MODES			
	ALT SEL (DESIGN)	ALT SEL (LOWER θ WEIGHT)	PITCH SEL	APR GS
v_e	0.719	0.79	0.753	0.704
v_a	----	----	----	----
v_r	----	----	----	----
v_T	-0.025	-0.018	-0.00928	-0.027
a_z	-0.021	-0.015	-0.011	-0.022
q	-0.428	-0.28	-0.294	-0.466
θ	-2.2	-1.48	-1.42	-2.34
z	0.0139	0.012	0.0	0.0
a_y	----	----	----	----
r	----	----	----	----
p	----	----	----	----
ϕ	----	----	----	----
ψ	----	----	----	----
d	----	----	----	-0.0144
y	----	----	----	----
ξ_{long}	0.000176	0.000183	-0.038	-0.000175
ξ_{lat1}	----	----	----	----
ξ_{lat2}	----	----	----	----
u_{mlong}	-0.0491	-0.029	1.08	2.49
u_{mlat1}	----	----	----	----
u_{mlat2}	----	----	----	----

* units are radians and meters

TABLE 10   CONTROL GAINS FOR THE ROLL SEL AND HDG SEL AUTOPILOTS

STATE*	AUTOPILOT MODES			
	AILERON		RUDDER	
	ROLL SEL	HDG SEL	ROLL SEL	HDG SEL
$\ddot{v}_e$	---	---	---	---
v_a	0.65	0.69	0.021	0.061
v_r	0.020	0.063	0.76	0.715
v_T	---	---	---	---
a_z	---	---	---	---
q	---	---	---	---
θ	---	---	---	---
z	---	---	---	---
a_y	-0.053	0.012	0.178	0.537
r	-0.126	0.25	-0.74	-2.0
p	-0.31	-0.26	0.011	0.087
ϕ	-2.16	-1.51	-0.53	-0.44
ψ	---	0.50	---	-5.9
d	---	---	---	---
y	---	---	---	---
y_{long}	---	---	---	---
y_{lat1}	-0.068	-0.014	-0.022	0.032
y_{lat2}	0.019	0.028	-0.512	0.013
u_{mlong}	---	---	---	---
u_{mlat1}	1.5	1.15	0.67	1.28
u_{mlat2}	-0.35	-1.19	0.81	-0.59

* units are radians and meters

TABLE 11 AILERON CONTROL GAINS FOR THE APPROACH AUTOPILOTS

STATE*	AUTOPILOT MODE		
	APR LOCI	APR LOCR	APR LOCP
v_e	---	---	---
v_a	0.69	0.69	0.69
v_r	0.032	0.048	0.074
V_T	---	---	---
a_z	---	---	---
q	---	---	---
θ	---	---	---
z	---	---	---
a_y	0.18	0.278	0.39
r	-0.26	-0.356	-0.38
p	-0.25	-0.245	-0.25
ϕ	-1.60	-1.55	-1.54
ψ	-2.15	-2.95	-4.19
d	---	---	---
y	-0.019	-0.014	-0.026
ξ_{long}	---	---	---
ξ_{lat1}	-0.021	0.000798	0.0075
ξ_{lat2}	-0.00026	0.0269	0.0012
u_{long}	---	---	---
u_{lat1}	1.57	1.74	-1.25
u_{mlat2}	0.0	-1.53	2.05

* units are radians and meters

98

TABLE 12   RUDDER CONTROL GAINS FOR THE APPROACH AUTOPILOTS

STATE*	AUTOPILOT MODE		
	APR LOCI	APR LOCR	APR LOCP
v_e	---	---	---
v_a	0.000277	-0.000674	-0.00068
v_r	0.827	0.821	0.824
V_T	---	---	---
a_z	---	---	---
q	---	---	---
θ	---	---	---
z	---	---	---
a_y	0.73	0.706	0.67
r	-1.22	-1.24	-1.18
p	-0.027	-0.021	-0.027
ϕ	-0.61	-0.66	-0.65
ψ	-5.54	-5.54	-5.45
d	---	---	---
y	-0.0224	-0.031	-0.028
y_{long}	---	---	---
y_{lat1}	0.0227	0.0123	0.00967
y_{lat2}	-0.000237	-0.00171	-0.000947
u_{mlong}	---	---	---
u_{mlat1}	1.41	1.59	1.16
u_{mlat2}	0.0	0.310	1.72

* units are radians and meters

TABLE 13 S_{11} MATRIX ELEMENTS FOR THE PIF AUTOPILOT MODES

ALT SEL

$$\begin{bmatrix} 0 \\ 0 \\ 0 \\ 0 \\ 1.0 \end{bmatrix}$$

PITCH SEL

$$\begin{bmatrix} 0 \\ 0 \\ 0 \\ 1.0 \end{bmatrix}$$

APR GS

$$\begin{bmatrix} 0 \\ 0 \\ 0 \\ 0 \\ 1.0 \end{bmatrix}$$

ROLL SEL

$$\begin{bmatrix} 0 & 0 \\ 0 & 0 \\ 0 & 0 \\ 1.0 & 0 \end{bmatrix}$$

HDG SEL

$$\begin{bmatrix} 0 \\ 0 \\ 0 \\ 0 \\ 1.0 \end{bmatrix}$$

APR LOCI

$$\begin{bmatrix} 0 & 0 \\ 0 & 0 \\ 0 & 0 \\ 0 & 0 \\ 0 & 1.0 \\ 1.0 & 0 \end{bmatrix}$$

APR LOCR

$$\begin{bmatrix} 0 & 0 \\ 0 & 0 \\ 0 & 0 \\ 0 & 0 \\ 0 & 1.0 \\ 1.0 & 0.31 \end{bmatrix}$$

APR LOCP

$$\begin{bmatrix} 0 & 0 \\ 0 & 0 \\ 0 & 0 \\ 0 & 0 \\ 0 & 1.0 \\ 1.0 & 0 \end{bmatrix}$$

TABLE 14 NAVION AIRPLANE PARAMETERS

Wing area, A	–	17.112 m^2 (184 ft^2)
Mean Aerodynamic Chord, $\bar{c}$	–	1.74 m (5.7 ft)
Wing Span, b	–	10.17 m (33.38 ft)
Gross Mass, WT	–	1540.6 kg (3400 lb)
I_X	–	1742.33 kg-m^2 (1284.08 slug-ft^2)
I_Y	–	3762.4 kg-m^2 (2772.86 slug-ft^2)
I_Z	–	4389.1 kg-m^2 (3234.72 slug-ft^2)
I_{XZ}	–	0.0
Control Surface		Deflection, deg
Flaps	–	0 to -40
Elevator	–	-19 to 29
Aileron	–	-18 to 19
Rudder	–	-20 to 25

TABLE 15   FLIGHT CONDITIONS FOR AERODYNAMIC DATA

	Ref. 31, Condition I	Ref. 31, Condition II	Ref. 38,
Altitude	1524.0 m (5000 ft)	1524.0 m (5000 ft)	1980.0 m (6500 ft)
Velocity (true airspeed)	73.2 m/sec (2400 ft/sec)	44.0 m/sec (144.0 ft/sec)	54.0 m/sec (176.0 ft/sec)
Flaps	0 deg	20 deg	10 deg

TABLE 16 LONGITUDINAL AERODYNAMIC PARAMETERS

Parameter	Condition I, Ref. 31	Condition II, Ref. 31 Design Values	Ref. 38 Analog Match
$C_{X\alpha}$	0.262	-1.37	---
$C_{X\dot{\alpha}}$	-4.33	-4.86	-4.6
C_{Zq}	-15.9	-27.13	0.0
$C_{Z\delta_e}$	0.511	0.52	0.29
$C_{M\dot{\alpha}}$	-0.77	-0.84	0.0
$C_{M\alpha}$	-6.5	-6.0	-0.64
C_{Mq}	-18.1	-16.4	-14.4
$C_{M\delta_e}$	1.42	1.55	0.96
θ_o	0.0055 rad	0.105 rad	0.036 rad
q_o	0.0 rad	0.0 rad	0.0 rad
w_o	0.4 m/sec(1.3 ft/sec)	4.6 m/sec(15.2 ft/sec)	1.1 m/sec (3.7 ft/sec)
u_o	73 m/sec(240.0 ft/sec)	44 m/sec(144.1 ft/sec)	55 m/sec (185 ft/sec)
α_o	0.0055 rad	0.105 rad	0.02 rad
C_{Xo}	0.0015	0.0015	---
C_{Zo}	-0.27	-0.75	---
C_{Mo}	0.0	0.0	---
$C_{X\delta_T}$	0.0061	0.0061	---
g	9.8 m/sec^2	9.8 m/sec^2	9.8 m/sec^2
ρ	0.00912 kg/m^3 (0.00205 slugs/ft^3)	0.00912 kg/m^3 (0.00205 slugs/ft^3)	0.00912 kg/m^3 (0.00205 slugs/ft^3)

TABLE 17   LATERAL AERODYNAMIC PARAMETERS

Parameter	Condition I, Ref. 31	Condition II, Ref. 31 Design Values	Ref. 38 Analog Match
C_{Yp}	0.0	0.0	0.0
C_{Yr}	0.0	0.0	0.0
$C_{Y\beta}$	-0.6	-0.74	-0.92
$C^*_{Y\delta_r}$	-0.33	-0.143	-0.21
$C^*_{L\delta_r}$	-0.026	-0.023	-0.025
$C_{L\beta}$	-0.07	-0.053	-0.086
C_{Lp}	-0.49	-0.53	-0.52
C_{Lr}	0.11	0.114	0.093
$C_{L\delta_a}$	0.154	0.16	0.16
$C_{L\delta_r}$	0.0	0.0	-0.025
$C_{N\beta}$	0.073	0.080	0.103
C_{Np}	-0.04	-0.147	-0.049
C_{Nr}	-0.09	-0.12	-0.11
$C_{N\delta_a}$	-0.004	-0.0015	-0.0039
$C_{N\delta_r}$	0.063	0.075	0.11
v_o	0.0 m/sec	0.0 m/sec	0.0 m/sec
r_o	0.0 rad	0.0 rad	0.0 rad
p_o	0.0 rad	0.0 rad	0.0 rad
ϕ_o	0.0 rad	0.0 rad	0.0 rad
ψ_o	0.0 rad	0.0 rad	0.0 rad
C_{Yo}	0.0	0.0	0.0
C_{Lo}	0.0	0.0	0.0
C_{No}	0.0	0.0	0.0

* different from Ref. 31 value.

WALLOPS FLIGHT CENTER FACILITIES
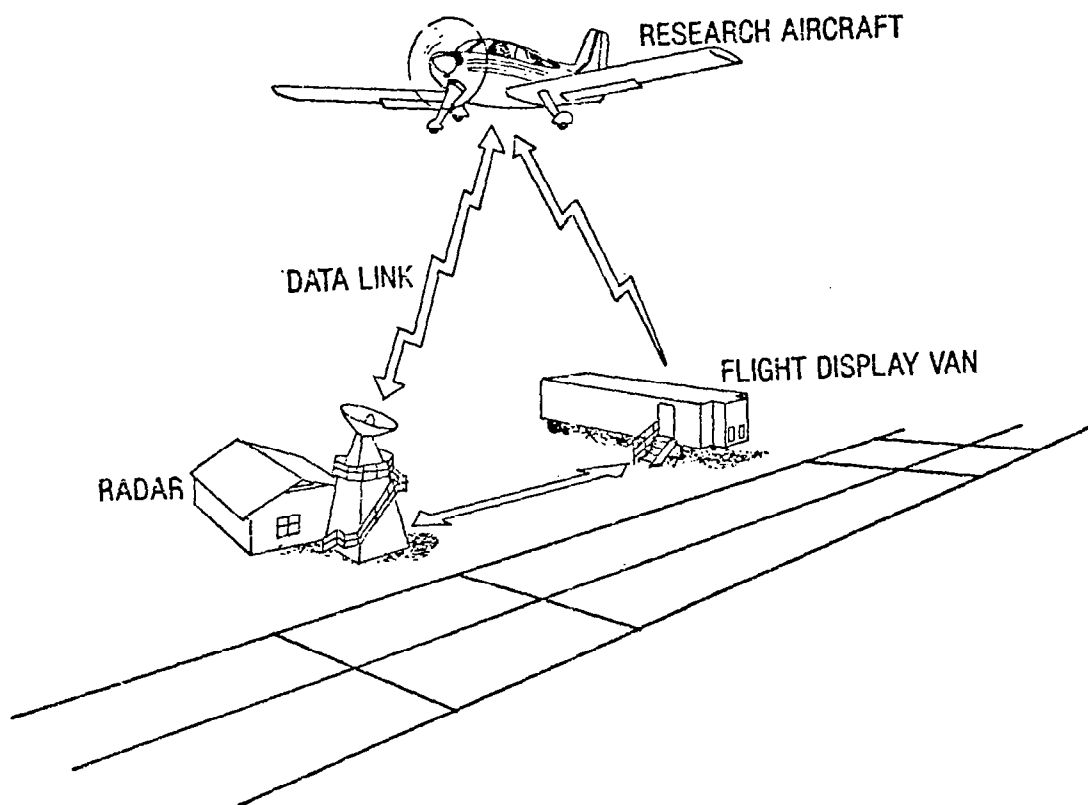
FIGURE 1 WALLOPS FLIGHT TEST FACILITIES
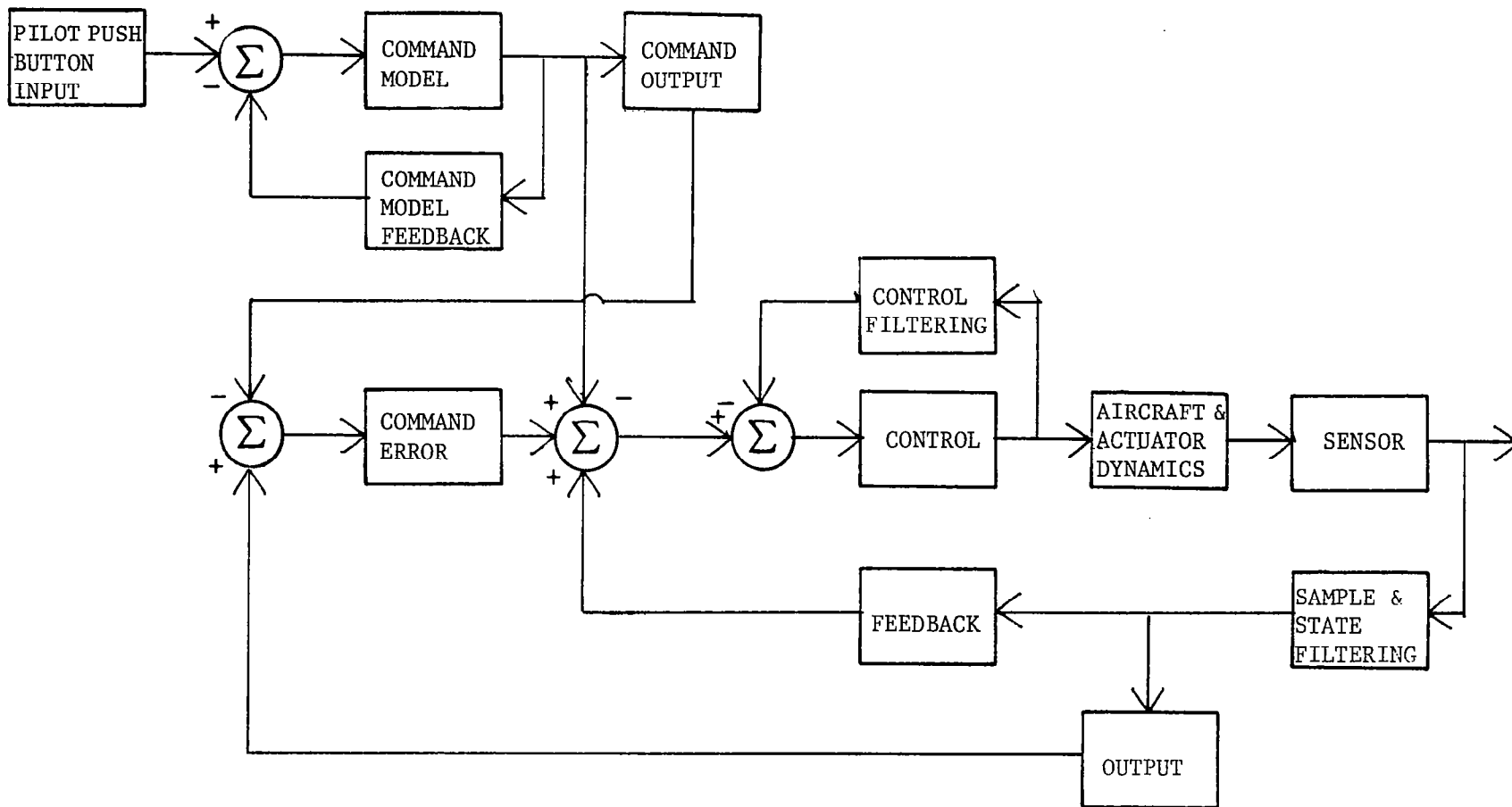
FIGURE 2 BASIC PIF CONTROL LAW
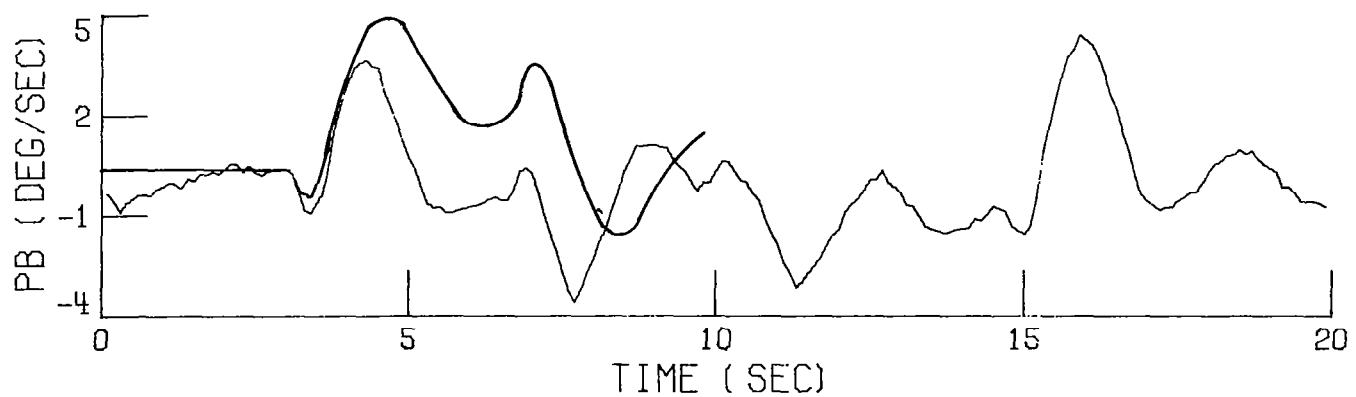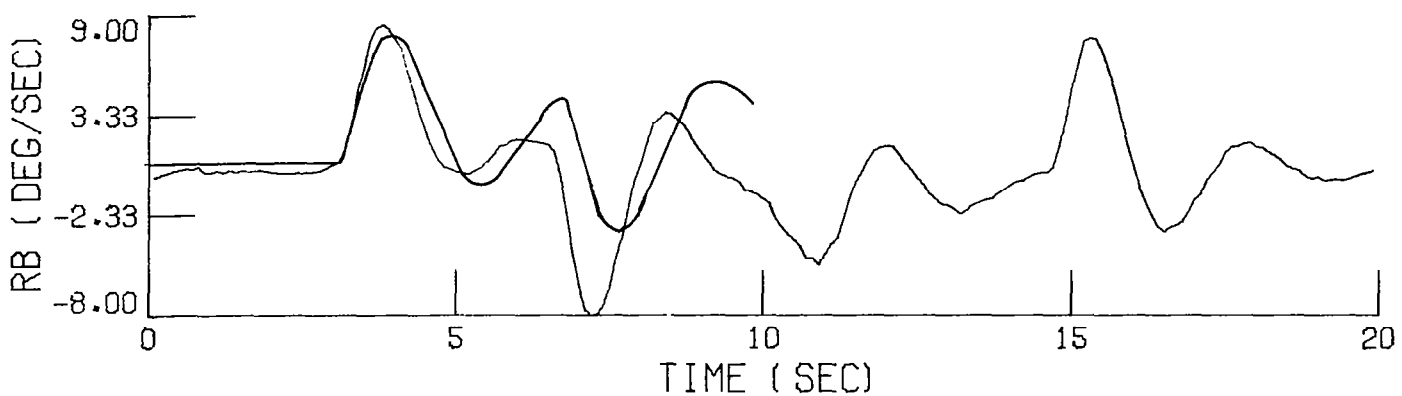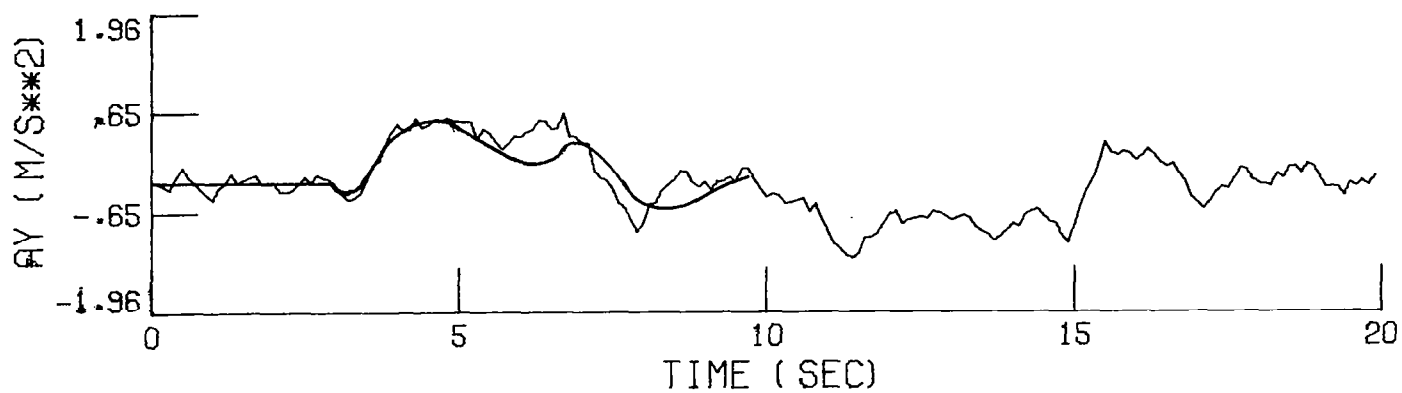
FIGURE 3   COMPARISON OF OPEN-LOOP LINEAR MODEL RESPONSE
WITH AIRCRAFT RESPONSE FOR A COMMAND IN RUDDER
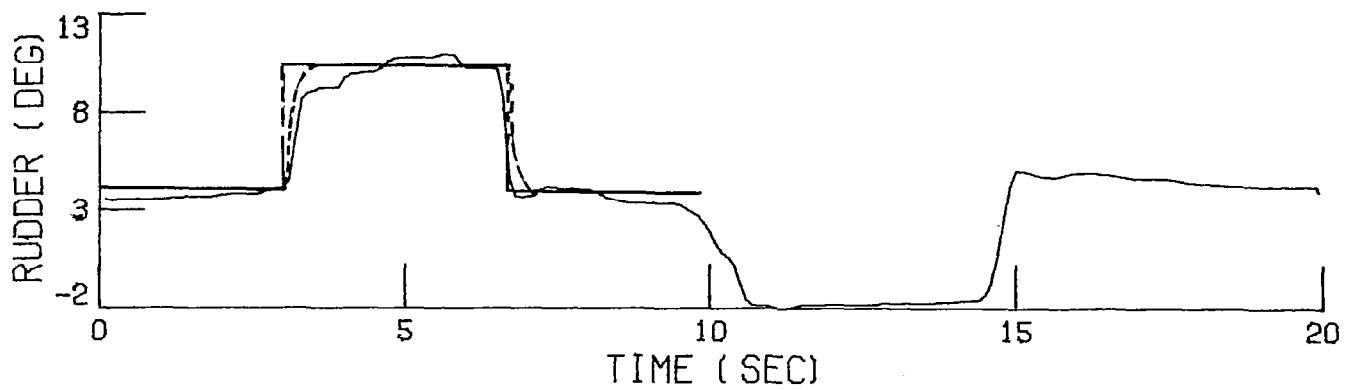
FIGURE 3   (CONTINUED) Comparison of Open-Loop Linear Model
Response with Aircraft Response for a Command in Rudder
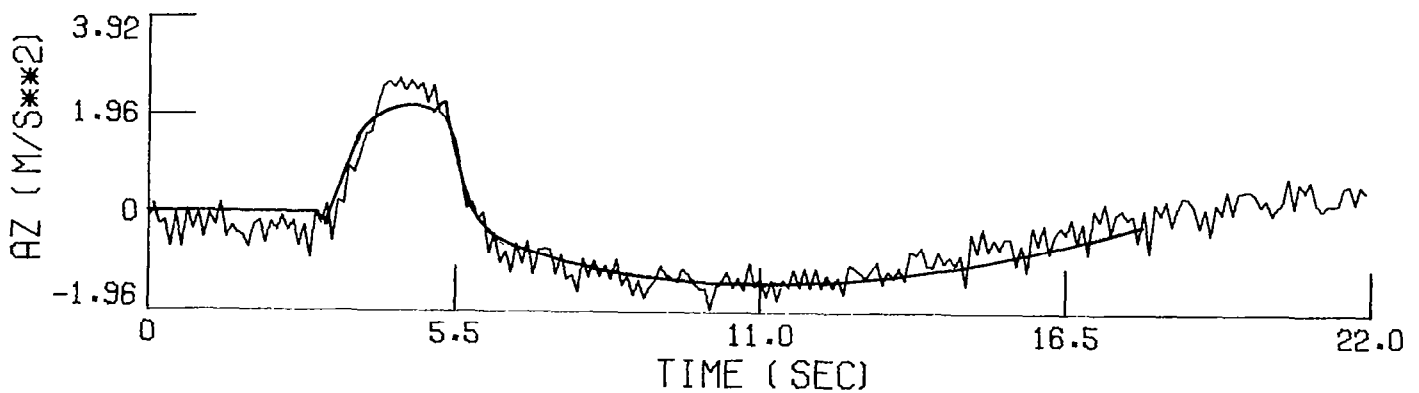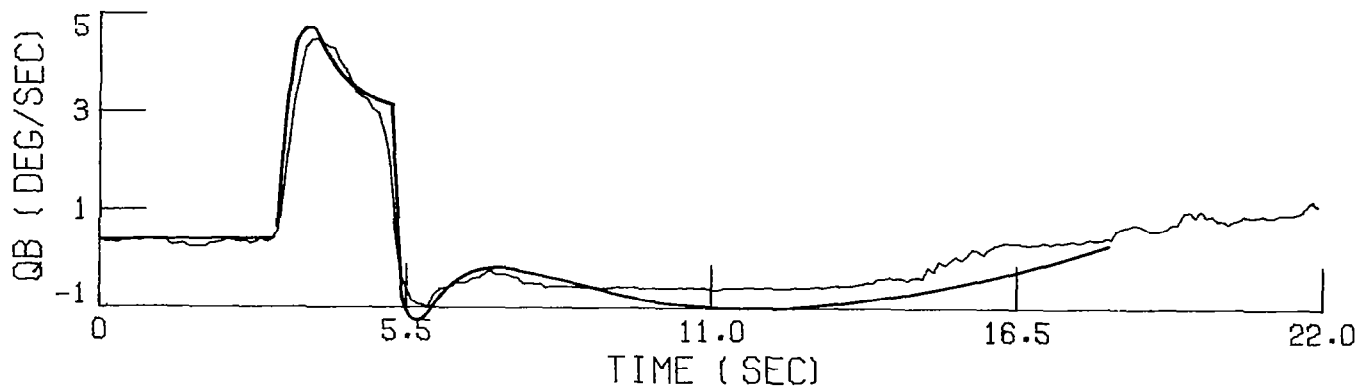
FIGURE 4   COMPARISON OF OPEN-LOOP LINEAR MODEL RESPONSE
WITH AIRCRAFT RESPONSE FOR A COMMAND IN ELEVATOR
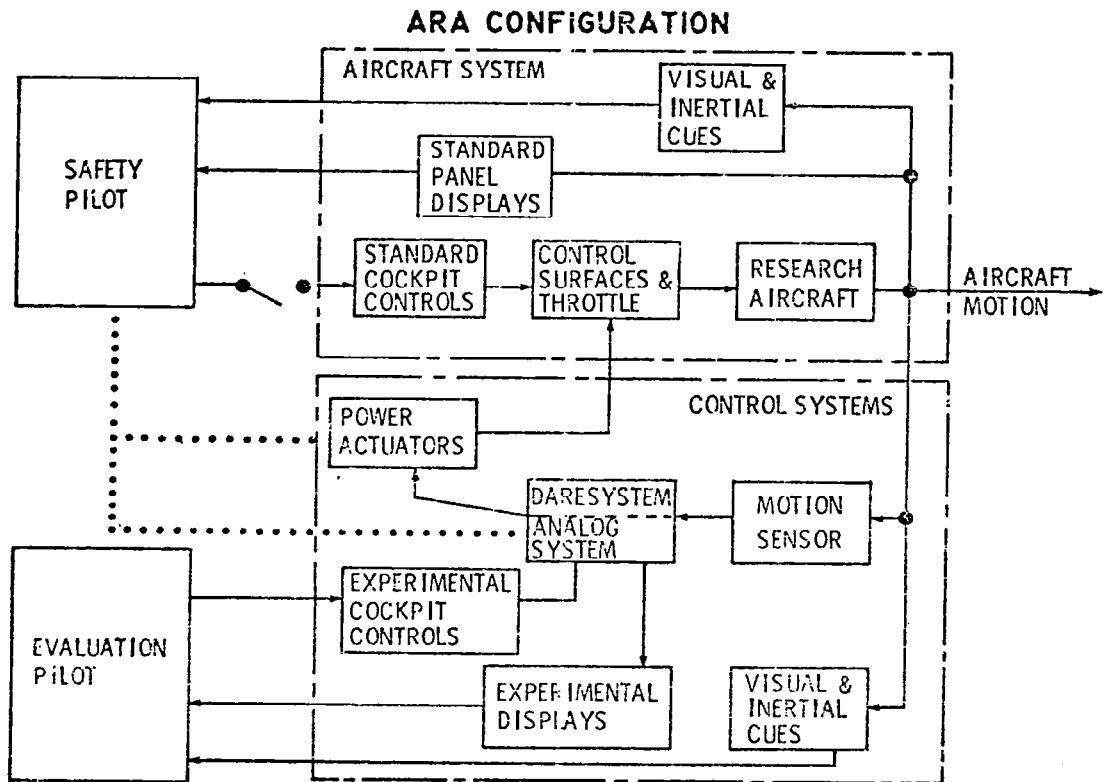
ARA CONFIGURATION

FIGURE 5   ARA CONFIGURATION

AVIONICS RESEARCH AIRCRAFT CONTROL/DISPLAY PANEL
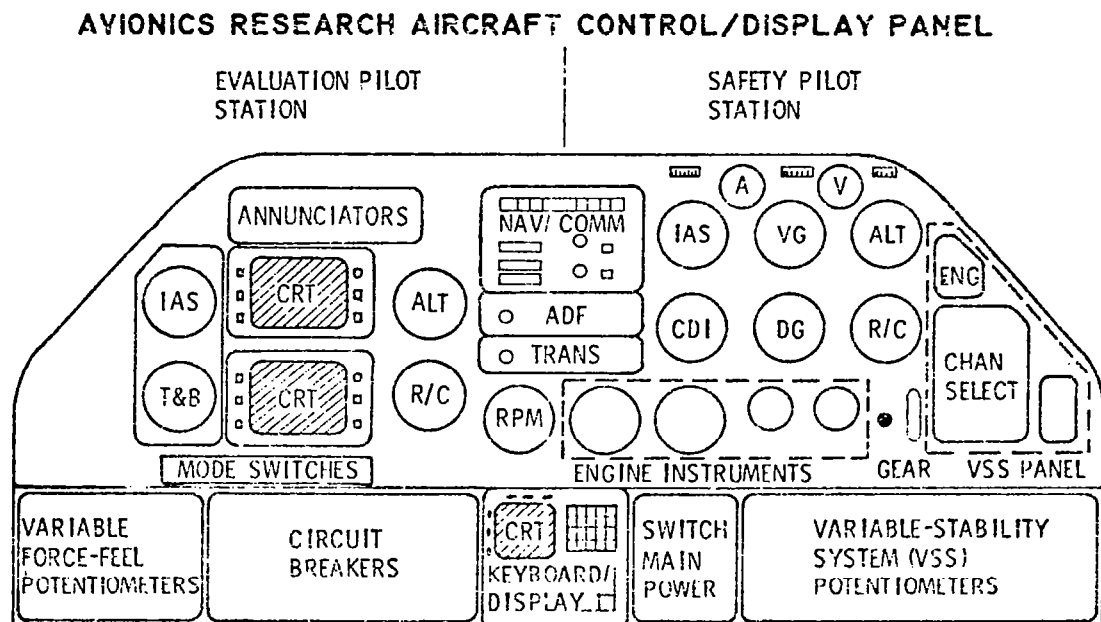
FIGURE 6   AVIONICS RESEARCH AIRCRAFT CONTROL/DISPLAY PANEL
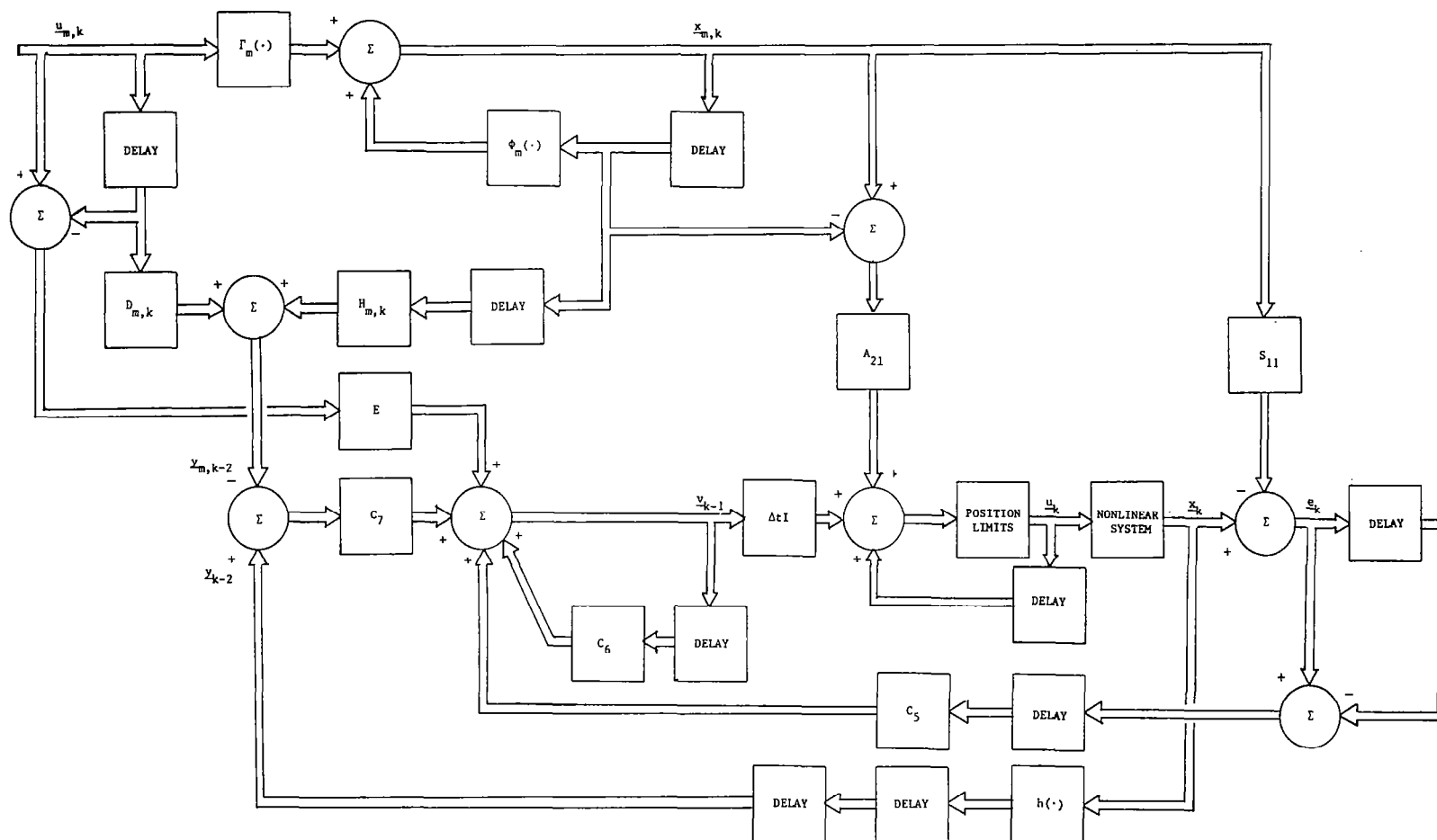
FIGURE 7 DETAILED PIF CONTROL LAW BLOCK DIAGRAM
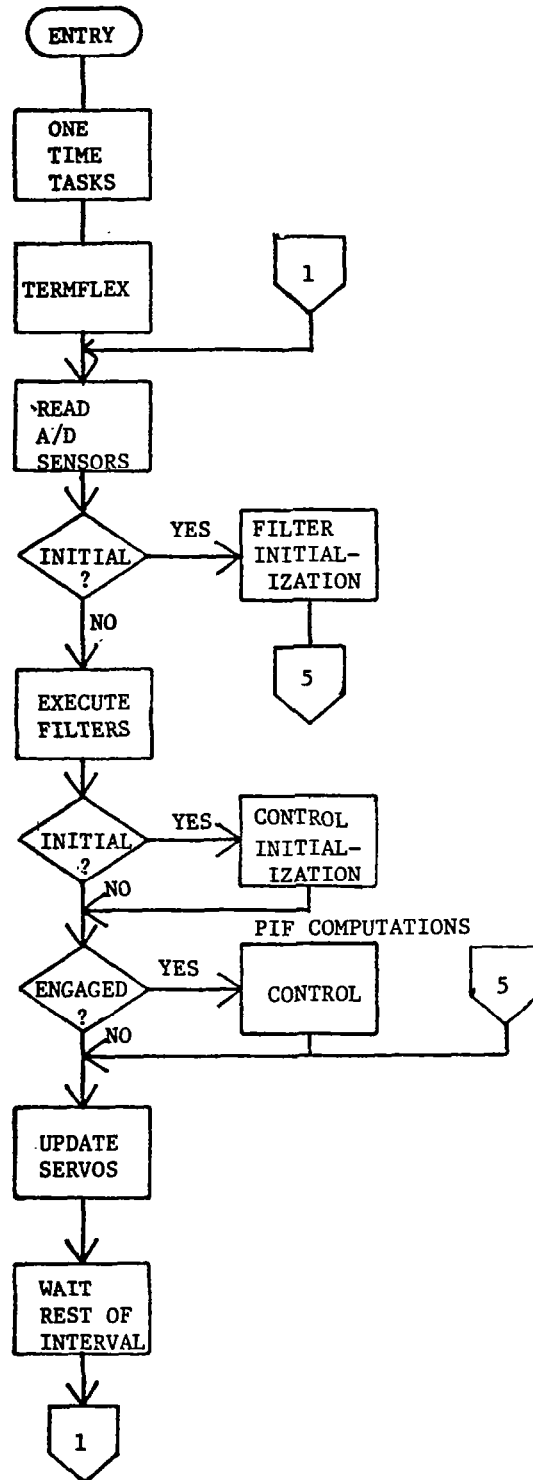
FIGURE 8   FLOW DIAGRAM FOR THE MAIN EXECUTIVE
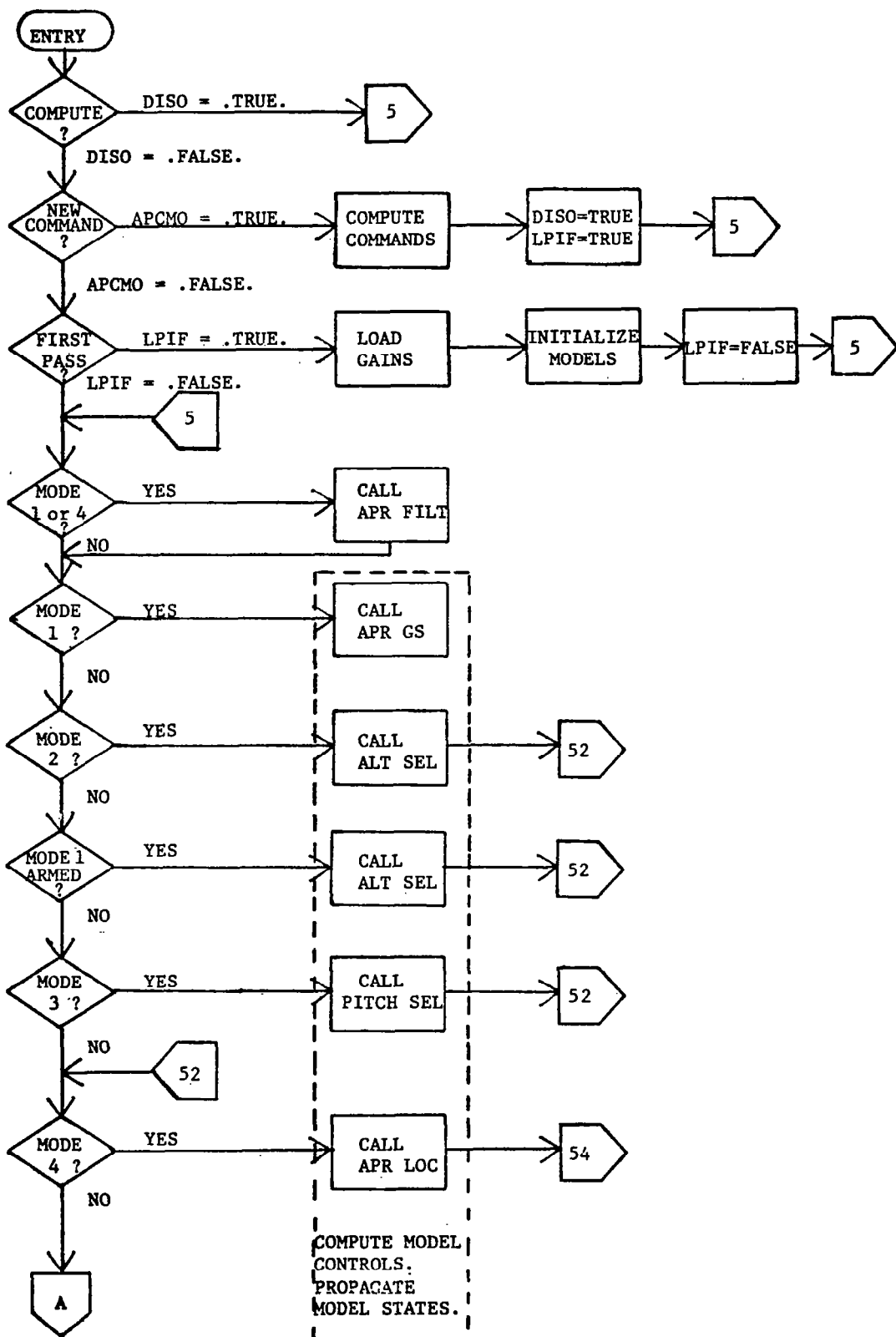
FIGURE 9   FLOW DIAGRAM FOR THE SUBROUTINE CONTROL
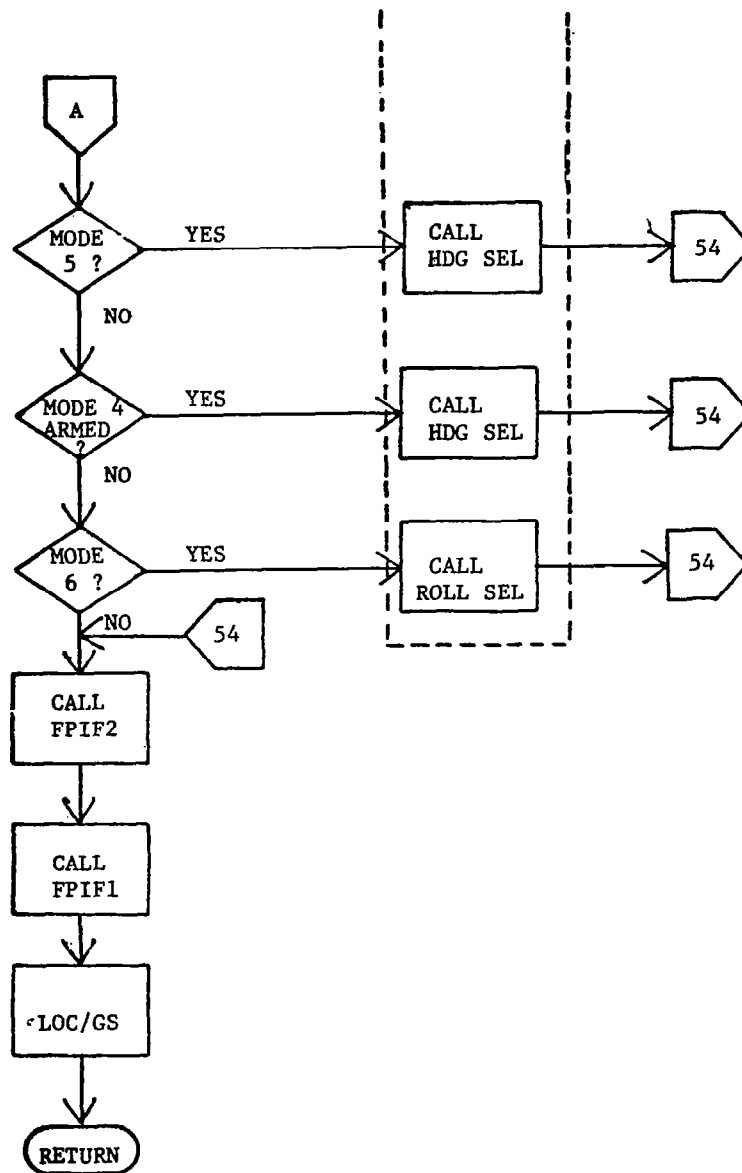
FIGURE 9 (CONTINUED)   FLOW DIAGRAM FOR THE SUBROUTINE CONTROL
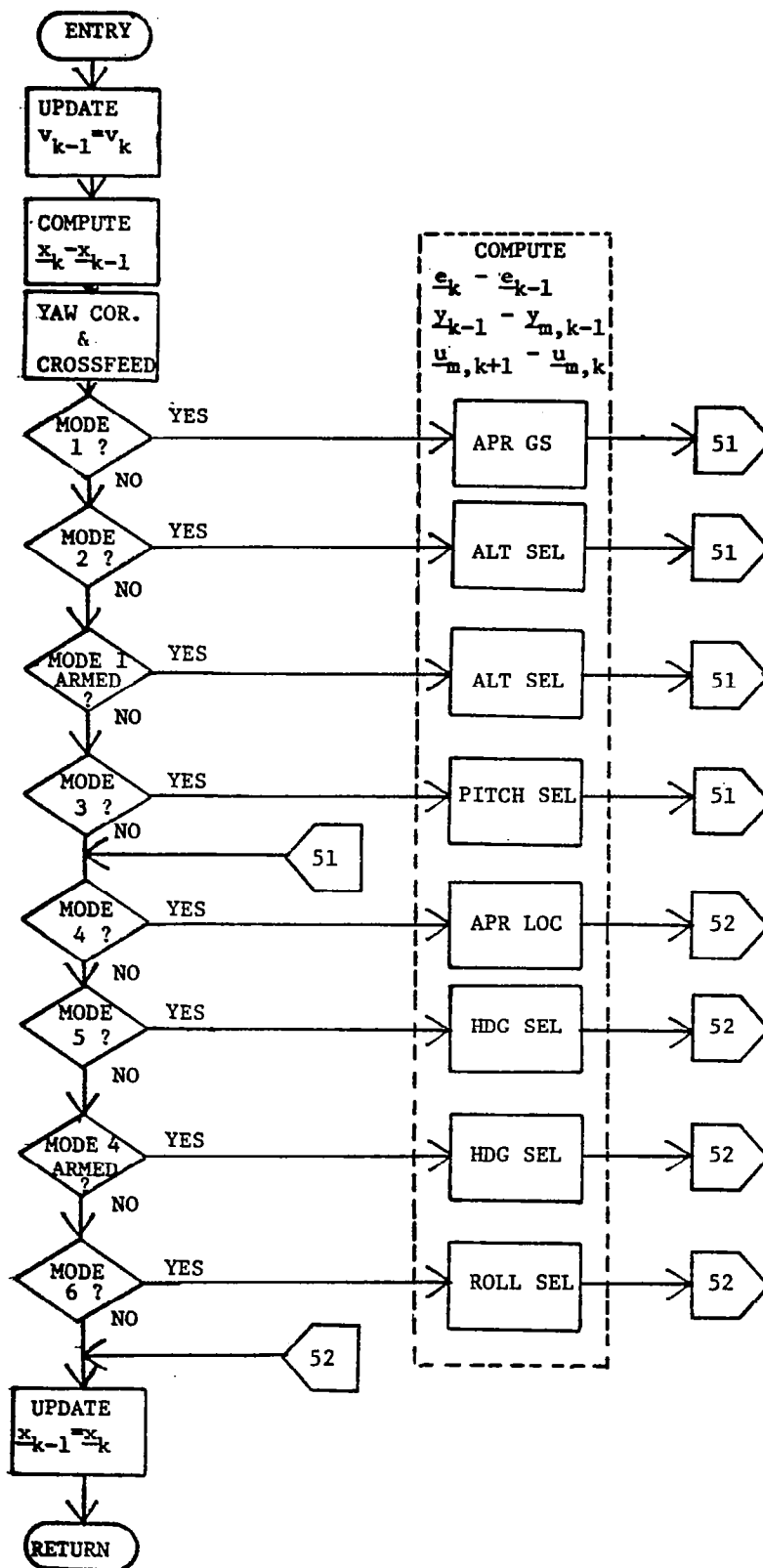
FIGURE 10   FLOW DIAGRAM FOR THE SUBROUTINE FPIF2
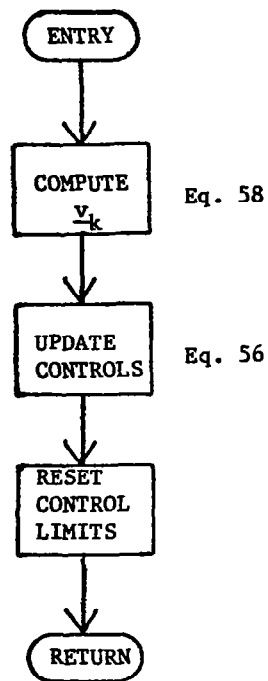
FIGURE 11   FLOW DIAGRAM FOR THE SUBROUTINE FPIF1
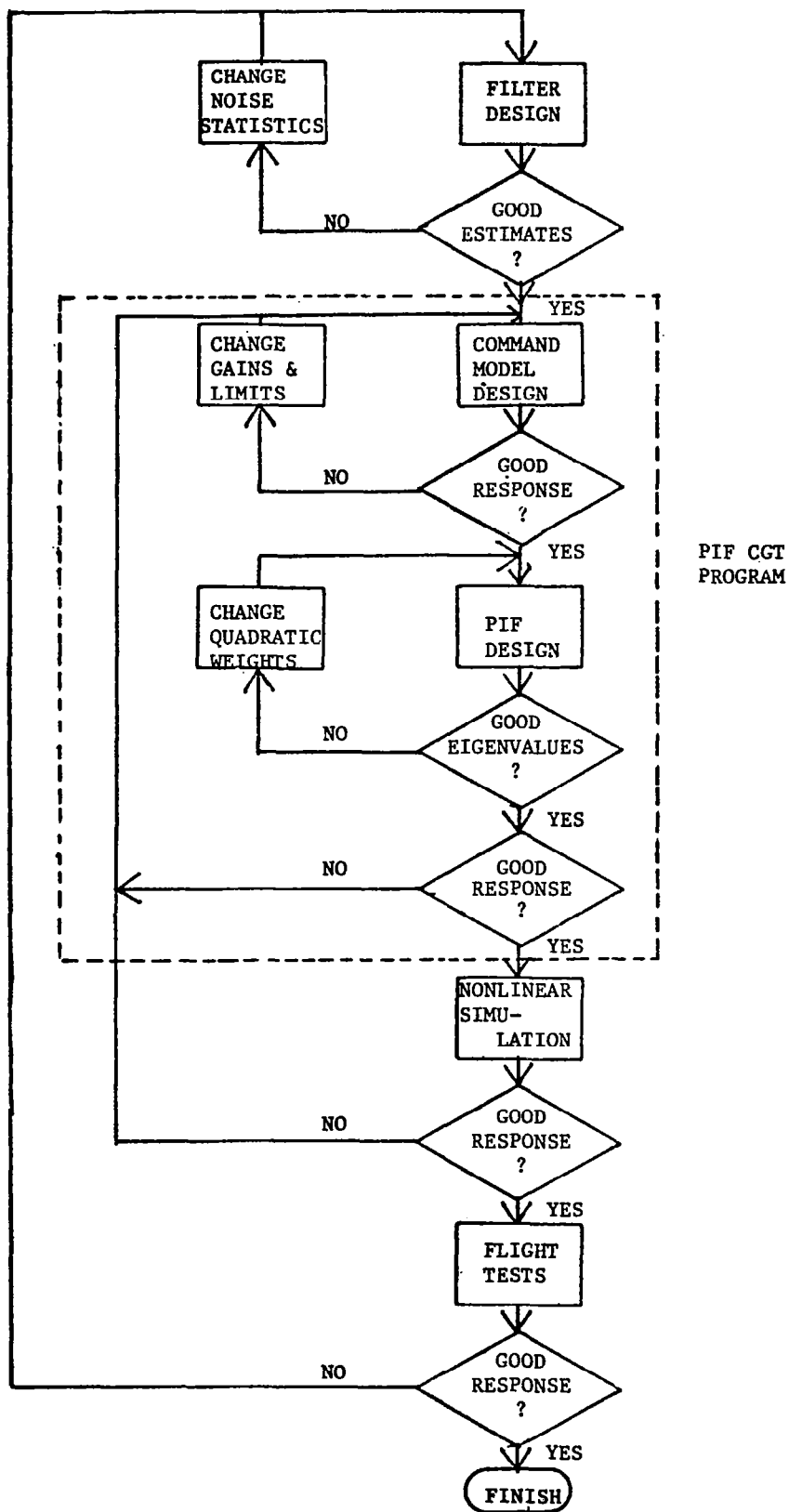
FIGURE 12   PIF DESIGN SEQUENCE
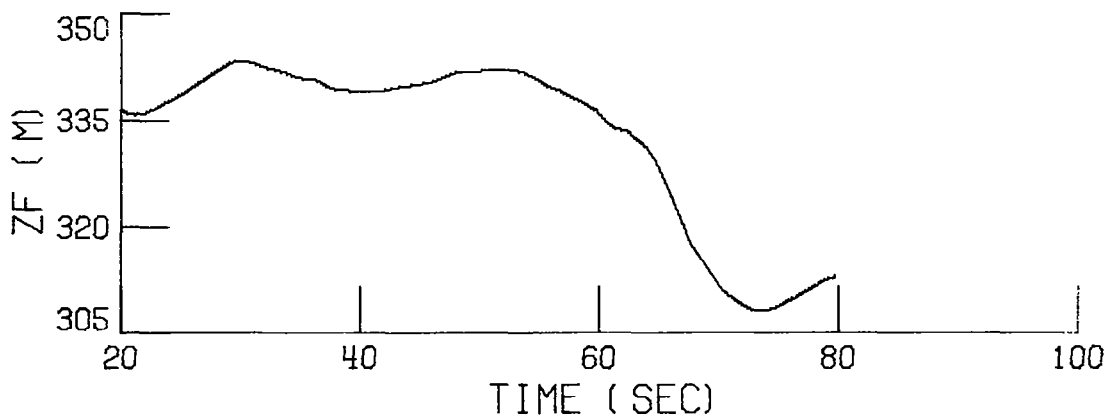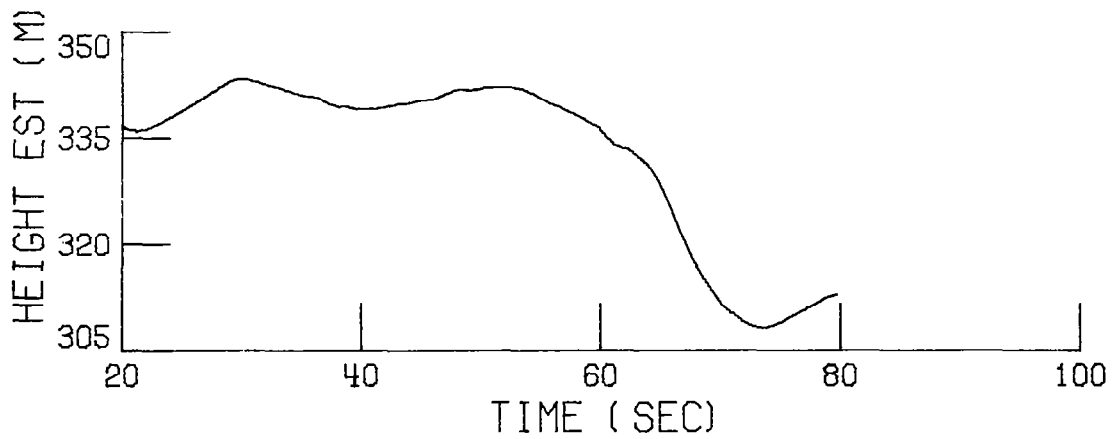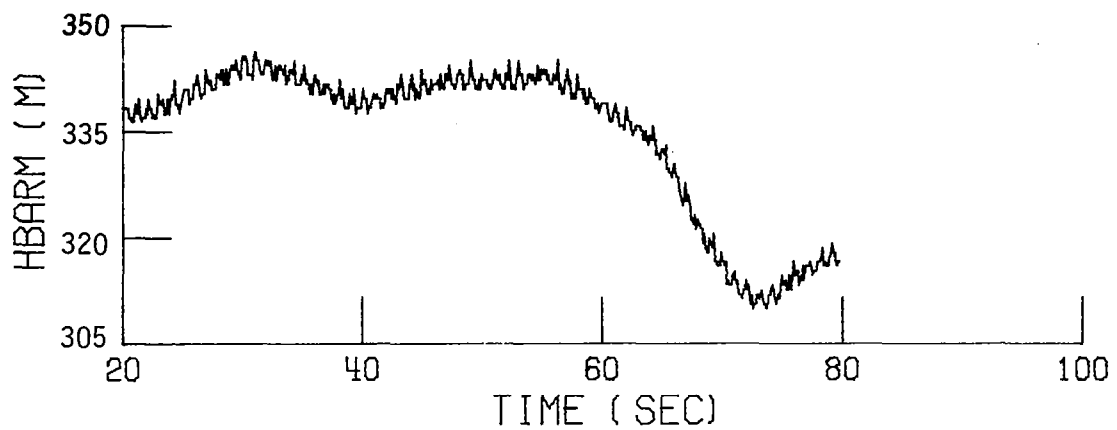
FIGURE 13 A COMPARISON OF THE BAROMETRIC ALTIMETER OUTPUT, HBARM,
THE COMPLEMENTARY FILTER HEIGHT ESTIMATE, HEIGHT EST,
AND THE RADAR COMPLEMENTARY FILTER HEIGHT ESTIMATE, ZF

116
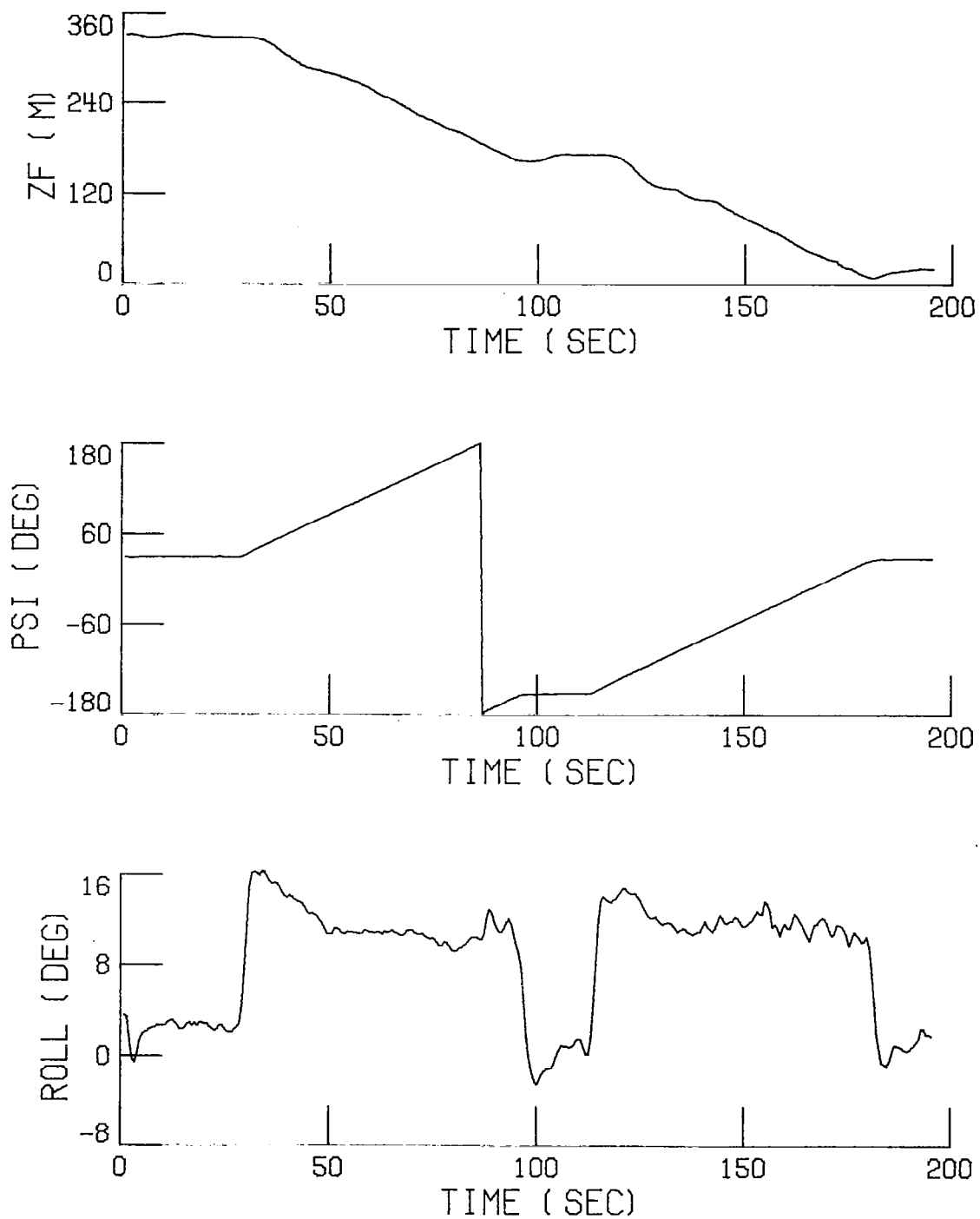
FIGURE 14   SPIRAL DESCENTS USING THE HDG SEL AND ALT SEL PIF
           AUTOPILOTS
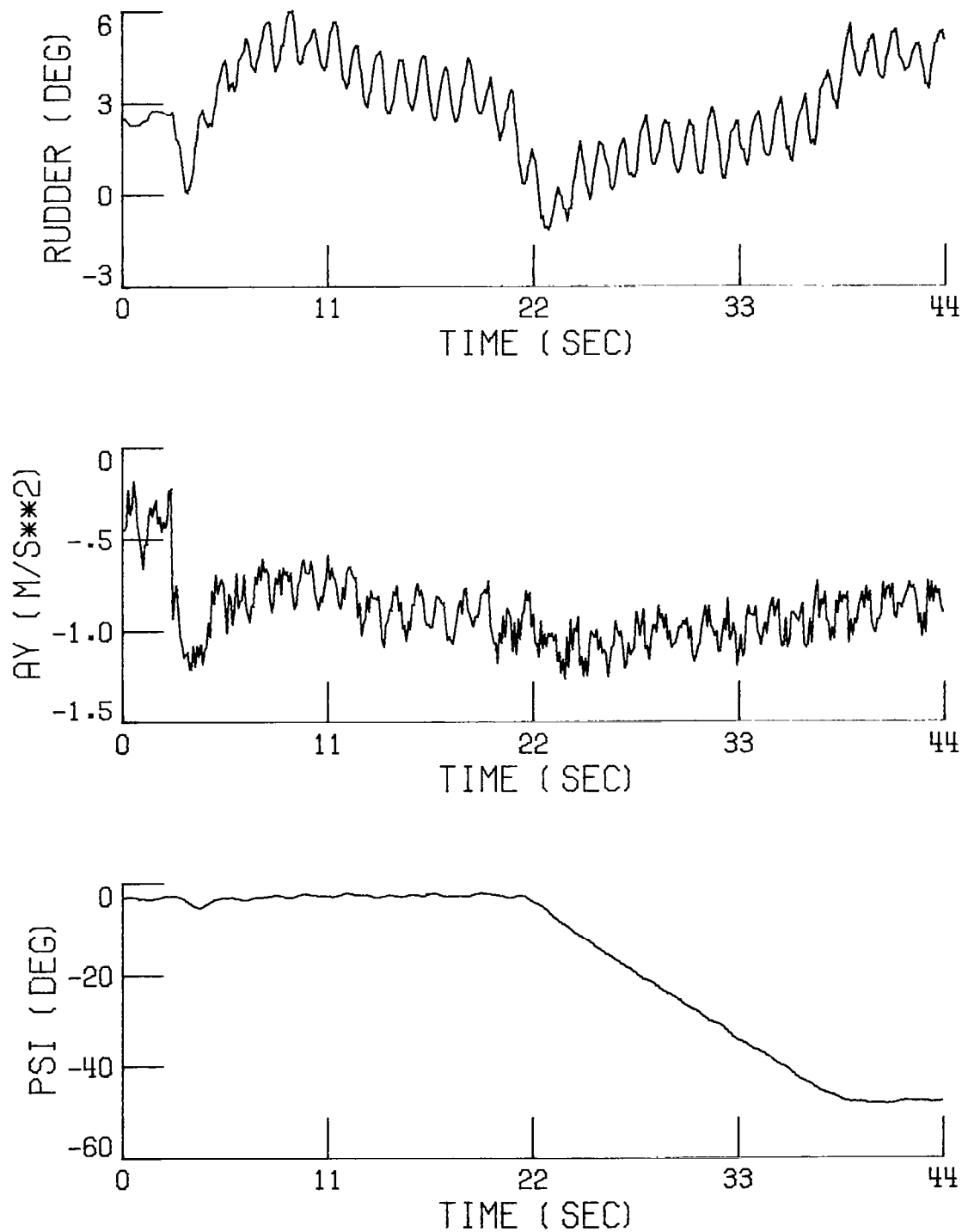
FIGURE 15   A 45 DEG HEADING CHANGE USING THE HDG SEL AUTOPILOT
AND AN a_y PREFILTER WITH A 0.01 SEC TIME CONSTANT

SAFETY PILOT PULSED RUDDER PEDAL
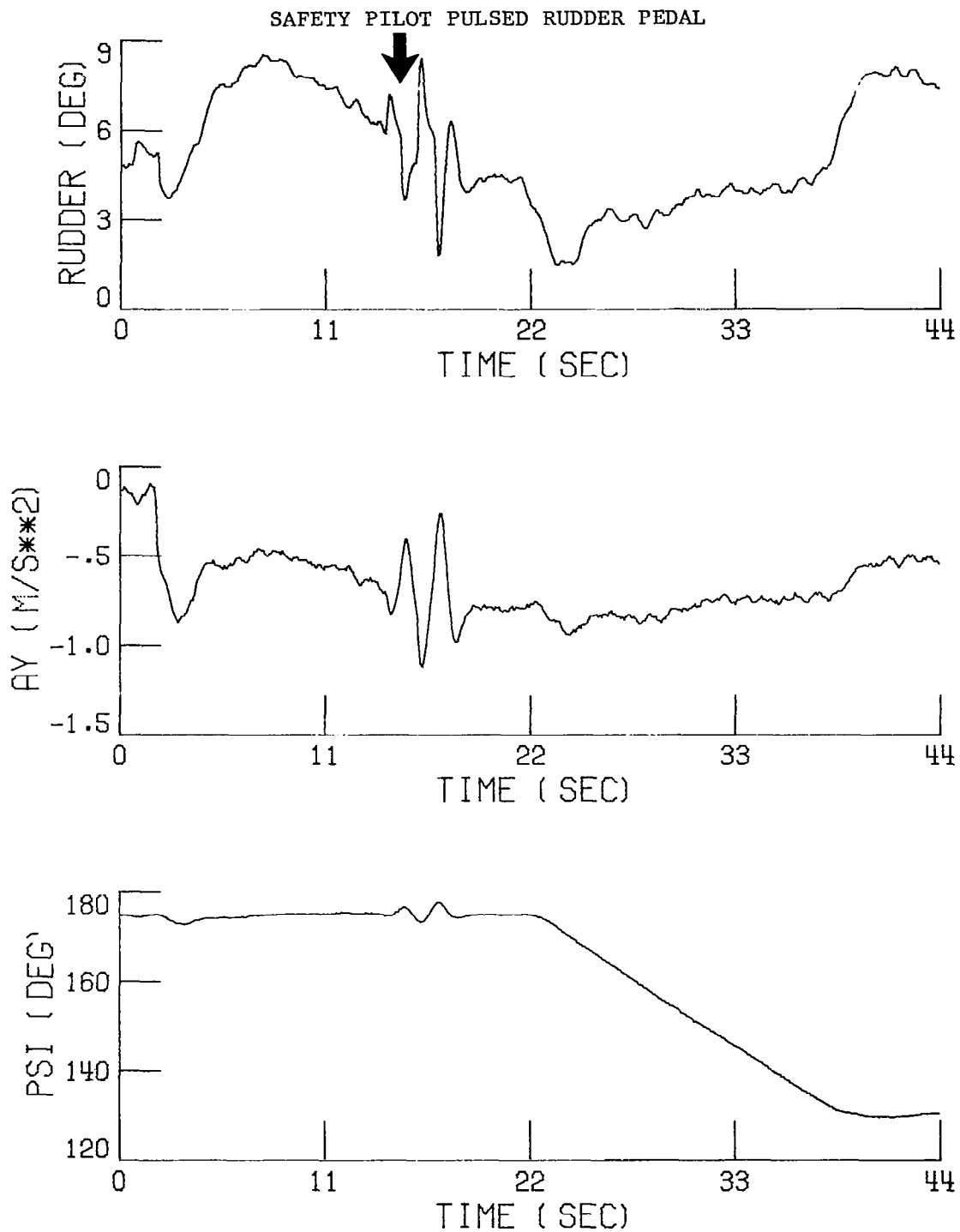
FIGURE 16   A 45 DEG HEADING CHANGE USING THE HDG SEL AUTOPILOT
AND AN a_y PREFILTER WITH A 0.10 SEC TIME CONSTANT
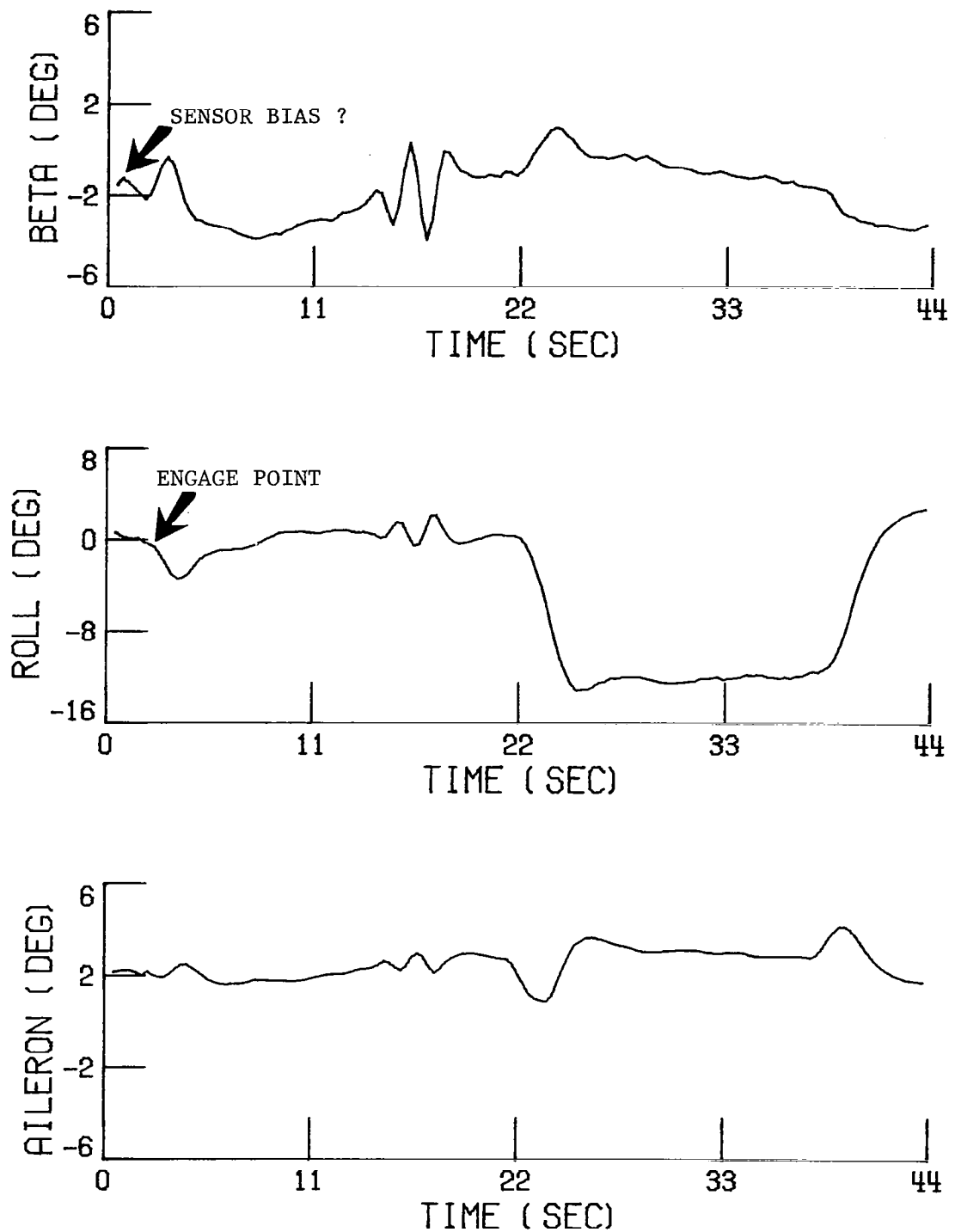
FIGURE 16 (CONTINUED)   A 45 DEG HEADING CHANGE USING THE HDG SEL
                        AUTOPILOT AND AN a_y PREFILTER WITH A 0.10 SEC
                        TIME CONSTANT

SAFETY PILOT PULSED RUDDER PEDAL
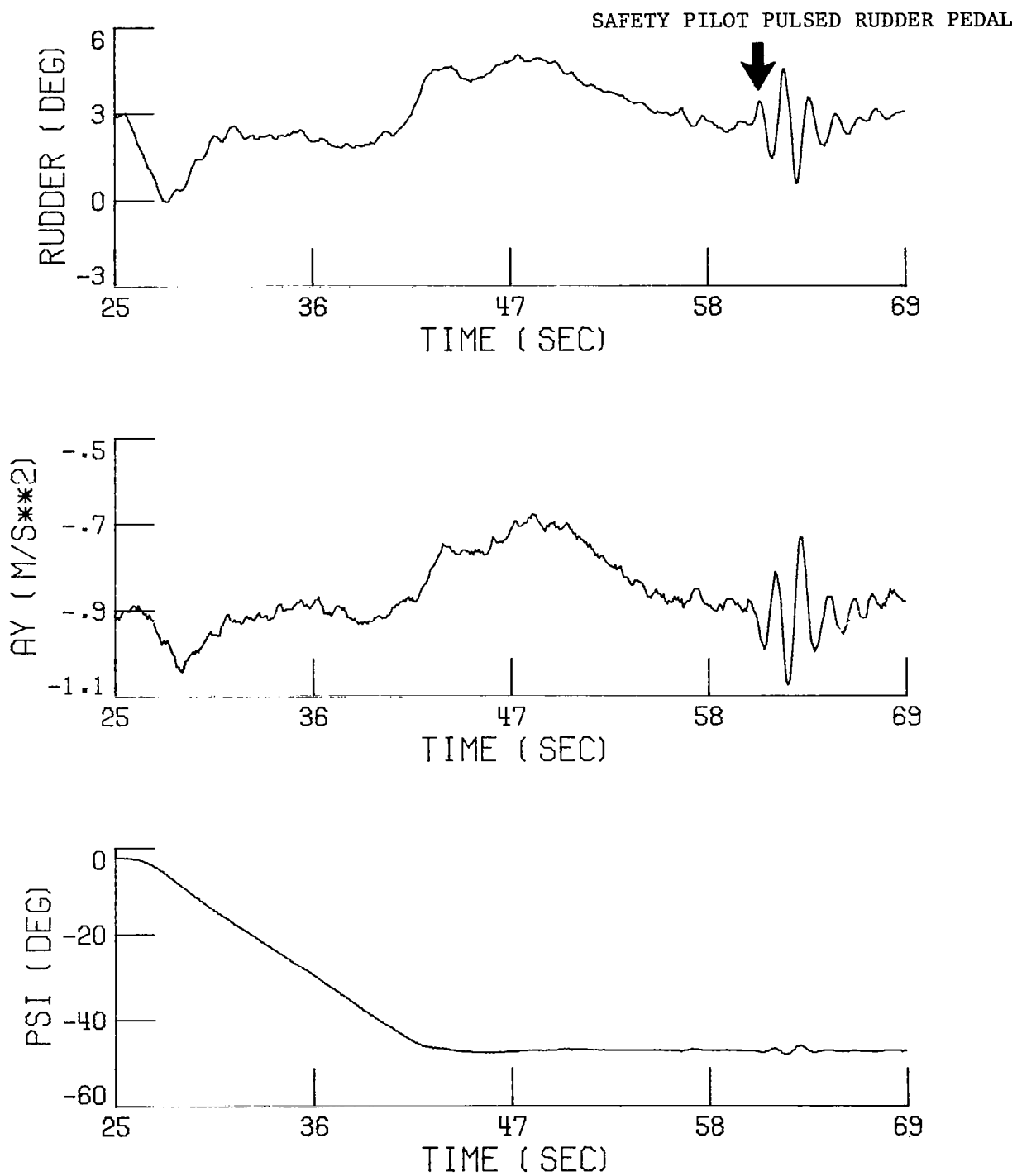
FIGURE 17   A 45 DEG HEADING CHANGE USING THE HDG SEL AUTOPILOT
AND AN a_y PREFILTER WITH A 0.22 SEC TIME CONSTANT
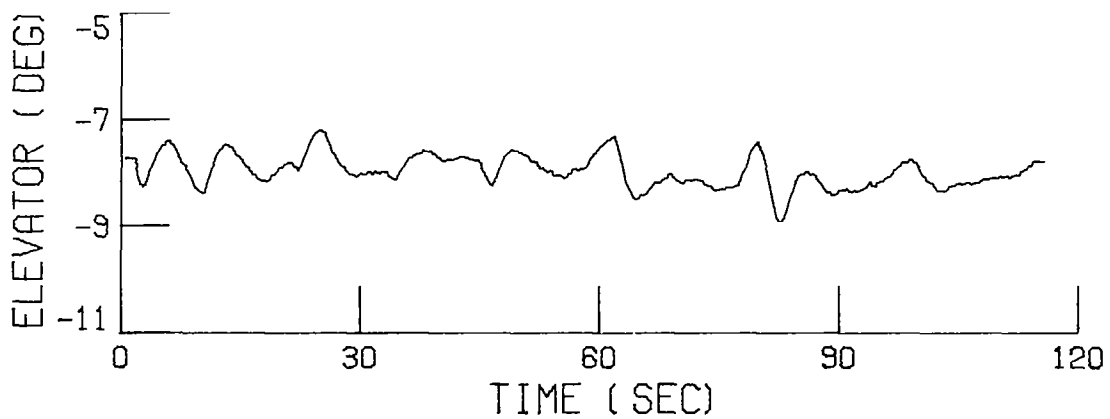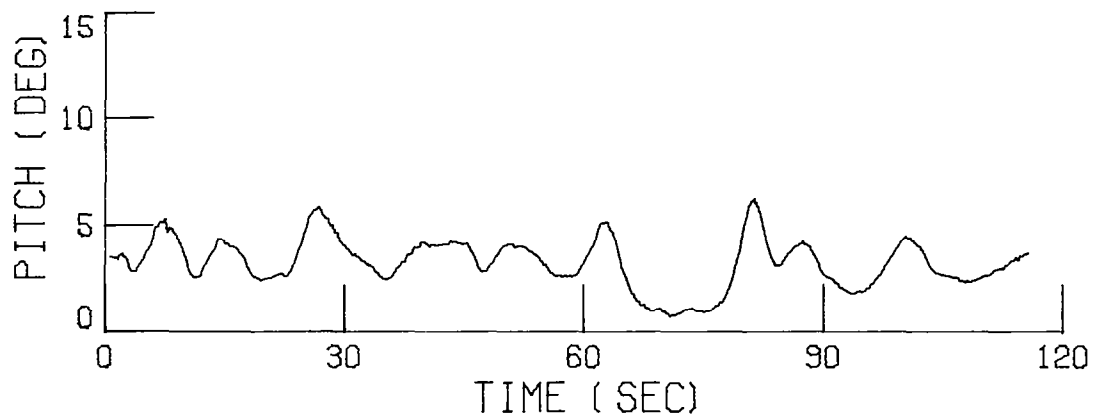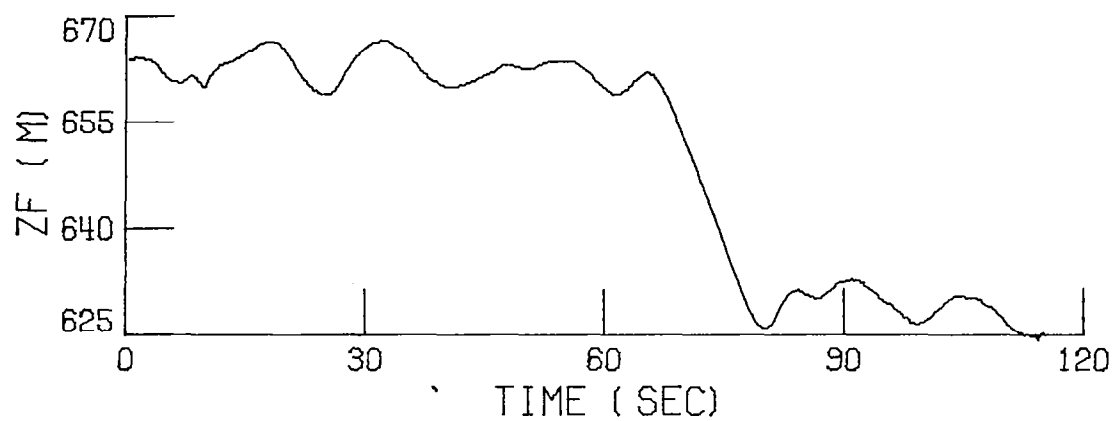
FIGURE 18 A 30.5 m (100 FT) ALTITUDE DESCENT USING THE ALT SEL
AUTOPILOT, NO THROTTLE ADJUSTMENT AND THE LOW PITCH
WEIGHT GAIN SET

122
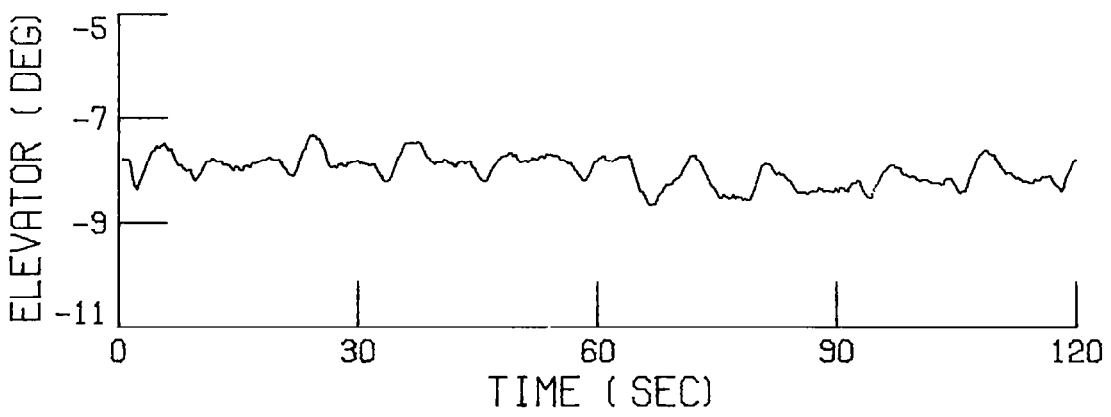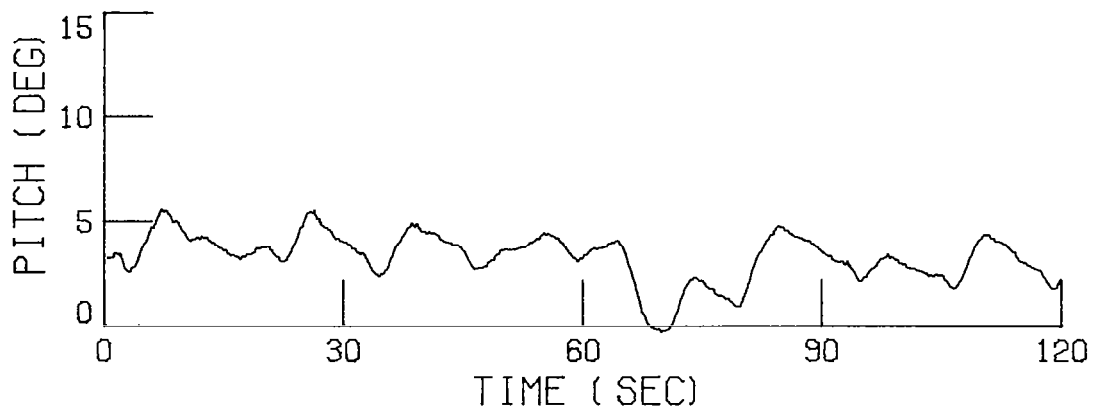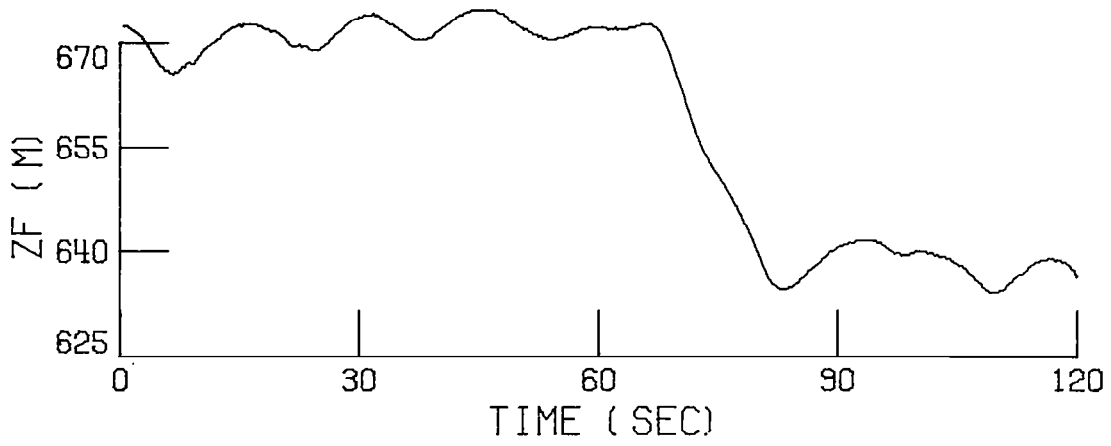
FIGURE 19   A 30.5 m (100 FT) ALTITUDE DESCENT USING THE ALT SEL
AUTOPILOT, NO THROTTLE ADJUSTMENT AND THE DESIGN GAIN SET
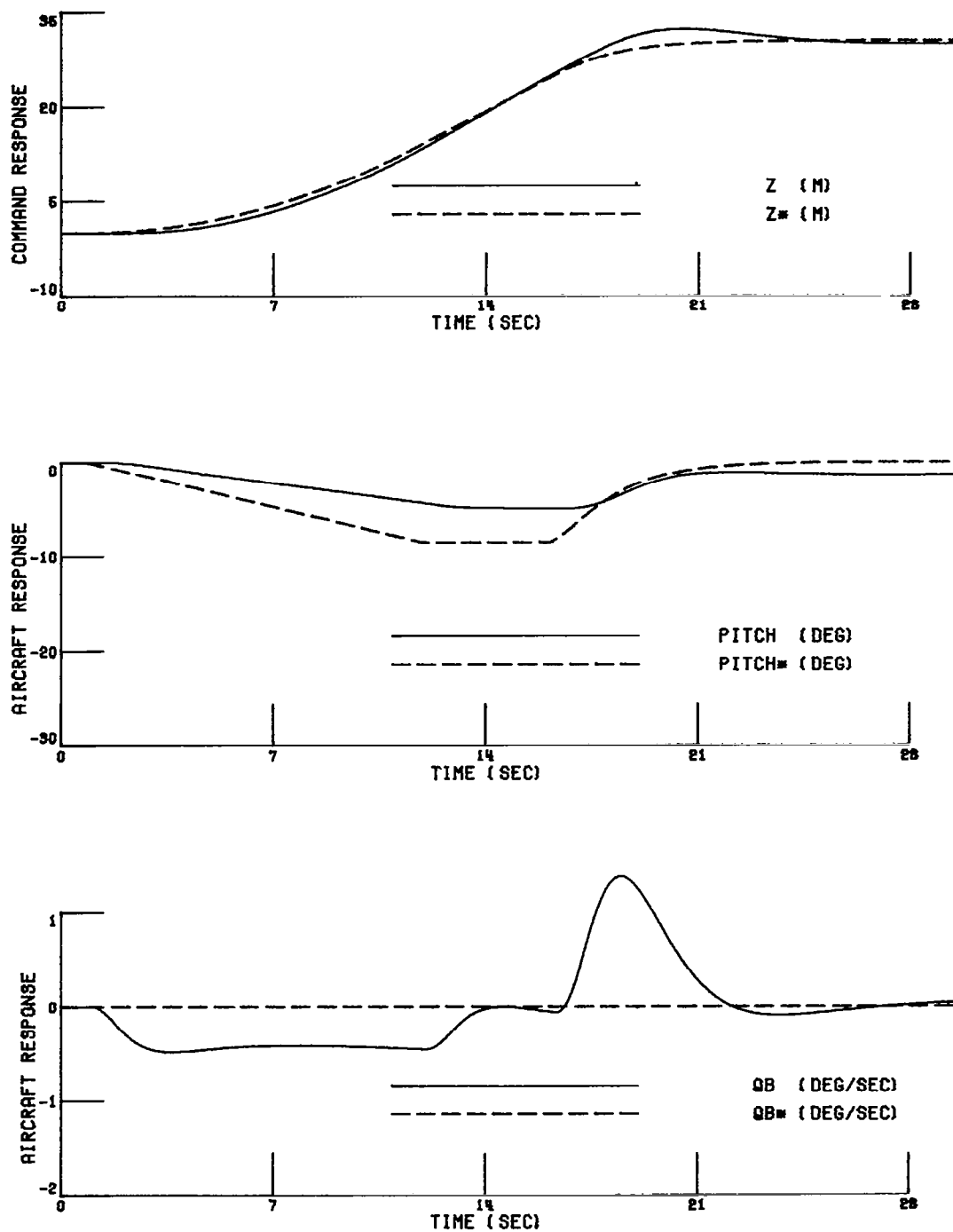
FIGURE 20   ALT SEL LINEAR AIRCRAFT MODEL RESPONSE SIMULATION

124
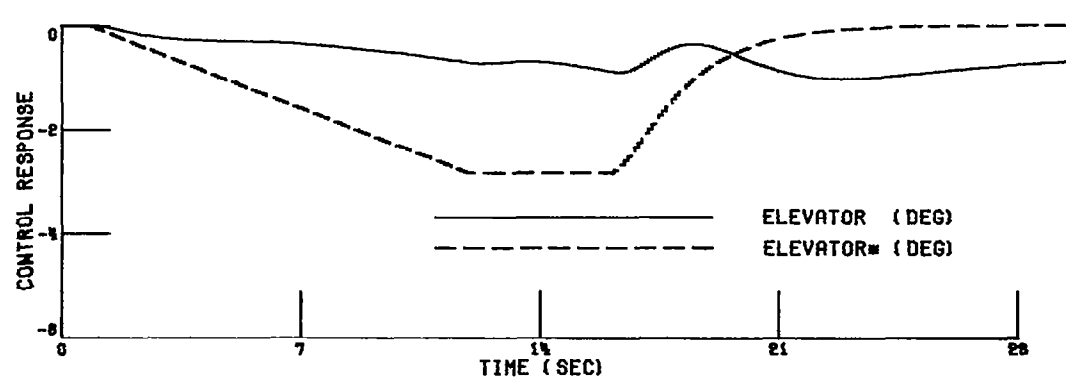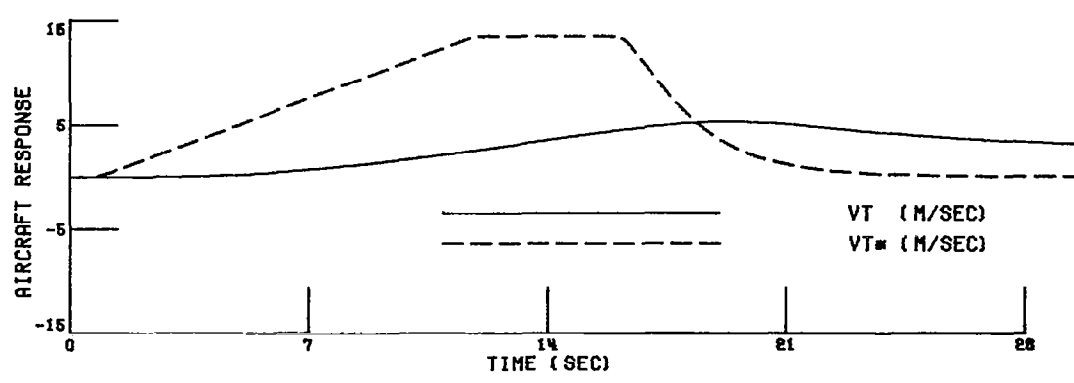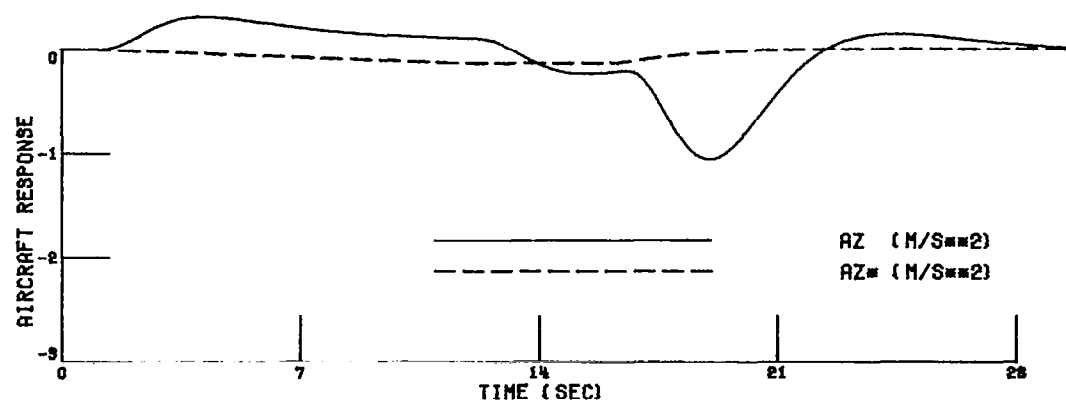
FIGURE 20 (CONTINUED)   ALT SEL LINEAR AIRCRAFT MODEL RESPONSE SIMULATION
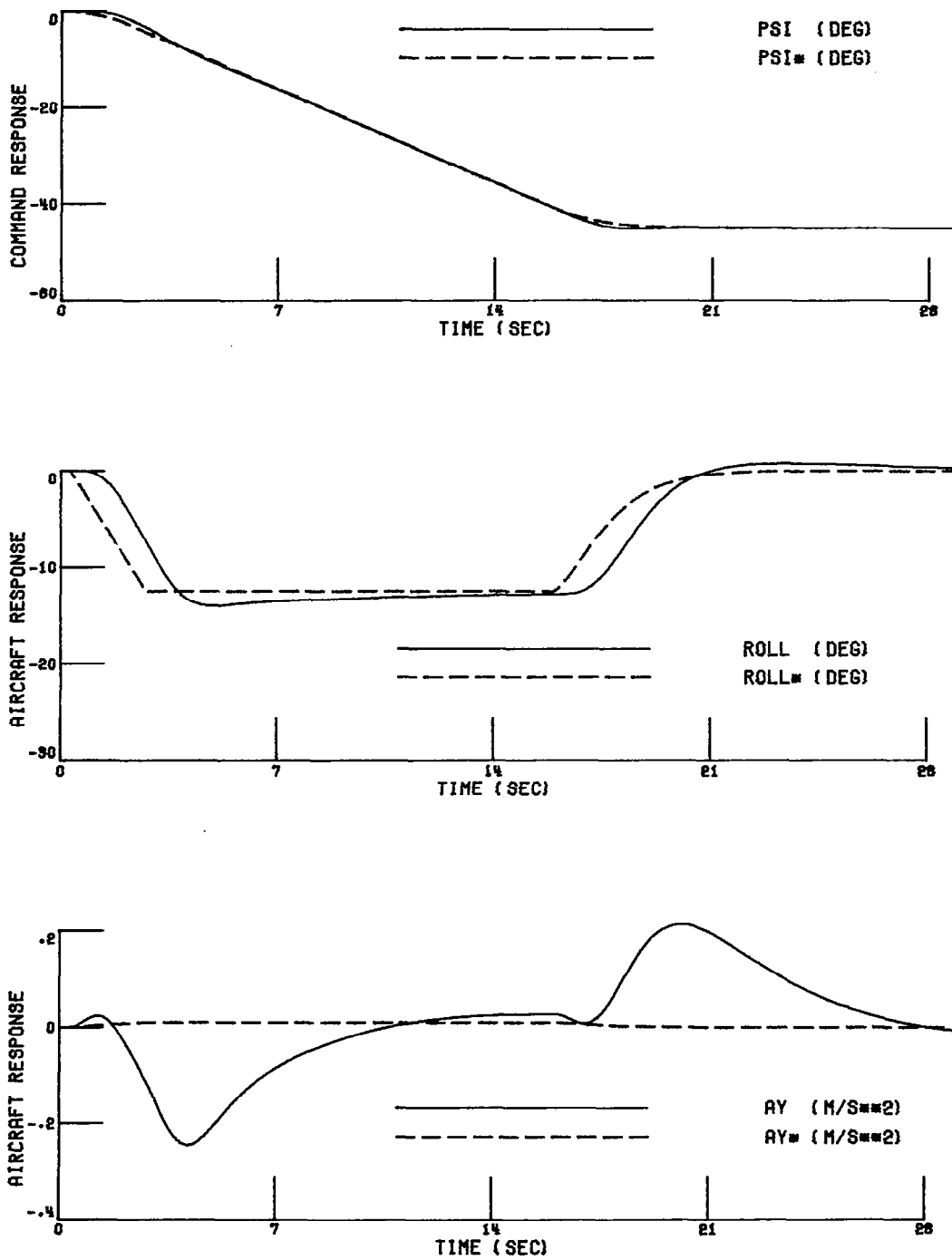
FIGURE 21   HDG SEL LINEAR AIRCRAFT MODEL RESPONSE SIMULATION
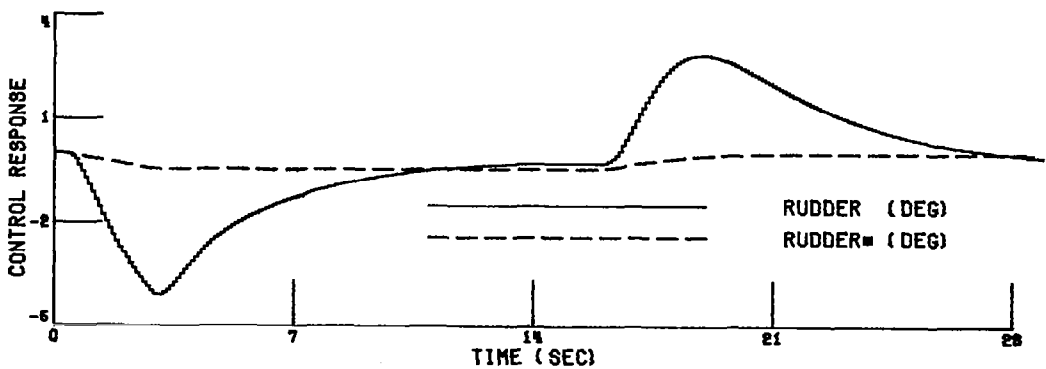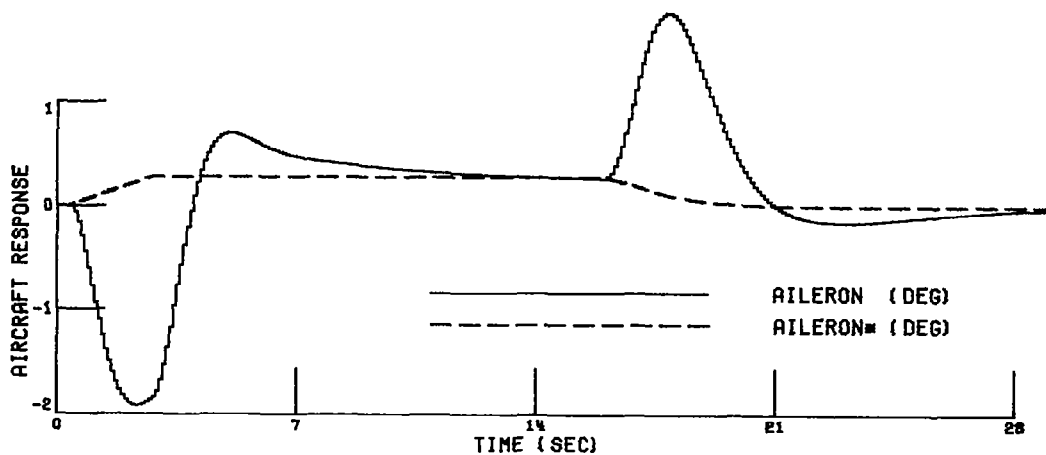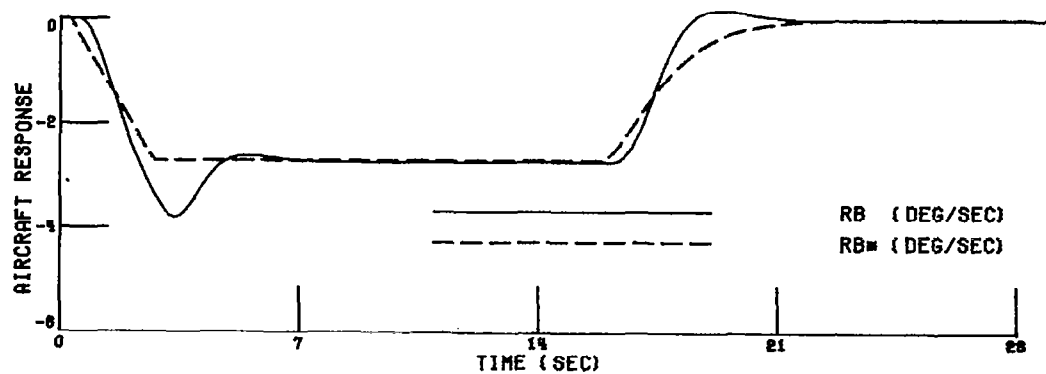
FIGURE 21 (CONTINUED) HDG SEL LINEAR AIRCRAFT MODEL RESPONSE SIMULATION

127
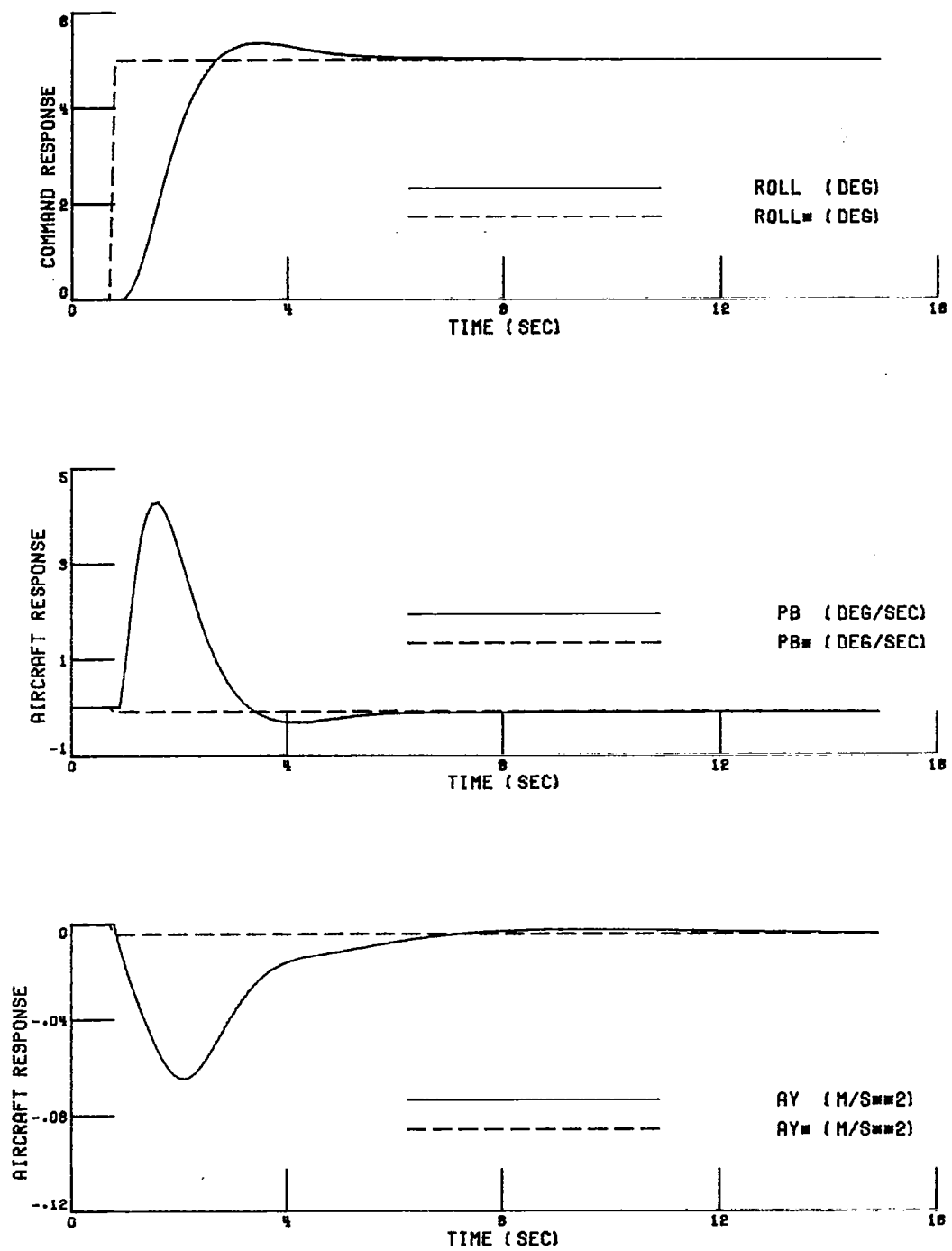
FIGURE 22   ROLL SEL LINEAR AIRCRAFT MODEL RESPONSE SIMULATION
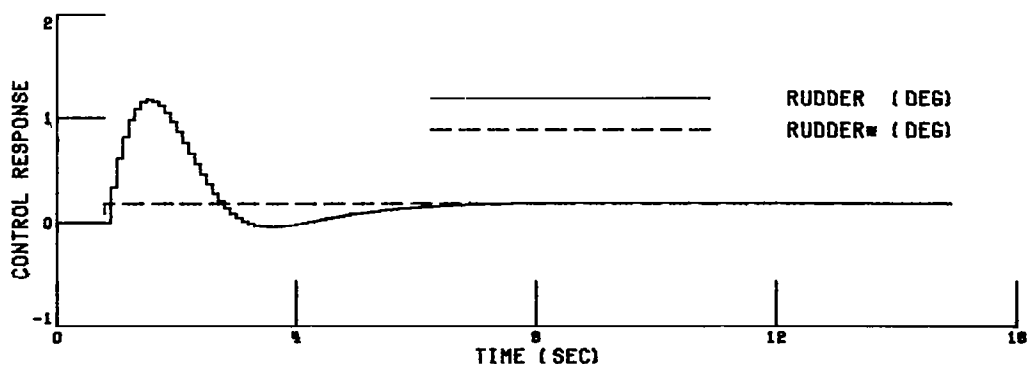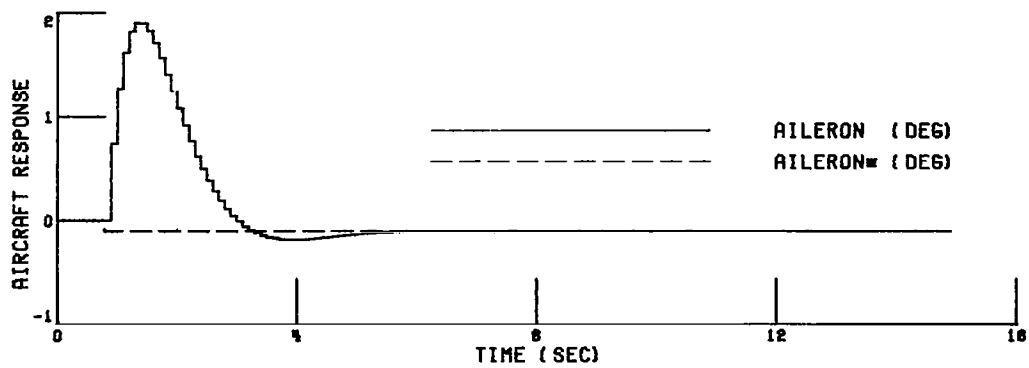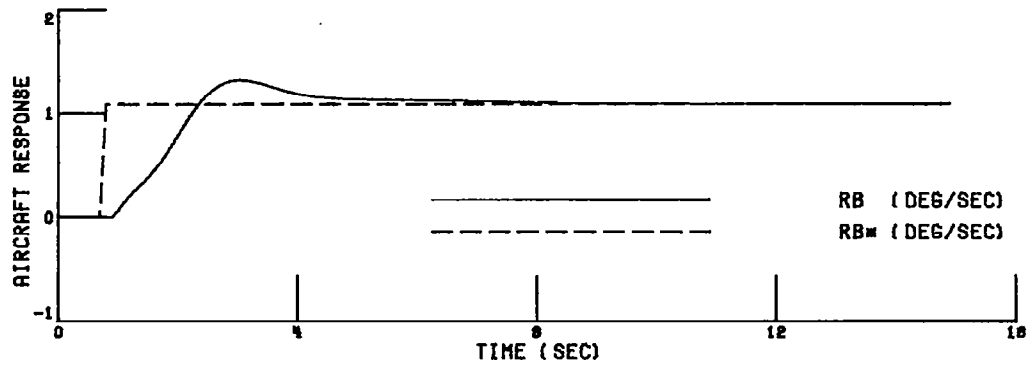
FIGURE 22 (CONTINUED) ROLL SEL LINEAR AIRCRAFT MODEL RESPONSE SIMULATION
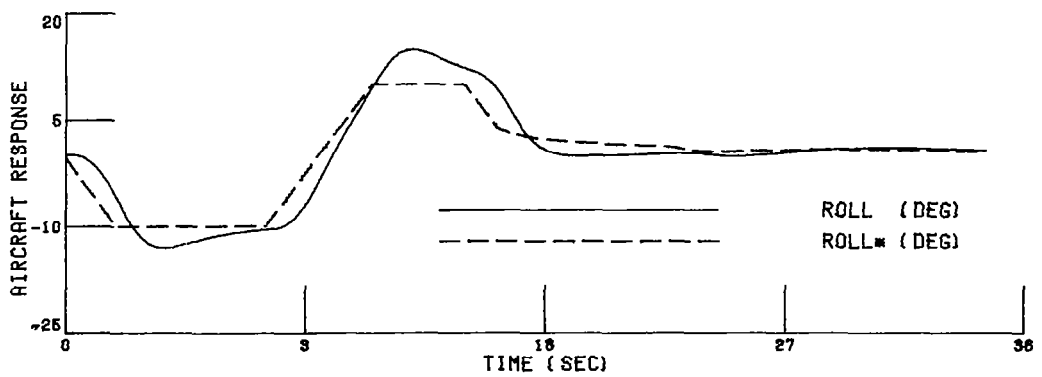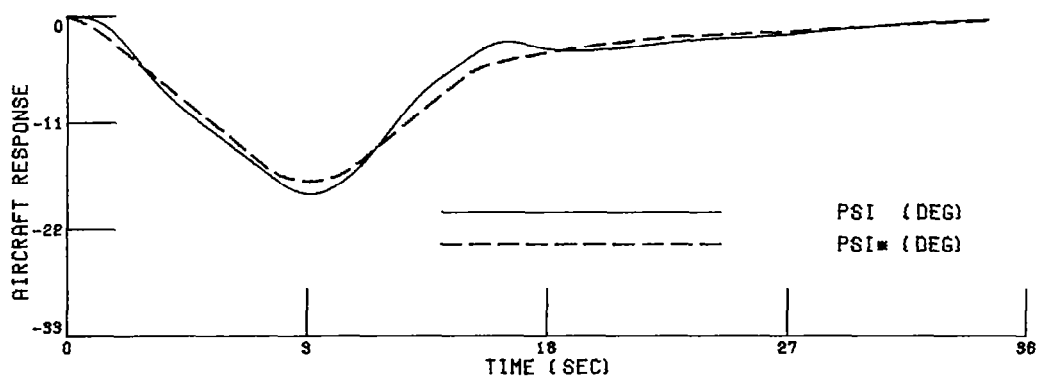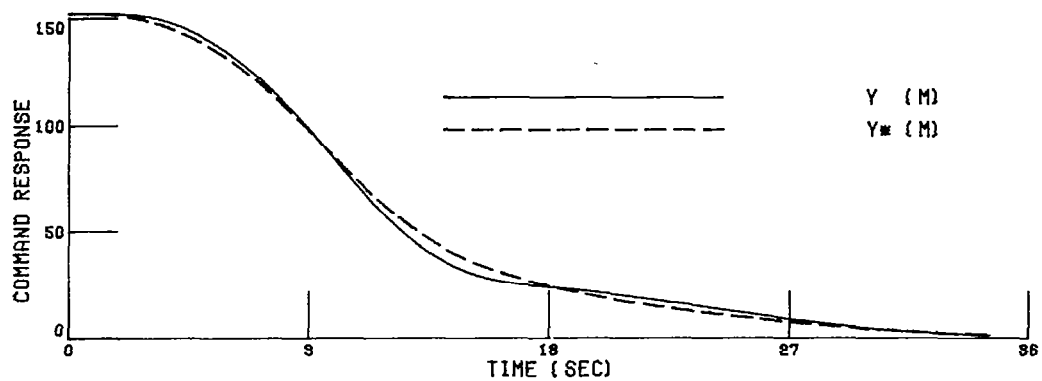
FIGURE 23 APR LOCI LINEAR AIRCRAFT MODEL RESPONSE SIMULATION
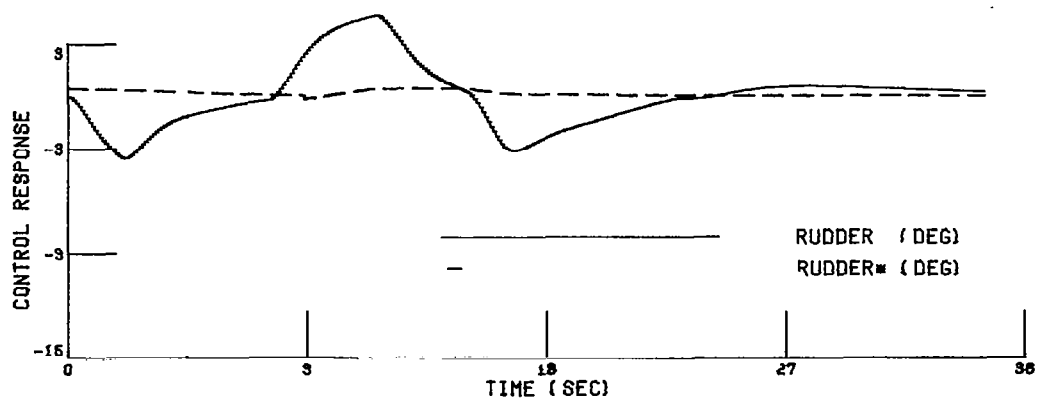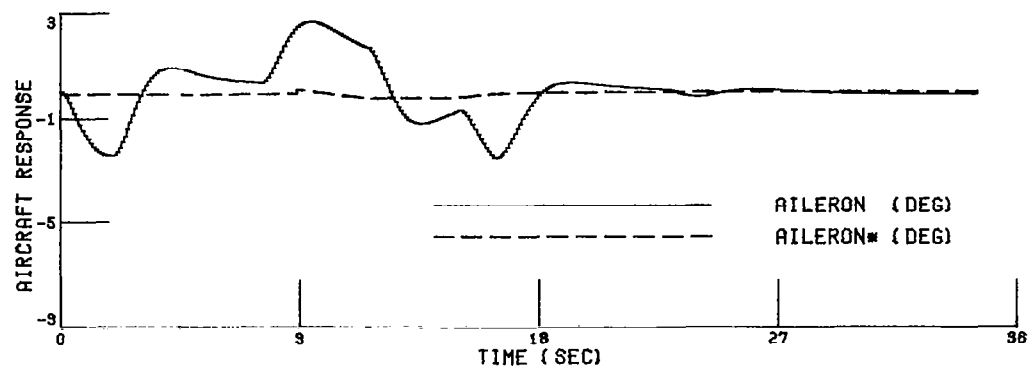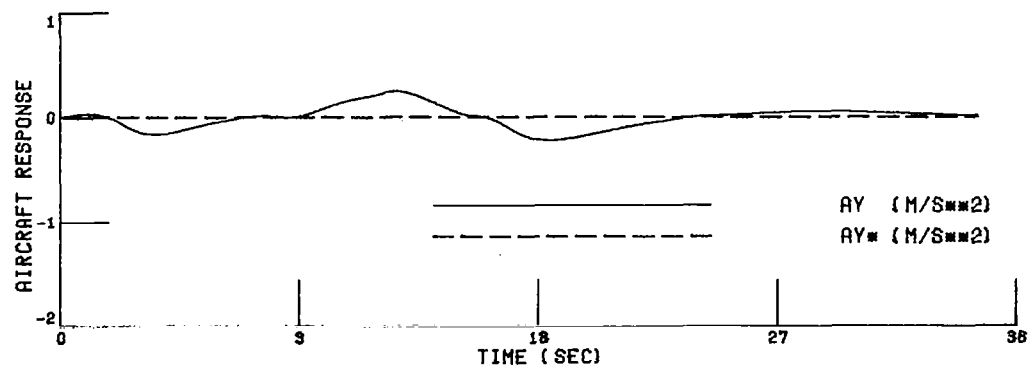
FIGURE 23 (CONTINUED)   APR LOCI LINEAR AIRCRAFT MODEL RESPONSE SIMULATION
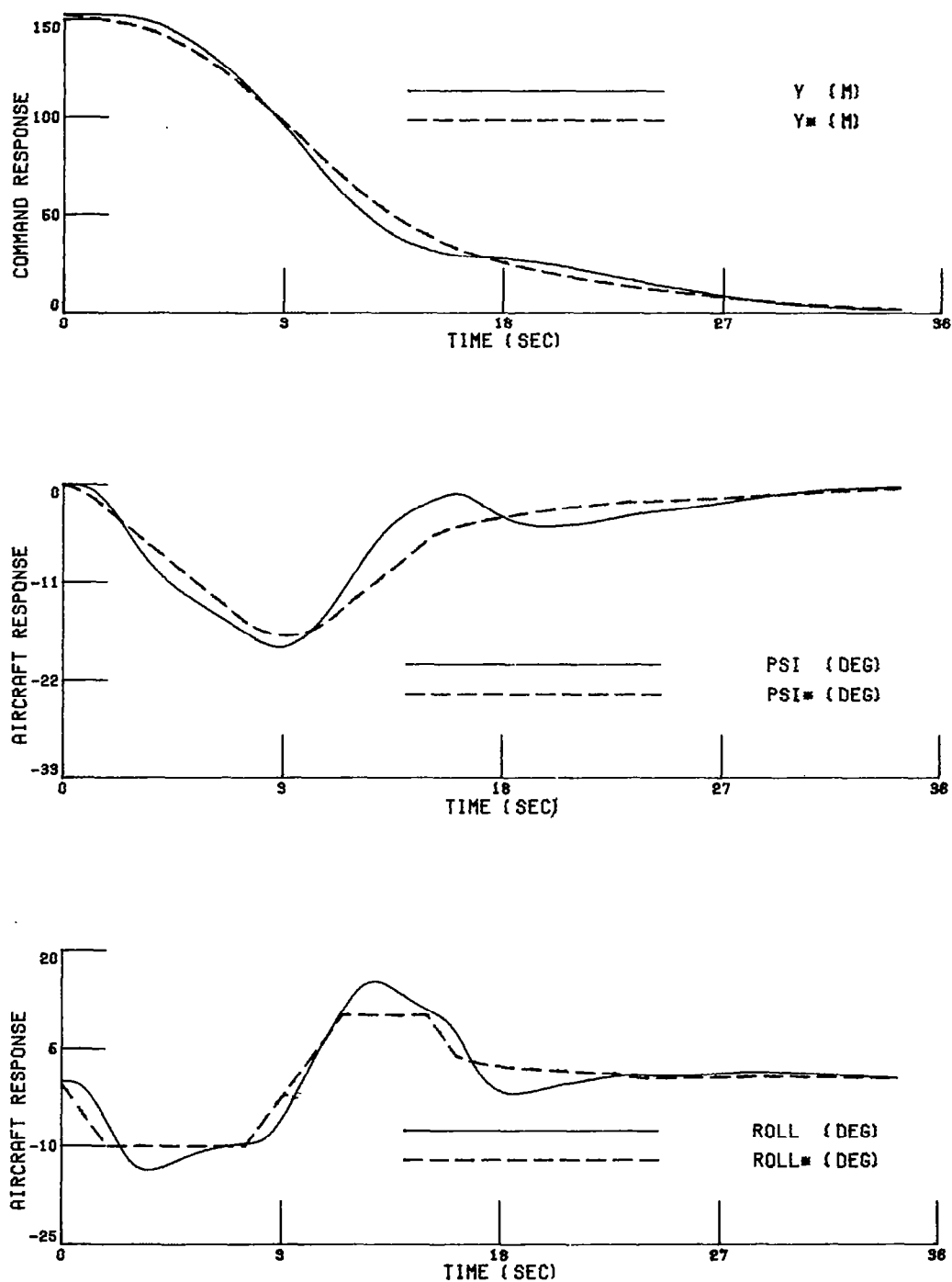
FIGURE 24   APR LOCR LINEAR AIRCRAFT MODEL RESPONSE SIMULATION
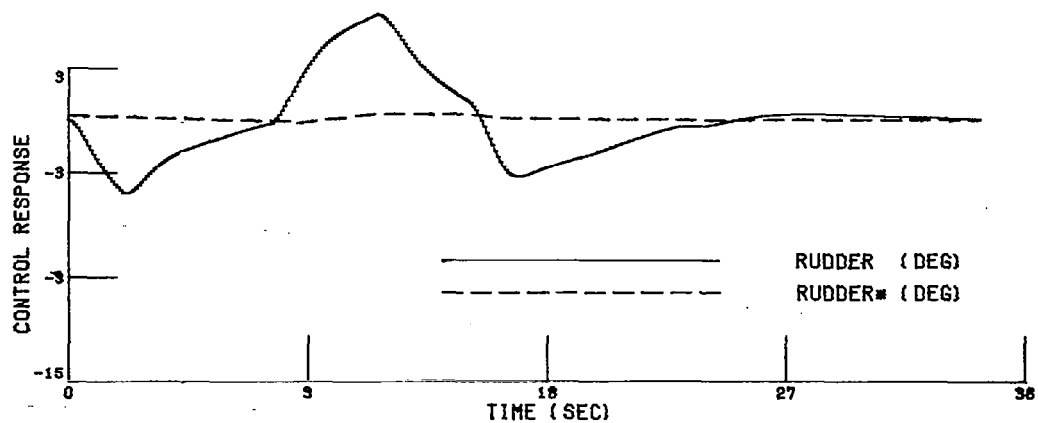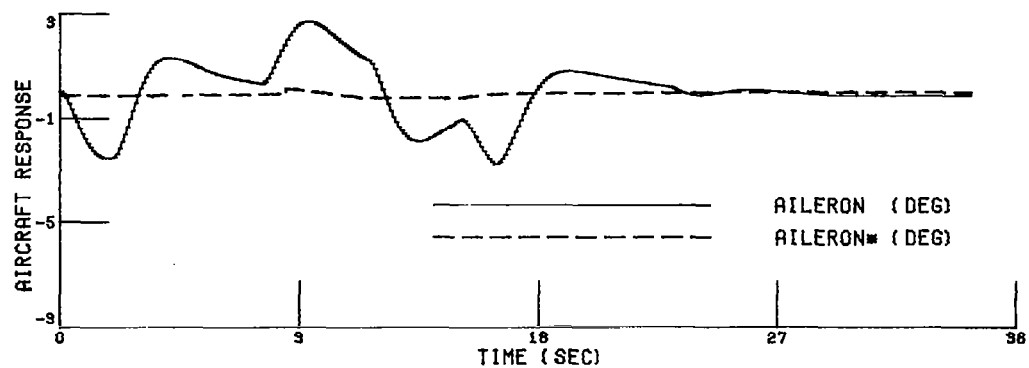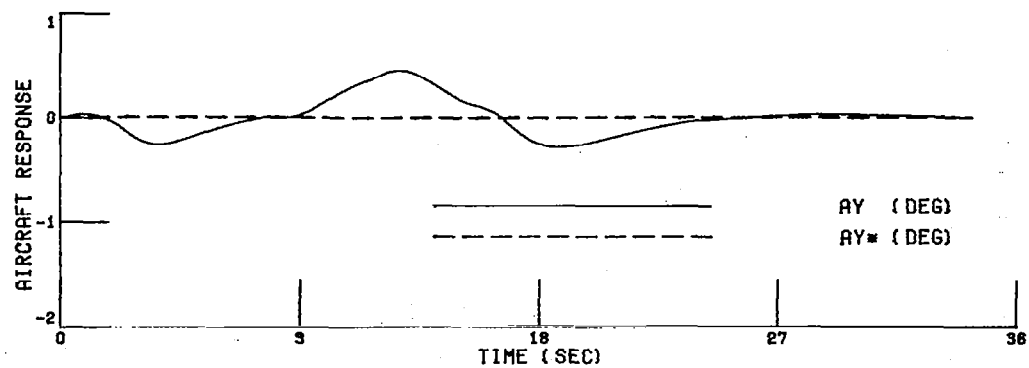
FIGURE 24 (CONTINUED)   APR LOCR LINEAR AIRCRAFT MODEL RESPONSE SIMULATION
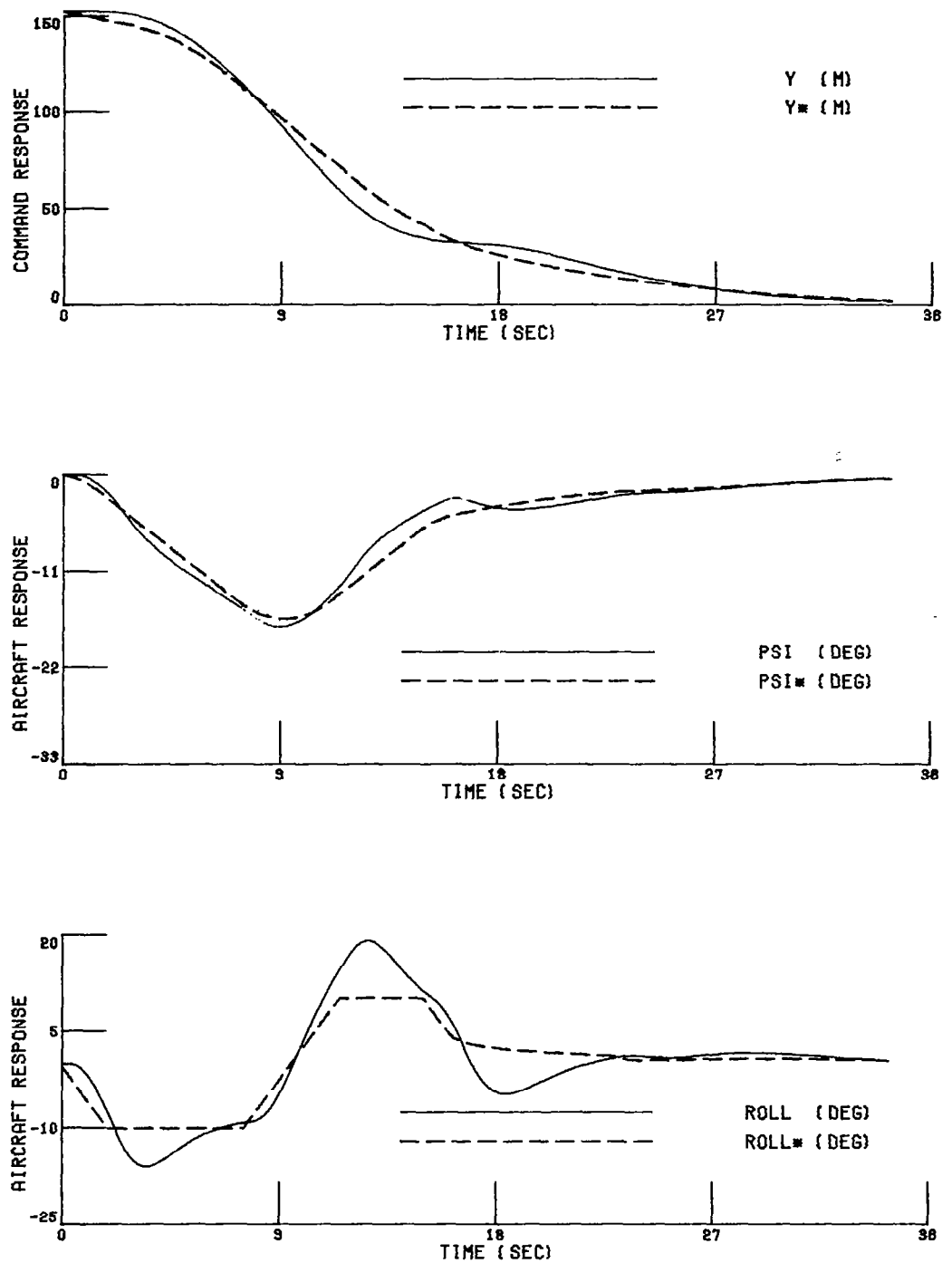
FIGURE 25   APR LOCP LINEAR AIRCRAFT MODEL RESPONSE SIMULATION
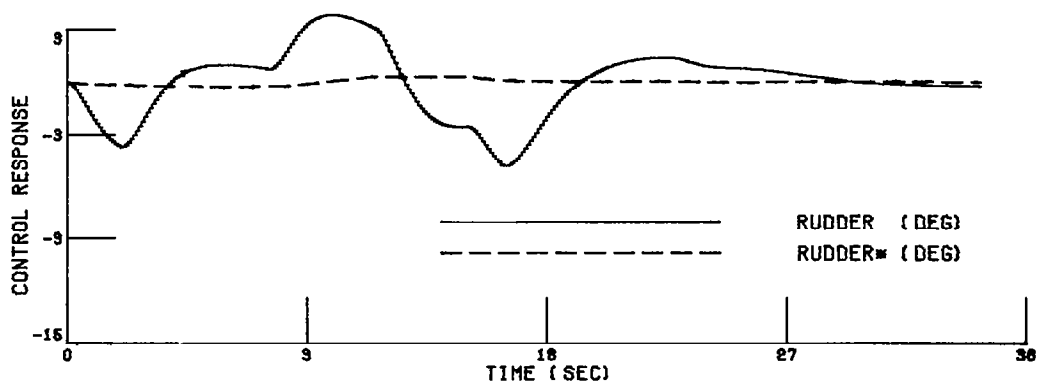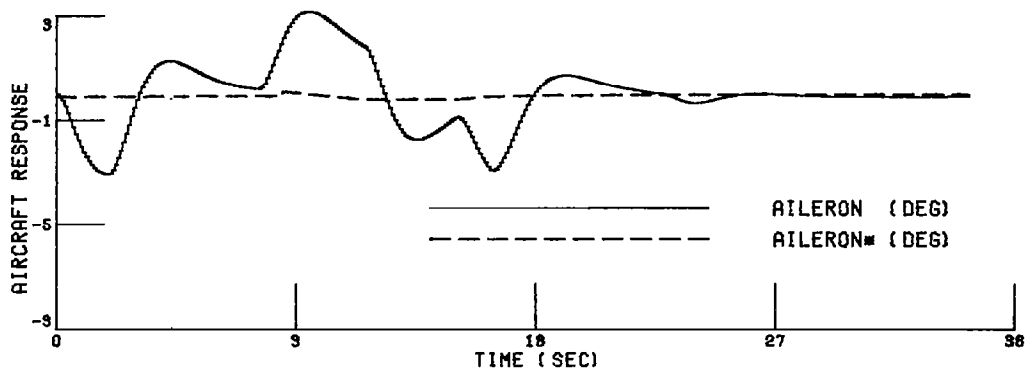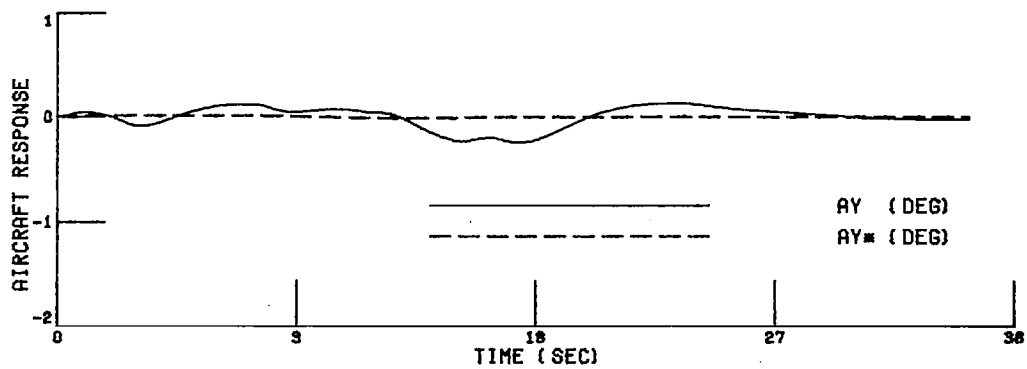
FIGURE 25 (CONTINUED)   APR LOCP LINEAR AIRCRAFT MODEL RESPONSE SIMULATION
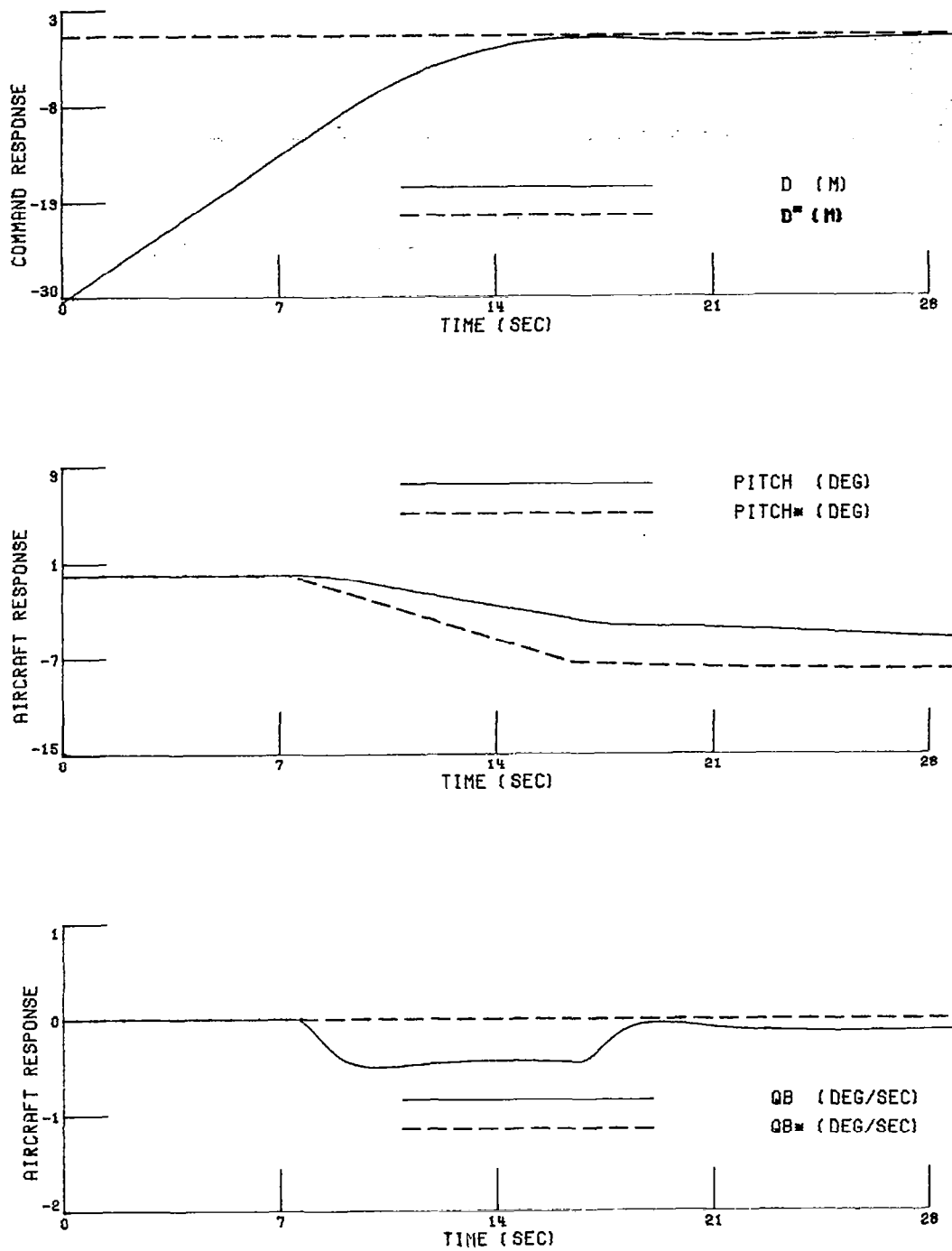
FIGURE 26   APR GS LINEAR AIRCRAFT MODEL RESPONSE SIMULATION
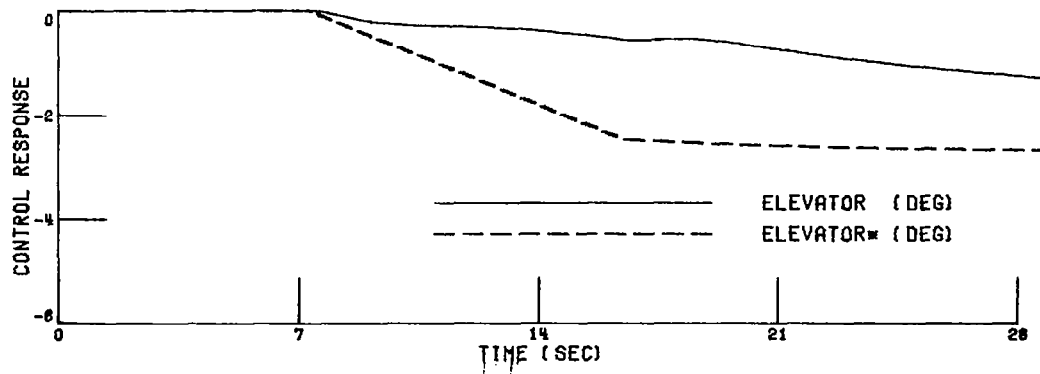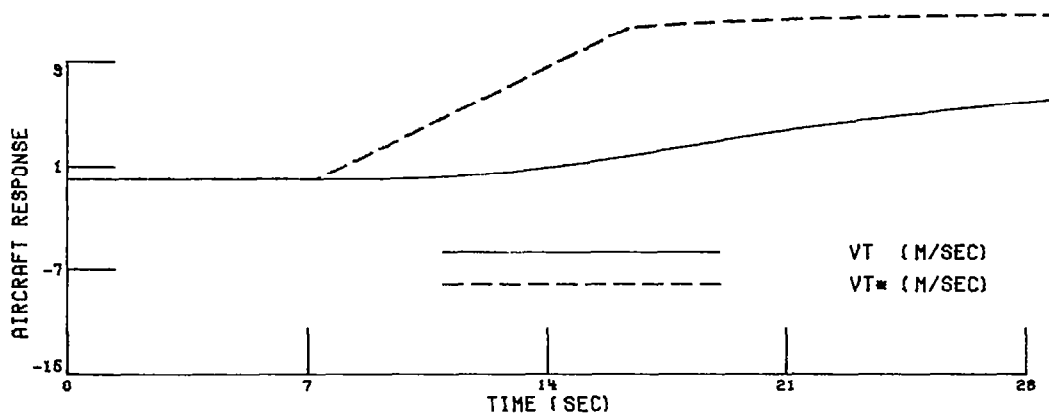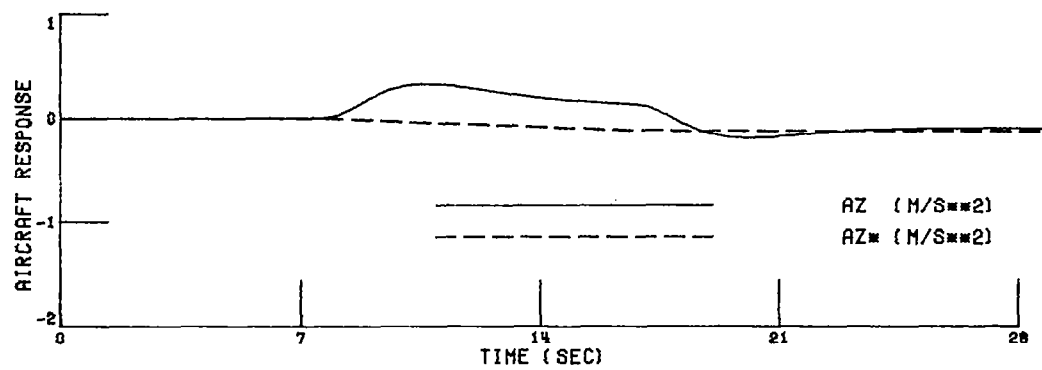
FIGURE 26 (CONTINUED) APR GS LINEAR AIRCRAFT MODEL RESPONSE SIMULATION
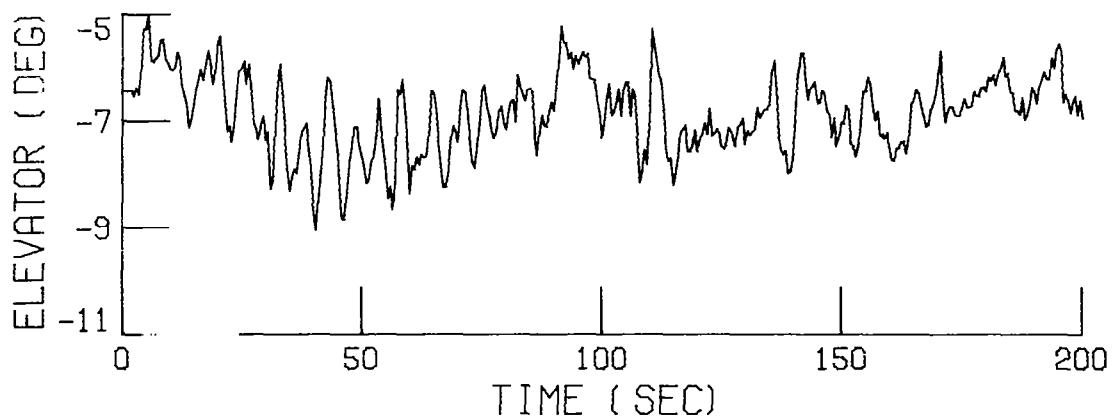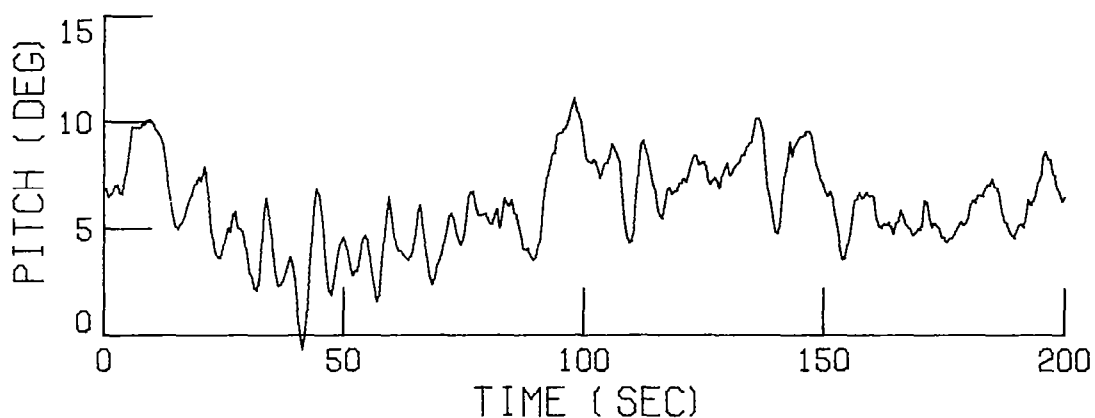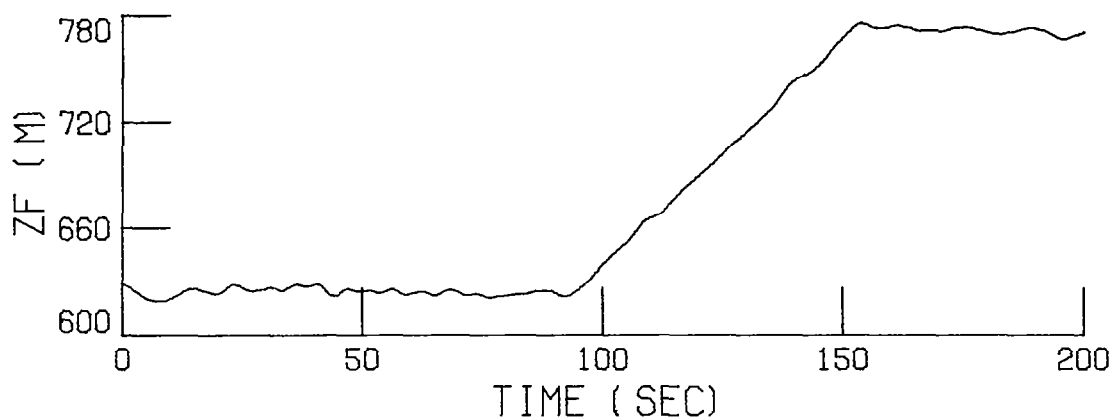
FIGURE 27   A 152.4 m (500 ft) ALITUTDE ASCENT USING THE ALT SEL AUTOPILOT, THROTTLE
ADJUSTMENTS, LOW PITCH WEIGHT GAIN SET AND HEAVY TURBULENCE CONDITION

138
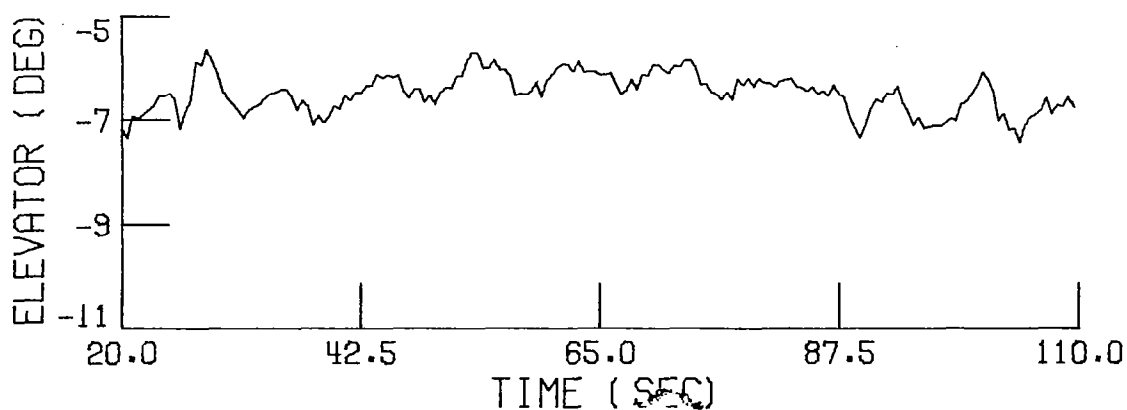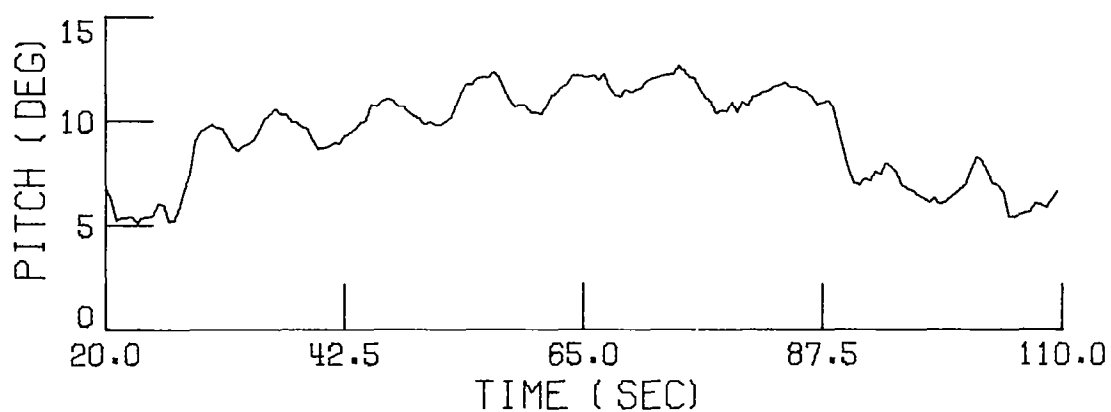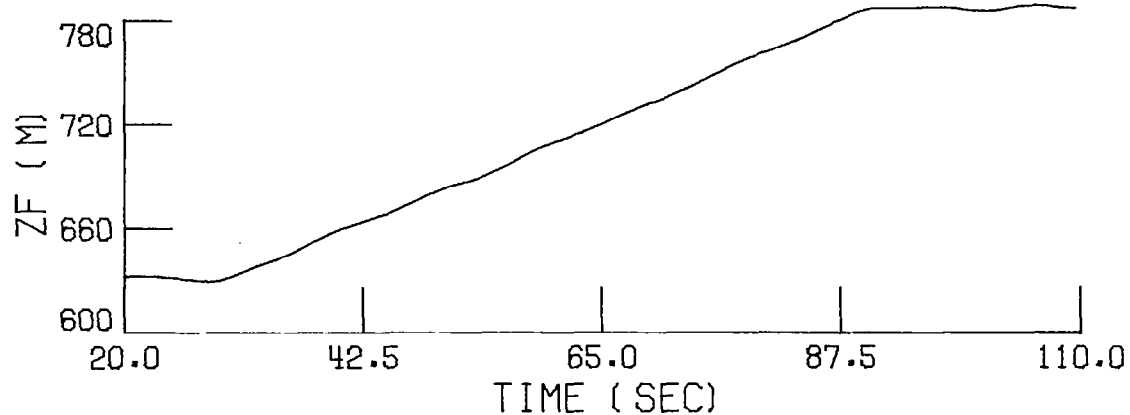
FIGURE 28   A 152.4 m (500 ft) ALTITUDE ASCENT USING THE ALT SEL AUTOPILOT, THROTTLE
ADJUSTMENTS, LOW PITCH WEIGHT GAIN SET AND MEDIUM TURBULENCE CONDITIONS
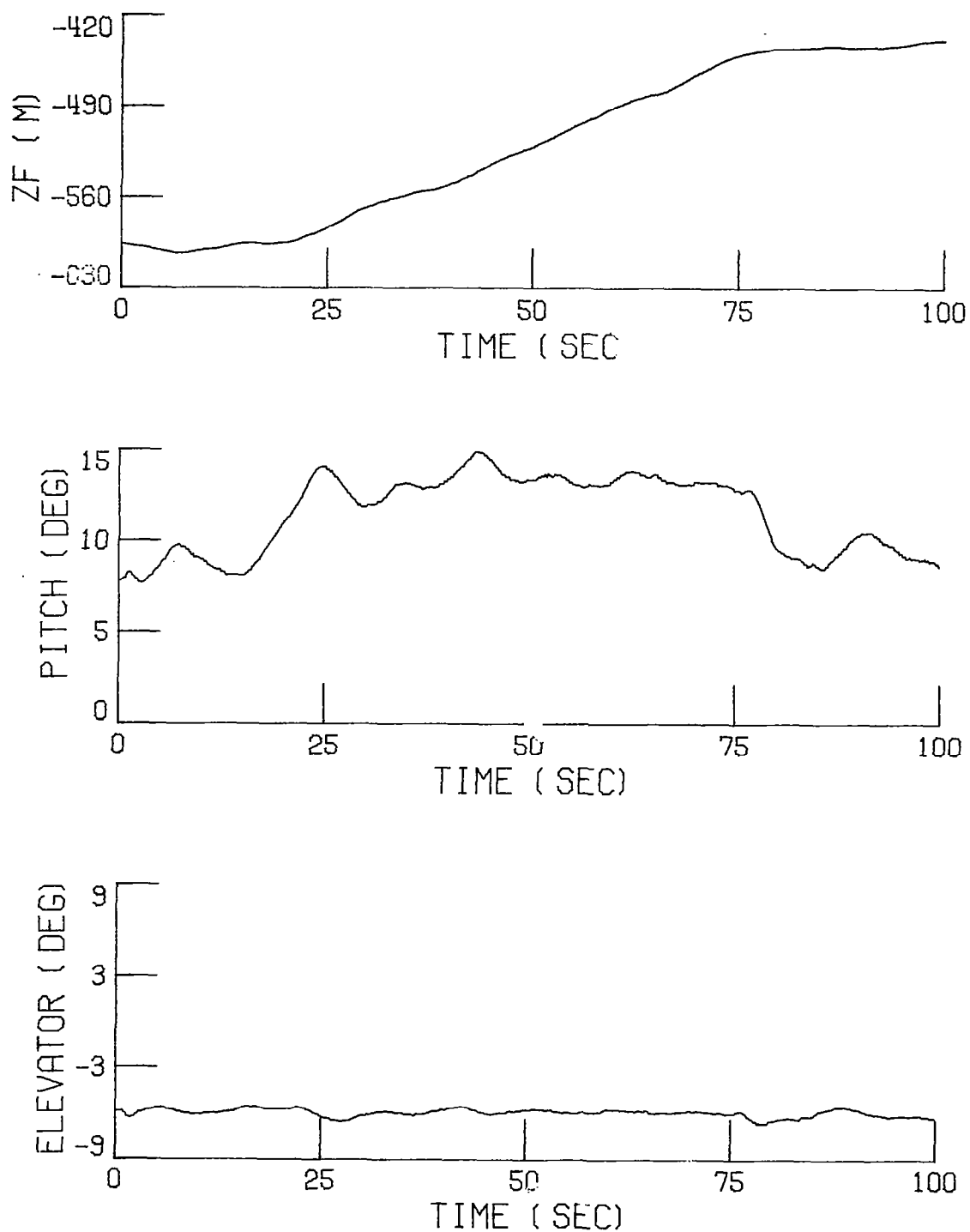
FIGURE 29 A 152.4 m (500 ft) ALTITUDE ASCENT USING THE ALT SEL AUTOPILOT, THROTTLE
ADJUSTMENTS, DESIGN GAIN SET AND LIGHT TURBULENCE
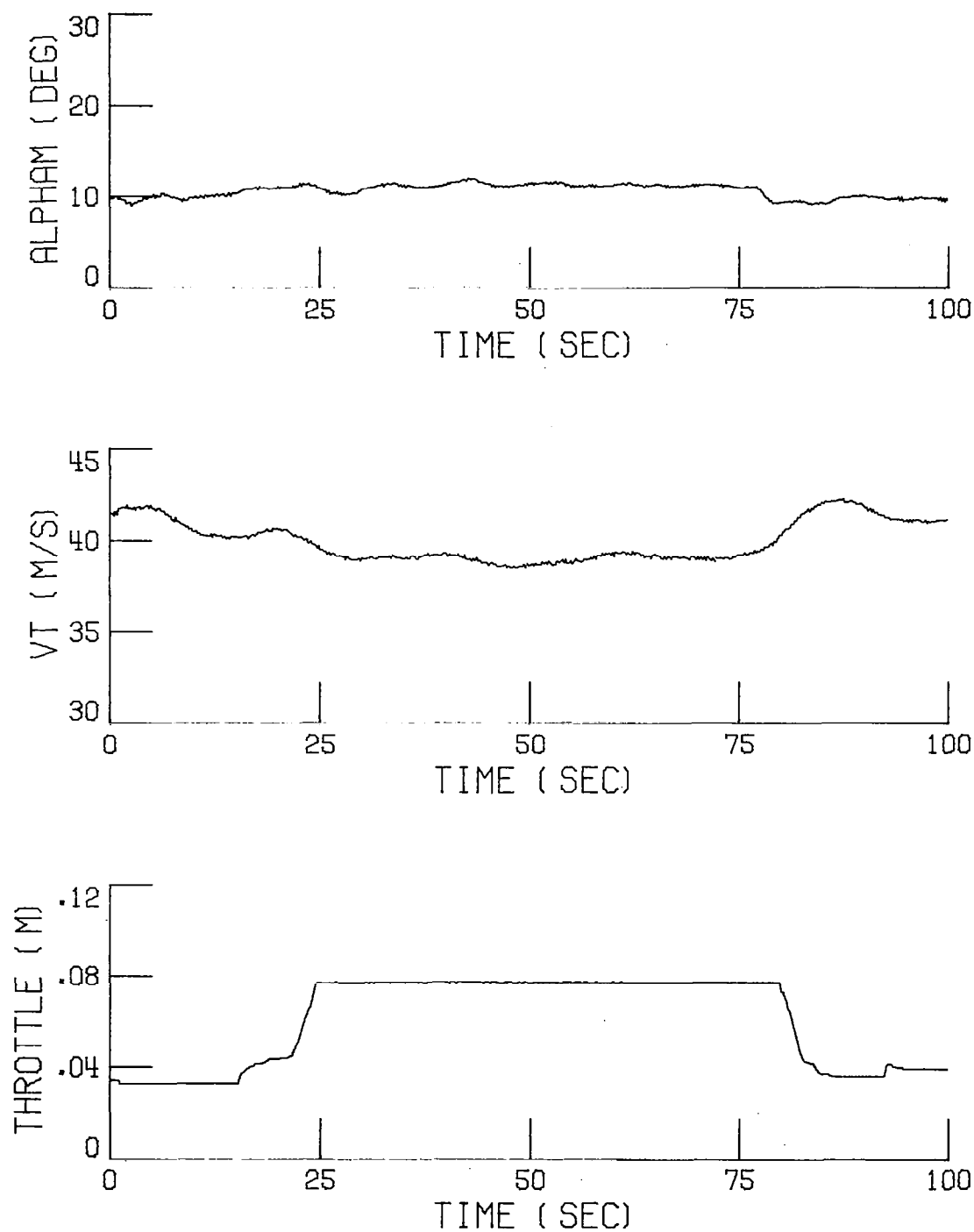
FIGURE 29 (CONTINUED)   A 152.4 m (500 ft) ALTITUDE ASCENT USING THE ALT SEL AUTOPILOT,
THROTTLE ADJUSTMENTS, DESIGN GAIN SET AND LIGHT TURBULENCE
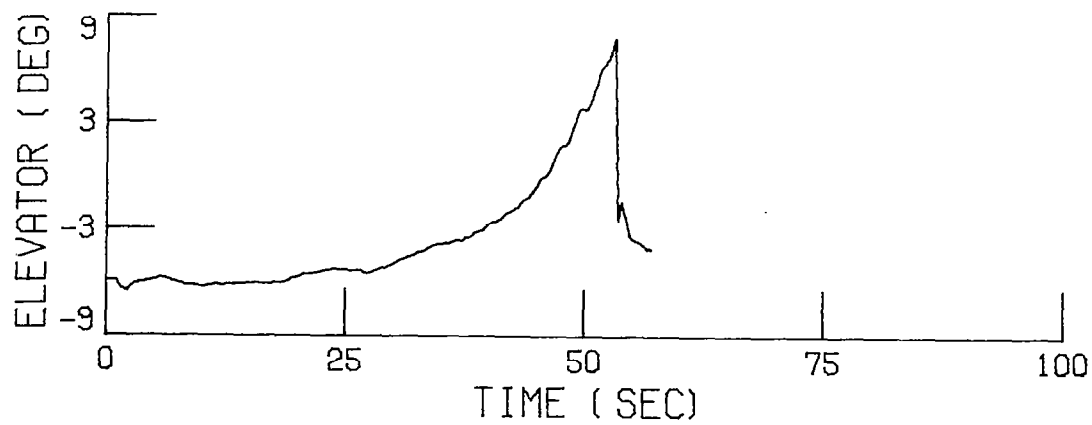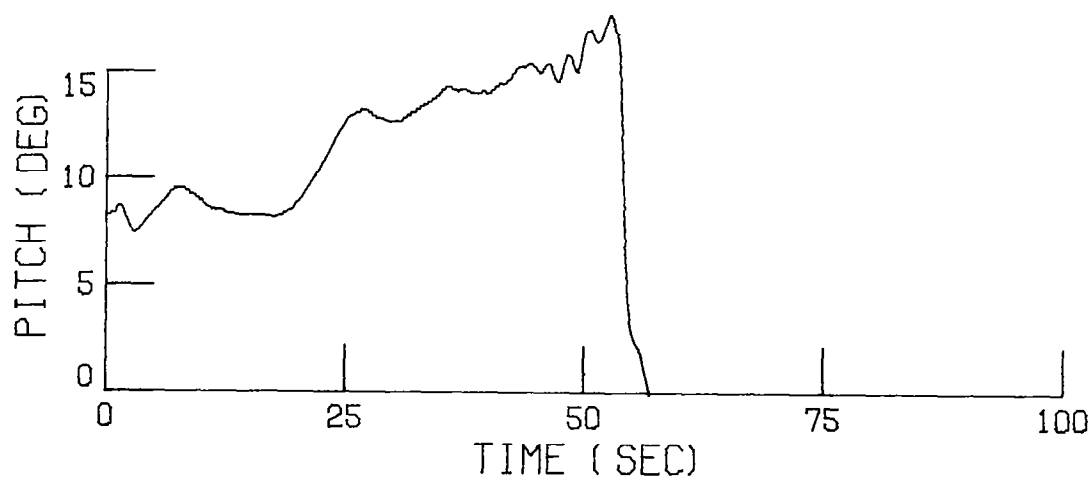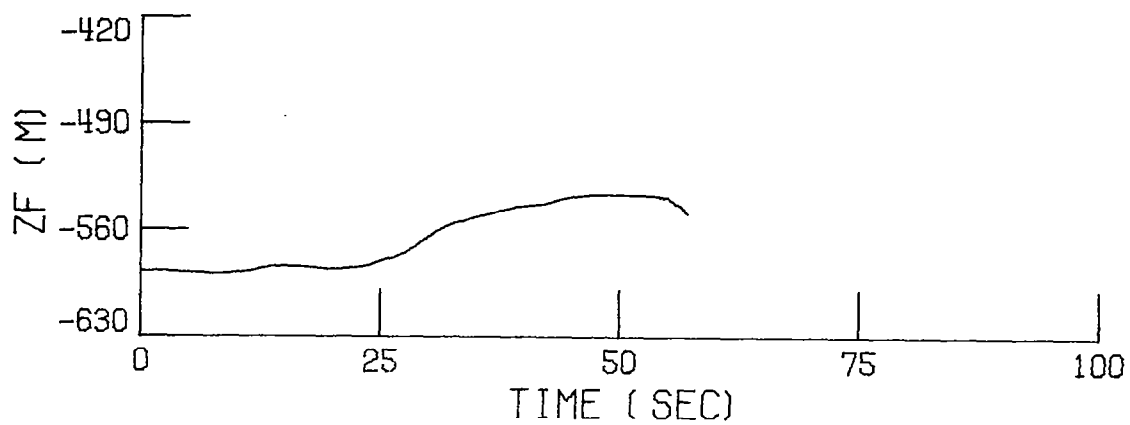
FIGURE 30   A 152.4 m (500 ft) ALTITUDE ASCENT USING THE ALT SEL AUTOPILOT, NO
THROTTLE ADJUSTMENTS, DESIGN GAIN SET AND LIGHT TURBULENCE
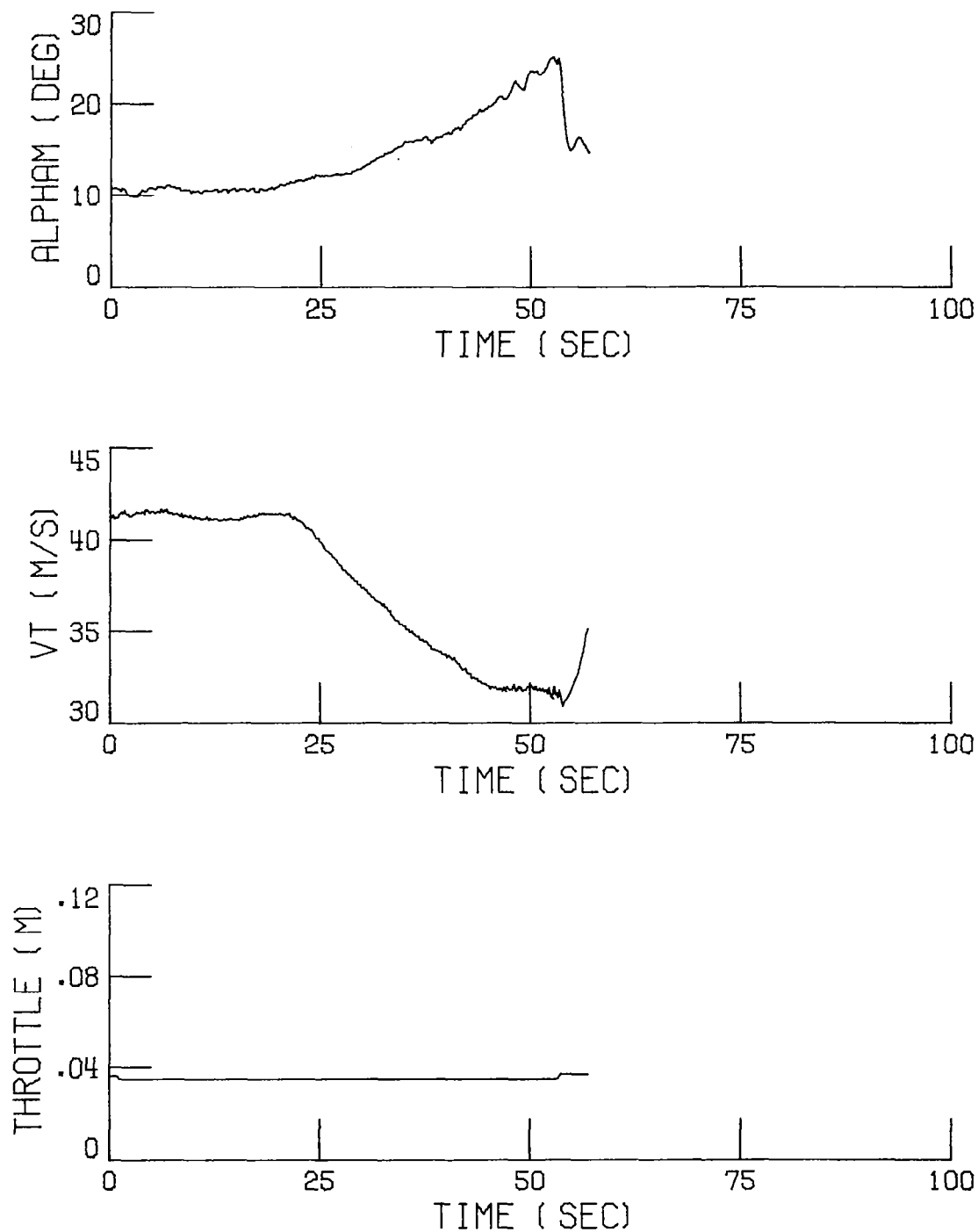
FIGURE 30 (CONTINUED)   A 152.4 m (500 ft) ALTITUDE ASCENT USING THE ALT SEL AUTOPILOT, NO THROTTLE ADJUSTMENTS, DESIGN GAIN SET AND LIGHT TURBULENCE
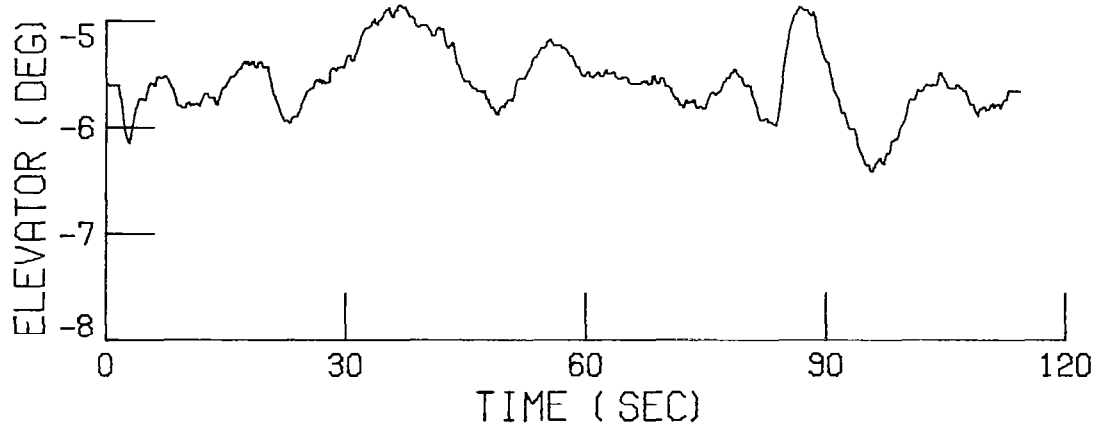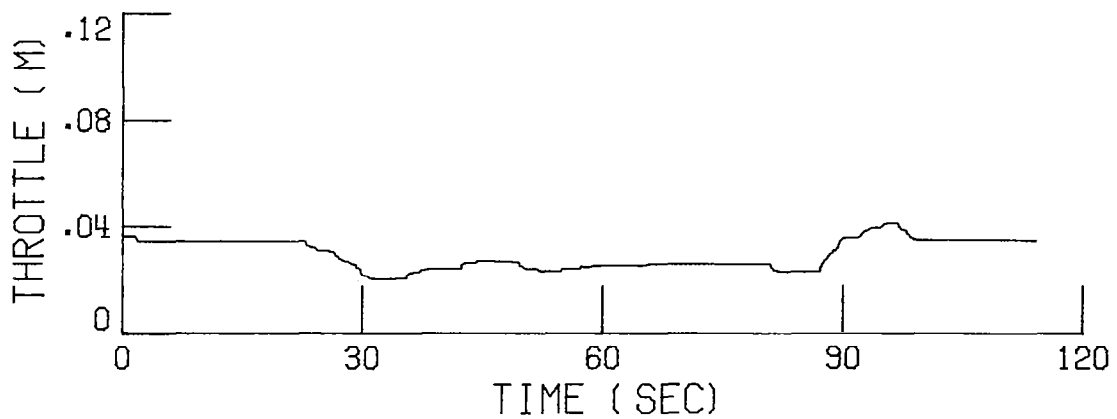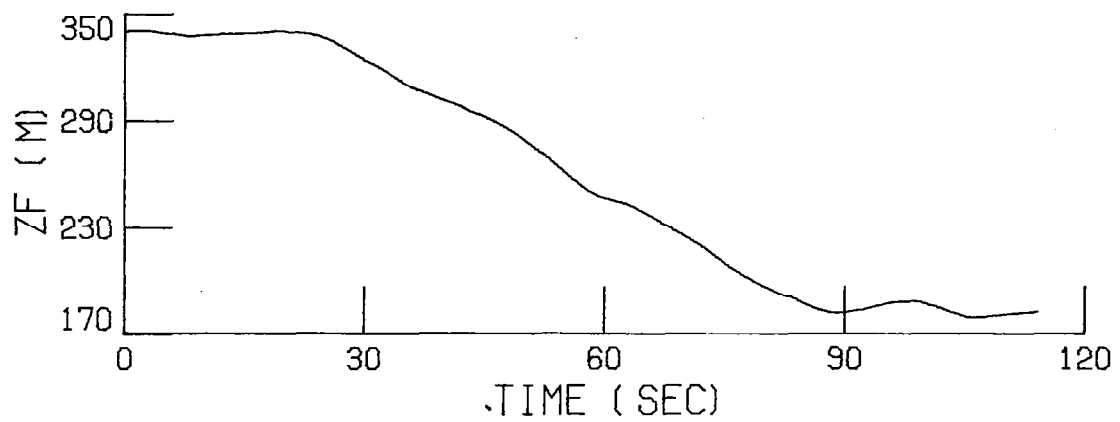
FIGURE 31 A 152.4 m (500 ft) ALTITUDE DESCENT USING THE ALT SEL AUTOPILOT, THROTTLE
ADJUSTMENTS, DESIGN GAIN SET AND LIGHT TURBULENCE

144
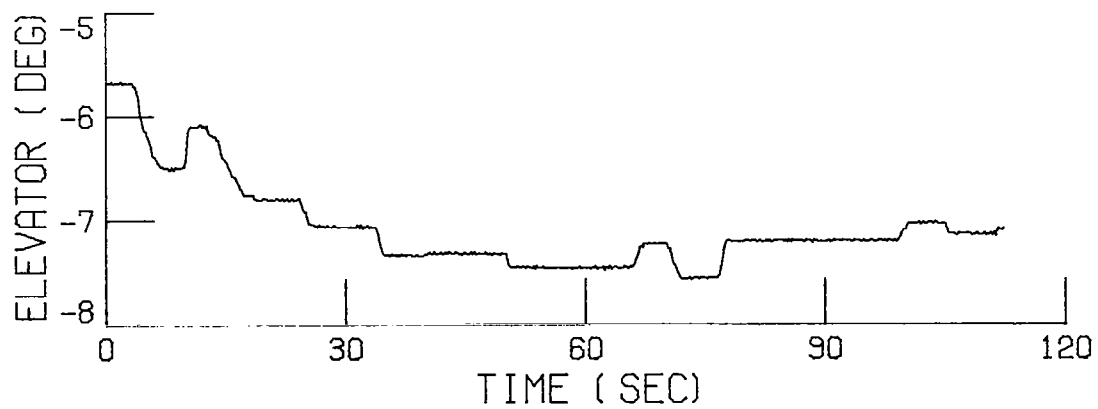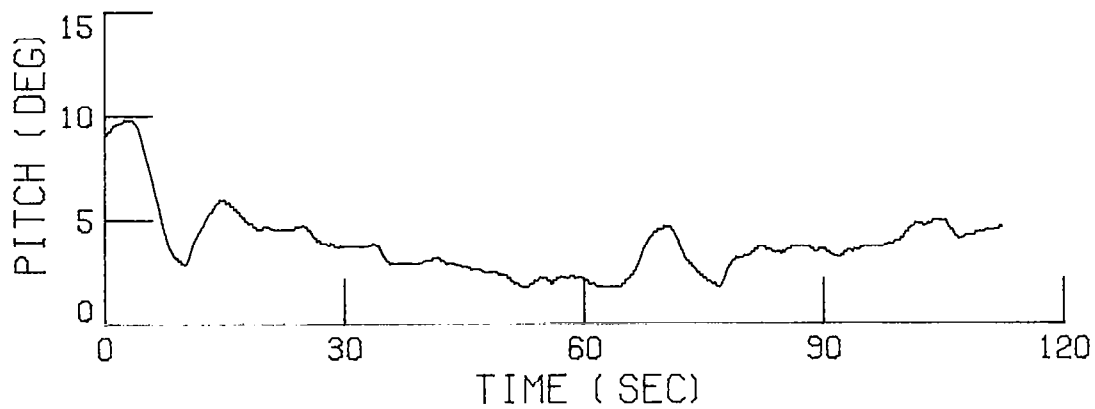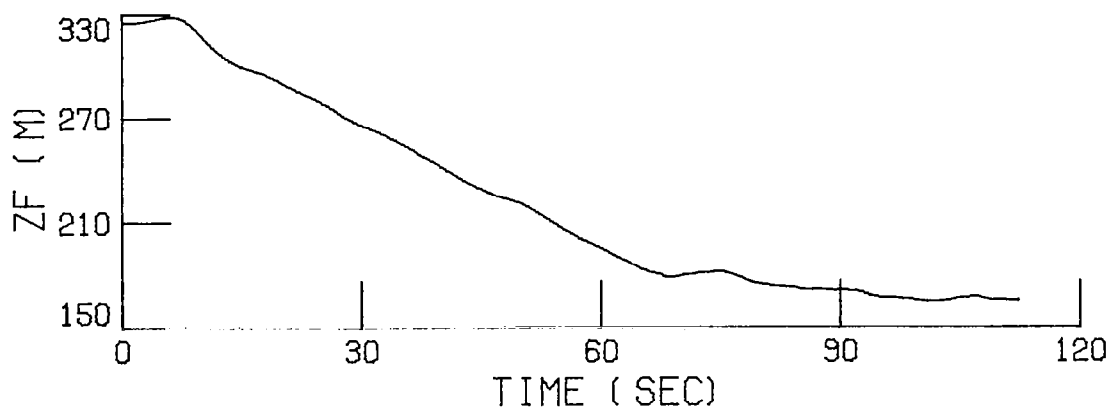
FIGURE 32   A 152.4 m (500 ft) MANUAL ALTITUDE DESCENT WITHOUT USING THROTTLE DURING LIGHT TURBULENCE
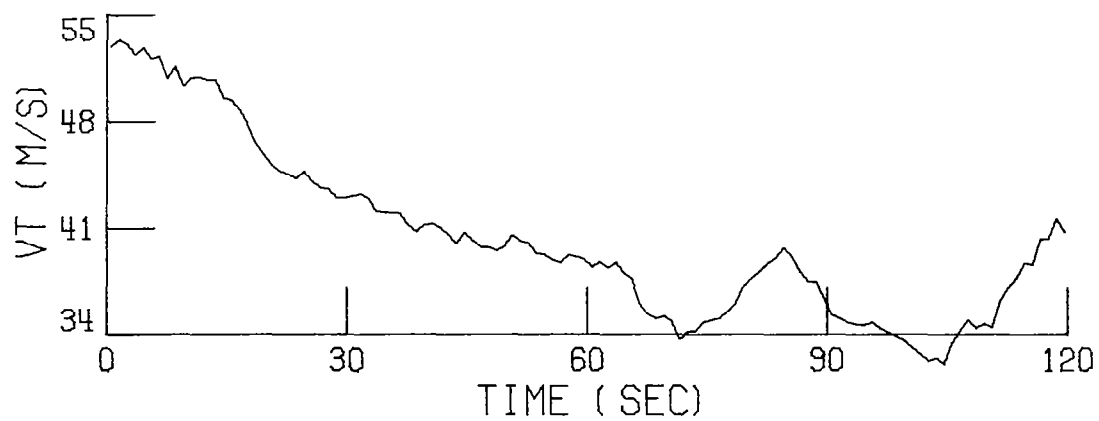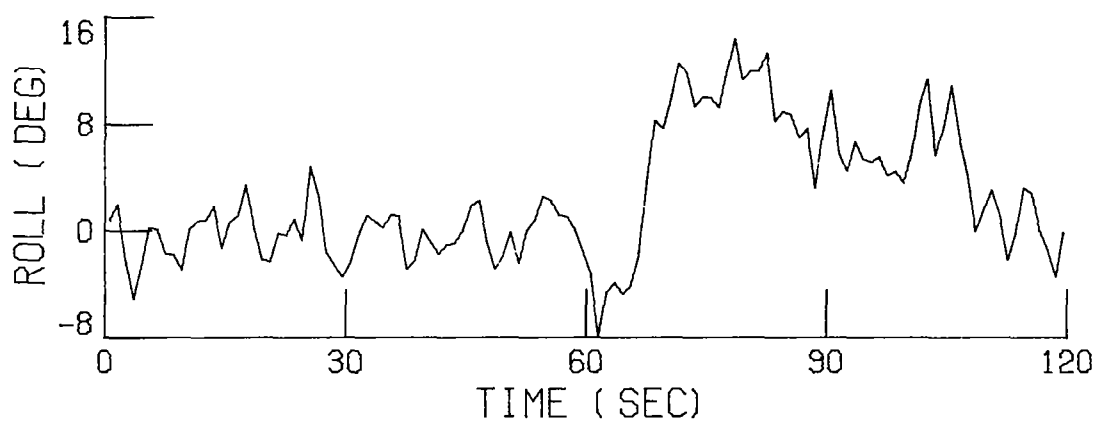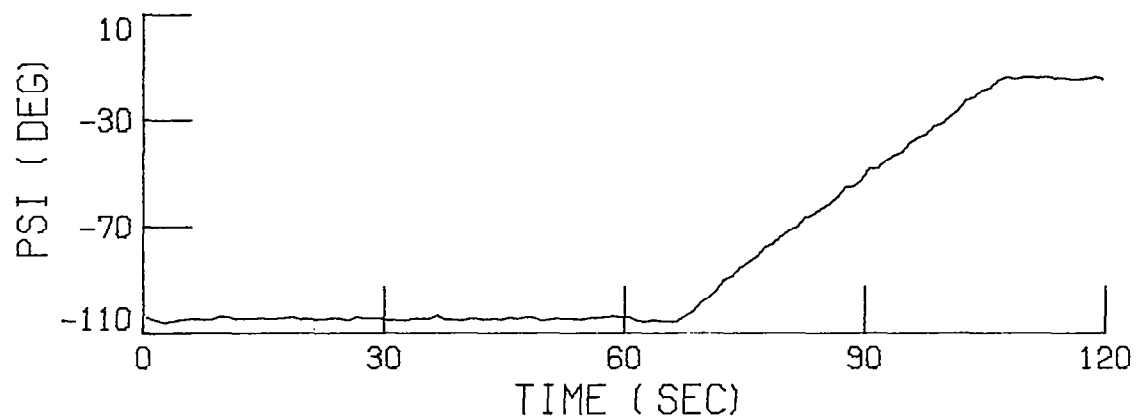
FIGURE 33   A 45 deg HEADING CHANGE USING THE HDG SEL AUTOPILOT IN HEAVY TURBULENCE
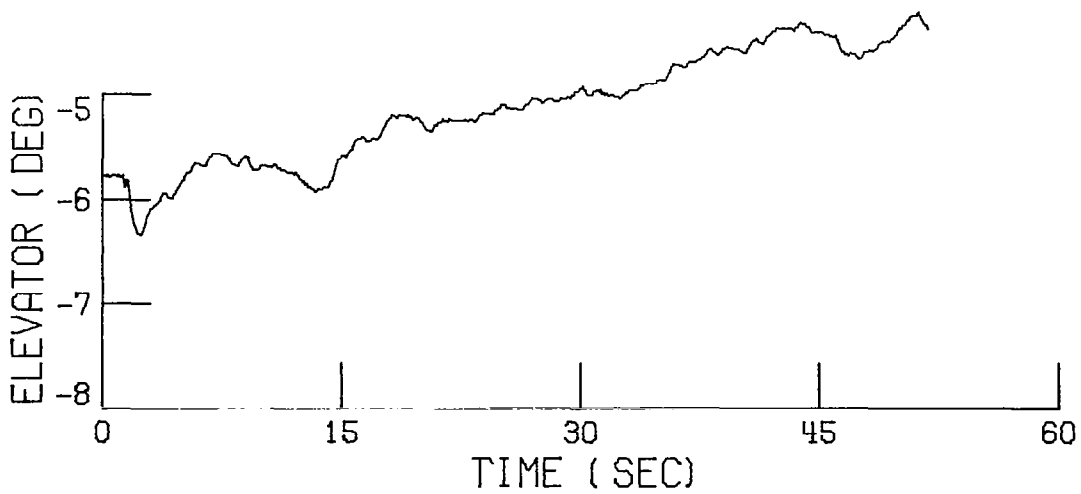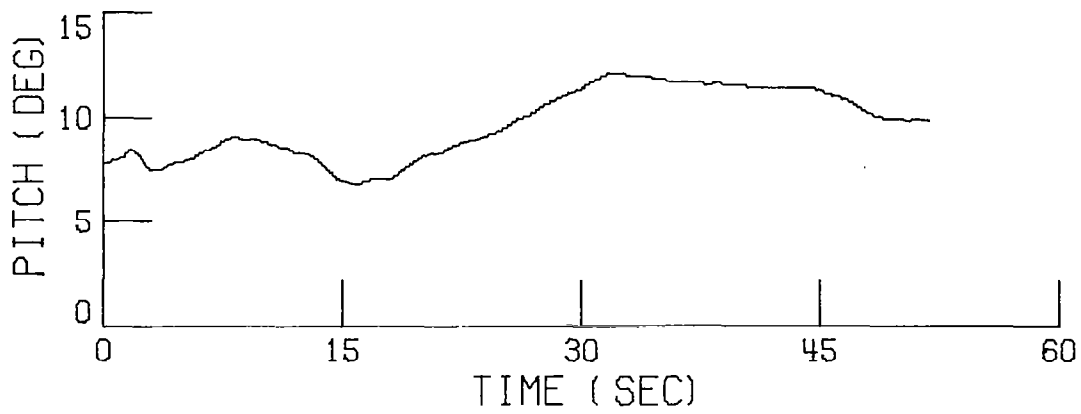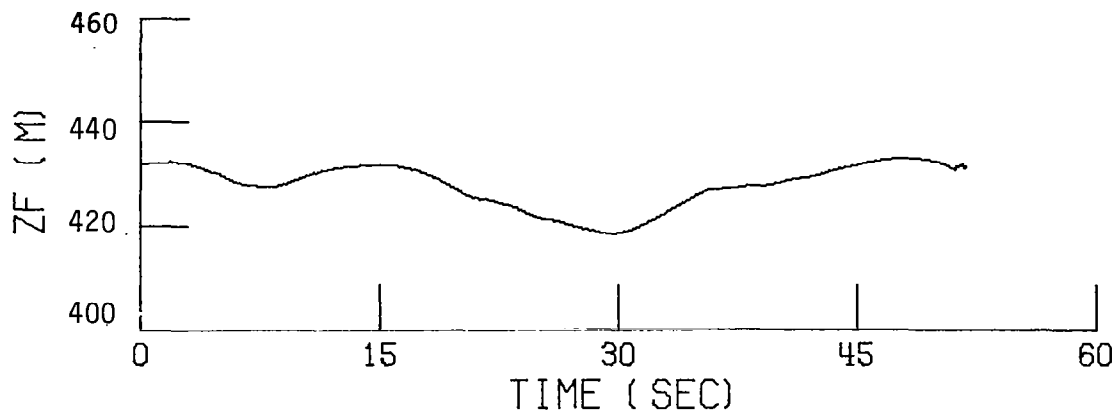
FIGURE 34   A 5 deg PITCH CHANGE USING THE PITCH SEL AUTOPILOT

147
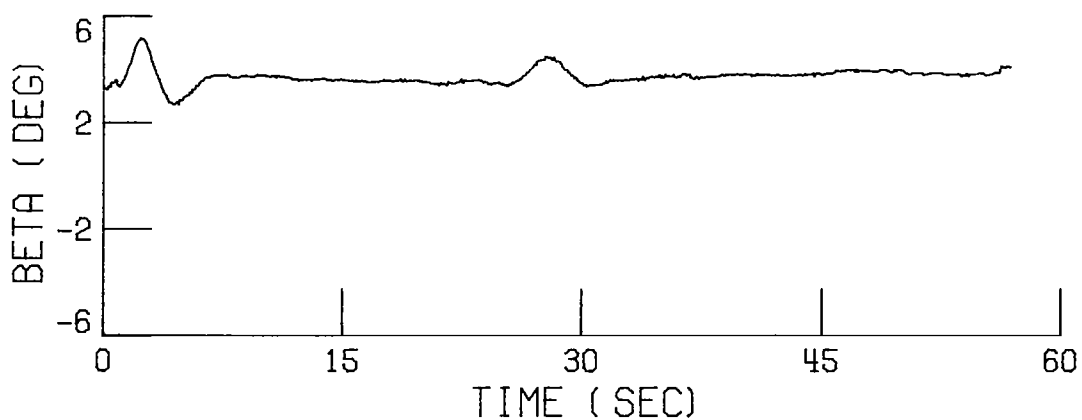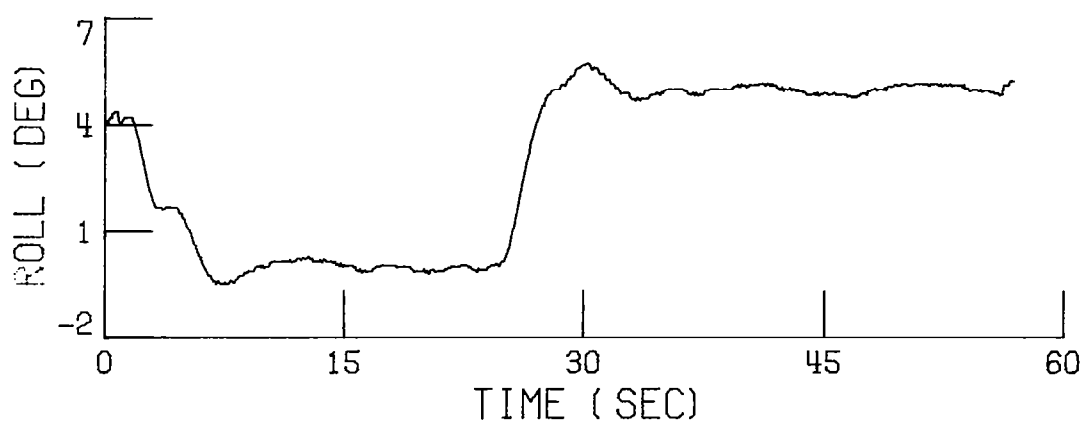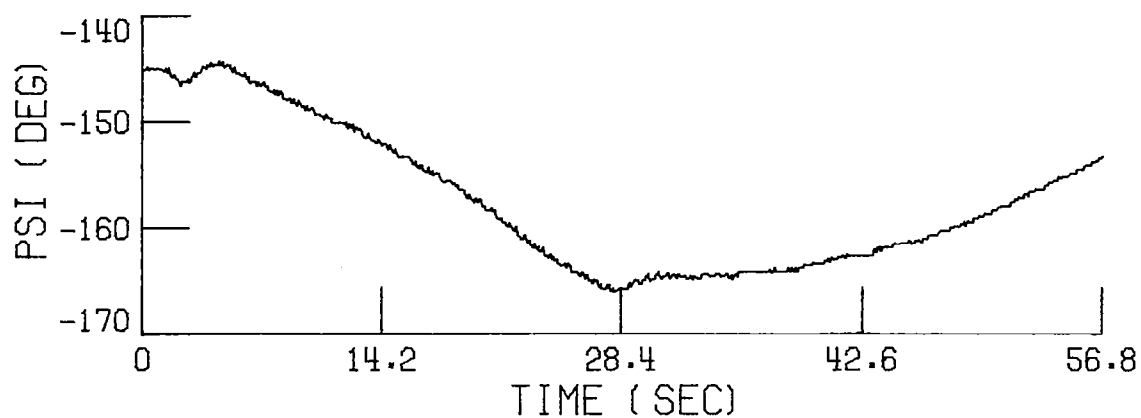
FIGURE 35   A 5 deg ROLL CHANGE USING THE ROLL SEL AUTOPILOT
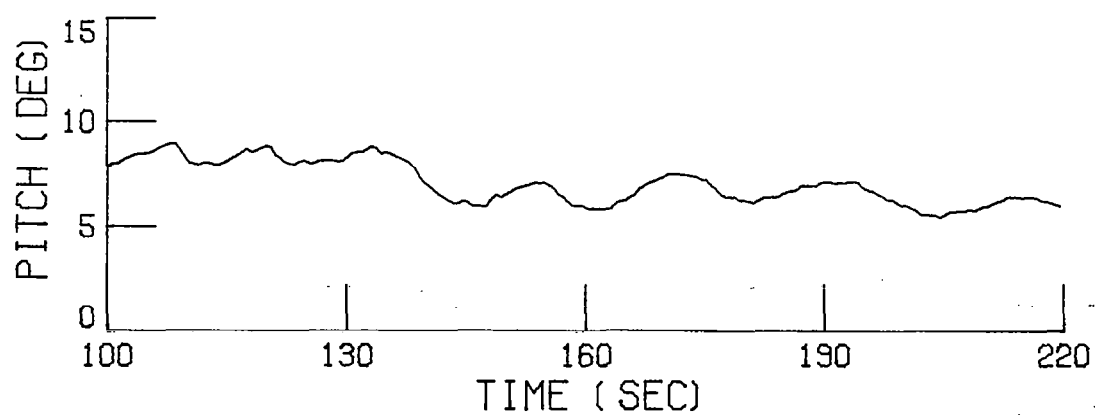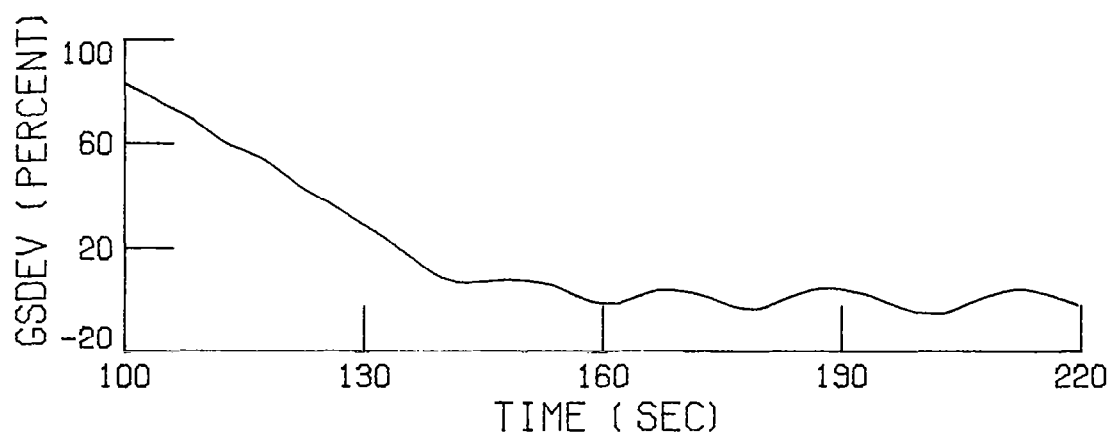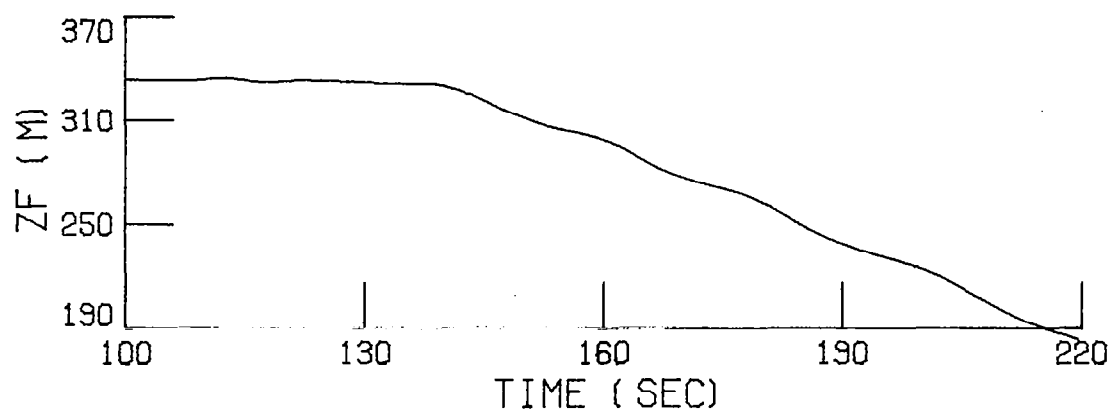
FIGURE 36   APR GS GLIDESLOPE CAPTURE AND TRACK WITH OPEN–LOOP RANGE ESTIMATION AND
THE AIRCRAFT CROSSING THE OUTER MARKER
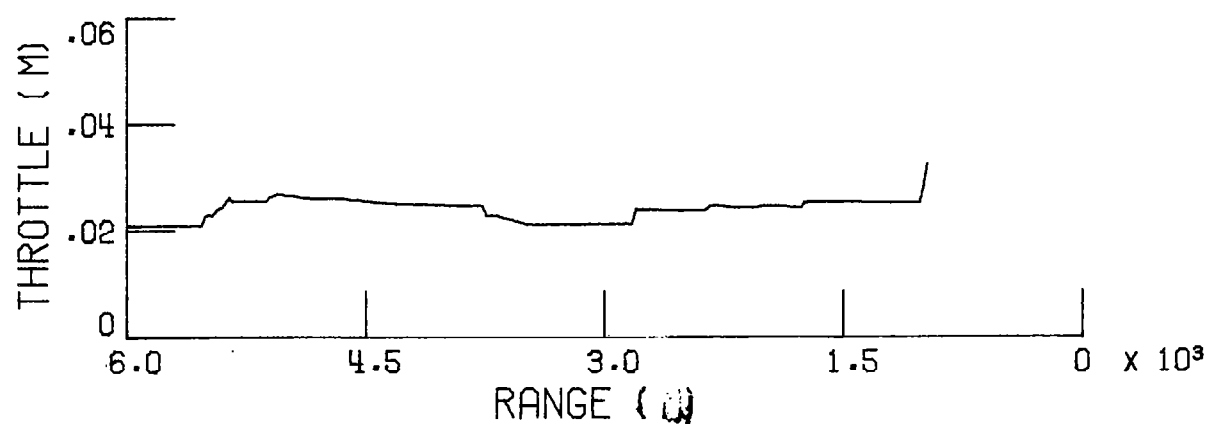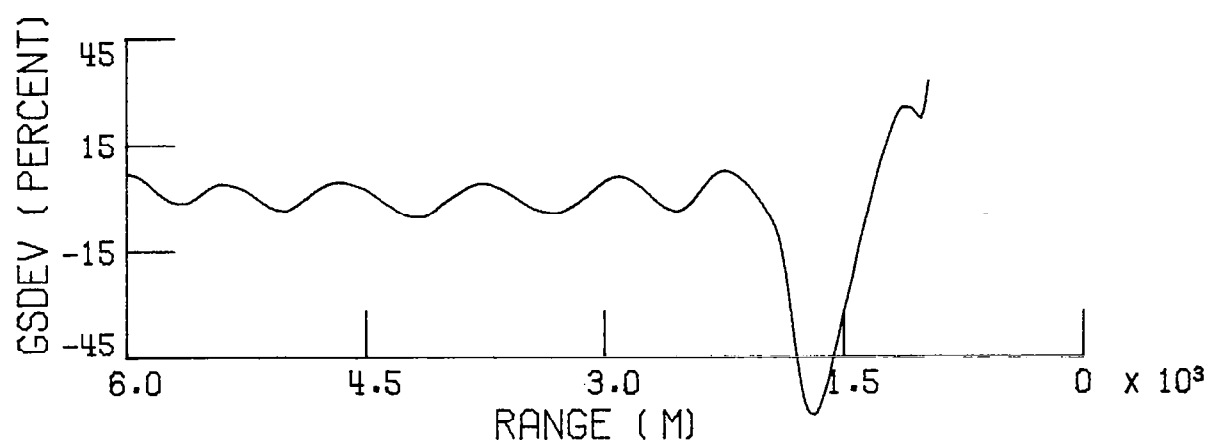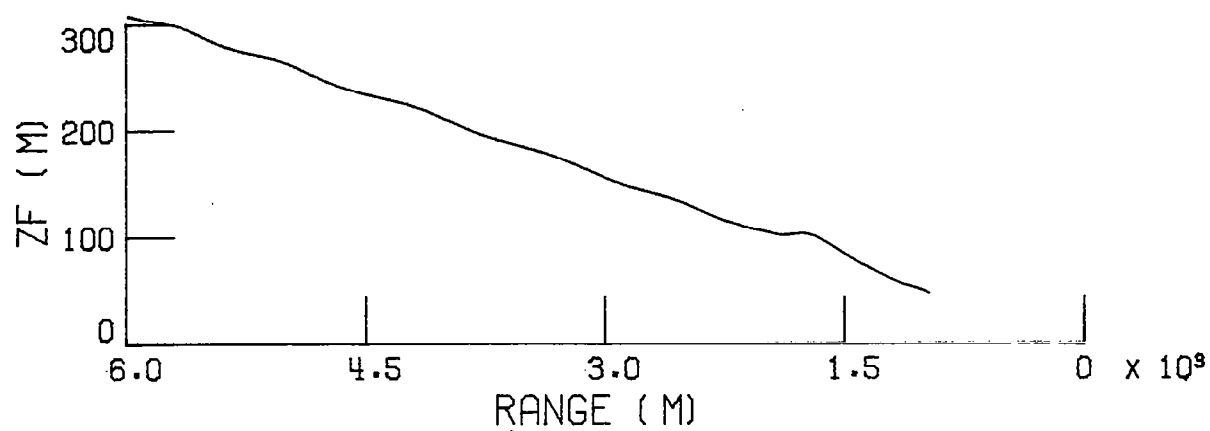
FIGURE 36 (CONTINUED)   APR GS GLIDESLOPE CAPTURE AND TRACK WITH OPEN-LOOP RANGE
ESTIMATION AND THE AIRCRAFT CROSSING THE OUTER MARKER
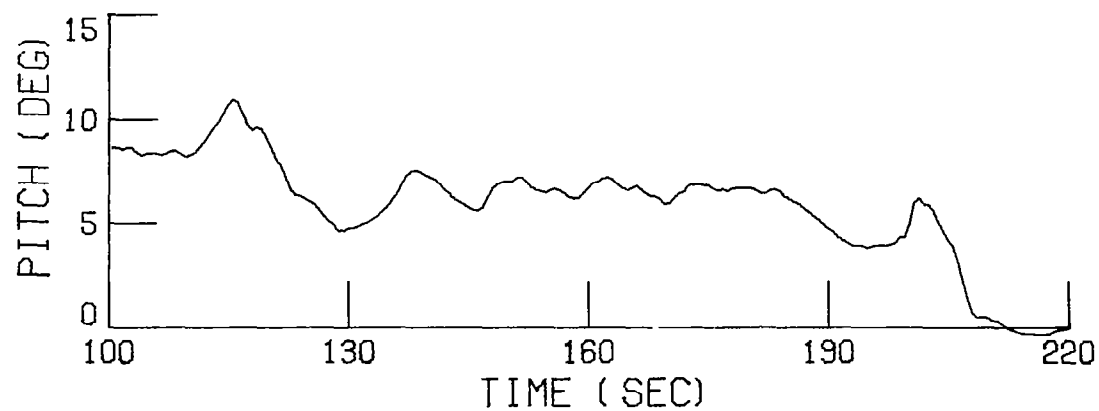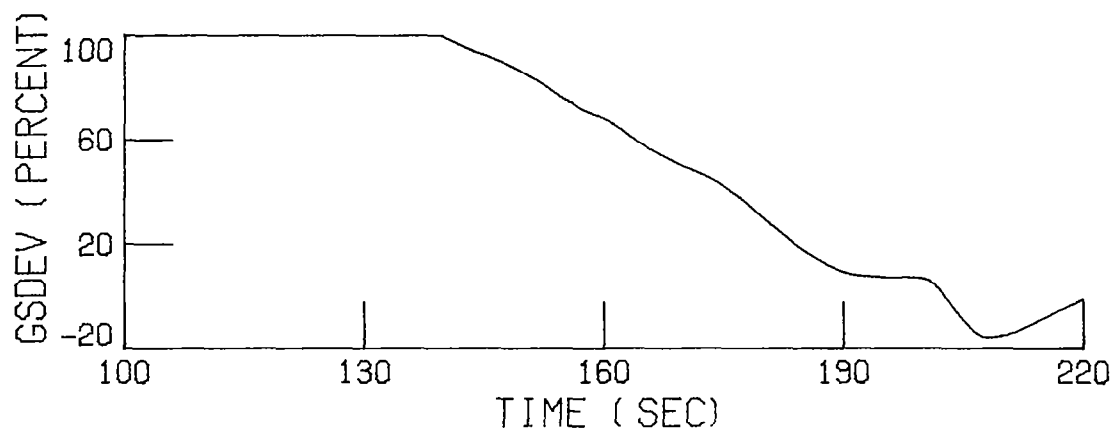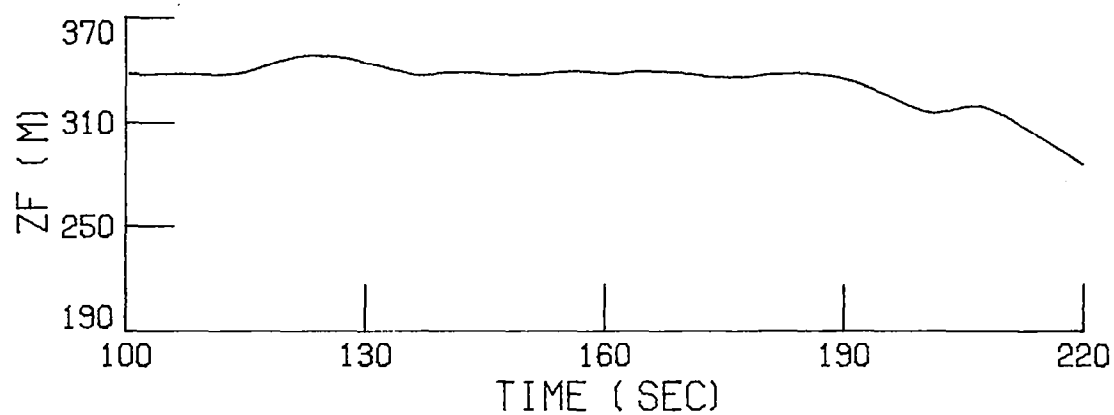
FIGURE 37   APR GS GLIDESLOPE CAPTURE AND TRACK WITH CLOSED-LOOP RANGE ESTIMATION AND
THE AIRCRAFT CROSSING THE OUTER MARKER
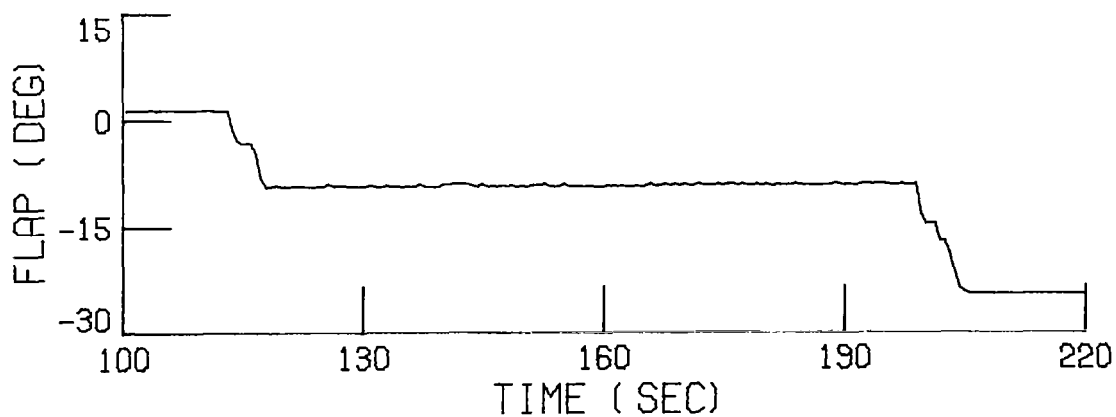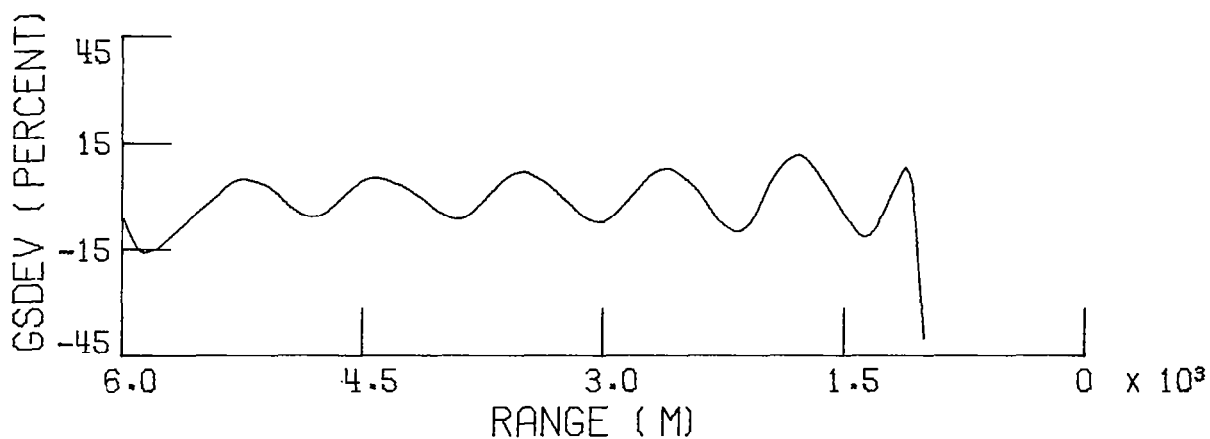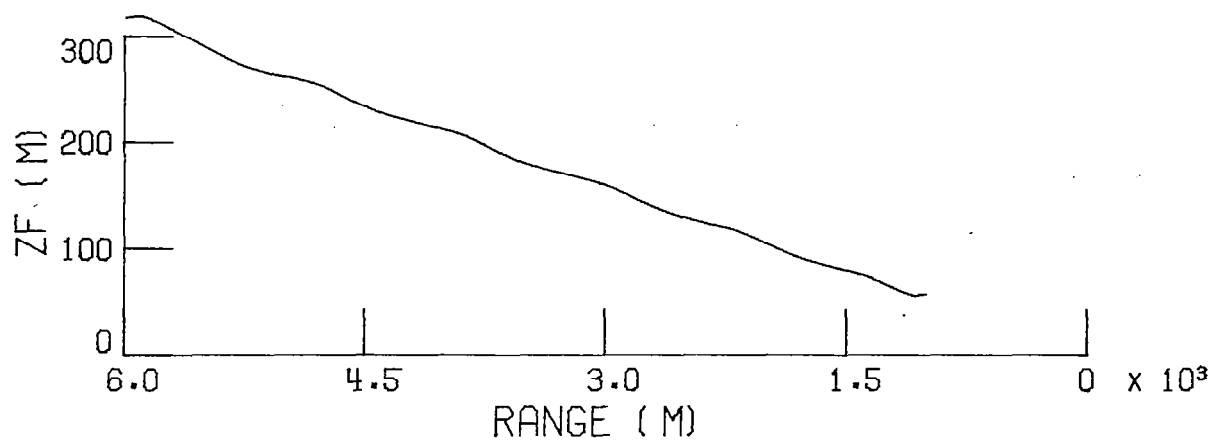
FIGURE 37 (CONTINUED)   APR GS GLIDESLOPE CAPTURE AND TRACK WITH CLOSED-LOOP RANGE
ESTIMATION AND THE AIRCRAFT CROSSING THE OUTER MARKER
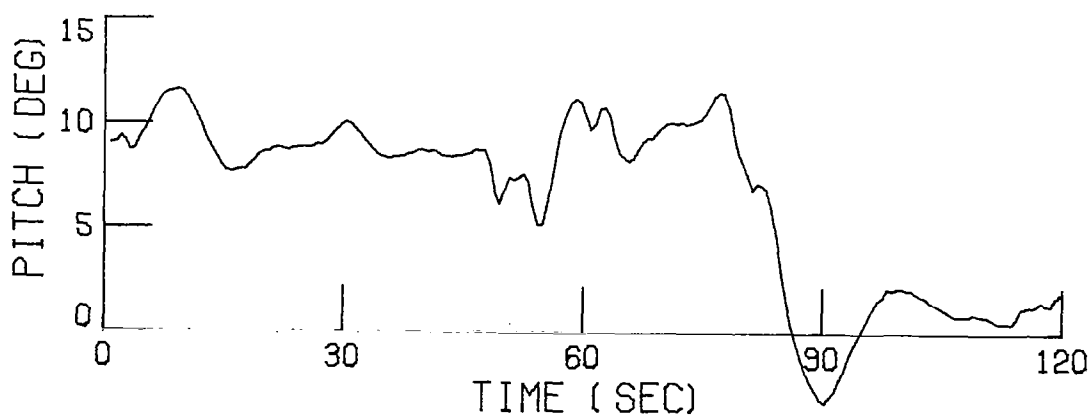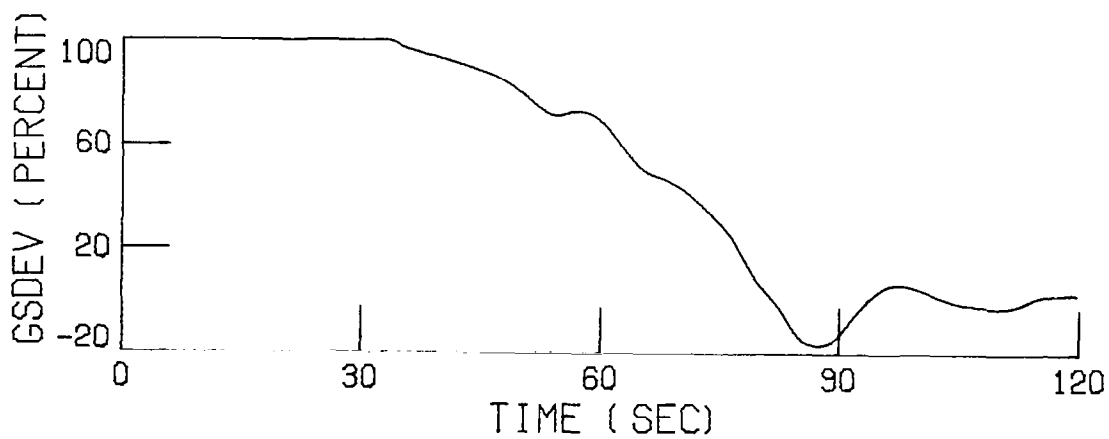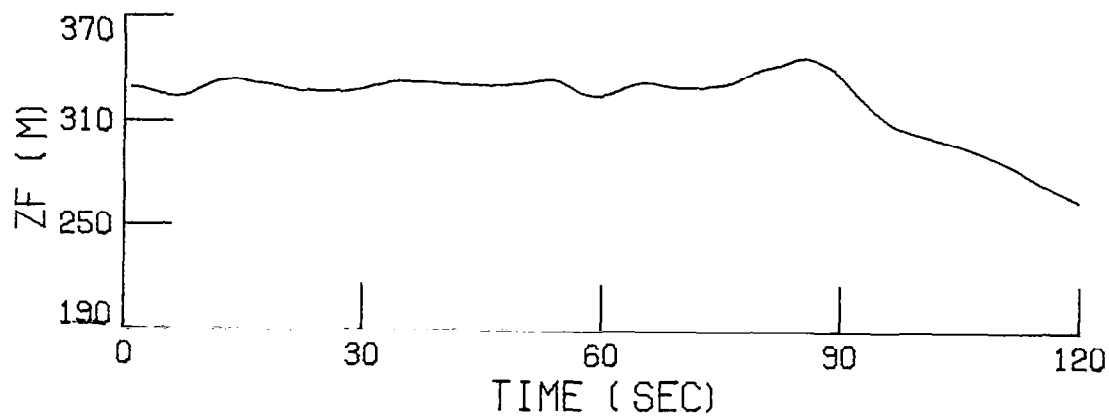
FIGURE 38   APR GS GLIDESLOPE CAPTURE AND TRACK WITH CLOSED-LOOP RANGE ESTIMATION
AND THE AIRCRAFT MISSING THE OUTER MARKER
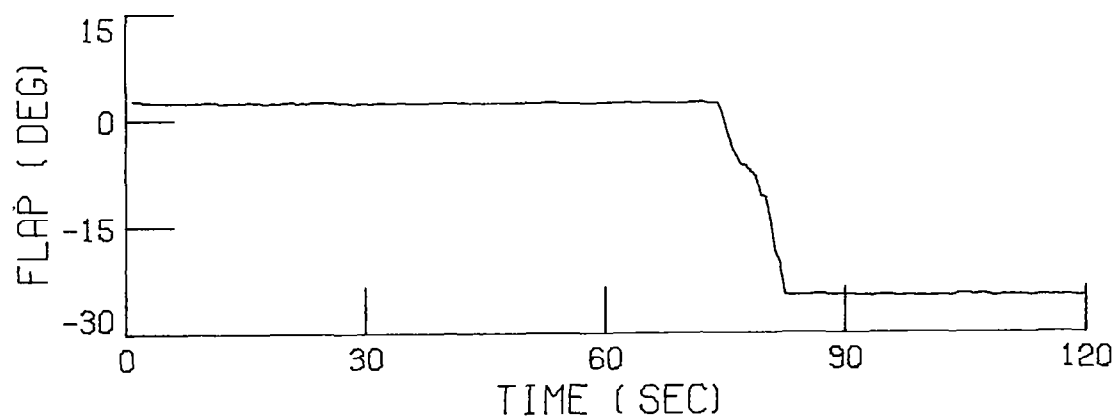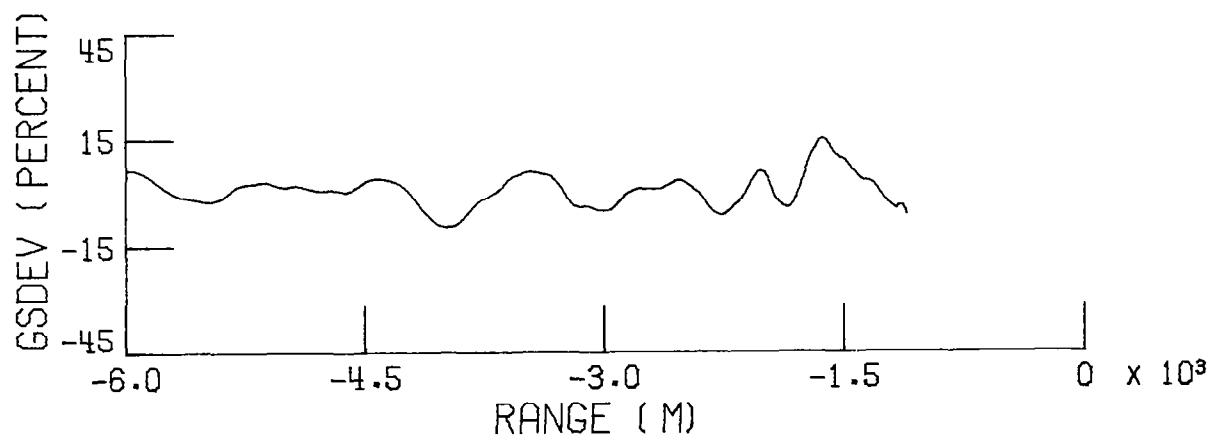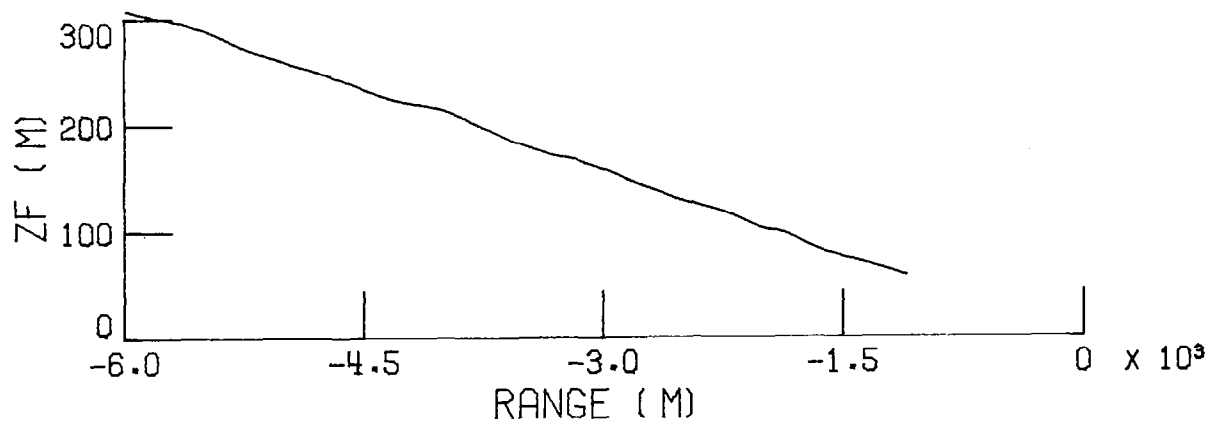
FIGURE 38 (CONTINUED)   ARP GS GLIDESLOPE CAPTURE AND TRACK WITH CLOSED-LOOP RANGE
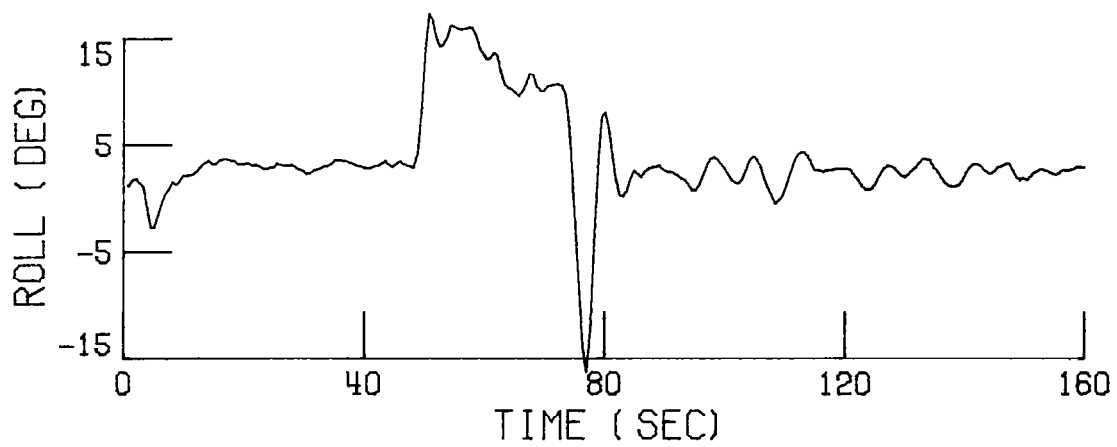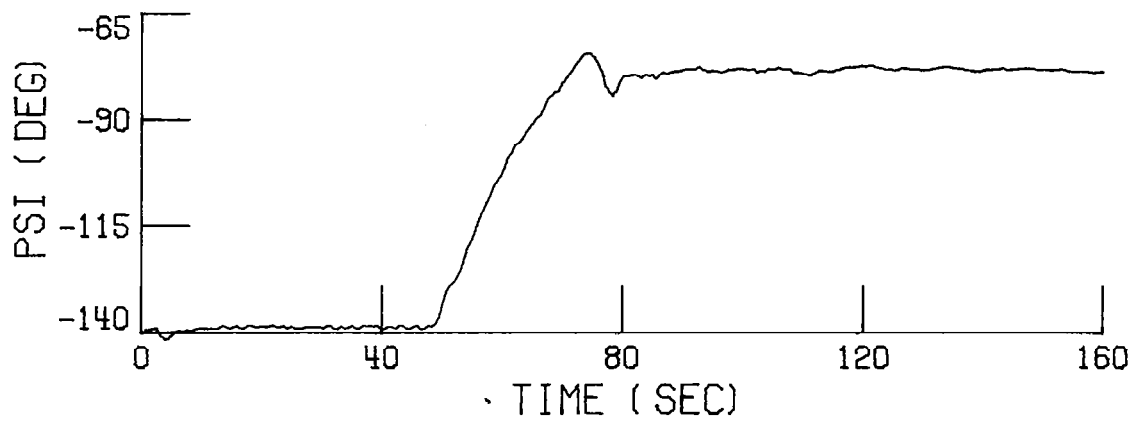ESTIMATION AND THE AIRCRAFT MISSING THE OUTER MARKER

154
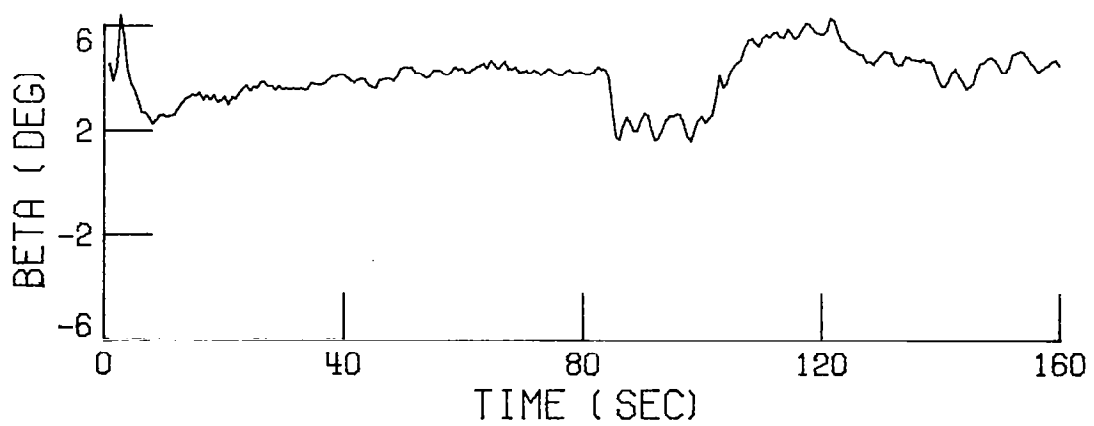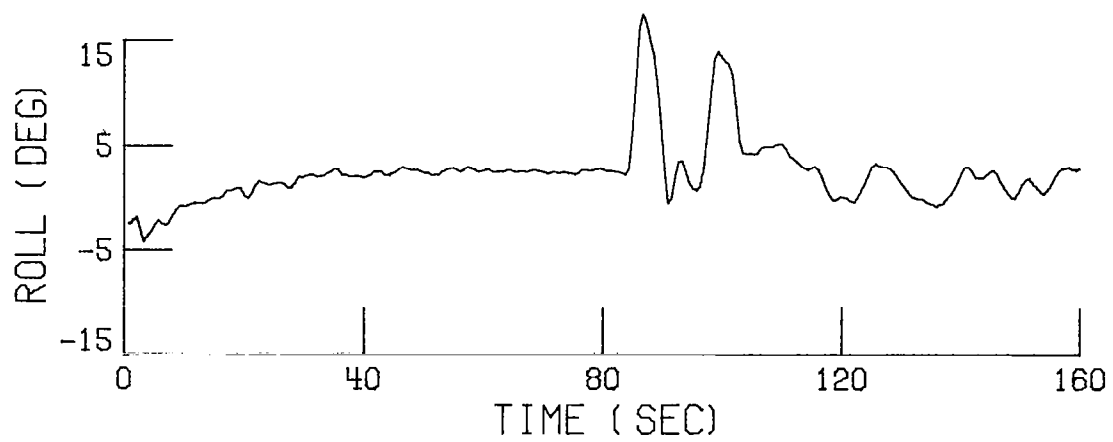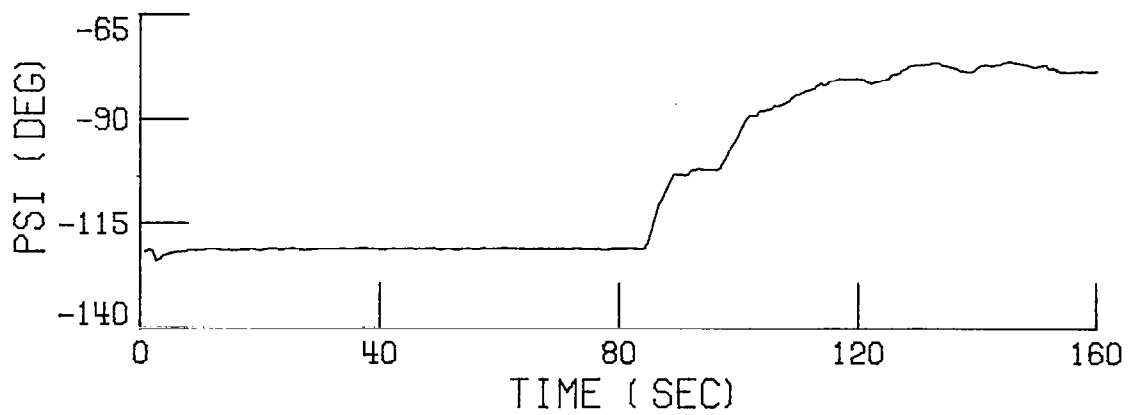
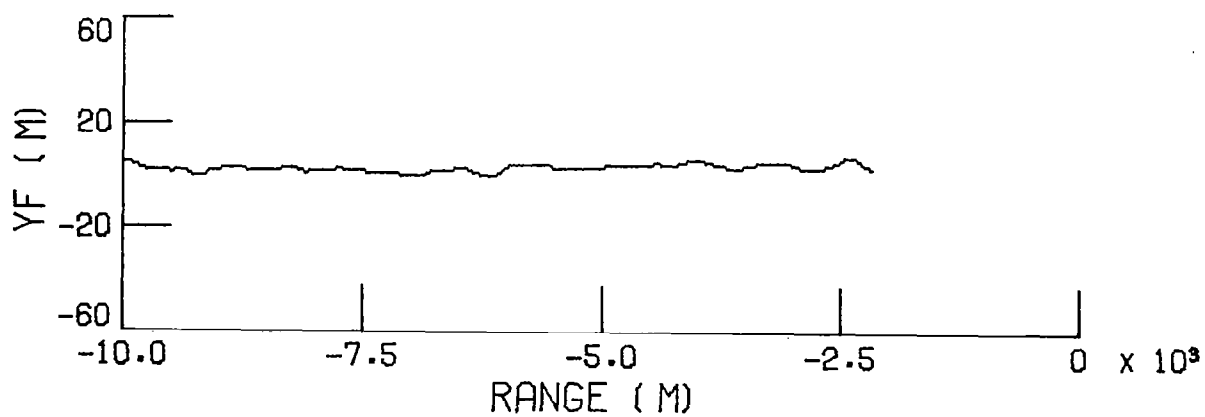FIGURE 39   APR LOCR LOCALIZER CAPTURE AND TRACK FOR A 45 deg INTERCEPT ANGLE
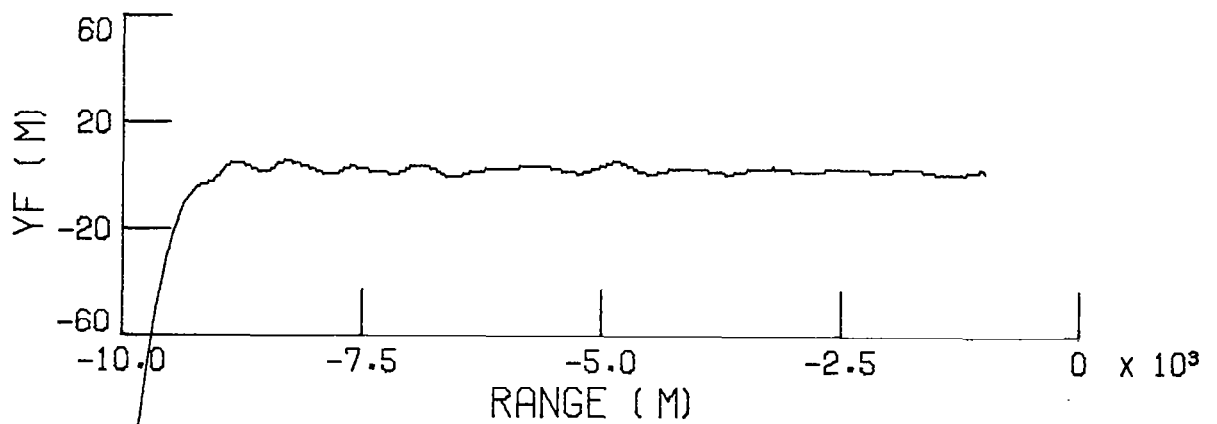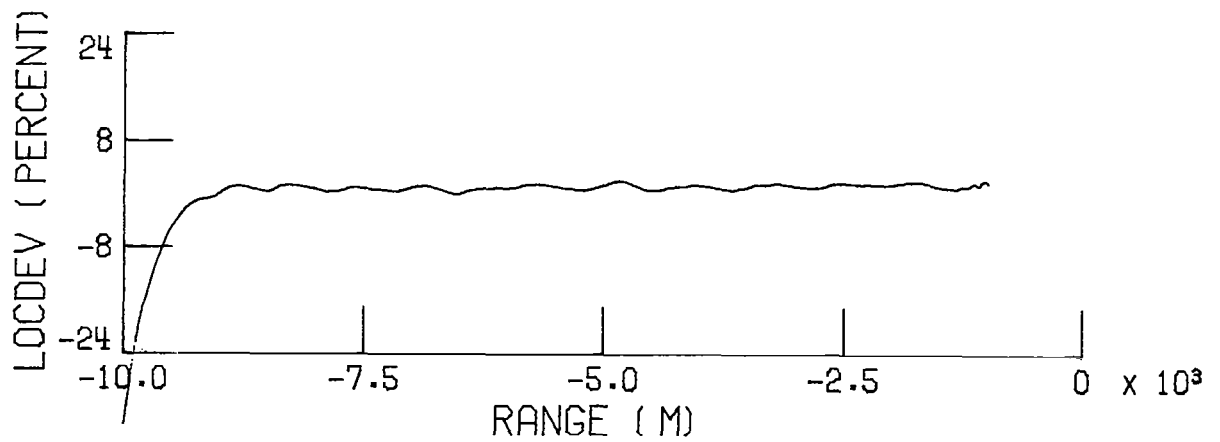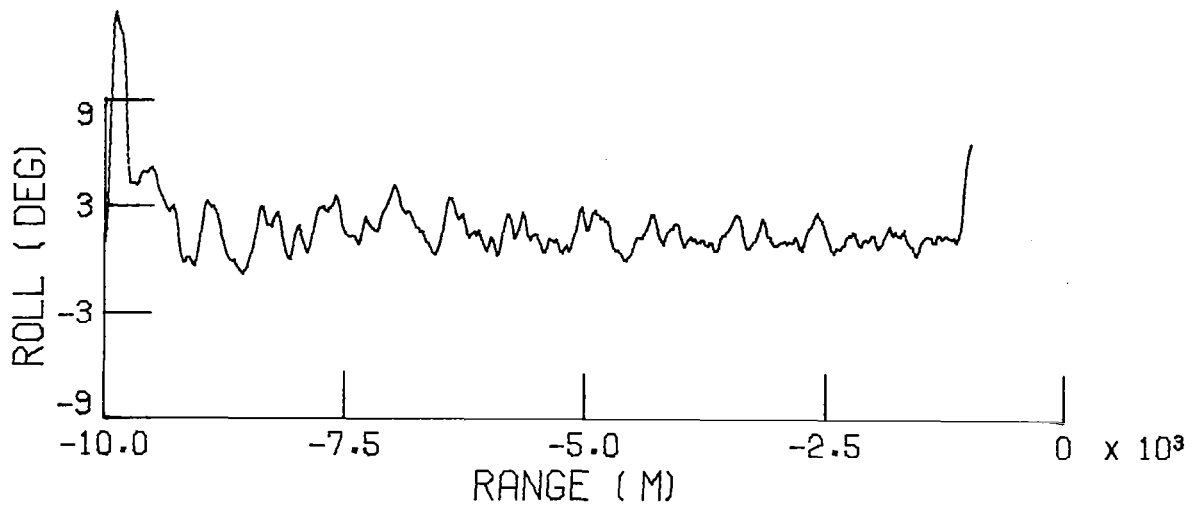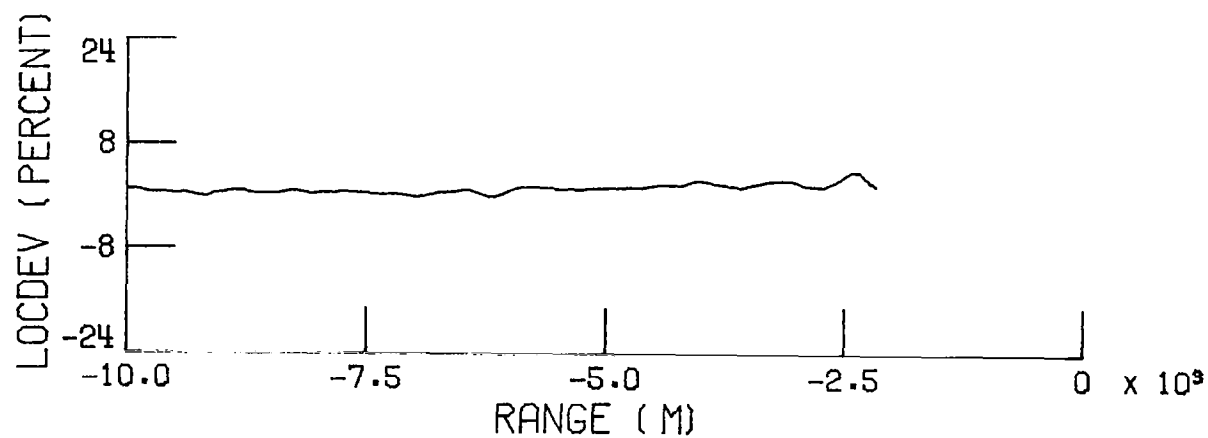
FIGURE 39 (CONTINUED)   APR LOCR LOCALIZER CAPTURE AND TRACK FOR A 45 deg INTERCEPT
ANGLE
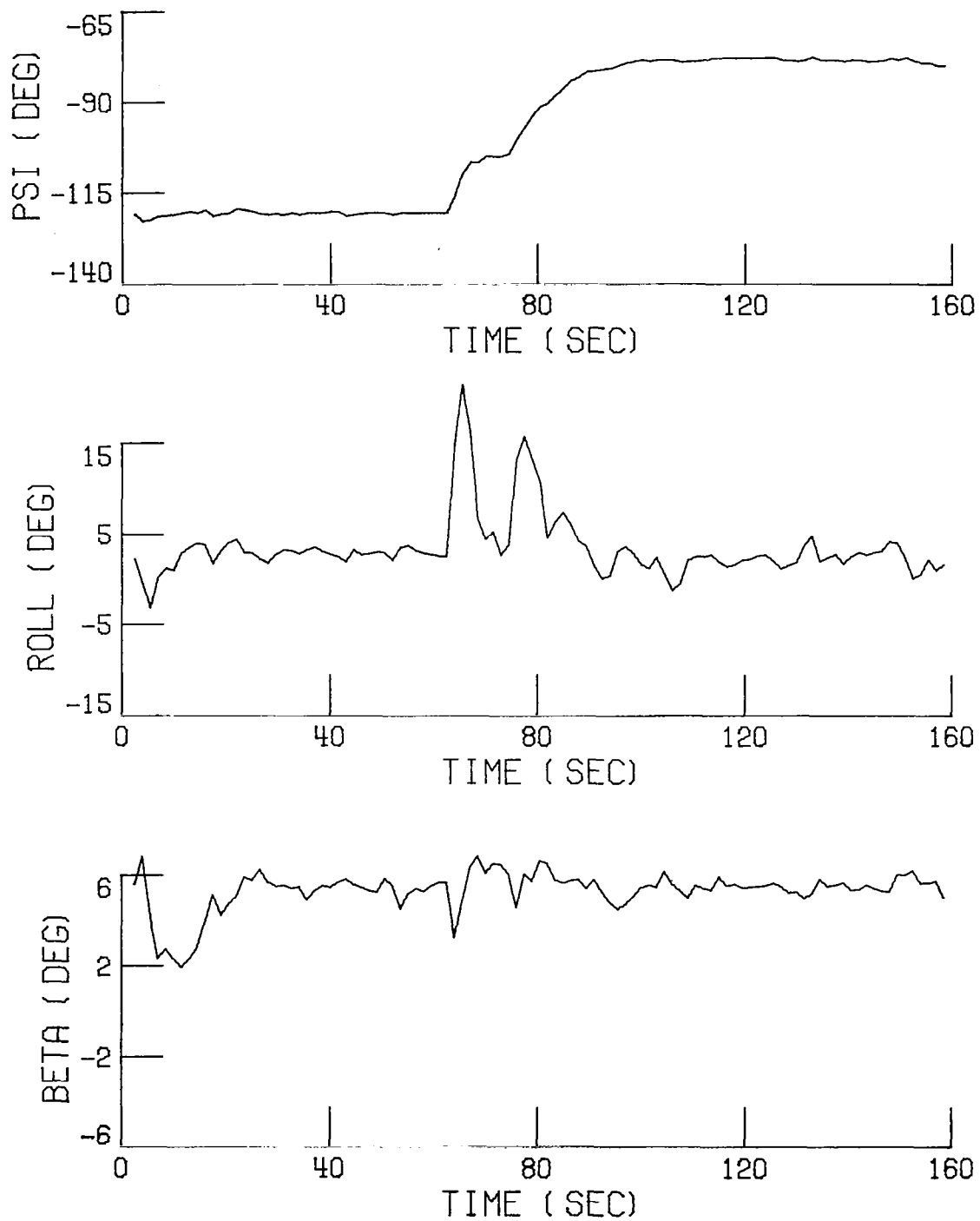
FIGURE 40   APR LOCP LOCALIZER CAPTURE AND TRACK FOR A 45 deg INTERCEPT ANGLE
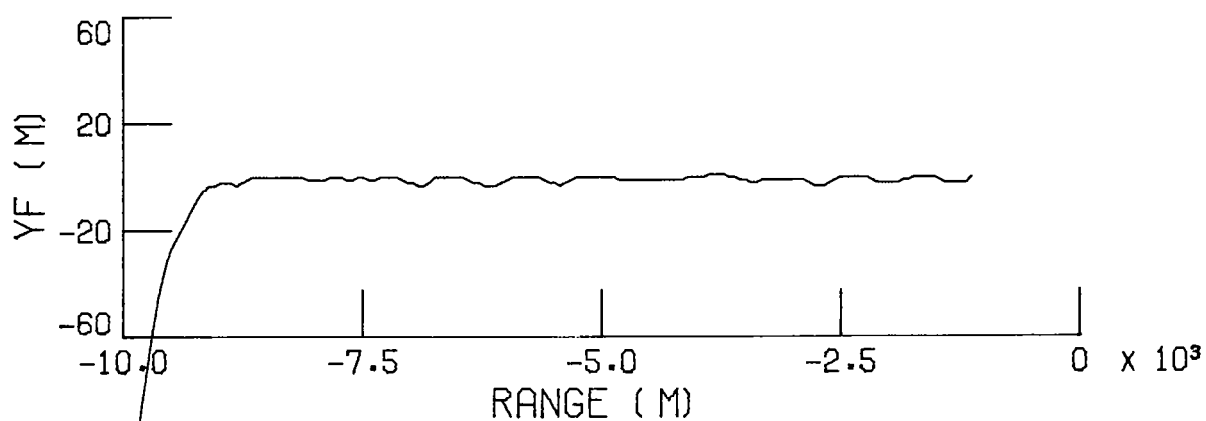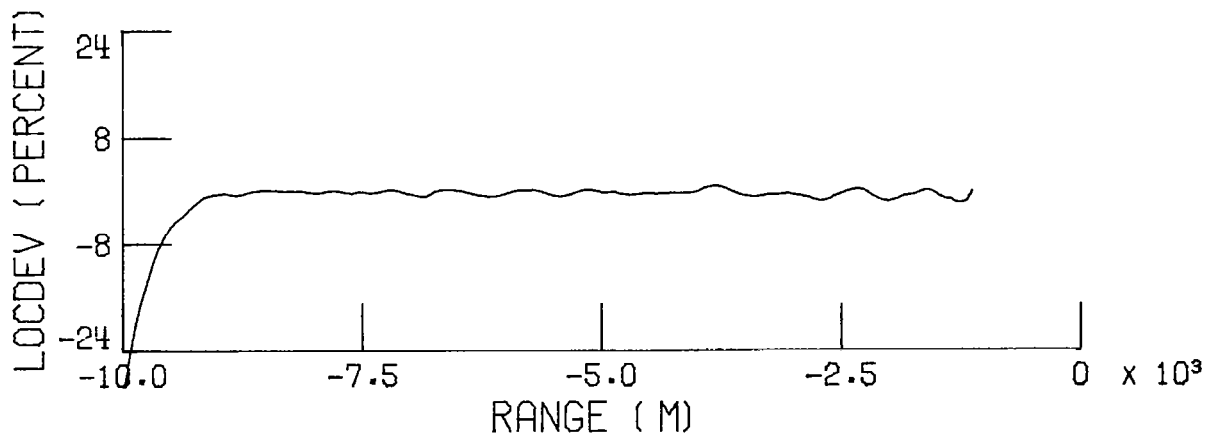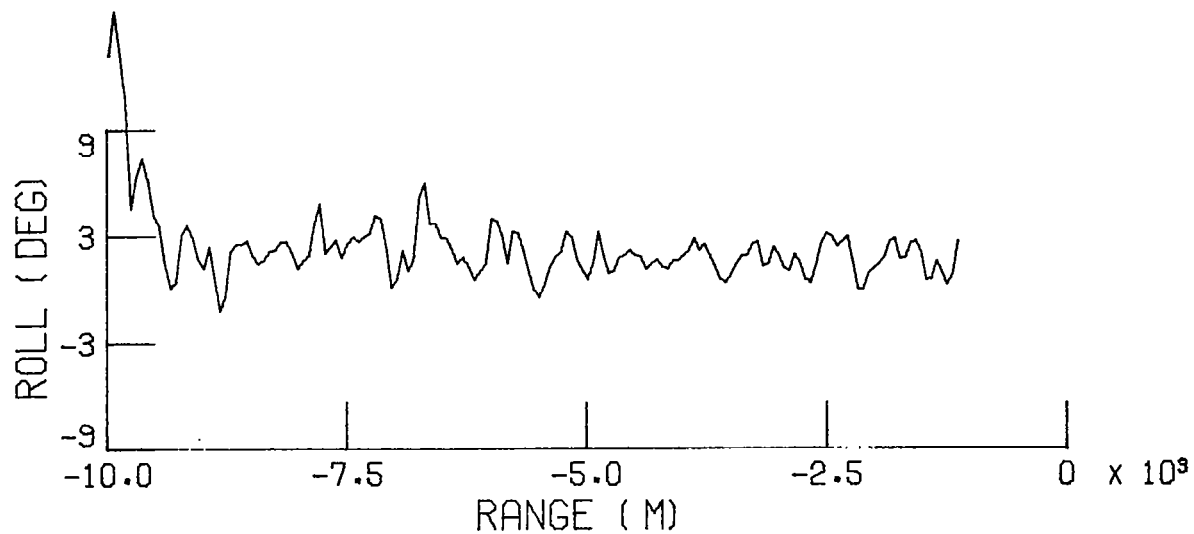
FIGURE 40 (CONTINUED) APR LOCP LOCALIZER CAPTURE AND TRACK FOR A 45 deg INTERCEPT
ANGLE

158
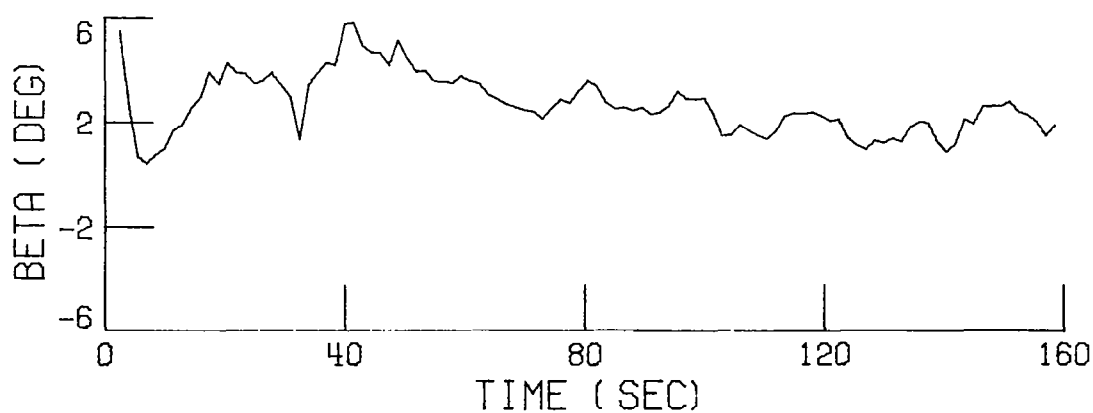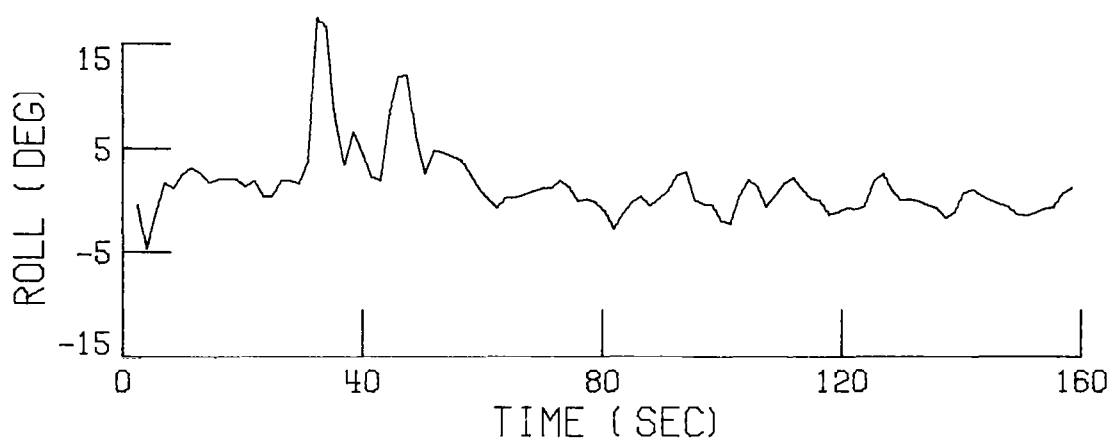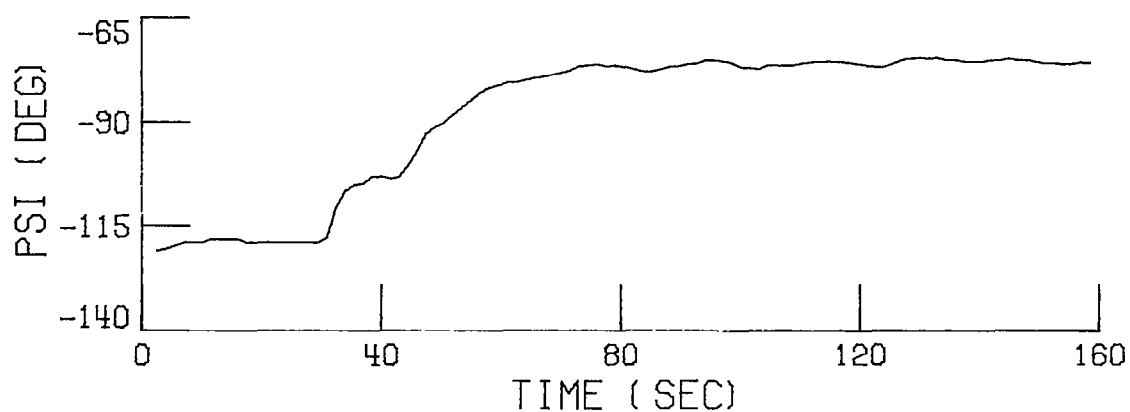
FIGURE 41   APR LOCI LOCALIZER CAPTURE AND TRACK FOR A 45 deg INTERCEPT ANGLE
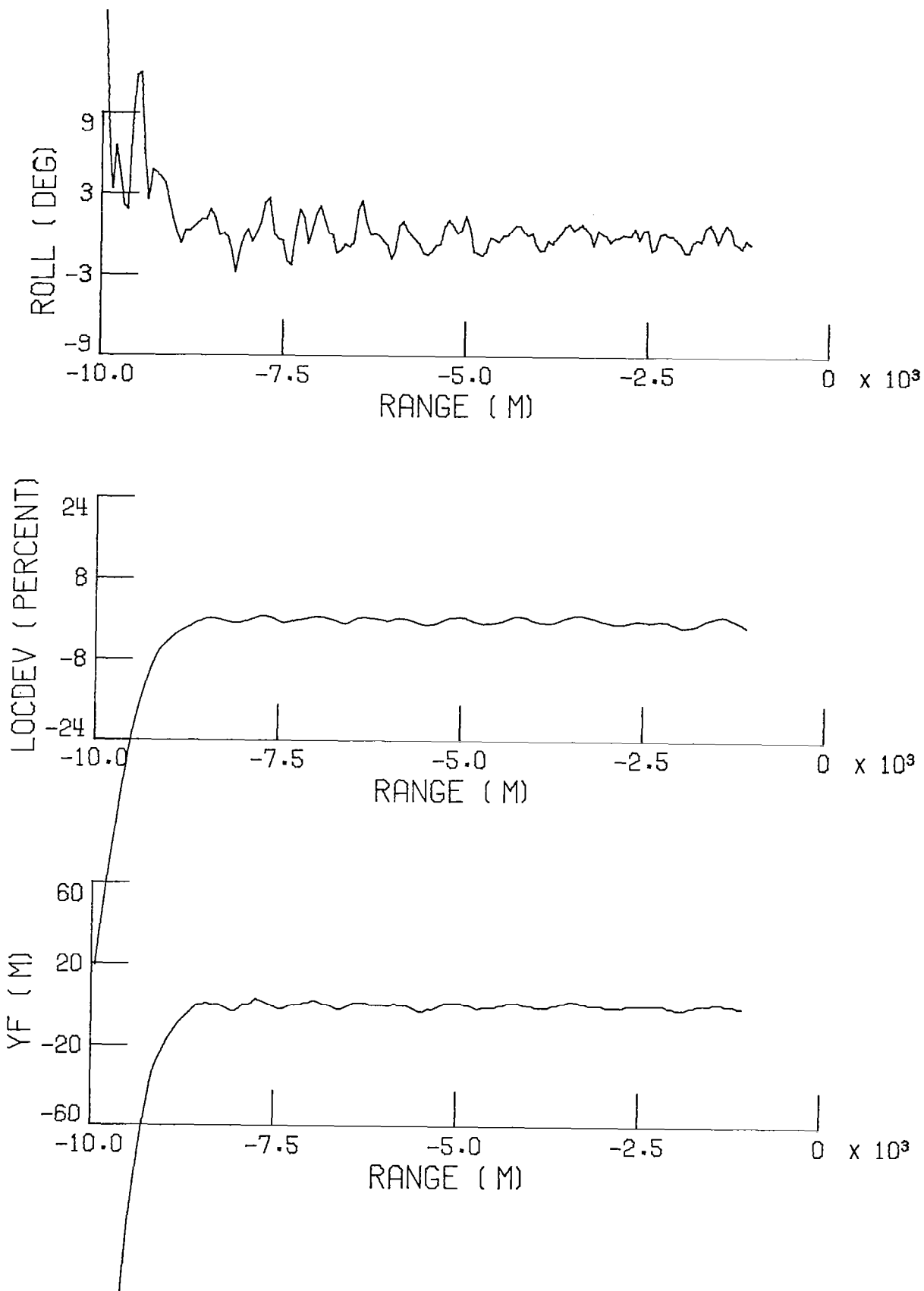
FIGURE 41 (CONTINUED)   APR LOCI LOCALIZER CAPTURE AND TRACK FOR A 45 deg INTERCEPT
ANGLE
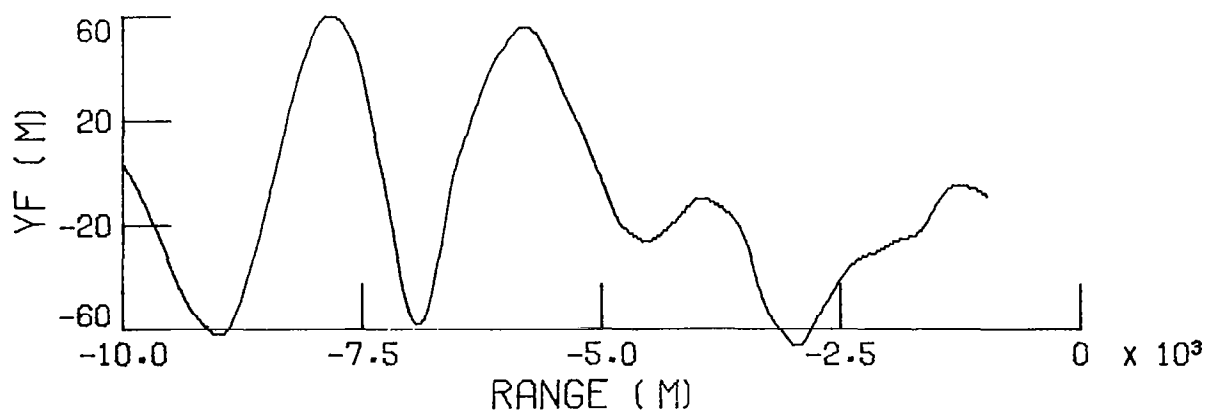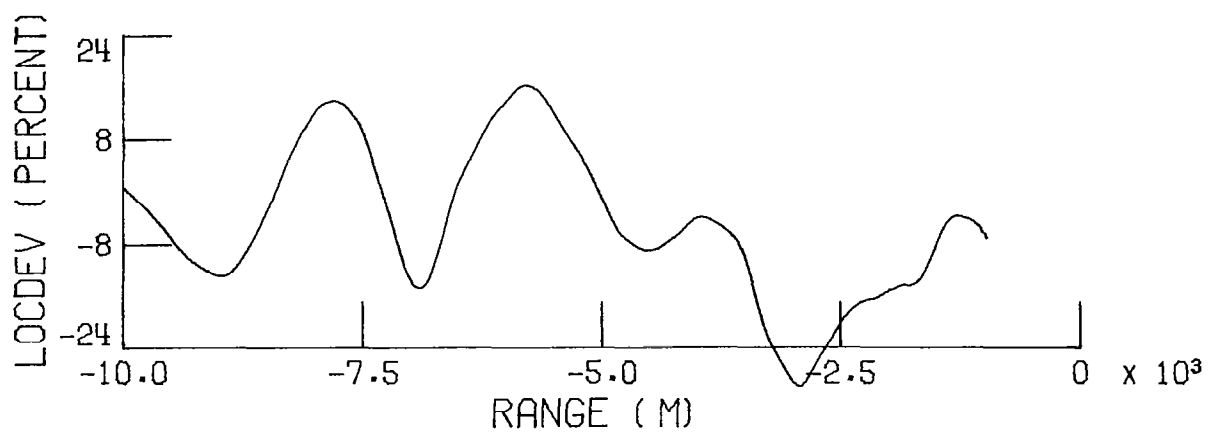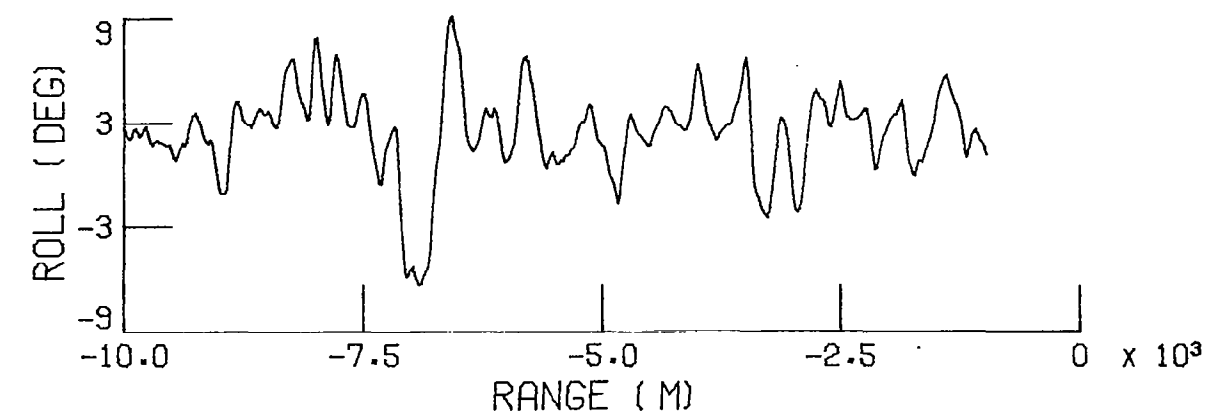
FIGURE 42   MANUAL LOCALIZER TRACKING
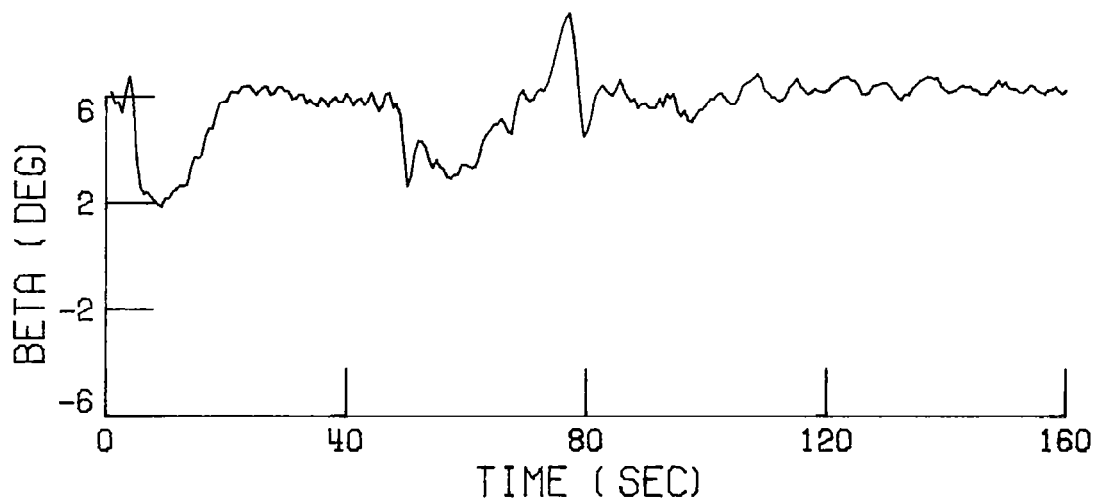
FIGURE 43 APR LOCR LOCALIZER CAPTURE AND TRACK FOR A 60 deg INTERCEPT ANGLE

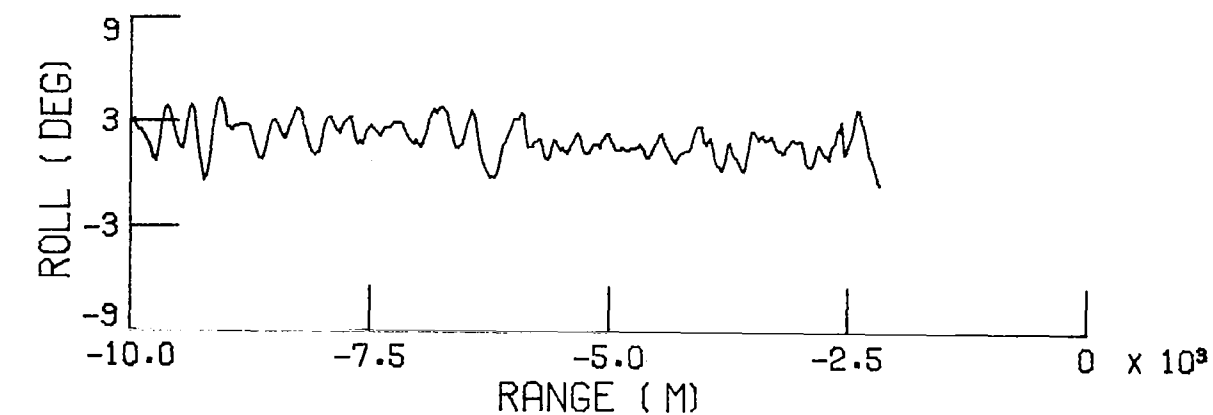FIGURE 43 (CONTINUED)   APR LOCR LOCALIZER CAPTURE AND TRACK FOR A 60 deg INTERCEPT
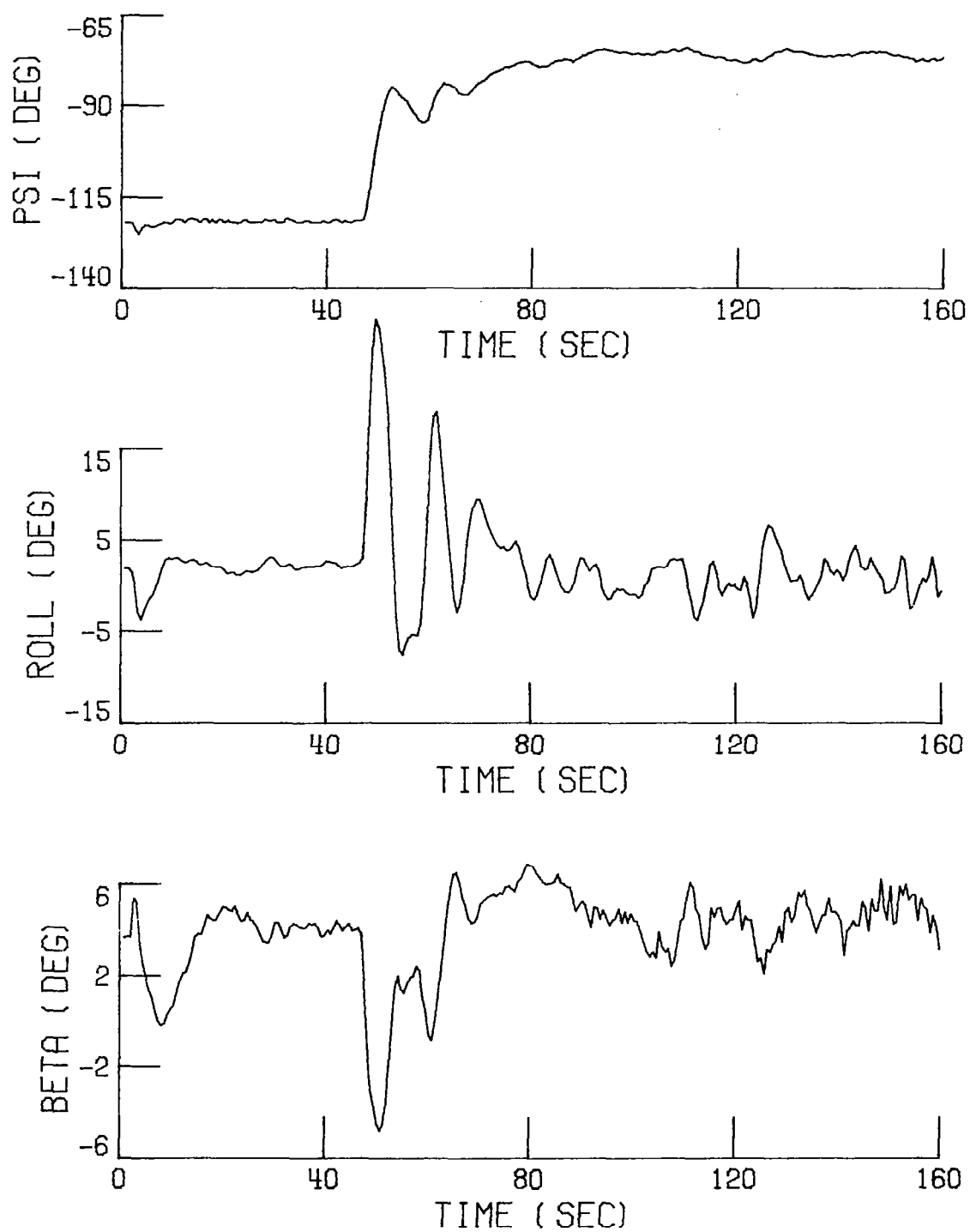ANGLE

FIGURE 44   APR LOCR LOCALIZER CAPTURE AND TRACK FOR A 45 deg INTERCEPT ANGLE AND
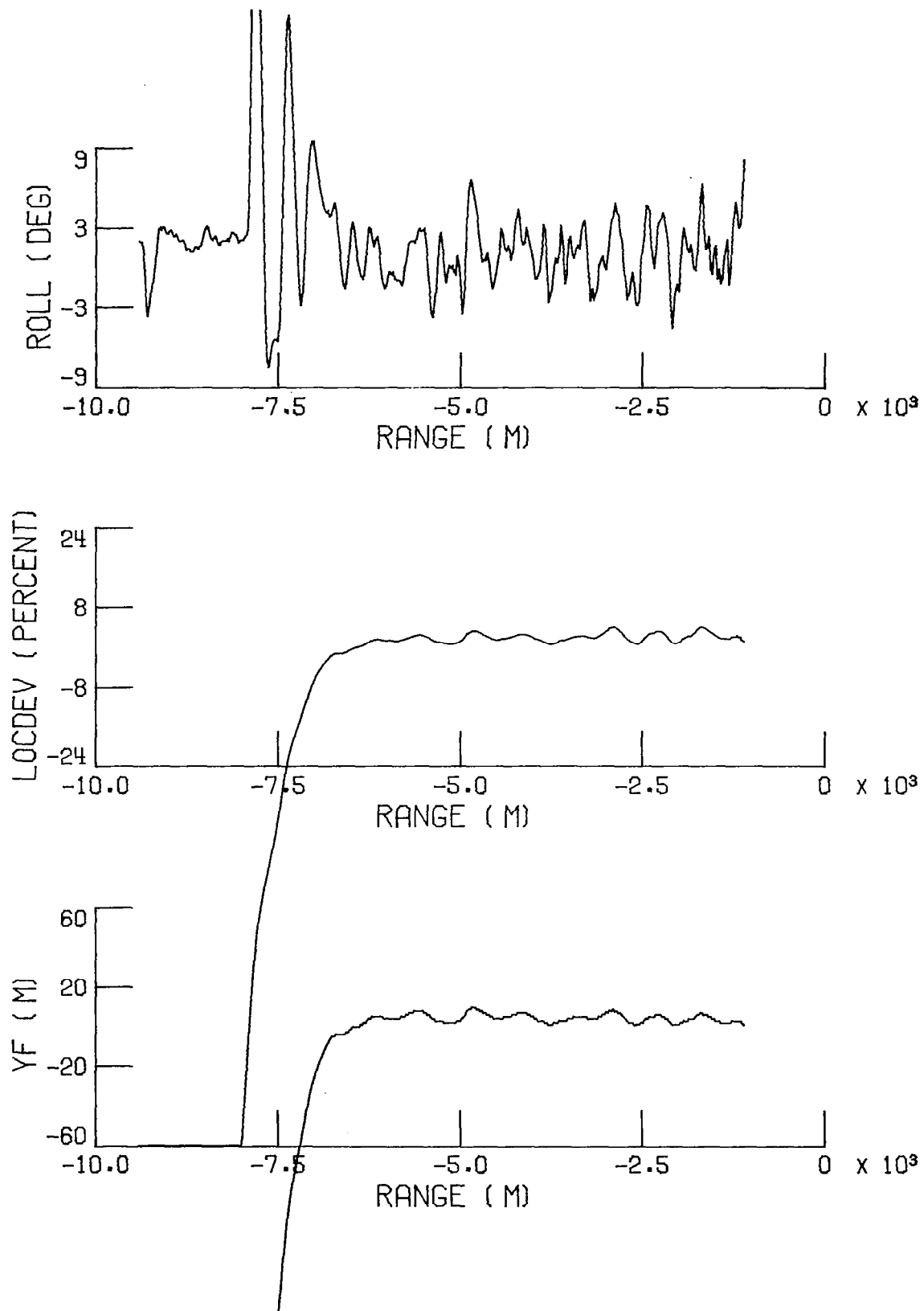THE AIRCRAFT MISSING THE OUTER MARKER

FIGURE 44 (CONTINUED)   APR LOCR LOCALIZER CAPTURE AND TRACK FOR A 45 deg INTERCEPT
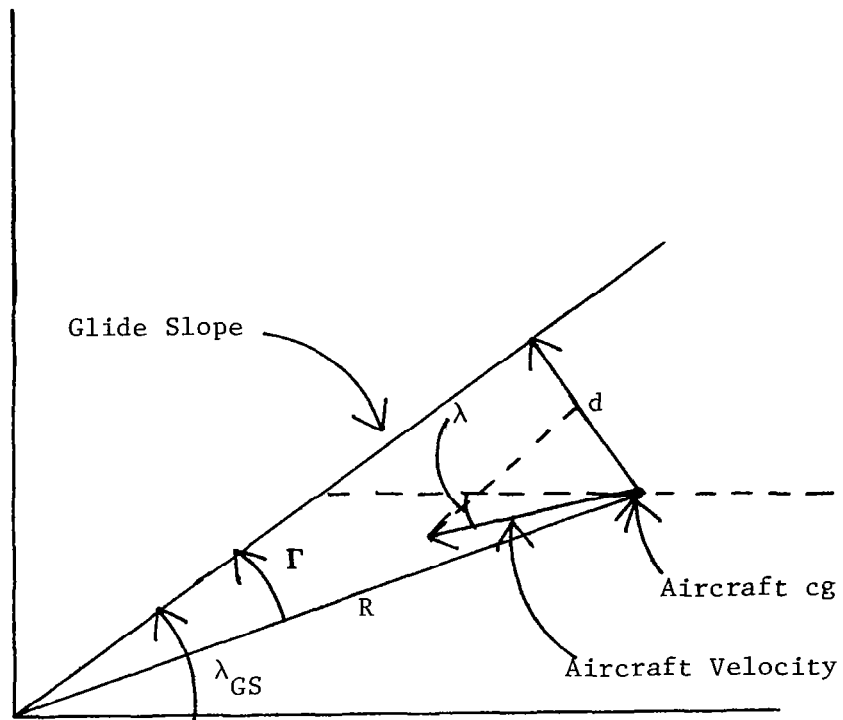ANGLE AND THE AIRCRAFT MISSING THE OUTER MARKER
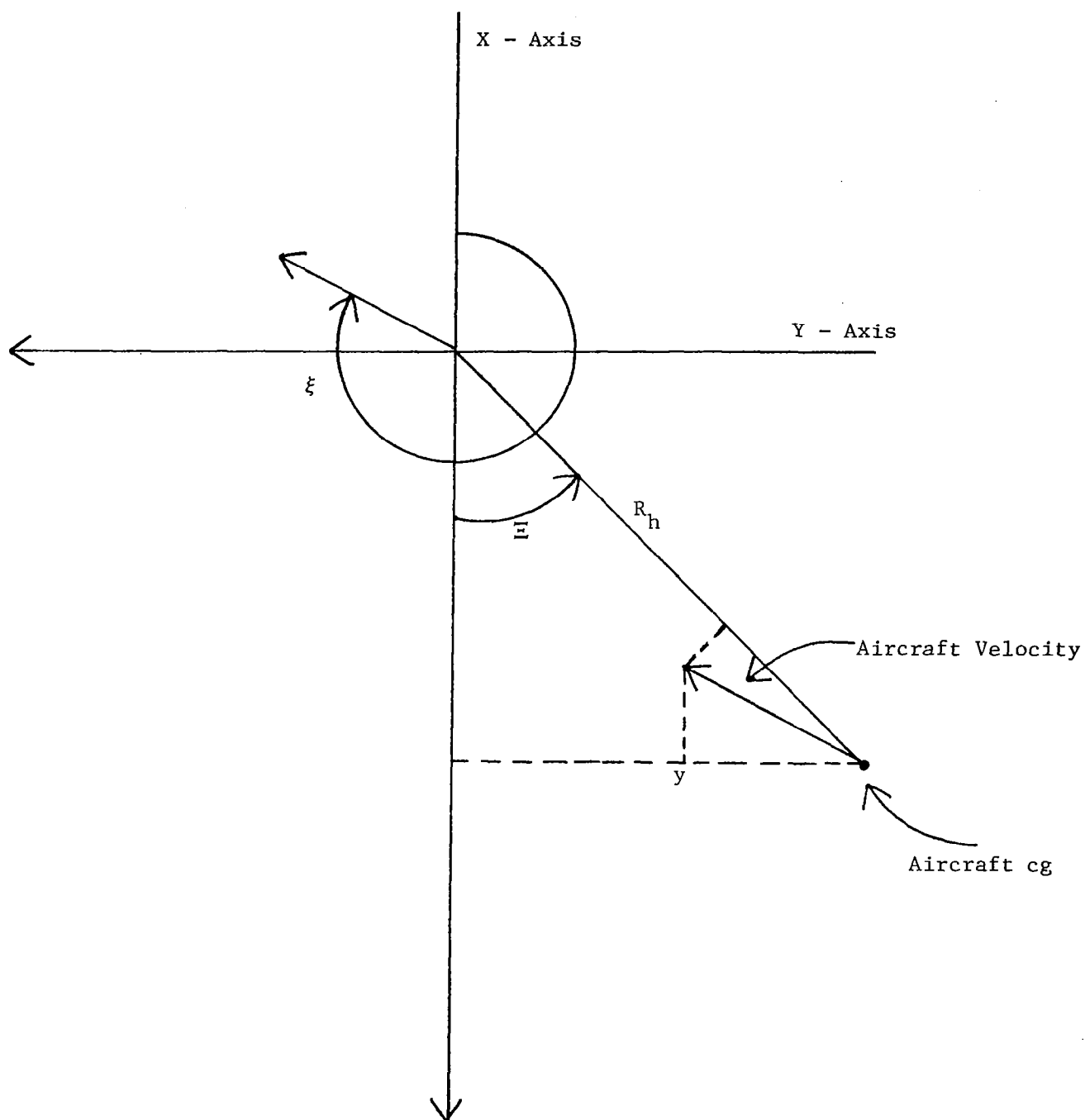
FIGURE 45   GLIDESLOPE GEOMETRY

FIGURE 46   LOCALIZER GEOMETRY

1. Report No. NASA CR-3709	2. Government Accession No.	3. Recipient's Catalog No.

4. Title and Subtitle	5. Report Date
DESIGN, IMPLEMENTATION AND FLIGHT TESTING OF PIF AUTOPILOTS FOR GENERAL AVIATION AIRCRAFT	July 1983
	6. Performing Organization Code

7. Author(s)	8. Performing Organization Report No.
JOHN R. BROUSSARD	TR-681102
	10. Work Unit No.

9. Performing Organization Name and Address	11. Contract or Grant No.
INFORMATION & CONTROL SYSTEMS, INCORPORATED 28 RESEARCH DRIVE HAMPTON, VA 23666	NAS1-16303
	13. Type of Report and Period Covered

12. Sponsoring Agency Name and Address	CONTRACTOR REPORT
NATIONAL AERONAUTICS AND SPACE ADMINISTRATION WASHINGTON, DC 20546	14. Sponsoring Agency Code

15. Supplementary Notes

NASA LANGLEY TECHNICAL MONITOR: WAYNE BRYANT

16. Abstract

  This report presents the designs of Proportional-Integrated-Filter (PIF) auto-pilots for a General Aviation (NAVION) aircraft. The PIF autopilot uses the sampled-data regulator and command generator tracking to determine roll select, pitch select, heading select, altitude select and localizer/glideslope capture and hold autopilot modes. The PIF control law uses typical General Aviation sensors for state feedback, command error integration for command tracking, digital complementary filtering and analog prefiltering for sensor noise suppression, a control filter for computation delay accommodation and the incremental form to eliminate trim values in implementation. Theoretical developments described in detail, were needed to combine the sampled-data regulator with command generator tracking for use as a digital flight control system.

  The digital PIF autopilots are evaluated using closed-loop eigenvalues and linear simulations. The implementation of the PIF autopilots in a digital flight computer using a high order language (FORTRAN) is briefly described. The successful flight test results for each PIF autopilot mode is presented.

17. Key Words (Suggested by Author(s))	18. Distribution Statement
Optimal Control-Theory Optimal Control-Application Autopilot Digital Flight Control System General Aviation Flight Control System Model Following	Unclassified-Unlimited Subject Category 08

19. Security Classif. (of this report)	20. Security Classif. (of this page)	21. No. of Pages	22. Price
Unclassified	Unclassified	180	A09